

Structure of the Subduction System in  
Southern Peru from Seismic Array Data

Thesis by  
Kristin Phillips-Alonge

In Partial Fulfillment of the Requirements for the Degree  
of  
Doctor of Philosophy



CALIFORNIA INSTITUTE OF TECHNOLOGY  
Pasadena, California  
2013  
(Defended November 21, 2012)

© 2013  
Kristin Phillips-Alonge  
All Rights Reserved

**ACKNOWLEDGEMENTS**

Robert Clayton

Younghee Kim

Richard Guy

Paul Davis

Igor Stubailo

Steve Skinner

Hernando Tavera

Victor Aguilar

Laurence Audin

Tectonics Observatory at Caltech

NSF

**ABSTRACT**

Southern Peru represents a subduction transition region from normal subduction in the southernmost part of Peru to flat slab subduction in central Peru. In order to learn more about the structure of southern Peru, causes of flat slab subduction, and the nature of the transition from normal to flat slab subduction, we installed three seismic arrays utilizing a total of about 100 broadband stations. The first installed array samples the normal subduction region, while the second samples the transition from normal to flat subduction, and the third samples the flat slab region near where the Nazca Ridge is presently subducting. Data from teleseismic events greater than 30 degrees distance from Peru was analyzed using the receiver function method that makes use of P to S converted phases at interfaces such as the Moho to provide information about the structure directly beneath each station. A strong signal from the Moho was observed for each array and was found to have a maximum depth of around 75 km beneath the Altiplano. The average crustal  $V_p/V_s$  ratio was also estimated and was found to have an average value of around 1.75 beneath the Altiplano. The shape of the slab was also clarified for the three arrays. The transition from normal to flat slab subduction appears to be a contortion rather than a break in the slab. In addition to those signals, a positive impedance midcrustal signal at about 40 km depth was widely observed for stations on the eastern side of the arrays. The midcrustal signal is indicative of a velocity increase in the lower crust and is suggested to be an observation of the underthrusting Brazilian shield which would have implications for the timing of uplift in the Andes. Finite difference modeling with velocity models that include a midcrustal structure produces synthetics which are consistent with receiver function observations. Receiver function results and other related methods provide a simple way of making direct observations of key structural interfaces and the current state of the subduction system which has relevance in studies of the tectonic evolution of the region and estimations of causes of flat slab subduction.

## Table of Contents

Table of Figures and Illustrations.....	vii
Nomenclature .....	vii
<i>Chapter 1: Introduction and Summary</i> .....	1
Chapter 1 References .....	7
<i>Chapter 2: Normal Subduction Region</i> .....	10
Structure of the Subduction System in Southern Peru.....	10
From Seismic Array Data.....	10
Abstract.....	10
2.1. Introduction .....	11
2.2 Data, Methods, and Results .....	15
2.2.1 Receiver Functions.....	15
2.2.1.1 Receiver Function Results.....	20
2.2.1.2 Receiver Function Waveform Modeling.....	24
2.2.2 P-Wave Tomography .....	30
2.3 Discussion.....	33
2.3.1 Crustal Thickness .....	33
2.3.2 Midcrustal Structure .....	35
Conclusions .....	38
Acknowledgements: .....	39
Chapter 2 References .....	39
<i>Chapter 3: Subduction Transition and Flat Slab</i> .....	45
Structure of the Subduction Transition Region from Seismic .....	45
Array Data in Southern Peru .....	45
3.1. Introduction .....	46
3.2. Methods .....	50
3.2.1 Stations and Data.....	50
3.2.2 Receiver Functions.....	52
3.2.3 Finite Difference Modeling.....	54
3.3. Results.....	56
3.3.1 Line 2 Results: Transition From Normal to Flat Slab Subduction .....	56
3.3.2 Line 3 Results: Flat slab region .....	59
3.4. Discussion.....	63
3.4.1 Moho Depth and Vp/Vs.....	63
3.4.2 Slab Structure .....	65
3.4.3 Nazca Ridge and Causes of Flat Slab Subduction .....	70
Chapter 3 References .....	76
<i>Chapter 4: Methods and Other Results</i> .....	84
4.1: Field Work in Peru .....	84
4.1.1 Installation Procedure.....	85
4.1.2 Second and Third Arrays.....	86
4.2: Processing Methods and Receiver Function Methods .....	87

4.2.1: Processing procedure .....	91
4.2.2 Deconvolution methods .....	92
4.2.2.1 Frequency Domain Deconvolution.....	92
4.2.2.2. Time Domain Deconvolution.....	93
4.3 Phases used for RFs.....	99
4.3.1. P, PP, and PKP .....	99
4.3.2. S wave RFs.....	103
4.5 Transverse Receiver Function Components.....	107
4.6 Imaging Methods (Backprojection, CCP) .....	117
4.7 Finite Difference Modeling .....	120
4.8 Local Events and Future Study.....	123
4.8.1. Local Receiver Functions.....	126
4.8.2. Precursors to pP or sS.....	129
4.8.3. Modeling Local Events .....	135
4.8.4. Future Work: Determination of EQ Loc. and Focal Mechanisms.....	143
4.9 Summary and Conclusions.....	145
Chapter 4 References .....	147
Appendix A Chapter 2 Supplementary Figures .....	152
Appendix B Chapter 3 Supplementary Figures.....	157
Appendix C Chapter 4 Supplementary Figures.....	163
Bibliography .....	187

## Table of Figures and Illustrations

Figure 1.1 Map of Peru.....	2
Figure 2.1 Line 1 tectonic settings .....	12
Figure 2.2: Local seismicity .....	14
Figure 2.3: Location of events.....	16
Figure 2.4: Data example.....	17
Figure 2.5: Line 1 receiver function.....	18
Figure 2.6 Stacking method.....	19
Figure 2.7 P/PP receiver function image, all directions, upper 120km.....	21
Figure 2.8: Line 1 P/PP RF, Moho and Vp/Vs results .....	22
Figure 2.9: Line 1 PKP receiver function image .....	24
Figure 2.10: Finite difference modeling.....	26
Figure 2.11: Comparison of data and synthetic results.....	27
Figure 2.12: Local event FD waveform modeling.....	29
Figure 2.13 Tomography .....	31
Figure 2.14 Checkerboard test.....	32
Figure 2.15 Gravity results .....	34
Figure 2.16 Line 1 model .....	38
Figure 3.1 Array map.....	49
Figure 3.2 Lines 2 and 3 seismicity cross sections .....	51
Figure 3.3 Line 2 results .....	55
Figure 3.4 Line 2 CCP plot.....	57
Figure 3.5 Line 2 RF migration.....	58
Figure 3.6 Line 3 RF image.....	59
Figure 3.7 Line 3 CCP and PKP image .....	60
Figure 3.8 Line 3 FD modeling .....	61
Figure 3.9 Lines 2 and 3 Moho and Vp/Vs results .....	62
Figure 3.10 Moho and slab models in 3D.....	67
Figure 3.11 Comparison of FD models and synthetics for all arrays.....	69
Figure 3.12 Comparison of normal and flat slab images.....	71
Figure 3.13 Seismicity and elevation comparison, Flat/Normal subduction regions .....	73
Figure 4.1 Station installation.....	86
Figure 4.2 Data from the Sandwich Islands on 12/08/2010 .....	87
Figure 4.3 Processing methods, filtering .....	89
Figure 4.4 One versus two second filtered receiver functions .....	91
Figure 4.5 Time versus frequency domain deconvolution, line 3.....	94
Figure 4.6 Time versus frequency domain from CCP stacks.....	95
Figure 4.7 Time versus frequency domain receiver functions for 12/08/2010.....	97
Figure 4.8 PG40 time and frequency domain deconvolution.....	98
Figure 4.9 PG50 frequency versus time domain deconvolution .....	99
Figure 4.10 PE46 receiver functions, all phases (P, PP, and PKP).....	101
Figure 4.11 Comparison of P/PP images with PKP for Line 1 .....	103
Figure 4.12 S wave RFs, Line 1 .....	105
Figure 4.13 Stacking for Moho and Vp/Vs for PG05.....	107

Figure 4.14 Radial and transverse receiver functions for PF25 .....	109
Figure 4.15 Radial and transverse receiver functions for PF37 .....	110
Figure 4.16 Transverse RF stacks for PF25 from different azimuthal directions.....	111
Figure 4.17 Transverse RF stacks from the NW and SE for PF42 .....	112
Figure 4.18 Stations PF42 and PF43 axis of symmetry in transverse RFs .....	113
Figure 4.19 Stations PF29 and PF31 symmetry axis .....	114
Figure 4.20 Stations PF23 and PF24 symmetry axis .....	115
Figure 4.21 Stations PF12 and PF13 symmetry axis.....	116
Figure 4.22 CCP stacks from each azimuthal direction for Line 3 .....	1177
Figure 4.23 Backprojection for station PE46 .....	119
Figure 4.24 Image for Line 1 based on CCP stacks .....	120
Figure 4.25 Large earthquakes near arrays during time of array operation .....	124
Figure 4.26 Deep events which can be used for local receiver functions .....	125
Figure 4.27 Processing of local receiver function on 11/22/2011 .....	127
Figure 4.28 Local RF bandpassed to 2 sec. for Line 1, 2011/11/22.....	128
Figure 4.29 Local RF, 2011/11/22, bandpassed to 2 Hz .....	129
Figure 4.30 Large and deep events used for analysis of pP and sS precursors.....	130
Figure 4.31 Precursor to pP phase from 08/26/2008 event in N. Peru.....	132
Figure 4.32 Stack to find precursors to sS phase for event on 07/12/2009.....	133
Figure 4.33 More checks for pP precursors in Peru events .....	134
Figure 4.34 Data from 7/12/2009 bandpassed to 1 and 10 sec.....	135
Figure 4.35 Data from 9/05/2009 bandpassed to 1 and 10 sec.....	136
Figure 4.36 Data from 9/30/2009 bandpassed to 1 and 10 sec.....	137
Figure 4.37 Structural models for southern Peru .....	138
Figure 4.38 Finite difference synthetics for 2009/07/12 .....	140
Figure 4.39 Finite difference synthetics for 2009/09/05 .....	141
Figure 4.40 Finite difference synthetics for 2009/09/30 .....	142
Figure 4.41 CMT solutions for 10/28/2011 .....	1444
Figure A.1 PKP receiver functions .....	152
Figure A.2 P wave velocity models .....	153
Figure A.3 PKP versus P/PP slab.....	154
Figure A.4 Synthetic RF image.....	155
Figure A.5 Brazilian Shield/Line 1 model .....	156
Figure A.6 Initial model of Sheild.....	156
Figure B.1 Midcrustal signal .....	157
Figure B.2 Different slab models for Line 2.....	158
Figure B.3 Seismicity across Nazca Ridge .....	159
Figure B.4 Migrated images of Lines 1 and 3, interpreted.....	161
Figure B.5 RF migrations of Lines 1 and 3, uninterpreted.....	162
Figure C.1 The team .....	163
Figure C.2 Obtaining wireless connectivity.....	164
Figure C.3 Wireless links between sites .....	165
Figure C.4 Installation procedure .....	166
Figure C.5 Field challenges .....	167
Figure C.6 PF11 transverse RFs.....	168

Figure C.7 PF11 Transverse RFs, stacks from NE/SW and NW/SE.....	169
Figure C.8 Transverse RFs for PF12.....	170
Figure C.9 Transverse RFs for PF12, stacks/average for NW/SE .....	171
Figure C.10 Transverse RFs for PF13.....	172
Figure C.11 Transverse RFs for PF13, stacks/average for NE/SW .....	173
Figure C.12 Transverse RFs for PF23.....	174
Figure C.13 Transverse RFs for PF24.....	175
Figure C.14 Transverse RFs for PF29.....	176
Figure C.15 Transverse RFs for PF37.....	177
Figure C.16 Transverse RFs for PF37, stacks/averages for NE/SW and NW/SE .....	178
Figure C.17 Transverse RFs for PF39.....	179
Figure C.18 Transverse RFs for PF06.....	180
Figure C.19 Transverse RFs for PF07.....	181
Figure C.20 Radial and transverse RFs for PG27.....	182
Figure C.21 Radial and transverse RFs for PG40.....	183
Figure C.22 Radial and transverse RFs for PG42.....	184
Figure C.23 Figure 4.28, no interpretive lines .....	185
Figure C.24 Figure 4.29, no interpretive lines. ....	186

## NOMENCLATURE

**Subduction.** Describes the movement of two tectonic plates in which a denser plate is forced beneath the lithosphere of a less dense plate

**Normal subduction.** Subduction in which the descending plate subducts at an intermediate angle close to 30 degrees.

**Flat slab subduction.** Subduction in which the descending plate subducts at a very shallow angle of less than 10 degrees for a portion of the subduction length. For example a plate which initially starts off subducting at a steep angle near the trench but flattens out to subduct almost horizontally beneath the overriding plate for a distance of several hundred kilometers before resuming subduction at a steeper dip angle would be considered flat slab subduction.

**Underthrusting.** A process during compression in which one rock body is thrust beneath another relatively stable rock structure.

**Shield.** Typically refers to exposed precambrian igneous and metamorphic rocks that form the stable interior of the continent

**Moho.** Short for Mohorovičić Discontinuity, the boundary between the crust and mantle marked by a seismic velocity increase

**Tectonic plate/slab.** Consists of lithosphere which is able to move on top of the viscous asthenosphere and interacts with other plates in a variety of tectonic settings such as subduction zones, strike slip regions, or divergent settings. A tectonic plate or slab includes continental or oceanic crust as well as mantle lithosphere. When used in the context of receiver functions, “slab” or “slab signal” is sometimes used to reference the subducting oceanic crust which is marked by receiver function pulses. However the subducting plate is understood to include the full lithosphere.

## *Chapter 1: Introduction and Summary*

The following chapters provide details of the methods, analysis, results, and discussion of seismic data collected by arrays of seismic stations installed in southern Peru. Each chapter is structured as a self-contained paper and will have its own set of references at the end. The second chapter is in press with *Journal of Geophysical Research-Solid Earth*, while the third chapter was recently submitted to *Geophysical Journal International*.

The subduction style of the Nazca plate beneath South America varies along strike from areas of “normal subduction” where the slab dips at angles around  $25^{\circ}$ - $30^{\circ}$ , to areas of flat slab subduction where the Nazca plate subducts at an angle less than  $10^{\circ}$  beneath South America, as observed from seismicity in the Wadati-Benioff zone. Areas of normal subduction include southern Ecuador ( $\sim 0^{\circ}$ - $2^{\circ}$  S), southern Peru/northern Chile ( $\sim 15^{\circ}$ - $27^{\circ}$  S), and southern Chile ( $\sim 33^{\circ}$ - $45^{\circ}$  S). Areas of flat slab subduction include central and northern Peru ( $2^{\circ}$ - $15^{\circ}$  S), central Chile ( $\sim 27^{\circ}$ - $33^{\circ}$  S) and central Ecuador ( $0^{\circ}$ - $2^{\circ}$  N) (Barazangi and Isacks 1976). Southern Peru represents a transition from normal to flat slab subduction. Three seismic arrays were arranged roughly in the shape of a box to sample the region of normal subduction (perpendicular to the trench), transition from normal to flat slab subduction (parallel to the trench), and region of flat slab subduction (perpendicular to the trench).

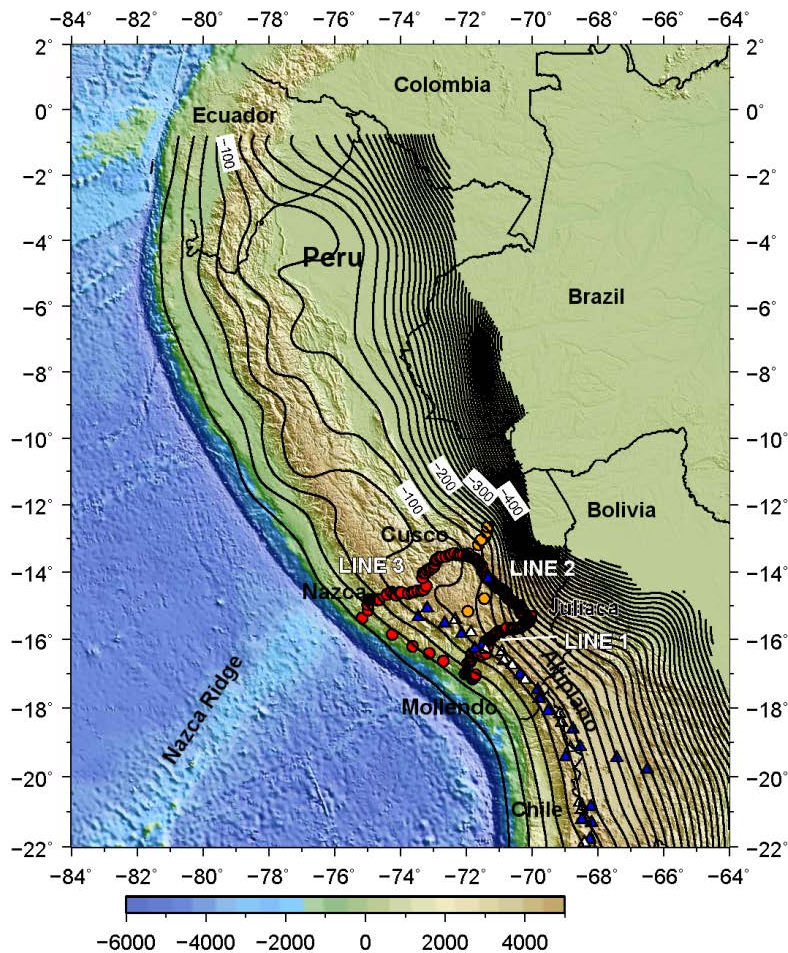


Figure 1.1. Topography and bathymetry map of Peru showing slab contours from the Slab 1.0 model. The seismic arrays are shown as red circles. Orange circles denote added stations from the CAUGHT/PULSE experiments. Dormant/active volcanoes are shown as blue/yellow triangles.

The purpose of the project is to clarify the structure beneath the arrays to learn more about the present state of the subduction system, compare the normal and flat slab regions, and study the nature of the transition between the two subduction regimes.

Overarching questions which stem from these observables are what are primary causes of flab slab subduction in Peru and what is the tectonic evolution of the area.

The array in the flat slab region is located near where the Nazca Ridge is presently subducting and can be useful in estimating the effect of the ridge on the subduction system. The thickened crust from subducting oceanic ridges, plateaus, and other such impactors has been suggested to be a possible cause or contributor to flat slab subduction by adding to the buoyancy of the subducting plate (Gutscher, Olivet, et al. 1999; Gutscher, Malavielle, et al. 1999, Gutscher et al. 2000; van Hunen et al. 2002a, 2002b, 2004; McGearry et al. 1985, and Rosenbaum and Mo 2011). This notion is supported by observations that many flat slab regions have corresponding buoyant impactors such as the Juan Fernandez ridge in Chile and the Carnegie Ridge in Ecuador. A difference between Peru and other flat slab regions is that the flat slab region in Peru is over 1500 km in length which is about three times the length of many other flat slab regions. The Nazca Ridge has been migrating south through time and is located near the southern end of the flat slab region but is not expected to have enough buoyancy to support the length of the flat slab region or keep the slab from returning to a normal dip angle in its wake.

The array in the normal subduction region intersects the present active volcanic arc which ends at the southern end of the flat segment where there is a volcanic gap. Gaps in volcanism are observable in many flat slab regions because the lack of asthenospheric wedge between the subducting and overlying plates inhibits partial melting (Gutcher, Malavielle, et al. 1999). A look at the migration of the volcanic arc through time provides information about the tectonic evolution of a region. For example when a steeply dipping slab begins to flatten, the arc is seen to advance or migrate inland away from the trench as is observed in Chile (Hascke 2002; Kay and Abbruzi 1996; Kay et al.

2005; Kay and Mpodozis 2002). As a flat slab begins to steepen again (or “roll back”), the volcanic arc is seen to move toward the trench which is thought to be happening in Mexico (Ferrari et al, 2001). In some areas both processes can be observed as the volcanic arc first migrates away from the trench and later migrates back to the trench as happened in western North America during the Laramide (Saleeby 2003). In Peru the volcanic arc was observed to move eastward before extinguishing (Soler and Bonhomme, 1990) and over time as the slab begins to steepen due to eclogitization and increasing pull from the already subducted material the arc will begin to migrate westward again.

The second chapter in this work presents results from “Line 1” running from Mollendo to Juliaca in the normal slab region where the slab is seen to be dipping at 30 degrees. The receiver function method is used to provide direct information about the structure beneath the stations. Signals are observed from the Moho at the base of the crust and the top of the subducting Nazca plate. One of the key observations is of a strong midcrustal positive impedance signal at 40 km depth beneath the eastern portion of the array where the Moho depth is observed to be around 70-75 km beneath the Altiplano. This is suggested to be a possible observation of the underthrusting of the Brazilian Shield which other authors have suggested underthrusts as far as the Eastern Cordillera (McQuarrie et al. 2005; Gubbels et al. 1993; Lamb and Hoke 1997; Beck and Zandt 2002). We suggest here that it underthrusts farther beneath southern Peru and even underlies a portion of the Altiplano. Such an observation has implications for the timing of uplift in the Altiplano. We suggest that the underthrusting of the Brazilian shield is more consistent with a gradual uplift model over the last 40 Ma rather than rapid uplift over the past 10 Ma caused by lithospheric delamination. Although such delamination and rapid uplift may

have occurred further south in the Andes in the Puna Plateau, we suggest that the dominant mechanisms for uplift in the Altiplano of southern Peru are crustal shortening accompanied by tectonic underthrusting from the Brazilian craton.

The third chapter presents results from “Line 2” and “Line 3” in the transition from normal to flat slab subduction and flat slab regions respectively. Line 2 shows the clearest signal from the midcrustal structure at 40 km depth. The shape of the slab is observed and is suggested to be a contortion rather than a tear in the slab. Results from Line 3 show the slab flattening out almost horizontally beneath the Altiplano at a depth of about 100 km. Results from this array are compared to the results from Line 1 in the normal subduction region.

The fourth chapter presents further details of the methods used including methods which are not presented in the papers. The results from this project are part of the PeruSE (Peru Seismic Experiment) which began with field work and installation of broadband seismic stations in 2008. The details of installation and seismic equipment used are presented. The second array was installed and began collecting data in late 2009 while half of the third array began collecting data in late 2010. The installation of the third array was completed in 2011. After the collection of seismic data, teleseismic events were analyzed with distances greater than 30 degrees and magnitudes greater than 5.8. The receiver function method was used to provide more information about the structure beneath the stations using deconvolution in the frequency domain. Both these results and results using iterative time domain deconvolution are described. Although most receiver function studies focus on P waves which convert to S waves at impedance contrasts, the

great distance of many events from Peru made it useful to be able to include PP and PKP phases. Results are compared using the various P-based phases to show the compatibility of the receiver functions using the different phases. In addition to P, PP, and PKP phases, S wave receiver functions were also attempted which have been used to look for the lithosphere-asthenosphere boundary (LAB). Multiple receiver functions for each station from similar azimuthal directions are stacked to obtain estimates for Moho depth and  $V_p/V_s$  from the maximum summation of receiver functions at the time of the converted phase and multiples. Although most of the analysis is done with radial receiver function, transverse receiver functions were also analyzed. The presence of energy on the transverse component can be suggestive of either a dipping interface or anisotropy. The structure beneath the stations, including interfaces such as the Moho and subducting oceanic crust can be clarified by plotting the amplitudes of receiver functions in cross section using methods such as backprojecting rays and CCP (common conversion point stacking). The backprojection method assumes an approximately linear ray path and plots the amplitudes of receiver functions from the direction in which the energy arrived so that each point along the receiver function is at the correct depth and distance from the station. The amplitude at any given point in the image is an average of the amplitudes of receiver functions which pass through that point. The CCP method is similar except it calculates the piercing point of the ray with the expected depth of the Moho. All other rays which pass through this region are stacked and the resulting stacks are plotted. The receiver function methods use an average P wave velocity model. Simple 2D velocity models are tested using finite difference modeling. Two different methods are used to model both teleseismic energy to produce synthetic receiver functions, and to model local

events allowing for the comparison of synthetic seismograms with data. Local events were also analyzed but further analysis of local earthquakes is an area for future study. In summary, the receiver function results shown in these chapters clarify the structure beneath southern Peru to elucidate the present state of the subduction system. Results are compared for the normal and flat slab regions which has implications for studying the causes of flat slab subduction. The transition from normal to flat slab subduction is also observed.

#### Chapter 1 References

- Barazangi, M., and B. L. Isacks (1976), Spatial distribution of earthquakes and subduction of the Nazca plate beneath South America, *Geology*, 4, 686–692.
- Beck, S., and G. Zandt (2002), The nature of orogenic crust in the Central Andes, *Journal of Geophysical Research*, 107, 2230.
- Ferrari, L., C. M. Petrone, and L. Francalanci (2001), Generation of oceanic-island basalt-type volcanism in the western Trans-Mexican volcanic belt by slab rollback, asthenosphere infiltration, and variable flux melting, *Geology*, 29 (6), 507-510.
- Gubbels, T., B. Isacks, and E. Farrar (1993), High-level surfaces, plateau uplift, and foreland development, Bolivian central Andes, *Geology*, 21, 695–698.
- Gutscher, M., J. Malavielle, S. Lallemand, J.-Y. Collot (1999), Tectonic segmentation of the North Andean margin: Impact of the Carnegie Ridge collision, *Earth and Planetary Science Letters* 168, 255–270.
- Gutscher, M., J. Olivet, D. Aslanian, J. Eissen, and R. Maury (1999), The “lost Inca Plateau”: Cause of flat subduction beneath Peru?, *Earth and Planetary Science Letters*,

- 171 (3), 335–341.
- Gutscher, M., W. Spakman, H. Bijwaard, and E. Engdahl (2000), Geodynamics of flat subduction: Seismicity and tomographic constraints from the Andean margin, *Tectonics*, 19 (5), 814–833.
  - Haschke M. (2002), Evolutionary geochemical patterns of Late Cretaceous to Eocene arc magmatic rocks in North Chile: implications for Archean crustal growth, EGU Stephan Mueller Special Publication Series, 2, 207–218.
  - Kay, S. M. & J. M. Abbruzzi (1996), Magmatic evidence for Neogene lithospheric evolution of the central Andean “flat-slab” between 30° S and 32° S, *Tectonophysics*, 259, 15–28.
  - Kay, S. M., E. Godoy, & A. Kurtz (2005), Episodic arc migration, crustal thickening, subduction erosion, and magmatism in the south-central Andes, *GSA Bulletin*, 117, (1/2), 67–88.
  - Kay, S. M. & C. Mpodozis (2002), Magmatism as a probe to the Neogene shallowing of the Nazca plate beneath the modern Chilean flat-slab, *Journal of South American Earth Sciences*, 15, 39–57.
  - Lamb, S., and L. Hoke (1997), Origin of the high plateau in the Central Andes, Bolivia, South America, *Tectonics*, 16 (4), 623–649.
  - McGearry S., A. Nur, and Z. Ben-Avraham (1985), Spatial gaps in arc volcanism: the effect of collision or subduction of oceanic plateaus, *Tectonophysics*, 119, 195–221.
  - McQuarrie, N., B. Horton, G. Zandt, S. Beck, and P. DeCelles (2005), Lithospheric evolution of the Andean fold-thrust belt, Bolivia, and the origin of the central Andean plateau, *Tectonophysics*, 399, 15–37.

- Rosenbaum, G., and W. Mo (2011), Tectonic and magmatic responses to the subduction of high bathymetric relief, *Gondwana Research*, 19, 571–582.
- Saleeby, J. (2003), Segmentation of the Laramide Slab—evidence from the southern Sierra Nevada region, *GSA Bulletin*, 115, 6, 655–668.
- Soler, P. & M. Bonhomme (1990), Relation of magmatic activity to plate dynamics in central Peru from Late Cretaceous to present, Geological Society of America, Special paper 241.
- van Hunen, J., A. van den Berg, and N. Vlaar (2002a), The impact of the South American plate motion and the Nazca Ridge subduction on the flat subduction below South Peru, *Geophysical Research Letters*, 29 (14).
- van Hunen, J., A. van den Berg, and N. Vlaar (2002b), On the role of subducting oceanic plateaus in the development of shallow flat subduction, *Tectonophysics*, 352, 317–333.
- van Hunen, J., A. van den Berg, N. Vlaar (2004), Various mechanisms to induce present-day shallow flat subduction and implications for the younger Earth: a numerical parameter study, *Physics of the Earth and Planetary Interiors* , 146, 179–194.

## *Chapter 2: Normal Subduction Region*

### **Structure of the Subduction System in Southern Peru from Seismic Array Data**

<sup>1</sup>Kristin Phillips, <sup>1</sup>Robert W Clayton, <sup>2</sup>Paul Davis, <sup>4</sup>Hernando Tavera, <sup>2</sup>Richard Guy,  
<sup>1</sup>Steven Skinner, <sup>2</sup>Igor Stubailo, <sup>3</sup>Laurence Audin, <sup>4</sup>Victor Aguilar

<sup>1</sup>Caltech Seismological Laboratory, Pasadena CA, United States

<sup>2</sup>UCLA Center for Embedded Networked Sensing, UCLA, Los Angeles, CA, United States

<sup>3</sup>IRD, Casilla 18-1209, Lima 18, Peru

<sup>4</sup>Instituto Geofisico del Peru, Lima, Lima 100, Peru

#### **Abstract**

The subduction zone in southern Peru is imaged using converted phases from teleseismic P, PP, and PKP waves and P wave tomography using local and teleseismic events with a linear array of 50 broadband seismic stations spanning 300 km from the coast to near Lake Titicaca. The slab dips at 30 degrees and can be observed to a depth of over 200 km. The Moho is seen as a continuous interface along the profile and the crustal thickness in the back-arc region (the Altiplano) is 75 km thick, which is sufficient to isostatically support the Andes, as evidenced by the gravity. The shallow crust has zones of negative impedance at a depth of 20 km, which is likely the result of volcanism. At the midcrustal level of 40 km, there is a continuous structure with a

positive impedance contrast, which we interpret as the western extent of the Brazilian Craton as it underthrusts to the west. The  $V_p/V_s$  ratios estimated from receiver function stacks show average values for this region with a few areas of elevated  $V_p/V_s$  near the volcanic arc, and at a few points in the Altiplano. The results support a model of crustal thickening in which the margin crust is underthrust by the Brazilian Shield.

## **2.1. Introduction**

The subduction of the Nazca plate in southern Peru represents a transition region from a shallow-dip system in northern and central Peru to normal-dip in southern Peru (Barazangi and Isacks, 1976; Norabuena et al., 1994). Similar alternating sequences are representative of the subduction of the Nazca plate beneath South America, which have evolved with time (Ramos, 2009). The flattening of the slab in northern and central Peru has been proposed to be due the subduction of the Nazca Ridge (Gutscher et al., 2000) which has been sweeping southward over the past 10 Myr due to its oblique subduction direction. The subduction angle between the Nazca and South American plates is about 77 degrees resulting in a normal component of subduction of 6.1 cm/yr and tangential velocity of 4.3 cm/yr (Hampel, 2002). The slab has been progressively flattening in the wake of this feature, and its present configuration is shown in figure 2.1, which shows the depth contours of the slab. Also shown is the location of the volcanic arc, which is extinguished in the flat slab regime.

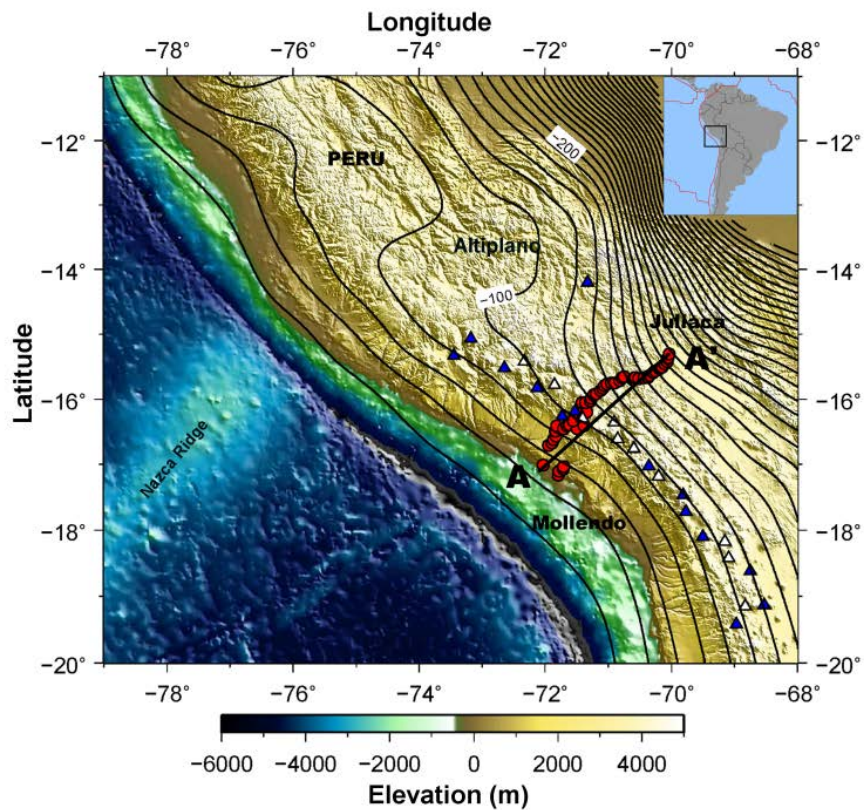


Figure 2.1. Topography and bathymetry of Peru showing the location of the subducting Nazca Ridge and the Altiplano of the central Andes. Variations in the dip angle of the Nazca plate can be seen through a contour model based on fits to seismicity. The locations of seismic stations installed in Peru as part of this study are denoted by red circles. The black line A-A' shows the location of the cross section plotted in Figure 2. Active and dormant volcanoes are denoted by blue and white triangles. The volcanic arc is located in the region of normal subduction dip angle in southern Peru while a volcanic gap is observable in the flat subduction regime in central and northern Peru.

In this chapter, we focus on the region of normal-dip subduction south of Nazca Ridge that we assume represents the subduction system before the flattening process.

According to Ramos (2009) this region has experienced uninterrupted normal subduction for the past 18 million years. An alternate model for the flattening of the

slab suggests that this zone has a natural cycle of normal/shallow subduction that is driven by lithospheric delamination (DeCelles et al., 2009). This process is also proposed as the cause of the rapid rise of the Andes in the last 10 Ma (Gregory-Wodzicki, 2000; Garzzone et al., 2006, 2008; Ghosh et al., 2006), however, more recent studies now propose the rise was a continuous process over the last 40 Ma., thus obviating the need of a rapid process such as delamination (Barnes and Ehlers, 2009; Ehlers and Poulsen, 2009; McQuarrie et al., 2005; Elger et al., 2005; Oncken et al., 2006). Results from this study support underthrusting of the Brazilian shield beneath Peru (McQuarrie et al., 2005; Allmendinger and Gubbels, 1996; Horton et al., 2001; Gubbels et al., 1993; Lamb & Hoke, 1997; Beck & Zandt, 2002), which is more consistent with a gradual uplift model for this section of the Altiplano. The eclogitization which would occur in the case of delamination needs a significant amount of water (Ahrens & Shubert, 1975; Hacker, 1996), which is not present in the Brazilian shield crust (Sighinolfi, 1971). Low silicic content also supports eclogitization since the water content of hydrous minerals increases with decreasing silica and increasing alumina (Tassara, 2006). Both argue that the granulites of the lower Brazilian shield (Sighinolfi, 1971) would be stable as we find here.

To image the subduction zone, a linear array of 50 stations was deployed perpendicular to the subduction trench for a distance of 300 km, with an average interstation spacing of 6 km. This configuration was chosen to provide an unaliased image of the system from the lower crust to the slab. The slab dip is well defined by seismicity down to a depth of 250 km where there is a gap in seismicity. Cross sections and event locations of earthquakes in Southern Peru are shown in figure 2.2.

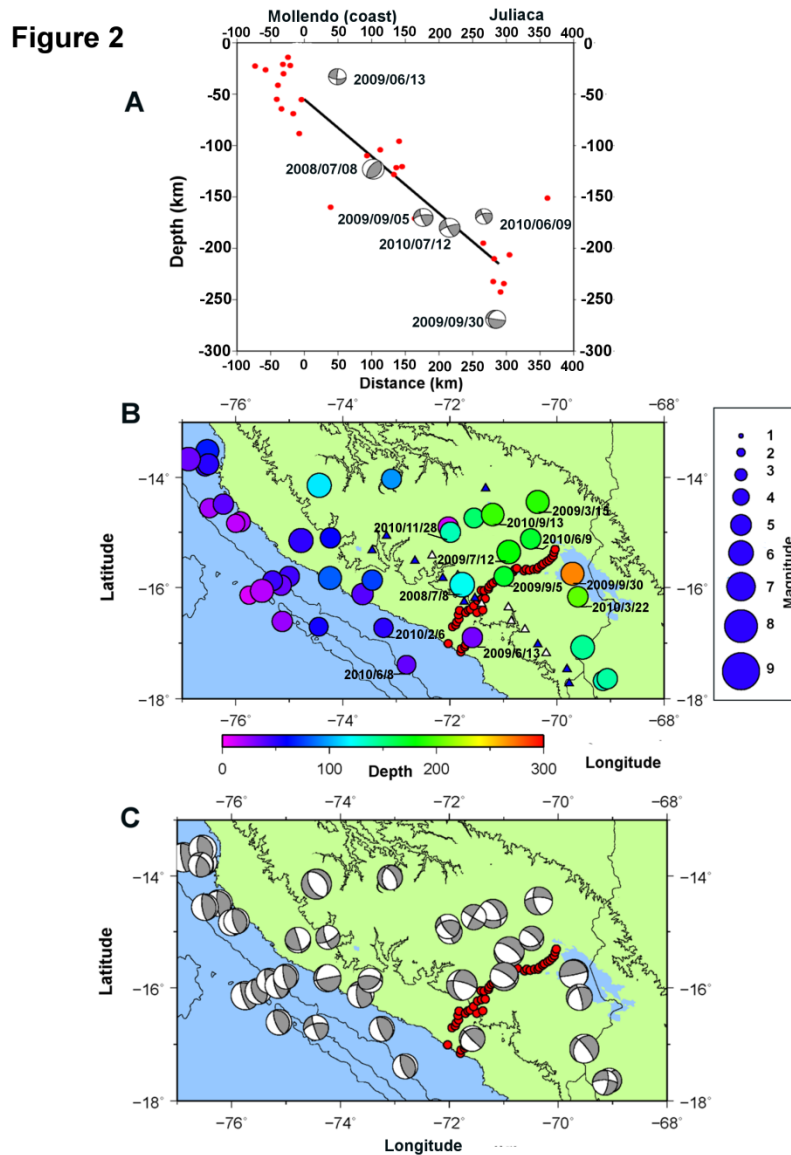


Figure 2.2. (A) Seismicity cross section along the seismic array. Hypocenters projected along the trend of the array are located within 60 km of the line. Earthquakes are from the EHB catalog (Engdahl et al. 1998; Engdahl & Villaseñor 2002) and are of magnitudes of 5.0 or greater. The black line is the location of the slab from receiver functions. Also shown are the focal mechanisms for several events near the line from the Harvard CMT dataset. (B) Locations of local earthquakes, as located by the Instituto Geofísico del Perú (IGP), which have occurred since the installation of the seismic arrays in Southern Peru. Small red circles denote the location of seismic stations. The size of the circles representing earthquake locations is scaled by magnitude and the color corresponds to depth. (C) Focal mechanisms of events from the Harvard CMT database for events shown in B.

In this study, we present a detailed image of the slab and lithosphere based on receiver functions and tomography that establishes the basic structure and properties of the normal-dipping part of the subduction in this region.

## **2.2 Data, Methods, and Results**

### **2.2.1 Receiver Functions**

The analysis in this paper is based on over two years of data (June 2008 to August 2010) recorded on the array shown in figure 2.1. The receiver functions utilize phases from teleseismic earthquakes with distance-magnitude windows designed to produce satisfactory signal to noise with minimal interference by other phases. The phases and their windows are: P-waves ( $>5.8$  Mw, 30–90 degrees), PP-waves ( $>6.0$  Mw, 90–180 degrees) and PKP waves ( $>6.4$  Mw, 143–180 degrees). In total there were 69 P-phases, 69 PP-phases, and 48 PKP-phase events used and their distribution shown in figure 2.3.

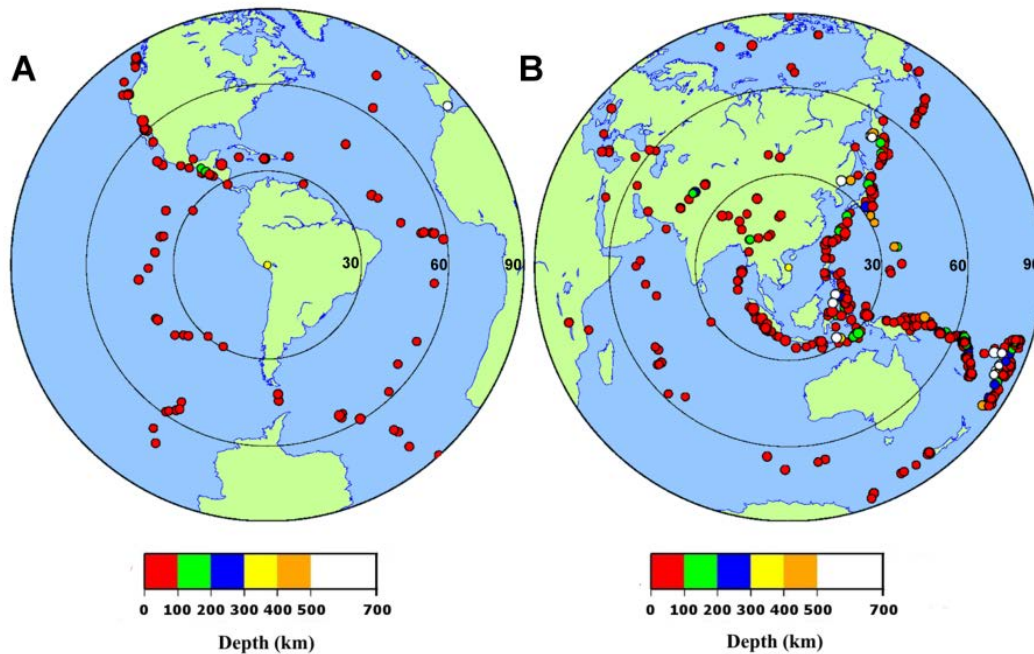


Figure 2.3. Location of events used in this study. (A) Teleseismic events between 30 and 90 degrees distance from Peru were used to make P-wave receiver functions. (B) Events greater than 90 degrees from Peru. The more distant events were used for studying converted arrivals of PP or PKP phases.

PKP phases were used because of the large number of useable events that are greater than 90 degrees from Peru (figure 2.3). Due to the almost vertical arrival angle of these phases, no conversion is expected at horizontal interfaces such as the Moho, however PKP phases are useful for imaging dipping interfaces such as the slab. Events were selected according to signal quality after bandpass filtering from 0.01 to 1 Hz. Similar, but less resolved results were obtained for a 0.01 – 0.5 Hz passband. An example of the data quality is shown in figure 2.4.

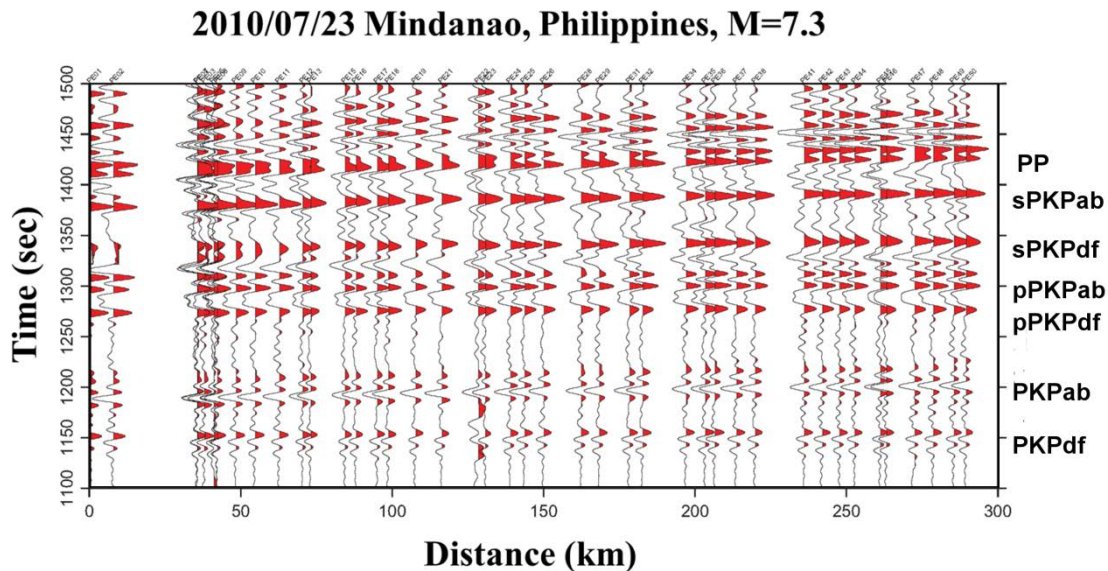


Figure 2.4. Seismic data measured by the array from the magnitude 7.3 earthquake in the Philippines which occurred on July 23, 2010. This section of the seismogram includes arrivals of PKP phases. Some phases are identified on the right of the record section. The distance axis represents distance from a reference point near the end of the seismic line closest to Mollendo on the coast and the time axis gives time after the origin time of the event. The bandpass filter used is from 0.01 to 1 Hz. See supplemental material for an example of a receiver function using the PKP phase.

Receiver functions are constructed by the standard method described in Langston (1979) and Yan and Clayton (2007). Source complexities and mantle propagation effects are minimized by deconvolving the radial component with the vertical.

Frequency-domain deconvolution (Langston, 1979; Ammon, 1991) was used, with a water level cutoff and Gaussian filter applied for stability. A time window of 120 seconds, a water level parameter of 0.01 and Gaussian filter width of 5 seconds were used during the deconvolution process. The processing of PKP receiver functions was similar to P and PP phases with the same factors used for deconvolution. Both PKPab and PKPdf branches were included in the analysis. An example of the RFs can be seen

in figure 2.5, which shows stacked RFs from a NW azimuth to Peru, as well as a single event occurring in New Zealand using the PP phase for comparison.

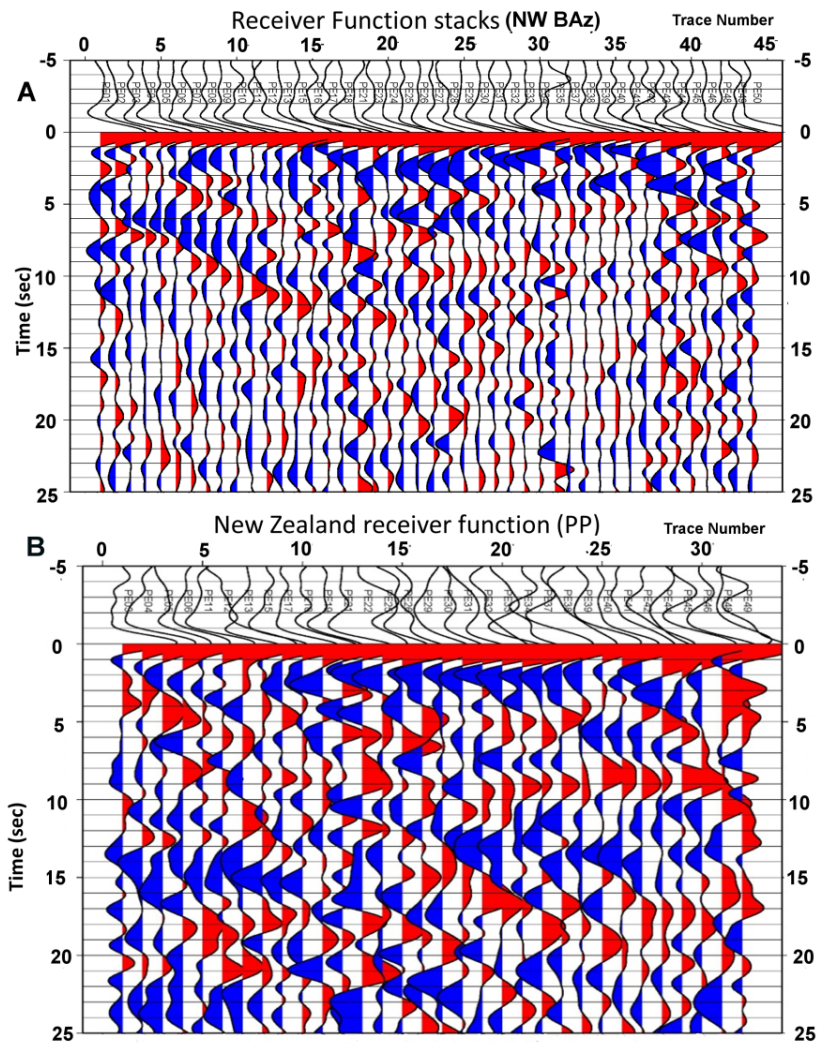


Figure 2.5. (A) The top set of receiver functions shows a stack for each station from events located at a northwest back azimuth from Peru. (B) The bottom receiver functions come from a magnitude 7.6 New Zealand earthquake on July 15, 2009. Time is shown on the y-axis with the P wave arrival occurring at time equals zero. The first positive pulse at 5 sec (corresponding to a depth of about 40 km) corresponds to a midcrustal structure. The next arrival which reaches a maximum time of about 9 seconds (70 to 74 km depth) represents the P-s conversion at the Moho. The deepest arrival dipping at about 30 degrees corresponds to a signal from the subducting slab.

RFs are stacked using the method of Zhu and Kanamori (2000) which uses the converted phase and multiples to obtain estimates of the depth of an interface and average  $V_p/V_s$  ratio above the interface by summing along moveouts of the converted phases as a function of ray parameter (Zhu and Kanamori, 2000). A search is done over a range of depths and  $V_p/V_s$  ratios based on stacks of many events from similar backazimuths. Figure 2.6 shows an example of stacking and grid search for individual stations. Uncertainty estimates are based on the 95 percent confidence interval.

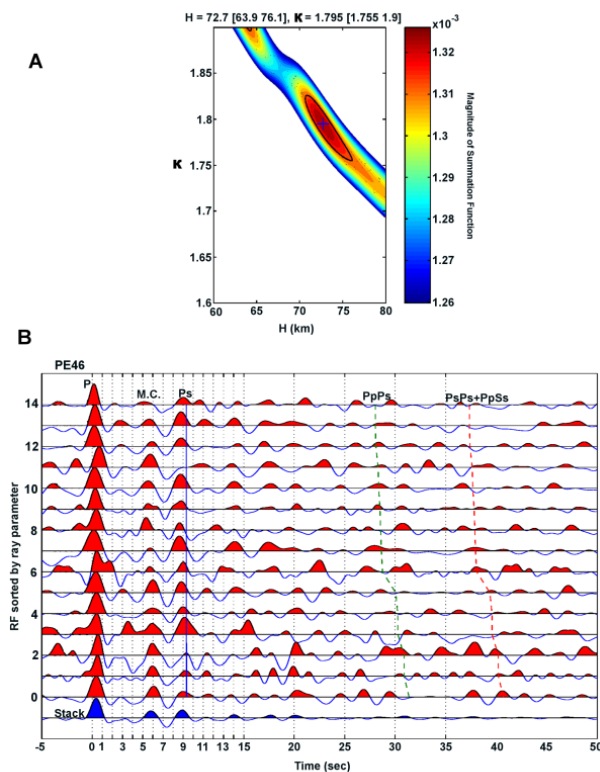


Figure 2.6. Example of stacking method for a single station (PE46). (A) The top figure is the grid search result corresponding to the maximum summation of the seismograms below over a given depth and  $V_p/V_s$  range.  $H$  is the depth to the discontinuity (below mean sea level) and  $\kappa$  is the  $V_p/V_s$  ratio. (B) The stack determines the maximum summation for the P-s converted phase (denoted Ps) and multiples (PpPs and PsPs/PpSs) which are denoted by dashed lines.

A simple migrated image is then constructed by backprojecting the receiver functions along their ray paths. The angle from the station is estimated using the ray parameter and event backazimuth, with corrections for the station elevation. A simple layered velocity model based on IASP91 was used to backproject the rays. This approximation was checked by comparison with other velocity models based on tomography and a thicker crust but the migrated images were found to have Moho depths similar to the results presented here.

#### **2.2.1.1 Receiver Function Results**

An image based on teleseismic P and PP receiver functions produced from data recorded by the seismic array with events from all azimuths is shown in figure 2.7. The Moho has an initial depth of around 25 km near the coast and deepens to around 75 km depth beneath the Altiplano. Also evident is a positive impedance midcrustal signal at around 40 km depth.

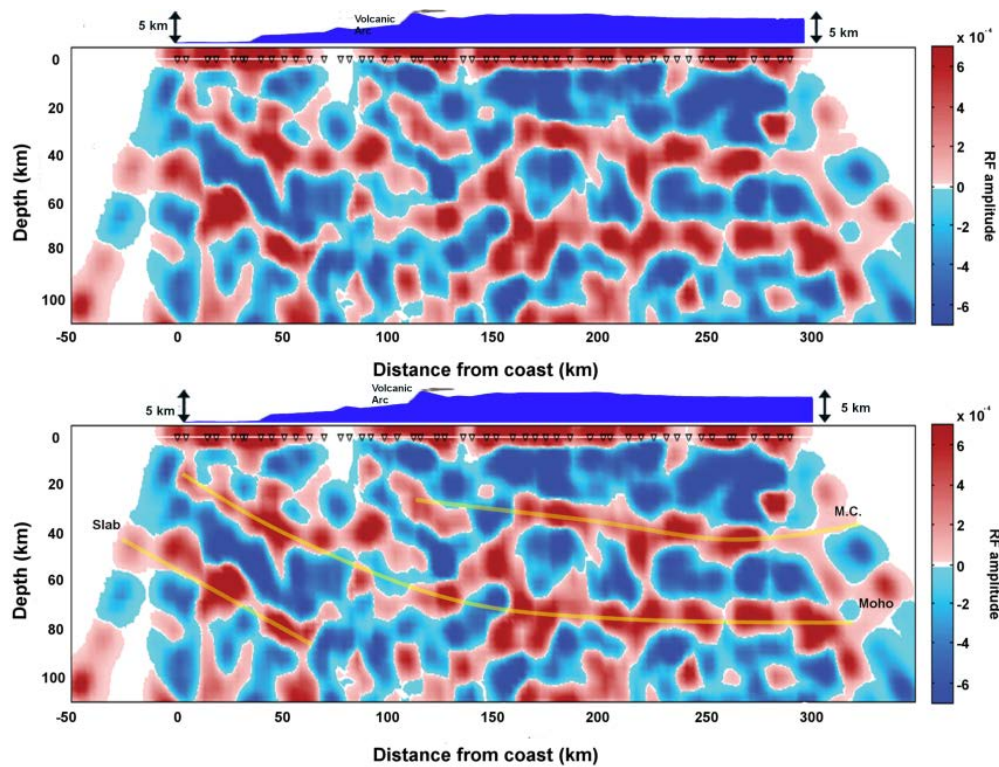


Figure 2.7. (A) Depth versus distance cross sectional image from Line 1 based on teleseismic P and PP receiver functions from all azimuthal directions showing the upper 120 km. Depth is the distance below mean sea level. (B) Same as in A showing interpretations of the mid crustal structure (MC) and Moho as well as a signal from the slab.

The subducting slab can be clearly observed in figure 2.8, which is a stack of data from the northwest azimuth. Receiver functions were stacked to obtain the depth of the Moho by the method of Zhu and Kanamori (2000) as shown in figure 2.6, and the resulting depth estimates are shown in figure 2.8, superimposed on the RF image. Also shown are the crustal  $V_p/V_s$  ratios along the line, which have an average value of around 1.75. There are three zones of elevated  $V_p/V_s$  ratios in the Altiplano, one of which corresponds to the current arc. These are coincident with negative impedances in the upper crust determined from receiver functions (see figures 2.5 and 2.7) and

hence are likely related to magmatic processes. This identification is clearest for the anomalies associated with the current arc. The other two may indicate the location of focused magmatic activity in the past. Similar features were observed in northern Chile (Leidig and Zandt, 2003; Zandt et al., 2003). The dense station spacing allows for an unambiguous tracing of the Moho, slab, and midcrustal feature.

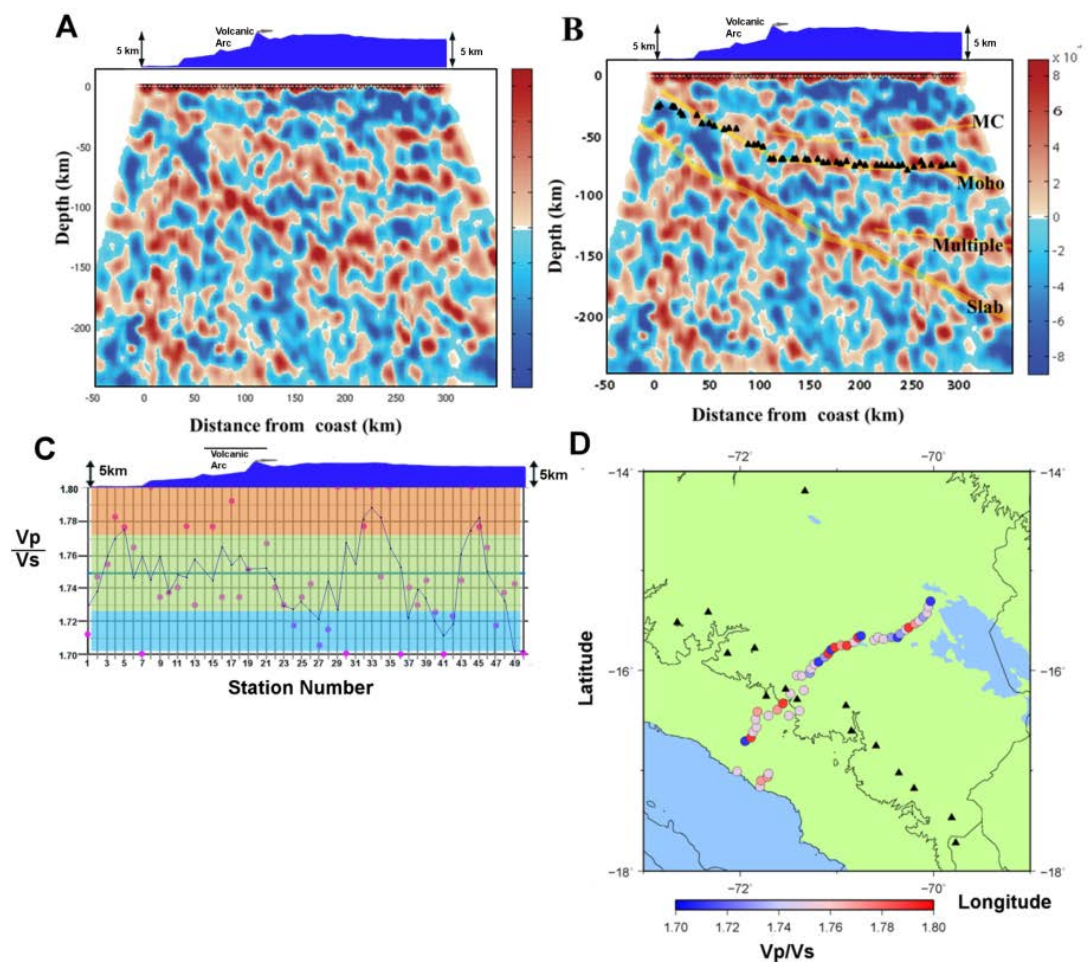


Figure 2.8. (A) Teleseismic P-wave Receiver function image based on events at a northwest azimuth to Peru with elevation along the array shown above. (B) Same image showing interpretation of the Moho, midcrustal structure, slab, and multiple of the midcrustal signal. Moho receiver function stacking results are plotted over the image. Elevation along the seismic line is shown above the image. (C) Average crustal

Vp/Vs values (y-axis) versus station number (proxy for distance). Orange shading represents high Vp/Vs values, green shading represents mid-range values, and light blue shading represents lower Vp/Vs values. The blue line shows the three-point running average of the Vp/Vs values. (D) Map of southern Peru showing a line with colors representing Vp/Vs ratios estimated from stacking of receiver functions. Black triangles represent active and dormant volcanoes in arc.

Receiver functions based on the PKP phase show a negative pulse corresponding to the top of the oceanic crust of the descending slab closely followed by a positive pulse at the transition to oceanic mantle. From the teleseismic P and PP phase receiver function results, this double pulse seen in the slab is observed most strongly down to a depth of around 100 kilometers. The receiver function images are consistent with the results of Kawakatsu and Watada (2007), which suggests that this is related to the transport of hydrous minerals in oceanic crust into the subduction zone. The transition between these signals is consistent with the location of the subducting Nazca plate as described by seismicity in the Wadati-Benioff zone (figure 2.9). The seismicity is centered near the transition between the positive and negative pulses. Note a phase difference in the slab signal between the PKP image and P/PP images due to a change in sign of the converted phase because of the steep angle of incidence of incoming PKP waves (see supplementary material) has been corrected.

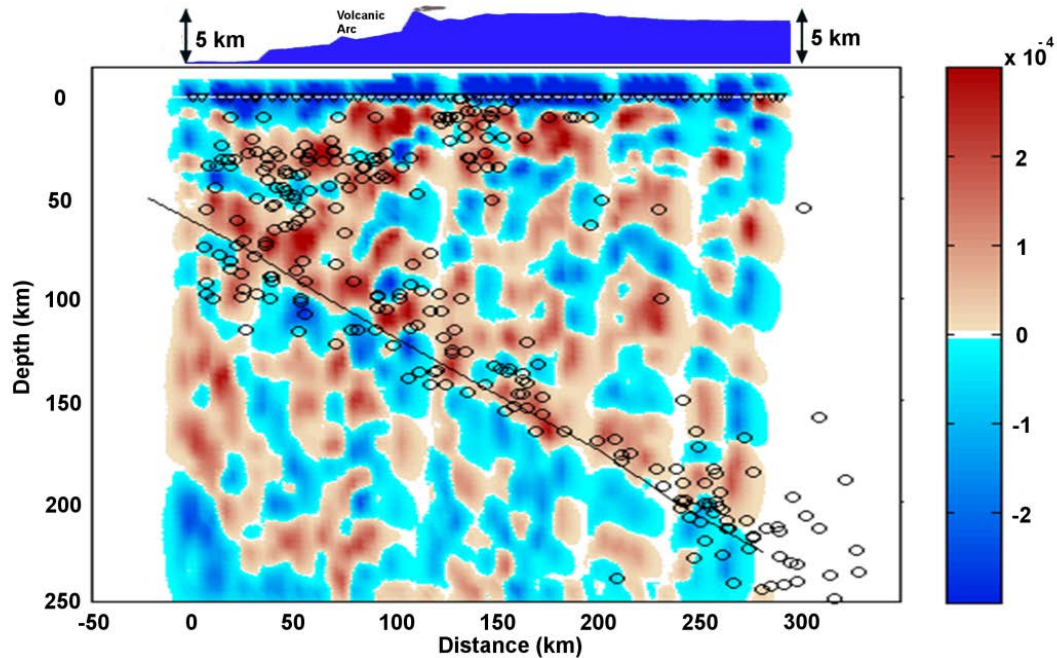


Figure 2.9. Backprojected receiver function image based on PKP receiver functions. Only the PKP<sub>df</sub> branch is included in this image. All events used come from the Indonesian region. Images show a sharp, well defined boundary at the expected location of the slab based on seismicity. Depth is the distance below mean sea level and distance is measured from the first station on the coast. Topography is shown above the image in blue.

### 2.2.1.2 Receiver Function Waveform Modeling

The receiver function images obtained above were checked using 2D finite-difference waveform modeling (Kim et al. 2010). The 2D velocity model includes depth information based on receiver function results and velocities consistent with averages taken from Cunningham and Roecker (1986) for southern Peru, which we modified to include a midcrustal layer contrast to model the positive-impedance feature. The more recent model of Dorbath et al. (2008) was also tested and compared with the southern Peru model (shown in the supplementary materials) and the results are similar to those shown here. A simplified velocity model, which incorporates average values consistent with these models for the crust, mantle wedge, subducting oceanic crust, and

underlying mantle was selected for modeling purposes. The model has dimensions of 500 km horizontal distance by 250 km depth. Synthetic receiver functions are produced with P-wave plane waves with varying ray parameters imposed on the bottom and sides of the model. Seismograms were produced with frequencies up to 1 Hz, and then processed as RFs with the same techniques and parameters used with the real data. A comparison of the synthetic and real receiver functions is shown in figure 2.10.

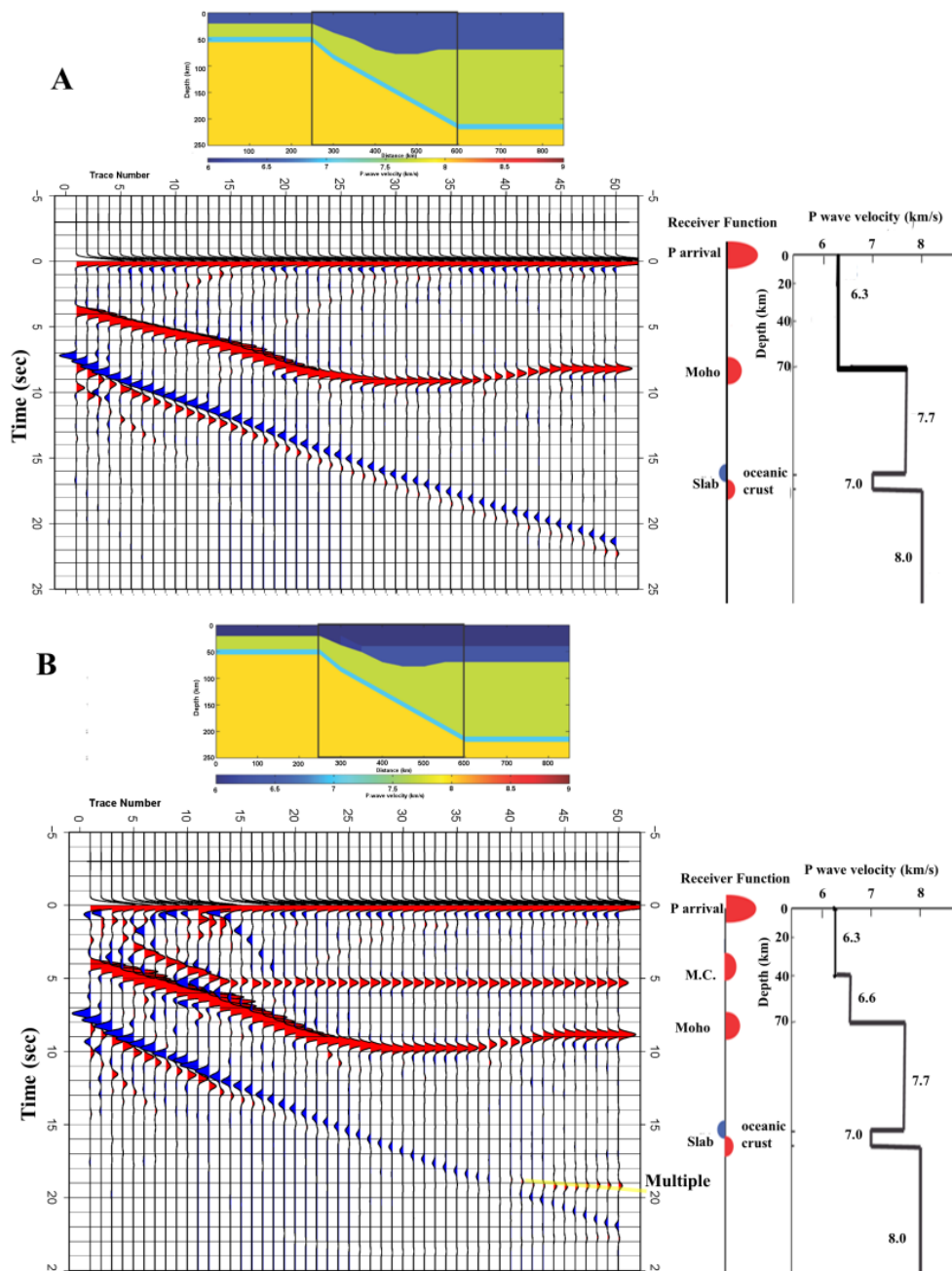


Figure 2.10. Velocity model and synthetic receiver functions obtained from finite difference modeling. To the right of the synthetics is an example of a receiver function and velocity model taken from the center of the model. A) Model with a homogenous crust, which recreates the Moho and slab signal as seen in receiver functions. B) Model that includes a midcrustal velocity jump recreates both the positive midcrustal signal seen at around 5 seconds and a multiple that also seen in the data. The signal from the Moho and slab are similar to the homogenous crustal model.

The synthetics, which incorporate midcrustal structure are observed to be consistent with RF data and results as seen in figure 2.11. They show a positive signal at around 5 seconds (midcrustal), which is observed in the receiver functions as well as an observed multiple that is not present in models without the midcrustal structure.

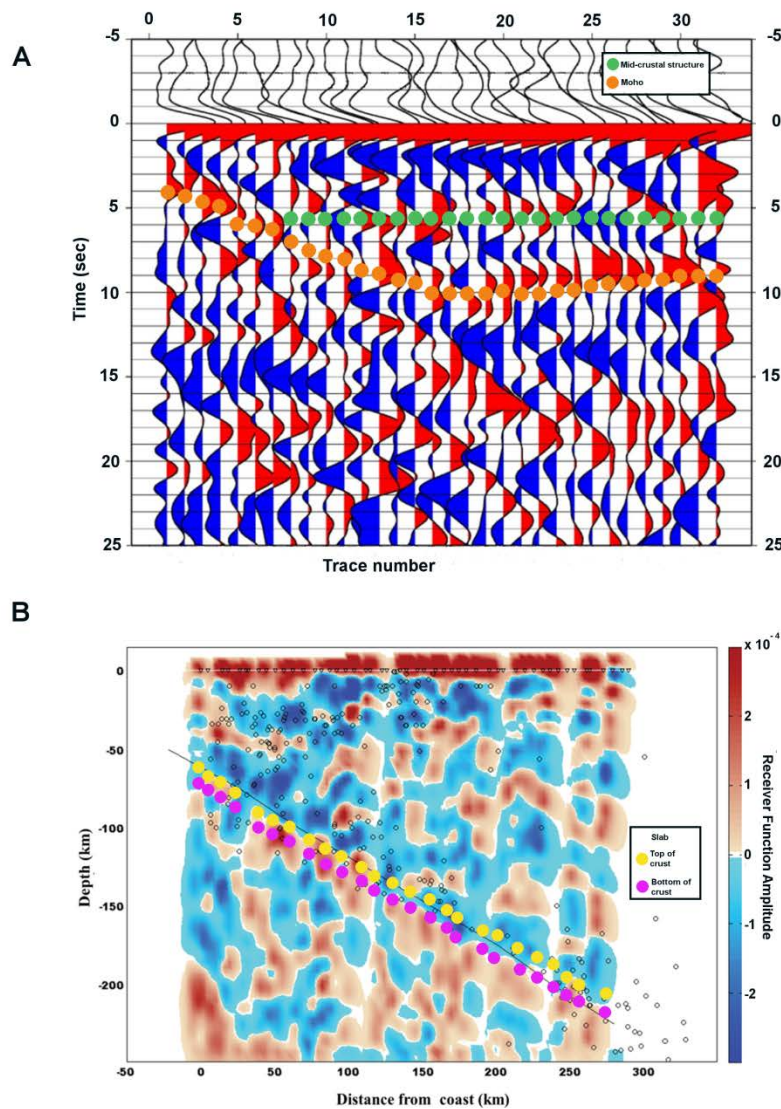


Figure 2.11. (A) Synthetic RF results from finite difference modeling are plotted over a sample receiver function from the magnitude 7.6 New Zealand earthquake on July 15, 2009 shown in figure 2.5. Green circles represent the midcrustal structure and orange

circles denote the depth of the Moho from synthetics. (B) Positive and negative pulses corresponding to the bottom and top of the oceanic crust of the slab as seen in FD synthetics are shown as magenta and yellow circles overlaying the PKP image from figure 2.10.

The velocity is then combined with a structural model derived from the receiver functions and is tested with a deep local event that occurred beneath the array on the slab interface (figure 2.12). The finite difference code is based on the one discussed in Vidale et al. (1985). The event is Mb 6.0 and is located at a depth of 199 km and about 60 km off the line. The resultant synthetics from finite difference modeling have P wave arrival characteristics and differential P to S wave travel times consistent with the data. The synthetics and data also have a similar arrival caused by a conversion at the Moho which provides confirmation of the Moho depth. An arrival due to phase conversions at the midcrust can be seen in the synthetics and also appears to also be present in the data, particularly towards the inland end of the seismic array suggesting that the midcrustal structure does not underlie the entire seismic array in agreement with receiver function observations.

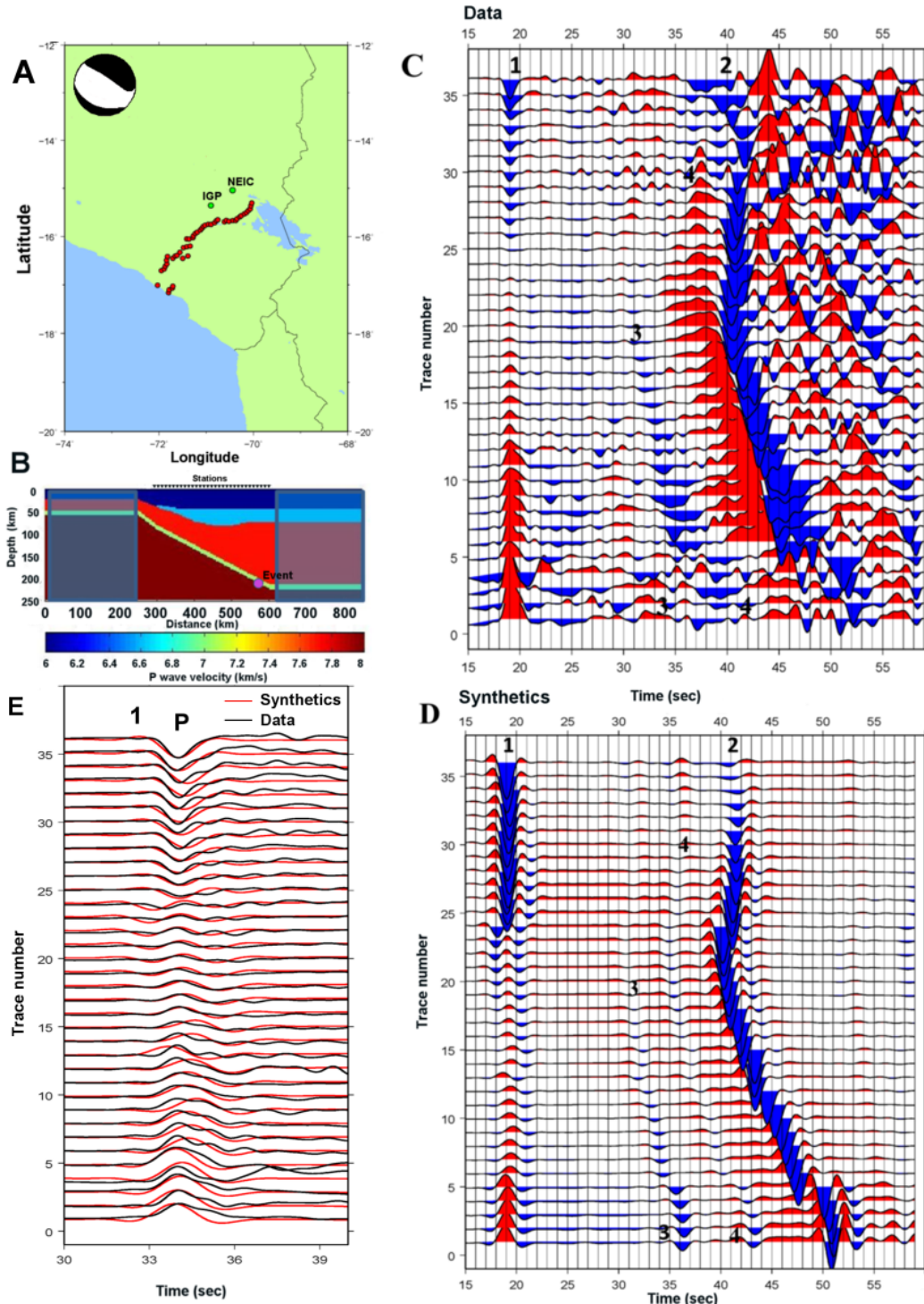


Figure 2.12. Local waveform finite-difference modeling of local event near end of Line 1 A) Map showing event locations provided by National Earthquake Information Center (NEIC) and Instituto Geofísico del Perú (IGP). Also shown is the centroid moment tensor from the Harvard CMT database. B) Model used in the finite-difference

modeling. Shaded portions are extensions of the model to avoid artificial reflections. The location of the event at about 199km depth is shown by the pink circle. C) Data from a magnitude 6 event occurring on July 12, 2009 aligned by the P wave arrival (1). Time is on the x-axis and distance from coast is on the y-axis. D) Synthetics also aligned on the P wave arrival (1). The S wave arrival (2) can also be seen as well as signals from the Moho (3) and midcrustal interface (4). E) Comparison of data and synthetics near the P wave arrival where the synthetics are in red and the data is shown by the black line.

### **2.2.2 P-Wave Tomography**

A total of 5677 travel-time residuals including 1674 teleseismic arrivals and 4003 local event arrivals were inverted to obtain the tomographic image shown in figure 2.13 using a 2D tomography program (Husker and Davis, 2009). The local events are restricted to depths greater than 30 km, and with 125 km of the 2D line. The 2D assumption appears justified by gravity based on gravity survey results (Fukao et al. 1989) and GRACE (Gravity Recovery and Climate Experiment) satellite data which show little along-strike gravity variation indicating an approximately 2D crust, as well as seismicity slab contours which show that the slab can also be considered approximately 2D within about 100km of the array. The local earthquakes were first located with an IASPEI (Kennett and Engdahl 1991) model that took into account the changing Moho depth determined by receiver functions. A finite-difference program was then used to relocate the events (Hole and Zeldt, 1995). The inversion consisted of 680 20 km blocks (20x34) and was performed with damped least squares. In the upper 350 km; the average number of hits/block was 142. The variance reduction was 88%. The final image was smoothed with a 2x2 block running average.

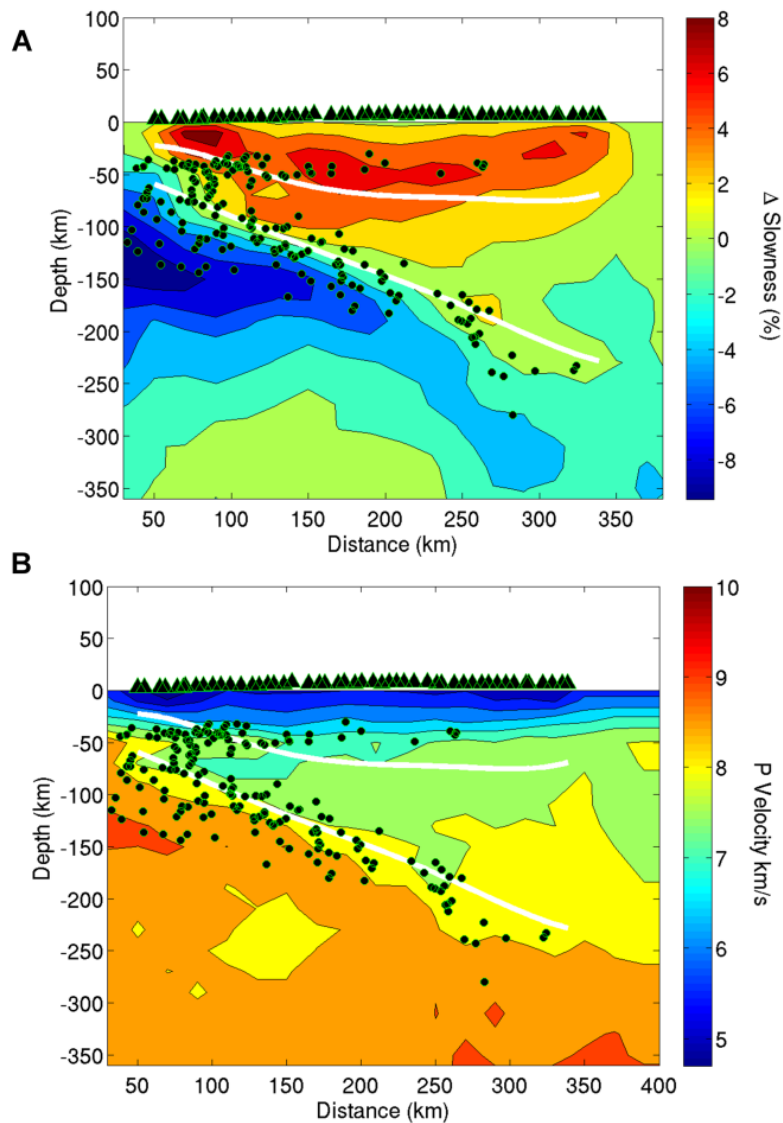


Figure 2.13. Tomographic image beneath the seismic line using a 2D tomography code. In A) the results are percent slowness changes from the IASPEI model, and in B) the result is in absolute velocity. Locations of the Moho and top of the Slab from the receiver function study are plotted as white lines. Station locations are shown as black triangles and local earthquake locations used for tomography are shown as black circles. The image supports the model of a steeply dipping slab and thickened Moho.

The tomography results are presented in figure 2.13. Figure 2.13A shows perturbations as percent deviations relative to the IASPEI starting model while figure 2.13B shows the absolute P wave velocity. The cross section chosen lies along a straight line

through the station locations. For comparison, locations of the Moho and top of the subducting slab from the receiver function analysis are superimposed on the figure and show good agreement with the transitions in the image from low to higher velocities. A standard checkerboard resolution test is shown in figure 2.14. The results are well resolved in both the horizontal and vertical directions except at depth greater than 350 km on the northern end of the line.

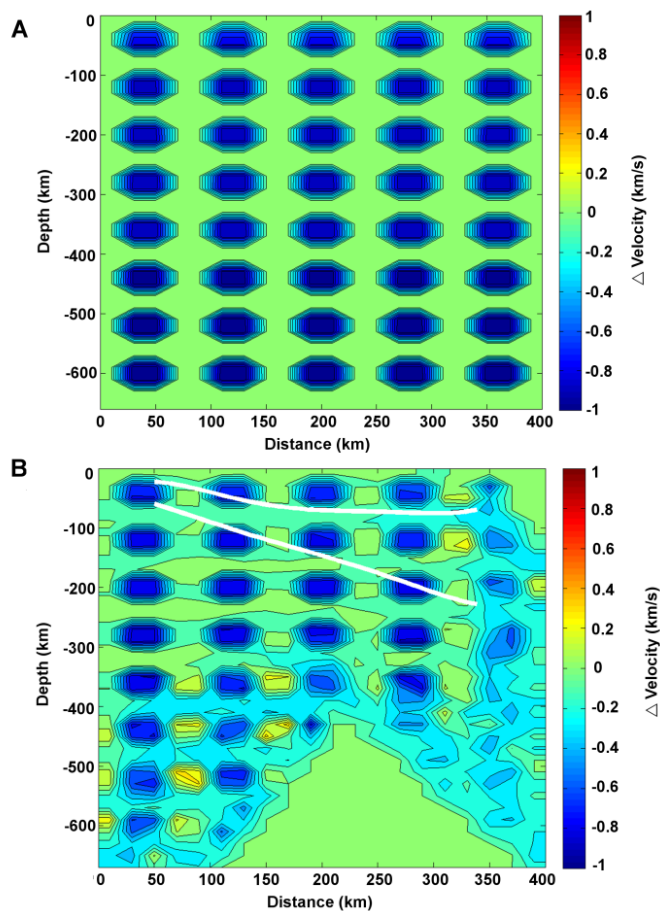


Figure 2.14. Tomographic resolution test. The results of a standard checkerboard resolution test are shown corresponding to the tomographic depth cross section for the array. Depth in kilometers is shown on the y-axis and distance in kilometers on the x-axis. A) The upper figure shows the checkerboard input model. B) The lower figure shows the output based on event coverage.

## **2.3 Discussion**

### **2.3.1 Crustal Thickness**

Receiver function results for the normal subducting region of southern Peru show a Moho that deepens from 25 km near the coast to a depth of around 75 km beneath the Altiplano. Previous estimates of crustal thickness of the Altiplano are about 70-75 km (Cunningham and Roeker, 1986; Beck et al., 1996; Zandt et al, 1994). McGlashan et al. (2008) also estimated thicknesses from 59 to 70 in Southern Peru. The 75 km crust of the Altiplano is approximately the thickness required for the region to be in Airy isostatic equilibrium and this is verified with the gravity observations (figure 2.15).

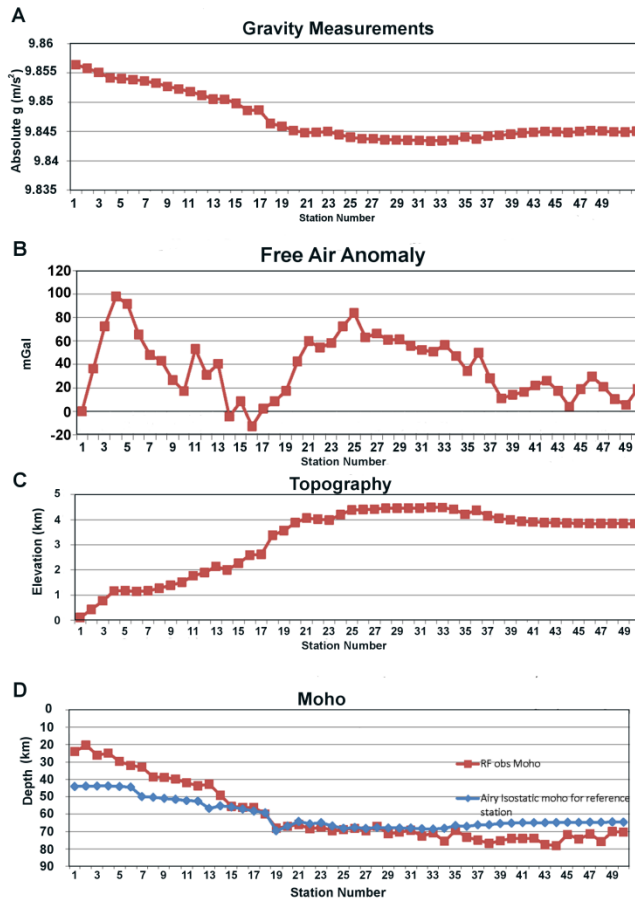


Figure 2.15. Results from a gravity survey performed along the seismic array by Caltech and UCLA students during a geophysical field course. A) Observed absolute gravity ( $m/s^2$ ) B) Free air anomaly in mGal relative to the first station, which shows an increase near the start of the line due to uplift near the coast. (C) Topography along the array (D) Moho estimates from receiver function stacking and Moho depth estimates expected for Airy isostasy relative to a reference station.

One of the major processes which could contribute to this thickness is crustal shortening. Gotberg et al. (2010) gave a preferred estimate of 123 km of shortening but said that 240-300 km of shortening would be required for a 70 km thick crust. Other suggested mechanisms for producing such a thickness include lower-crustal flow, shortening hidden by the volcanic arc (Gotberg et al., 2010), thermal weakening (Isacks, 1988; Allmendinger et al., 1997; Lamb and Hoke, 1997), regional variation in

structure from tectonic events prior to orogeny (Allmendinger and Gubbels, 1996), magmatic additions, lithospheric thinning, upper mantle hydration (Allmendinger et al., 1997), plate kinematics (Oncken et al., 2006), shortening related to the Arica bend (Kley & Monaldi, 1998; Gotberg et al., 2010), tectonic underplating (Allmendinger et al., 1997; Kley & Monaldi, 1998), and other factors. The mechanism of tectonic underthrusting is supported by our observations of a midcrustal structure and provides a simple mechanism for explaining the crustal thickness in southern Peru.

### **2.3.2 Midcrustal Structure**

The positive impedance structure observable at a depth of around 40 km is an unusual crustal feature because the crust does not normally have an interface with a sharp increase in velocity. One hypothesis that could explain this feature is underthrusting by the Brazilian Craton. It is generally accepted that this underthrusting exists as far as the Eastern Cordillera (McQuarrie et al., 2005; Gubbels et al., 1993; Lamb & Hoke, 1997; Beck & Zandt, 2002). However the results presented here appear to support the idea that it extends further to the west, as was suggested by Lamb and Hoke (1997). The midcrustal signal at 40 km depth is observed continuously across multiple stations on the eastern half of the array. The Conrad discontinuity, which is sometimes observed at midcrustal depths of around 20 km was considered, but the processes involved in crustal shortening and thickening are not expected to produce such a flat and strong positive impedance feature at 40 km. The strength of the midcrustal signal relative to the Moho signal (see figure 2.6), and the observation that the signal is limited to the easternmost stations in the array rather than across the whole array support

underthrusting as a more reasonable explanation. If the Brazilian craton underthrusts as far as the Altiplano, it would substantially increase the thickness of the crust under the Altiplano and hence affect the timing of the rise of the Andes. The rapid rise model of Garzzone et al. (2008), proposes a gradual rise of 2 km over approximately 30 Myrs, followed by a rapid rise of 2 km over the last 10 Myrs. This is then used as evidence of removal of the dense lower crust and/or lithospheric mantle (Ghosh et al. 2006) because it is a process that can result in rapid uplift. An alternative model of the rise suggests that the total rise proceeded gradually over 40 Myrs. This latter model is favored by the midcrustal layer found in this study. The timing of underthrusting and nature of the underthrusting Brazilian craton suggests that rather than eclogitization and delamination of the lower crust and mantle lithosphere resulting in rapid uplift, the process was more gradual. The underthrusting Brazilian craton would have removed some of the preexisting lower crust and mantle lithosphere beneath the Altiplano and replaced it with the Shield crust and underlying mantle lithosphere, thus contributing to the crustal thickening observed beneath the Altiplano. Some of the uppermost crust of the underthrusting Brazilian craton may have been eroded and deformed. The remainder of the Shield crust is assumed to be denser than the upper Altiplano crust resulting in higher seismic velocities. The lithosphere of the Brazilian craton is suggested to taper off prior to the subducting Nazca plate as the subducting plate is observed continuously to 250 km depth and is not impacted by the underthrusting craton. The western limit of the underthrusting is not well defined in the images but it does not appear to extend beyond the volcanic arc. The presence of the underthrusting material is not expected to interfere with processes or arc magmatism.

Comparing the model of evolution in Southern Peru with the overall evolution in the central Andes, several authors (Allmendinger et al., 1997; Babeyko and Sobolev, 2005) have suggested that there has been north–south variation in mechanisms and rates of crustal thickening and uplift in the central Andes. The tectonic evolution in the Altiplano may have differed from the uplift and evolution of the Puna plateau (Allmendinger et al, 1997). Babeyko and Sobolov (2005) suggested that the type of shortening (e.g., pure versus simple shear as discussed by Allmendinger and Gubbels, 1996) may be controlled by the strength of the foreland uppermost crust and temperature of the foreland lithosphere. Hence, a weak crust and cool lithosphere in the Altiplano could be supportive of underthrusting, simple shear shortening, and gradual uplift while further south in the Puna the strong sediments and warm lithosphere supports pure shear shortening, lithospheric delamination, and resultant rapid uplift.

In addition to crustal information, receiver functions also show the subducting Nazca plate dipping at an angle of about 30 degrees from both the P/PP and PKP phases for Line 1. Figure 2.16 shows a cartoon interpretation of the array data. With the exception of the midcrustal positive-impedance and its interpretation of underthrusting by the Brazil Craton, the subduction appears to be normal.

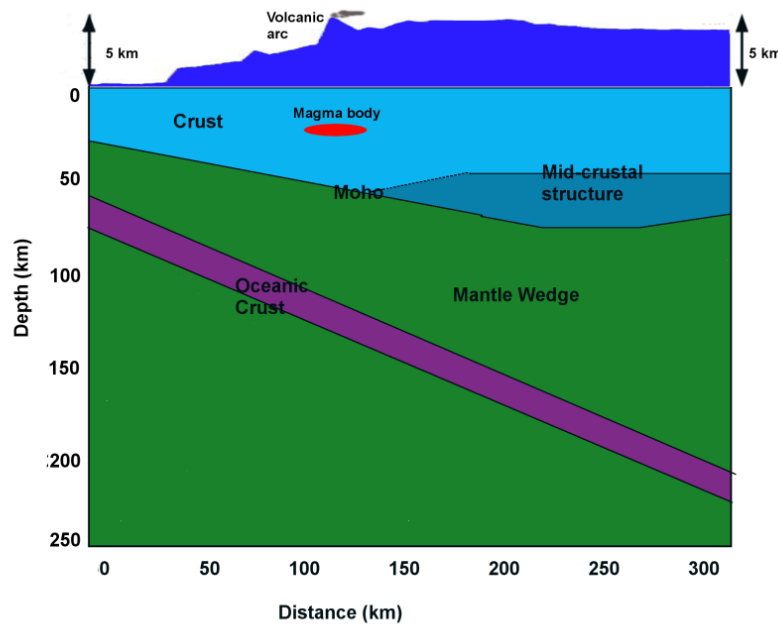


Figure 2.16: Schematic model of receiver function images showing the underthrusting Brazilian shield (colored teal), light blue representing the upper crust, purple representing the subducting oceanic crust, and green representing mantle. The small area of red represents a possible low velocity zone at around 20 km depth, which may correspond to magmatism.

### Conclusions

Receiver function and tomographic studies using data from an array of 50 broadband stations in Southern Peru image the region of normal subduction beneath the Altiplano. Both approaches confirm previous estimates of Moho depth beneath the Altiplano which reach a maximum value of about 75 km. The dipping slab is also clearly seen in the images. A positive impedance midcrustal structure at about 40 km depth is seen in the receiver functions indicating an increase in velocity in the lower crust. This feature may be due to underthrusting of the Brazilian shield, previously believed to underlie the Eastern Cordillera but not extend beneath the entire Altiplano.

### Acknowledgements

We thank the Betty and Gordon Moore Foundation for their support through the Tectonics Observatory at Caltech. This research was partially support by NSF award EAR-1045683. Contribution number 199 from the Tectonics Observatory at Caltech.

### Chapter 2 References

- Ahrens, T. J., and G. Schubert (1975). Gabbro-Eclogite reaction rate and its geophysical significance, *Reviews of Geophysics and Space Physics*, 13 (2), 383-400
- Allmendinger, R., and T. Gubbels (1996), Pure and simple shear plateau uplift, Altiplano-Puna, Argentina and Bolivia, *Tectonophysics*, 259, 1–13.
- Allmendinger, R., T. Jordan, S. Kay, and B. Isacks (1997), The evolution of the Altiplano-Puna Plateau of the Central Andes, *Annu. Rev. Earth Planet. Sci.*, 25, 139–174.
- Ammon, C., (1991), The isolation of receiver effects from teleseismic P waveforms, *Bull. Seismo. Soc. Am.*, 81, 6, 2504-2510.
- Babeyko, A., and S. Sobolev (2005), Quantifying different modes of the late Cenozoic shortening in the central Andes, *Geology*, 33 (8), 621–624.
- Barazangi, M., and B. L. Isacks (1976), Spatial distribution of earthquakes and subduction of the Nazca plate beneath South America, *Geology*, 4, 686–692.
- Barnes, J., and T. Ehlers (2009), End member models for Andean Plateau uplift, *Earth-Science Reviews*, 97 (105-132).
- Beck, S., and G. Zandt (2002), The nature of orogenic crust in the Central Andes, *J. of Geophys. Res.*, 107, 2230.

- Beck, S., G. Zandt, S. Myers, T. Wallace, P. Silver, and L. Drake (1996), Crustal-thickness variations in the central Andes, *Geology*, 24 (5), 407–410.
- Cunningham, P., and S. Roecker (1986), Three-dimensional P and S Wave Velocity Structures of Southern Peru and Their Tectonic Implications, *J. of Geophys. Res.*, 91 (B9), 9517–9532.
- DeCelles, P., and M. Ducea, P. Kapp and G. Zandt (2009), Cyclicity in Cordilleran orogenic systems, *Nature Geoscience*, 2, pp 251-257, doi:10.1038/NGEO469.
- Dorbath, C., M. Gerbault, G. Carrier, and M. Guiraud (2008), Double seismic zone of the Nazca plate in Northern Chile: High-resolution velocity structure, petrological implications, and thermomechanical modeling, *Geochemistry, Geophysics, Geosystems*, 9 (7), Q07, 2006.
- Ehlers, T., and C. Poulsen (2009), Influence of Andean uplift on climate and paleoaltimetry estimates, *Earth and Planetary Science Letters*, 281, 238–248.
- Elger, K., O. Oncken, and J. Glodny (2005), Plateau-style accumulation of deformation: Southern Altiplano, *Tectonics*, 24 (TC4020).
- Engdahl, E. R., R. van der Hilst, and R. Buland (1998), Global teleseismic earthquake relocation with improved travel times and procedures for depth determination, *Bull. Seism. Soc. Am.* 88, 722-743
- Engdahl, E. R. and A. Villaseñor (2002), Global Seismicity: 1900-1999, in W.H.K. Lee, H. Kanamori, P. C. Jennings, and C. Kisslinger (editors), *International Handbook of Earthquake and Engineering Seismology*, Part A, Chapter 41, 665-690
- Fukao, Y., A. Yamamoto, and M. Kono (1989), Gravity anomaly across the Peruvian Andes, *Journal of Geophysical Research*, 94, (B4)

- Garzione, C., P. Molnar, J. Libarkin, and B. MacFadden (2006), Rapid late Miocene rise of the Bolivian Altiplano: Evidence for removal of mantle lithosphere, *Earth and Planetary Science Letters*, 241, 543–556.
- Garzione, C., G. Hoke, J. Libarkin, S. Withers, B. MacFadden, J. Eiler, P. Ghosh, and A. Mulch (2008), Rise of the Andes, *Science*, 320, 1304–1307.
- Ghosh, P., C. Garzione, and J. Eiler (2006), Rapid uplift of the Altiplano revealed through  $^{13}\text{C}$ - $^{18}\text{O}$  bonds in paleosol carbonates, *Science*, 311, 511–515.
- Gotberg, N., N. McQuarrie, and V. Caillaux (2010), Comparison of crustal thickening budget and shortening estimates in southern Peru ( $12^{\circ}$ – $14^{\circ}$  S): Implications for mass balance and rotations in the “Bolivian orocline”, *GSA Bulletin*, 122 (5–6), 727–742.
- Gregory-Wodzicki, K. (2000), Uplift history of the Central and Northern Andes; a review, *GSA Bulletin*, 112 (7), 1091–1105.
- Gubbels, T., B. Isacks, and E. Farrar (1993), High-level surfaces, plateau uplift, and foreland development, Bolivian central Andes, *Geology*, 21, 695–698.
- Gutscher, M., W. Spakman, H. Bijwaard, and E. Engdahl (2000), Geodynamics of flat subduction: Seismicity and tomographic constraints from the Andean margin, *Tectonics*, 19 (5), 814–833.
- Hacker, B.R. (1996), Eclogite formation and the rheology, buoyancy, seismicity, and  $\text{H}_2\text{O}$  content of oceanic crust, AGU Monograph, p337-346.
- Hampel, A. (2002), The migration history of the Nazca Ridge along the Peruvian active margin: a re-evaluation, *Earth and Planetary Science Letters*, 203, 665–679.
- Hole, J. A., and B. C. Zelt (1995), 3-D finite-difference reflection traveltimes,

- Geophys. J. Int.*, 121, 427-434.
- Horton, B., B. Hampton, and G. Waanders (2001), Paleogene synorogenic sedimentation in the Altiplano Plateau and implications for initial mountain building in the Central Andes, *GSA Bulletin*, 113, 1387–1400.
  - Husker, A. and P. M. Davis (2009), Tomography and thermal state of the Cocos plate subduction beneath Mexico City, *J. Geophys. Res.*, 114, B04306.
  - Isacks, B. (1988), Uplift of the Central Andean Plateau and bending of the Bolivian Orocline, *J. of Geophys. Res.*, 93 (B4), 3211–3231.
  - Kawakatsu, H., and S. Watada (2007), Seismic evidence for deep-water transportation in the mantle, *Science*, 316, 1468-1471.
  - Kennett, B. L. N., and E. R. Engdahl (1991), Traveltimes for global earthquake location and phase identification, *Geophys. J. Int.*, 105, 429-465.
  - Kim, Y., R. W. Clayton, and J. M. Jackson (2010), Geometry and seismic properties of the subducting Cocos plate in central Mexico, *J. Geophys. Res.*, 115, B06310.
  - Kley, J. and C. R. Monaldi (1998), Tectonic shortening and crustal thickness in the Central Andes: How good is the correlation? , *Geology*, 26, 8, 723-726.
  - Lamb, S., and L. Hoke (1997), Origin of the high plateau in the Central Andes, Bolivia, South America, *Tectonics*, 16 (4), 623–649.
  - Langston, C. (1979), Structure under Mount Rainier, Washington, inferred from teleseismic body waves, *J. Geophys. Res.*, 84, 4749–4762.
  - Leidig, M., and G. Zandt (2003), Modeling of highly anisotropic crust and application to the Altiplano-Puna volcanic complex of the central Andes, *J. Geophys. Res.*, 108 (B1).

- McGlashan, M., L. Brown, and S. Kay (2008), Crustal thickness in the Central Andes from teleseismically recorded depth phase precursors, *Geophys. J. Int.*, 175, 1013-1022.
- McQuarrie, N., B. Horton, G. Zandt, S. Beck, and P. DeCelles (2005), Lithospheric evolution of the Andean fold-thrust belt, Bolivia, and the origin of the central Andean plateau, *Tectonophysics*, 399, 15–37.
- Norabuena, E., J. Snoke, and D. James (1994), Structure of the subducting Nazca Plate beneath Peru, *J. Geophys. Res.*, 99, 9215–9226.
- Oncken, O., J. Kley, K. Elger, P. Victor, and K. Schemmann (2006), *Deformation of the Central Andean Upper Plate System-Facts, Fiction, and Constraints for Plateau Models*, Berlin, Springer, p. 569.
- Ramos, V. (2009), Anatomy and global context of the Andes: Main geologic features and the Andean orogenic cycle, in Kay, S.M., Ramos, V.A., and Dickinson, W.R., eds., *Backbone of the Americas: Shallow Subduction, Plateau Uplift, and Ridge and Terrane Collision: Geological Society of America Memoir*, 204, p31065,doi: 10.1139/2009.1204(02).
- Sighinolfi, G.P. (1971), Investigations into deep crustal levels: fractionating effects and geochemical trends to high-grade metamorphism, *Geochim. Cosmochim. Acta*, 35, pp. 1005-1021.
- Tassara, A. (2006), Factors controlling the crustal density structure underneath active continental margins with implications for their evolution, *Geochem. Geophys. Geosyst.*, 8, Q01001.
- Vidale, J., D. Helmberger, and R. Clayton, (1985), Finite-difference synthetic

- seismograms for SH-waves, *Bull. Seismo. Soc. Am.*, 75, 6, 1765-1782.
- Yan, Z. and R.W. Clayton (2007), Regional mapping of the crustal structure in southern California from receiver functions, *J. of Geophys. Res.*, 112, B05311.
  - Zandt, G., M. Leidig, J. Chmielowski, D. Baumont, and X. Yuan (2003), Seismic detection and characterization of the Altiplano-Puna magma body, Central Andes, *Pure Appl. Geophys.*, 160, 789–807.
  - Zandt, G., A. Velasco, and S. Beck (1994), Composition and thickness of the southern Altiplano crust, Bolivia, *Geology*, 22, 1003–1006.
  - Zhu, L., and H. Kanamori (2000), Moho depth variation in southern California from teleseismic receiver functions, *J. Geophys. Res.*, 105 (B2), 2969–2980.

*Chapter 3: Subduction Transition and Flat Slab***Structure of the Subduction Transition Region from Seismic****Array Data in Southern Peru**

Kristin Phillips and Robert W. Clayton

**Abstract**

Data from three seismic arrays installed in southern Peru was analyzed using receiver functions from P, PP, and PKP wave phases, in order to image the subducted Nazca slab. The arrays cover the transition region from flat slab subduction in central Peru to normal subduction with an angle of about 30° further south. The results provide an image of the flattened slab from the coast to approximately 300 km inland and also across the transition region from flat to 30-degree subduction, which appears to be a bend rather than a tear in the slab. In the flat slab region, the slab is well defined near the coast and flattens out at 100 km depth beneath the Altiplano. The slab appears to start flattening some 400 km in advance of the subduction of the Nazca Ridge and the flattening is maintained for 1300 km after its passage. The Moho begins at a depth of around 30 km near the coast and has a maximum depth of 75 km beneath the Altiplano, consistent with the results of the other arrays. The  $V_p/V_s$  ratios for both arrays exhibit average values between 1.73 and 1.75 indicating that the region is most likely not actively volcanic. The images also show a positive-impedance midcrustal structure at

around 40 km depth, which is suggested to be a result of underthrusting of the Brazilian shield. This would explain the missing crust needed to support the Altiplano.

### **3.1. Introduction**

The dip of the subducted Nazca plate beneath southern Peru changes from shallow or flat slab beneath central Peru to a steeper dip angle (“normal” subduction) of around 30 degrees beneath southern Peru. This transition is evident in the seismicity (Barazangi & Isacks, 1976; Cahill and Isacks, 1992; Grange et al, 1984; Suarez et al, 1983), and by a gap in the arc-volcanism (Gutsher, Olivet et al, 1999; Gutscher, Spakman et al. 2000; McGearry et al, 1985). Adakitic magmas have also been associated with flat slab regions (Gutscher, Maury, et al. 2000) and have been reported in southern Ecuador/northern Peru (Beate et al, 2001). They are suggested to result from partial melting of subducted oceanic crust (Gutscher, Maury, et al. 2000). Besides the observed correspondence between adakites and flat slab regions, the partial melting resulting in such magmas could also be a result of slab tearing at the transitions from flat slab to a steeper dip angle (Yogodzinski et al, 2001). The lack of reported adakites in southern Peru might indicate that the southern transition is slab bending rather than a tear. The change in dip is coincident with the subduction of Nazca Ridge. This is one of three zones of slab-dip changes along the western margin of Southern America. In central Chile, the subduction of the Juan Fernandez Ridge is cited as the cause of the flattening along its subduction trajectory (Pilger, 1981; Gutscher, Spakman et al, 2000; von Huene et al, 1997), and the study of Anderson et al (2007) show that the zone of

flattening tightly conforms to the shape of the ridge. In Ecuador, the Carnegie Ridge also apparently causes the slab to flatten (Gutscher, Malavielle et al. 1999).

Various mechanisms have been proposed as to the cause of flat slab subduction. Some authors have noted a correlation between regions of flat slab subduction and the presence of thickened oceanic crust such as that due to a subducting plateau or ridge which could increase the buoyancy of the subducting slab (Gutscher, Maury et al. 2000). Gutscher et al. (1999) proposed that the length of flat subduction in Peru was due to buoyancy effects resulting from two subducting ridges; the Nazca ridge and a previously unknown impactor referred to as the Inca Plateau which is believed to be the mirror image of the Marquesas plateau although recent plate movement reconstructions call into question the proposed location and timing of the Inca plateau (Skinner and Clayton 2012). Both plateaus were suggested to have formed at the Pacific-Farallon spreading centre based on tectonic reconstructions. According to Hampel (2002), the Nazca Ridge originally began subducting at 11°S around 11.2 Ma. Since then it has been sweeping south and presently has a migration rate of around 43 cm per year. The area of flat subduction in Peru corresponds to the area swept out by the Nazca Ridge. Thus the Nazca Ridge may have had an impact on the evolution and shape of the subduction zone. In addition to buoyancy effects caused by a subducting ridge or plateau, other factors could influence flat subduction such as the age of the lithosphere being subducted (Sacks 1983), delay in the basalt to eclogite transformation (Gutscher, Spakman et al. 2000; Pennington 1984), absolute motion of the upper plate (Olbertz et al. 1997), the convex curvature of the Peruvian margin (Bevis, 1986; Cahill and Isacks,

1992), intraplate hydrostatic suction (Jischke, 1975), or cycles of flat subduction caused by rebound after a steepening slab breaks off (Haschke et al, 2002). Modeling has been done in several studies to address the relative importance of different causes for flat slab subduction. Van Hunen et al (2002a) suggested that relative motion of the upper plate could be equally or more important than plateau subduction based on numerical studies; however this is a factor that is present in the region of normal subduction as well. The dominant mechanism for flat slab subduction needs to be considered independently for each subduction zone since some factors are present in both normal and flat slab regions, while other factors can be observed in only some flat slab regions and not in others. One of the puzzling aspects of the flat subduction in southern Peru is the fact that the slab does not return to a normal dip angle after the impactor has passed. This contrasts with central Chile where the slab returns to normal dip at a distance of about 150 km on either side of the track of the JFR (based on contours from Anderson et al, 2007).

In this study, we examine the details of the transition zone between normal and flat subduction using dense seismic arrays, which include instruments both in the flat-slab zone as well as an array parallel to the trench to sample the subduction transition. The array in the flat slab region near the Nazca Ridge provides an opportunity to study the effect of the Nazca Ridge on the subduction zone in Southern Peru. A previous study (Phillips et al, 2012) has described the results of a line (Line 1, figure 3.1) that is in the normal-dip part of the zone. It succeeded in imaging the slab down to 250 km, and found a midcrustal velocity increase at about 40 km depth suggested to be

underthrusting by the Brazilian shield. In this study we expand on those results by presenting details of the transition and flat slab subduction regions.

Receiver function studies performed here provide details of the structure of the subduction system including Moho depth and shape of the slab as well as velocity information such as  $V_p/V_s$  ratio. Corresponding images show the transition from normal to flat slab subduction and the shape of the slab in the flat slab region, which is affected by the subducting Nazca Ridge. The structure of the flat slab region is compared to the study of the normal subduction regime.

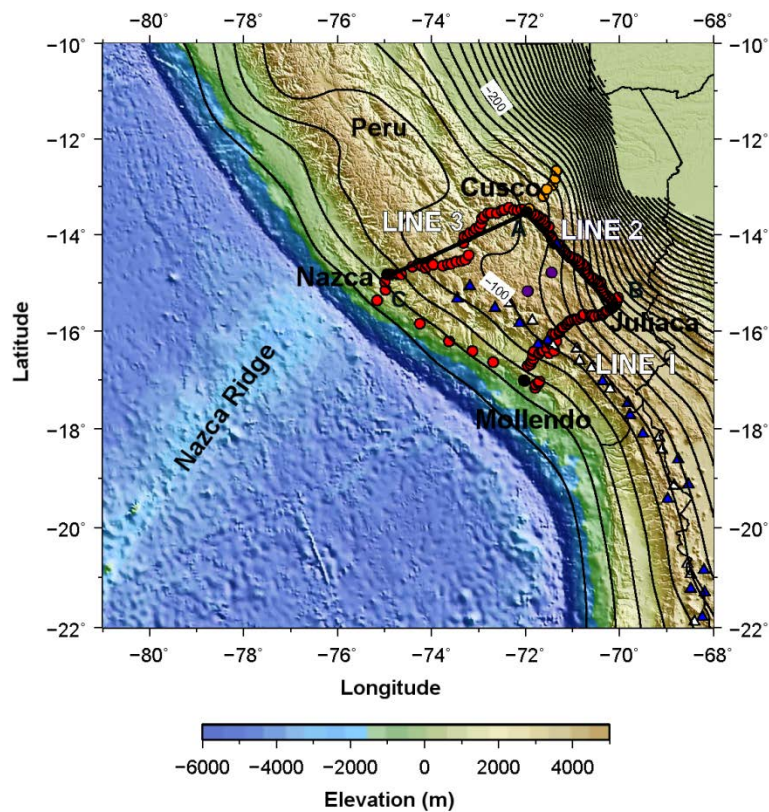


Figure 3.1. Location of the seismic arrays in Southern Peru as denoted by red circles. Added stations from the PULSE and CAUGHT experiments are shown as orange and purple circles respectively. The topography and bathymetry shows the incoming Nazca

Ridge and the Altiplano of the Andes. Slab contours are based on fits to seismicity and comes from the Slab 1.0 model (Hayes et al, 2012). Active and dormant volcanoes are denoted by white and blue triangles. The three seismic arrays are labeled “Line 1,” “Line 2,” and “Line 3.” Line 1 is located in the region of normal subduction, Line 2 samples the transition from normal to flat slab subduction, and Line 3 is in the flat slab region. The black lines along Lines 2 and 3 with endpoints labeled A, B, and C correspond to cross section profiles in figure 3.2.

## **3.2. Methods**

### **3.2.1 Stations and Data**

Three lines of broadband sensors were installed as part of the Peru Subduction Experiment (PeruSE) as seen in figure 3.1. The first line (Line 1) deployed perpendicular to the trench from Mollendo on the coast to Juliaca near Lake Titicaca, samples the region of normal subduction dip (Phillips et al, 2012). The second seismic array (Line 2) runs parallel to the trench from Juliaca to Cusco sampling the transitional region where the subduction regime changes to shallow subduction. It includes 50 broadband seismic stations over a distance of about 300 km resulting in an average station spacing of about 6 kilometers. Line 3 is perpendicular to the trench starting on the coast near the city of Nazca and runs inland through Cusco for 509 km. It consists of 40 stations from the PeruSE network plus 5 stations from the PULSE network (Eakin et al, 2011). Line 3 is located near where the Nazca Ridge is subducting beneath South America and samples the flat slab region. In addition, 2 stations from the CAUGHT network (Ryan et al, 2011) that are in the interior of the box defined by the networks described above are used.

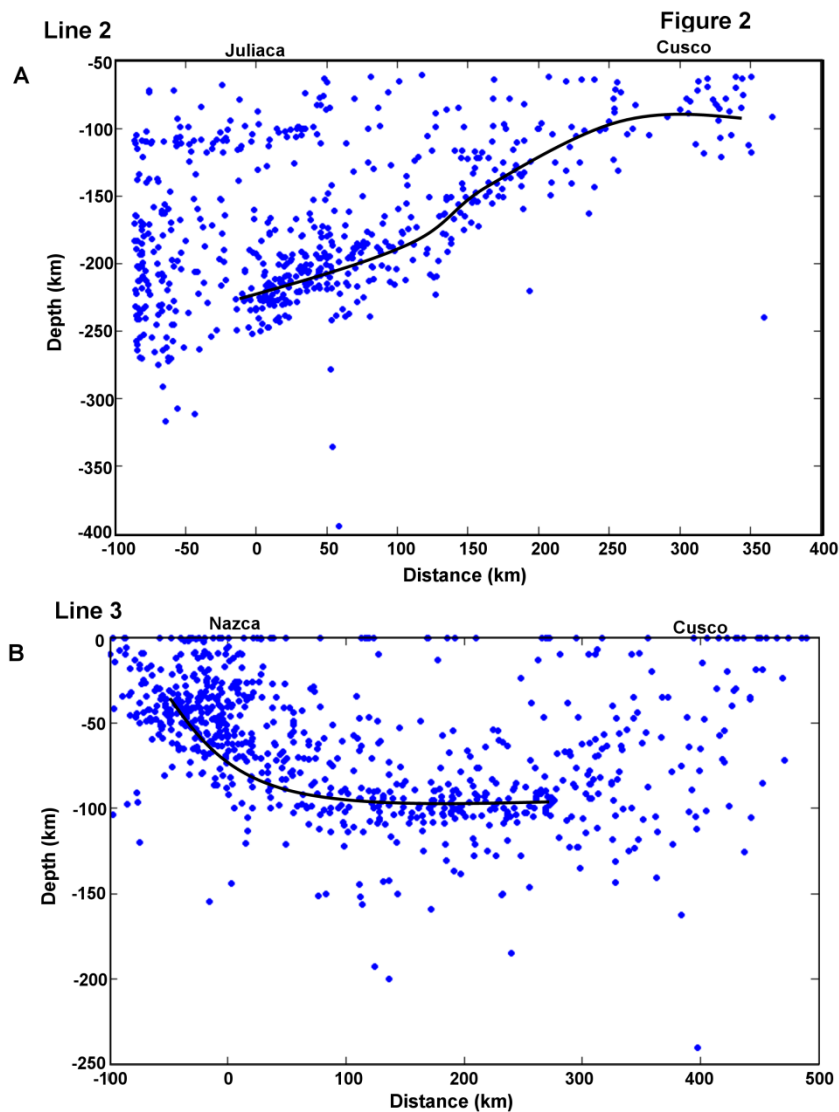


Figure 3.2. Seismicity cross-sections along the projections of Lines 2 and 3 shown as black lines in figure 3.1. Earthquakes locations are from the ISC reviewed catalogue (International Seismological Centre, 2010). The black lines show the estimated slab location from seismicity. (A) Seismicity cross-section parallel to the trench from Cusco to Juliaca as shown as black line A-B in figure 3.1. Cusco is located in the region of flat slab subduction while Juliaca further south is in the region of normal subduction. (B) Seismicity cross-section from Nazca to Cusco in the region of flat slab subduction shown by line C-B in figure 3.1.

The flat slab and the transition from normal to flat slab subduction can be roughly delineated by the seismicity of the Wadati-Benioff zone as is shown in figure 3.2. Event

locations are from the ISC reviewed catalog. The black lines show an average value for slab location based on best fit to seismicity. The seismicity shows the slab flattening out at 100 km depth beneath the Altiplano in the flat slab region and the shape of the curve in the transition region between Cusco and Juliaca.

Teleseismic data collected by the array was used in receiver function studies.

Earthquakes between 30 and 90 degrees away from Peru were used to make receiver functions based on the P wave arrival. However since many events are located beyond 90 degrees from Peru, PP and PKP phases were also analyzed for events occurring at distances greater than 90 degrees distance from Peru. PKP phases are used at distances between 143 and 180 degrees and can be useful for detecting dipping interfaces. For Line 2, a total of 73 events using the P wave phase, 175 PP and 50 PKP wave phase events were used in this study. For Line 3, 50 P wave, 106 PP and 21 PKP phase events were used. To ensure higher signal to noise, events are of magnitude 5.8 or greater for distances less than 90 degrees from Peru and greater than magnitude 6.0 for distance greater than 90 degrees. The data was generally bandpassed from 1 to 100 seconds, but this was narrowed to 2–100 seconds for some distant events with higher apparent noise. Data was included if the signal to noise ratio appeared adequate for both the raw seismic data and resultant receiver functions.

### **3.2.2 Receiver Functions**

Receiver functions were formed using the method described in Langston (1979) and Yan and Clayton (2007). Mantle and source effects are minimised by deconvolving the radial with the vertical component in the frequency domain (Langston, 1979; Ammon,

1991). Time domain iterative deconvolution (Ligorria and Ammon, 1999) was also tried, but produced noisier results. Receiver functions were stacked using the method of Zhu and Kanamori (2000) using multiple events from a similar backazimuth for each station to perform stacks. A maximum weighted summation function for stacking over the Moho and multiple arrivals provides estimates for depth to the impedance contrast and the  $V_p/V_s$  ratio. Average crustal P wave velocities used in the estimate of depth and  $V_p/V_s$  from stacking of receiver functions for each station were derived mostly from averages of the 3D P wave velocity structure of Cunningham and Roecker (1986) for southern Peru. Their model was also compared with more recent velocity models such as the model of Dorbath et al (2008) from northern Chile. Uncertainty in the stacking method described above is given by the 95% maximum contour. Estimates of depth uncertainty due to uncertainty in the velocity model used for stacking are on the order of 2 km or less based on performing stacks with variations in average crustal  $V_p$  of up to 0.2 km/sec from the velocity model used.

Receiver function images were produced by backprojecting along rays from the direction that the energy arrived to plot receiver function amplitudes as a function of distance and depth. A simple velocity model based on IASP91 was used for the conversion from receiver function time to depth.

In addition to backprojected images, receiver function migration is done using information about the station, ray parameter, incidence angle, and a simple homogenous half space velocity model. A starting model uses an average crustal P

wave velocity of 6.3 and the average  $V_p/V_s$  ratio of 1.75. The velocity was varied to test sensitivity of the migration results to the velocity.

### **3.2.3 Finite Difference Modeling**

A simple 2D velocity model was used to produce synthetic receiver functions using a 2D finite difference code (Kim et al, 2010) to compare with receiver function results for both Lines 2 and 3. The model for Line 2 is 300 km wide in distance and 250 km in depth. It has an average crustal P-wave velocity of 6.3 km/sec with a midcrustal velocity jump to 6.6 km/sec. The velocity jump is constrained by the amplitude of the midcrustal arrival. The mantle wedge is taken as having an average velocity of 7.7km/sec and the subducting oceanic crust as 7.0 km/sec (Abers et al, 2006; Abers, 2000; Kim et al 2010). The underlying mantle is taken as having an average velocity of 8.0 km/sec down to 250 km. Synthetic receiver functions are produced by modeling plane waves with variable ray parameters to simulate teleseismic sources.

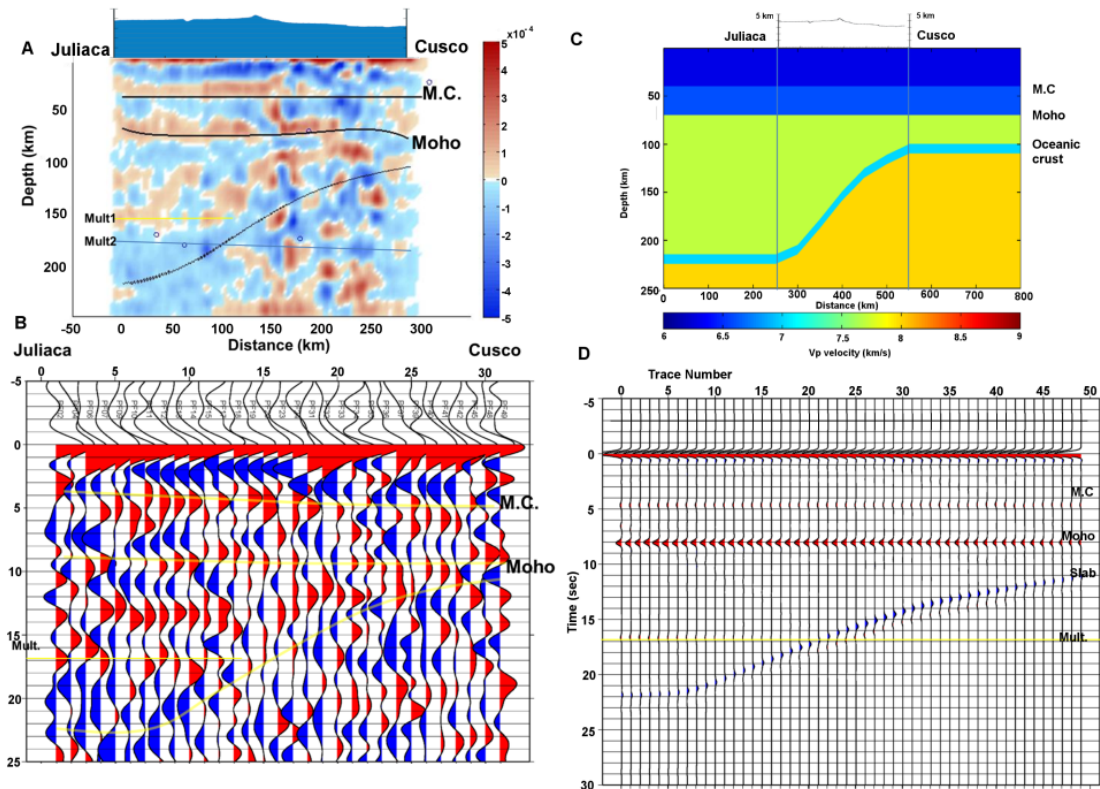


Figure 3.3. Results from Line 2 showing the transition from normal subduction in the southernmost part of Peru near Juliaca to shallow or flat slab subduction to the north near Cusco. (A) Receiver function image for Line 2 based on stacks of P and PP receiver functions for each station. Distance from Juliaca in kilometers is plotted against depth in kilometers. The black lines show a positive impedance midcrustal structure at around 40 km depth, the Moho at around 70–75 km depth, and the shape of the slab which is delineated primarily by a negative impedance signal. Also observable is a positive impedance arrival above the negative slab signal which also appears to be related to the slab. The positive pulse can be compared to the positive slab arrival for Line 1 in figure 3.12B. (B) The receiver function plot below shows receiver functions from a magnitude 7.3 earthquake occurring near Vanuatu Islands on August 10, 2010. (C) Simple 2D P-wave velocity model used for finite difference modeling based on receiver function results. (D) Synthetic receiver functions from finite difference model showing P wave arrival, midcrustal structure, Moho, slab, and multiple arrival.

### 3.3. Results

#### 3.3.1 Line 2 Results: Transition From Normal to Flat Slab Subduction

Line 2 samples the transition from normal to flat subduction. On the SE end (near Lake Titicaca) the slab is at a depth of approximately 215 km, while on the NW end (near Cusco) the slab is at a depth of 100km. An image of the Moho and the slab can be seen in the receiver functions shown in figure 3.3A. Also observable is a midcrustal positive impedance signal at a depth of about 40 km, which was interpreted by Phillips et al (2012) to result from the underthrust Brazilian Shield. The strength of the midcrustal signal relative to the Moho can be seen in the supplementary materials which show that a very similar Moho and midcrustal signal are seen at multiple stations across the array. Both features appear to be relatively flat and the Moho has an average depth between 70 and 75 km beneath the Altiplano. This depth is consistent with the relatively flat elevation profile and suggests that the topography is isostatically supported by the crustal root (see figure 3.9 which shows consistency with Airy Isostasy). Receiver function traces from a magnitude 7.3 Vanuatu earthquake on August 10, 2010 (figure 3.3B) shows a result consistent with all other receiver function images based on multiple events. The receiver function traces show signals from the midcrustal structure, Moho, slab, and crustal multiples. Finite-difference modeling based on receiver function results for Line 2 using a simplified 2D velocity model produces synthetic receiver functions consistent with the receiver function data (figure 3.3C,D). Common conversion point (CCP) stacks were done for both the P/PP and PKP receiver functions and the resultant images are shown in figure 3.4 which is consistent with

figure 3.3A. Although the primary slab signal observed for Line 2 is a negative impedance signal consistent with finite difference modeling results, a positive impedance signal roughly following the shape of the slab is observed above the negative slab signal as seen in figures 3.3 and 3.4.

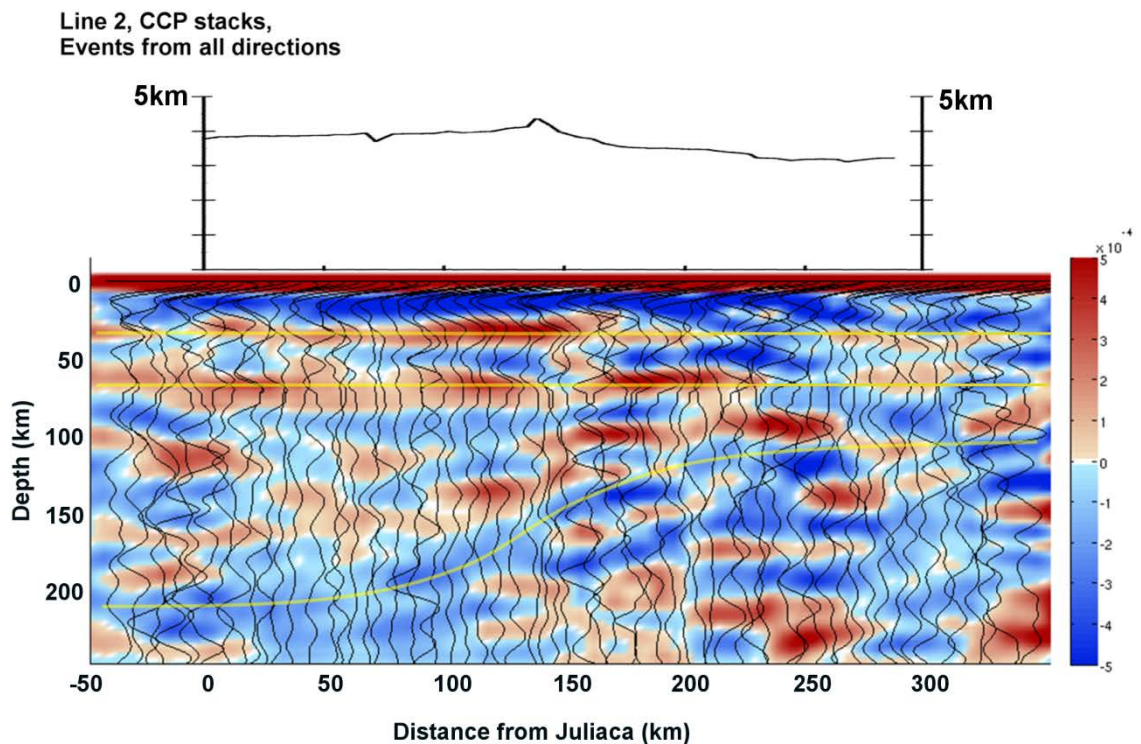


Figure 3.4. Plot of common conversion point (CCP) stacks with bin spacing equal to station spacing. The stack traces are shown overlying the amplitude of the stack with some horizontal smoothing. Receiver functions included in the stacks come from all azimuthal directions. The images show the midcrustal structure, Moho signal (positive impedance signals) which are both relatively flat, and the slab signal which is observed as a negative impedance signal underlying a positive slab arrival. The station elevation is shown above the image (note the different scale from the CCP image).

Another check on the shape of the slab is receiver function migration using a simple homogenous velocity model for the crust. The results are shown in figure 3.5 which

shows a discontinuous signal from the Moho and midcrustal structure and a clear change from negative to positive impedance near where the top of the slab is expected.

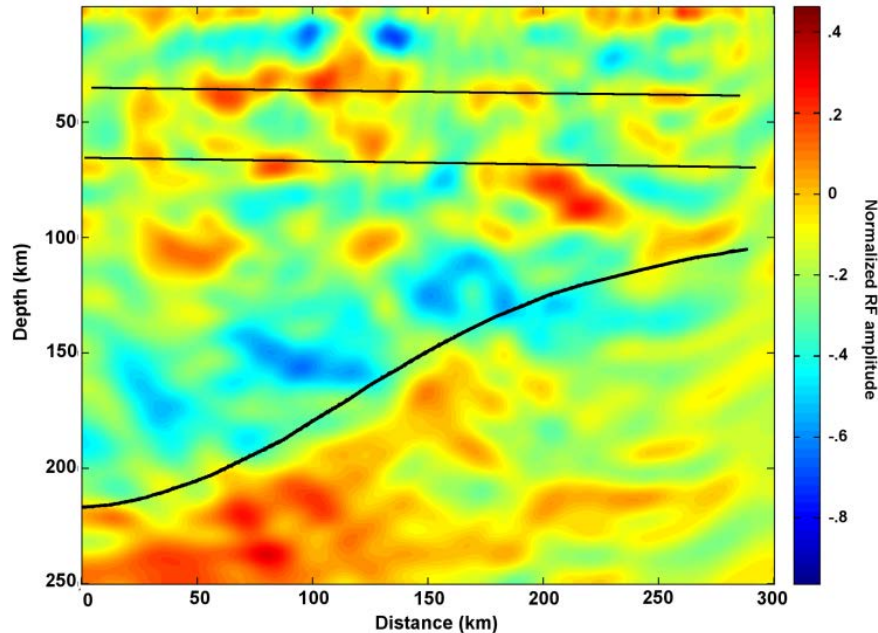


Figure 3.5. Line 2 receiver function migration plotted as distance from Juliaca on the x-axis and depth on the y-axis. Black lines show an interpretation of the image showing the expected location of the midcrustal structure, Moho, and slab. Notice the change from negative to positive receiver function impedance corresponding with the expected location of the slab.

Several different models for the shape of the slab were considered and modeled using the finite difference method for comparison with the receiver function data, including a linear transition, an abrupt transition consistent with a slab break, and a gently curving model shown in figure 3.3 (see supplementary materials for alternative models). The receiver function results such as figure 3.4 best match the gradually curving model.

The Moho and  $V_p/V_s$  results obtained from receiver function stacking using the method of Zhu and Kanamori (2000) are summarized in figure 3.9, which shows station

elevation, Moho depths, and  $V_p/V_s$  ratios. The Moho is relatively flat for Line 2 and increases with depth to a maximum depth of 75 km near Line 3 with a decrease in crustal thickness noticeable where station elevation begins to decrease.

### Line 3 RF Results, P/PP phase, NW baz

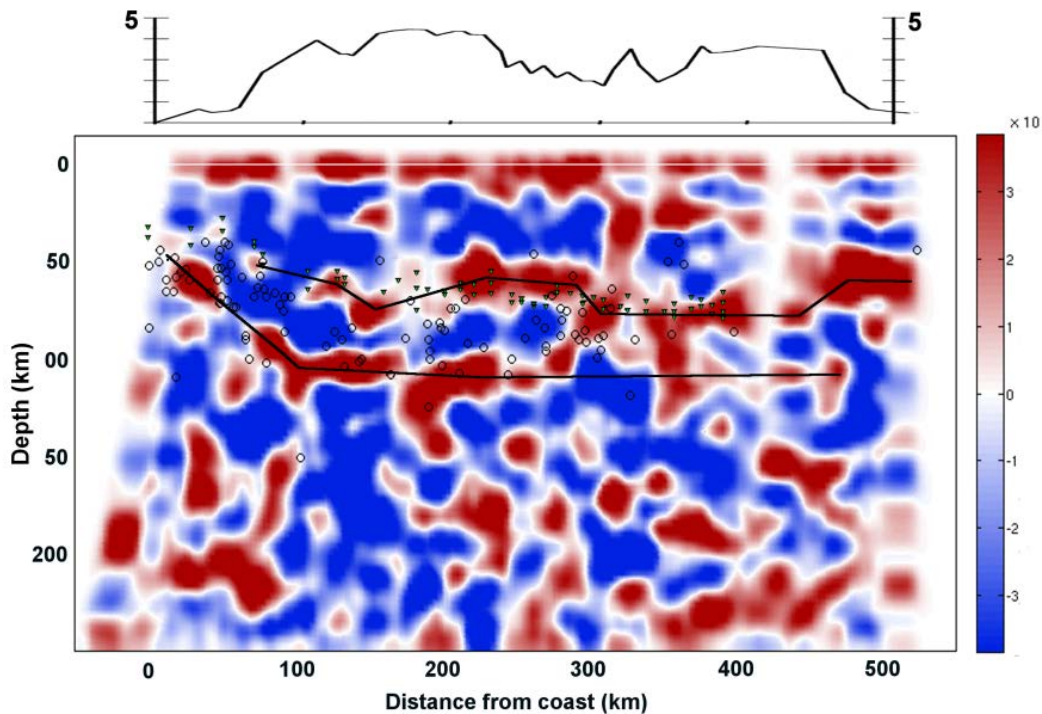


Figure 3.6. Receiver function image for Line 3 based on P and PP receiver functions from a NW azimuth from Peru. The image was formed by backprojecting the rays from the direction in which the energy originated. Distance is from the coast near Nazca to Cusco. Black lines show an interpretation of the Moho with individual station picks from stacking shown as green triangles, and interpretations of the slab and midcrustal structure. The slab can be seen flattening out at 100 km depth with the Moho just above it at around 70 km depth. Note a shallowing of Moho depth between about 200 and 300 km distance and near 500 km distance where topography decreases in elevation, indicating a good correspondence between topography and Moho depth.

### 3.3.2 Line 3 Results: Flat Slab Region

The third seismic array runs from the coast near Nazca northeast to Cusco in the region of shallow subduction just south of where the continuation of the Nazca Ridge is subducting. The shallow slab can be clearly seen to a depth of about 100 km in figure

3.6, as well as the Moho at an average depth of 70 to 75 km. A midcrustal structure is observed as well (see figure 3.7A for clarification).

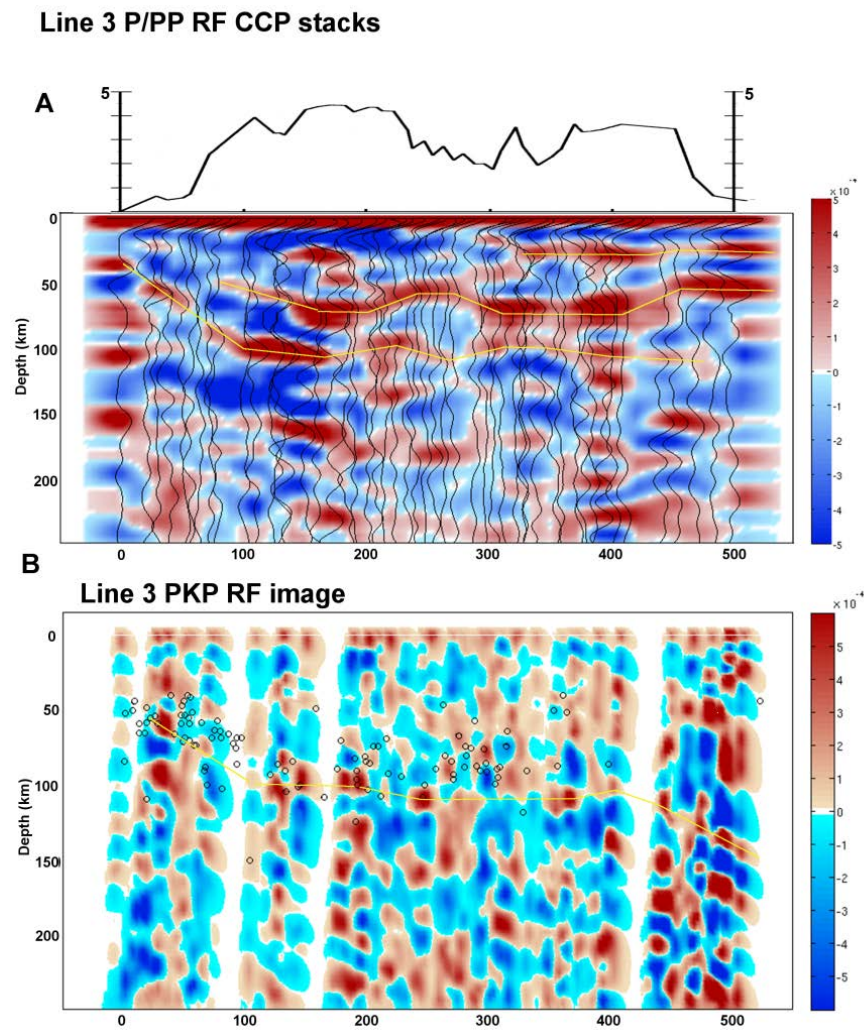


Figure 3.7. (A) CCP plot for Line 3 showing the stacks with background colours showing amplitude. The midcrustal structure, Moho, and slab interpretations are delineated with yellow lines (B) PKP image for Line 3 for comparison. Note that the Moho is less well defined but the slab is visible and appears to descend in the easternmost stations.

The receiver function traces from the NW backazimuth in figure 3.8B also show the Moho signal clearly as well as the signal from the slab as it flattens at 100 km depth. A more complete image showing that the slab remains flat for the extent of the array can be seen in the CCP stacks plotted in figure 3.7A. The same slab signal is also seen in an image based on PKP receiver functions which appears to show that the Nazca plate begins descending deeper into the mantle at a distance of about 450 km from the start of the seismic array (figure 3.7B).

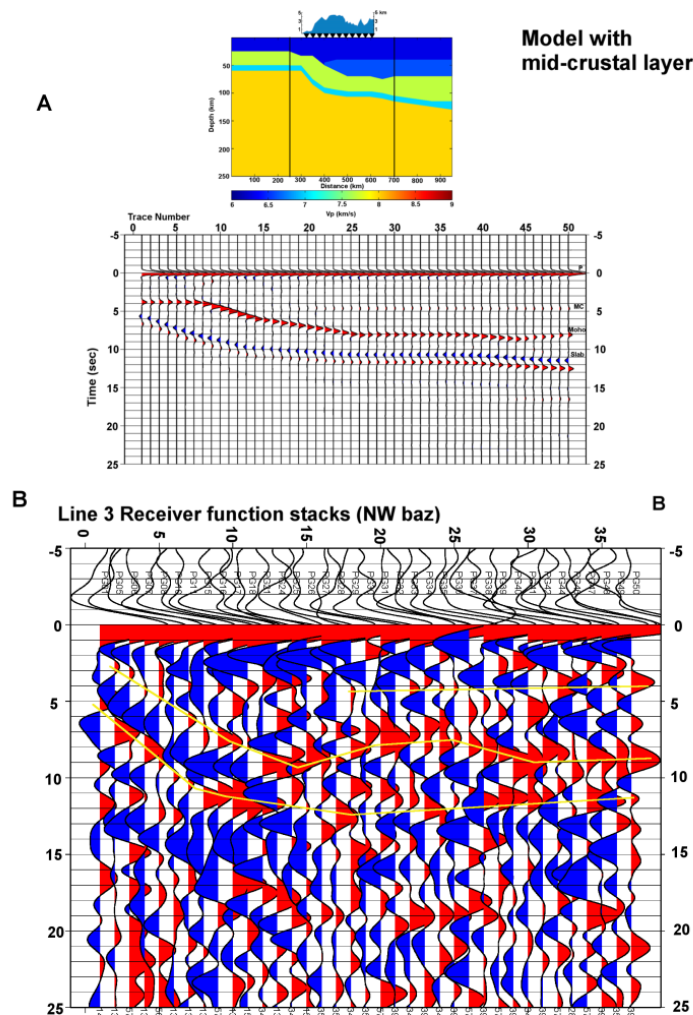


Figure 3.8. (A) Finite difference modeling for Line 3. The model includes a midcrustal velocity increase. Synthetic receiver functions are consistent with receiver function

results showing the double pulse structure of the slab, the positive Moho signal, and midcrustal structure.

(B) Receiver function plot showing stacks for each station based on events from the northwest consistent with the images in figure 3.6. Major arrivals such as the slab signal, Moho depth, and midcrustal structure are marked by yellow lines and can be compared to the synthetics in part A.

The receiver function results can be compared to 2D finite-difference models as in figure 3.8A. The model that fits the data best includes a velocity increase between the upper and lower crust. The synthetic receiver functions show a double pulse structure the full length of the subducting oceanic crust which is consistent with figure 3.7A which includes receiver function data from all azimuths while in single azimuth images such as figure 3.6 the positive impedance signal from the base of the oceanic crust is more difficult to detect at greater distances and depths.

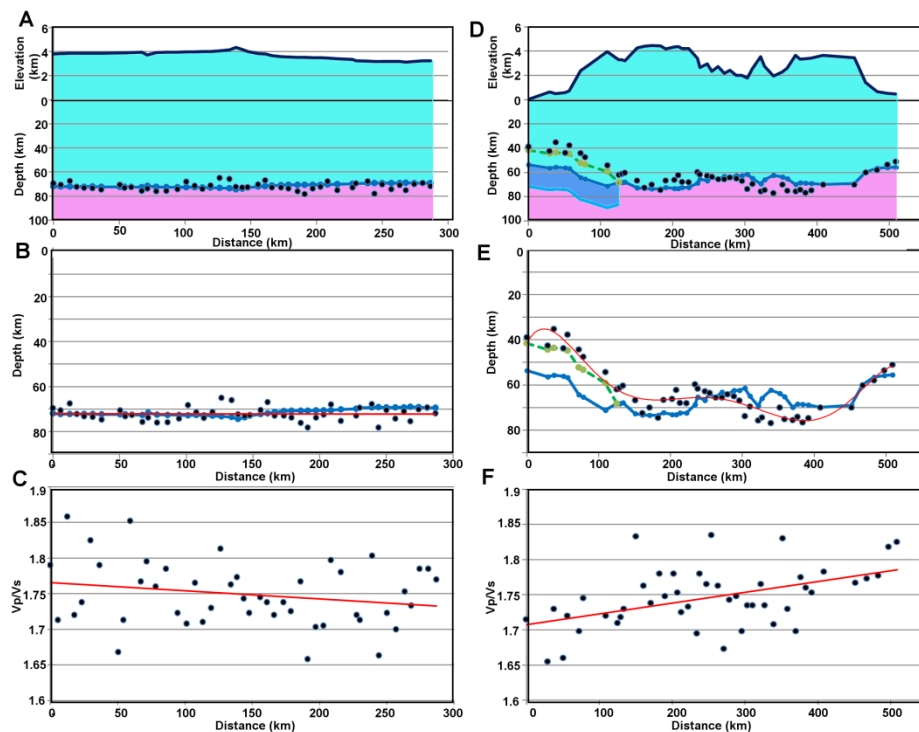


Figure 3.9. Moho and  $V_p/V_s$  results for Lines 2 and 3. A) Isostasy model for Line 2 including station elevation. Note the differing scales between elevation and Moho

depth. The blue line is a calculation of expected depth for Airy isostasy relative to a reference station assuming an average crustal density of 2.7g/cc and average mantle density of 3.3g/cc. B) Line 2 Moho depth from stacking. The red line shows a linear fit to the data. The blue line shows the Moho depth that would be expected for Airy isostatically compensated topography. C) Line 2 Vp/Vs ratio estimates from stacking with a red line showing linear least squares regression. Most of the Vp/Vs values are in the average range around 1.75. D) Line 3 isostatic model including elevation (note scales for elevation and Moho depth). The blue line shows a calculation for airy isostasy assuming the same average densities as in A. The fit to the data is not as good near the coast unless we include additional buoyant material from the subducting oceanic crust. The crust could be expected to be slightly thicker than normal oceanic crust due to the proximity of the Nazca Ridge which is expected to have a crustal thickness of 18 km (Hampel, 2002). The effect of this addition on the isostasy is noted by the green dashed line which is a better match to the data. E) Line 3 Moho depth with a red line showing a polynomial regression curve to the data points. The blue line shows isostatic compensation depth and the green dashed line shows the correction for subducting oceanic crust. F) Line 3 Vp/Vs ratio showing a linear regression curve to the data. There appears to be a general trend from lower Vp/Vs values near the coast to higher values near Cusco.

Moho depths for Line 3 in figure 3.9 indicate isostatic compensation under much of the Altiplano but the fit to Airy isostasy is not as good near the coast where the slab depth is shallower, possibly as a consequence of the presence of the Nazca Ridge. The crust appears compensated within the uncertainty of the data if buoyant material is present near the coast with dimensions comparable to that of the Nazca Ridge (see figure 3.9D). The Vp/Vs ratio varies with most values falling between 1.7 and 1.8 with an average value of 1.75 and shows no strong trends other than an overall slight increase in Vp/Vs with distance from the coast.

### 3.4. Discussion

#### 3.4.1 Moho Depth and Vp/Vs

The maximum Moho depth of 75 km beneath the Altiplano is consistent with results for the first seismic array (Line 1) in the region of normal subduction dip (Phillips et al,

2012). Previous studies in the Central Andes have resulted in comparable estimates for crustal thickness. Most estimates have an average value of 70 km with ranges between 59 and 80 km for crustal thickness beneath the Western and Eastern Cordilleras and Altiplano (Baumont et al, 2001; Beck et al, 1996; Beck & Zandt, 2002; Cunningham & Roecker, 1986; Lloyd et al, 2010; McGlashan et al, 2008; Myers et al, 1998; Yuan et al, 2002; Zandt et al, 1994). The crust in the Altiplano region is isostatically compensated primarily through crustal thickening (Whitman et al, 1993), and crustal shortening due to compression generated by plate coupling or through the Arica bend provides a significant mechanism for contributing the crustal thickness. Gotberg et al (2010) show that 70 km of thickness in to the Andes would require 240–300 km of shortening, but their preferred shortening estimate left a significant proportion of this shortening budget unaccounted for. Other possible mechanisms for thickening include processes such as shortening related to the Arica bend (Kley & Monaldi, 1998; Gotberg et al, 2010), magmatic additions or shortening hidden by the volcanic arc (Gotberg et al, 2010), thermal weakening, upper mantle hydration (Allmendinger et al, 1997), or other factors. Another possible mechanism which would help explain crustal thickness not accounted for by shortening is tectonic underthrusting which would be consistent with the idea that the midcrustal structure observed at 40 km depth is a result of underthrusting of the Brazilian shield (Whitman et al, 1993). This mechanism is more consistent with a gradual uplift model for this part of the Altiplano (Barnes and Ehlers, 2009; Ehlers and Poulsen, 2009; McQuarrie et al., 2005; Elger et al., 2005; Oncken et al., 2006). Vp/Vs ratios appear to have an average value between 1.73 and 1.75 with few discernible patterns in terms of areas of higher or lower Vp/Vs. A Vp/Vs ratio of 1.73-

1.75 corresponds to a Poisson's ratio of 0.25 to 0.2576, which is compatible with previous results for the Altiplano (Beck et al, 1996; Swenson et al, 2000; Zandt & Ammon, 1995). The observed values of the  $V_p/V_s$  ratio support the conclusion that the crust in the transition and flat slab region are nonvolcanic since there are no regions with abnormally high values as might be expected where a magma body is present. The location of the active volcanic arc relative to the arrays can be seen in figure 3.1 which confirms that Lines 2 and 3 are located outside of the volcanic region.  $V_p/V_s$  results for Line 1 in the region of normal subduction showed a few areas of higher  $V_p/V_s$  values near the active volcanic arc, which may be indicative of magmatism (Phillips et al, 2012). The amount of variation in  $V_p/V_s$  measurements is partly due to uncertainty in cases where the multiples on which they rely are not readily apparent in the receiver function data resulting in less constraint on  $V_p/V_s$  results. An example is seen in the supplementary materials where the signal from the Moho is observed more clearly than the multiple arrivals. The uncertainty is given by the 95% contour line and gives a  $1\sigma$  value of about 0.035 which is an average uncertainty estimate for error due to sources such as noise and unclear multiple arrivals.

### **3.4.2 Slab Structure**

The shape of the slab is delineated through various images from different backazimuths and the use of both P/PP and PKP receiver functions. For Line 2 the slab signal appears as a primarily negative impedance signal (see figures 3.3, 3.5 and 3.7), which agrees with the finite-difference modeling results. The transition from normal (~30 degree) subduction near Juliaca to flat slab subduction near Cusco appears to be

gradual, thus there is no evidence that the subducting Nazca Ridge caused a break in the slab. A subduction transition, which appears as a smooth bend in the slab is consistent with seismicity results of Grange et al, 1984. If the slab were tearing we would expect to see a whole series of tears as the Nazca Ridge propagated down the coast. Note that the point where the slab is starting to flatten is some 400 km ahead to the projection of the Nazca ridge. There is no indication in the seismicity that the slab returns to normal dip after the passage of the Nazca ridge. Note the contrast with Central Chile where the uplift is 130 km ahead of the projection of the Juan Fernandez Ridge and returns to its original dip within 150 km in its wake (estimated from slab contours, see Anderson et al 2007).

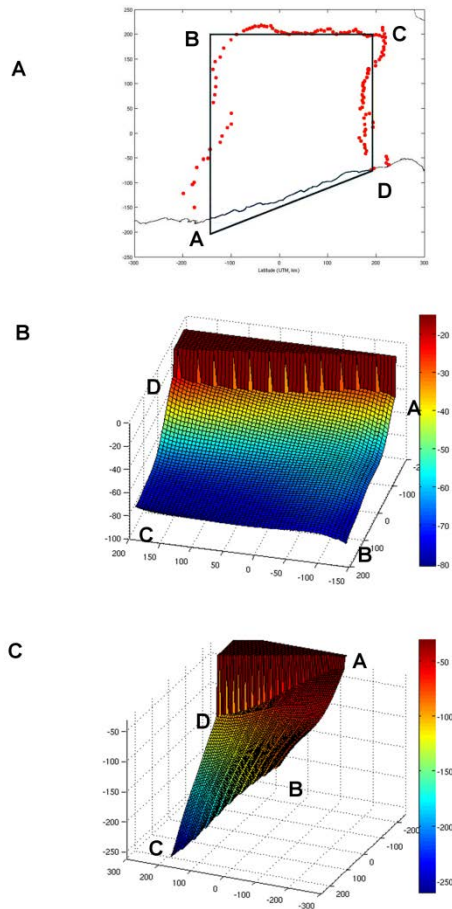


Figure 3.10. Interpolation of the Moho and slab estimates across the region enclosed by the seismic arrays in three dimensions. (A) Black lines represent region that was interpolated over. The letters correspond to corners of the 3D models below, (B) 3D model of the Moho depth, (C) 3D model of the slab.

The slab shape can be seen in a 3D model showing an interpolation of expected slab and Moho depths for all of the arrays in figure 3.10. In contrast to the negative impedance slab signal from the transition region, a positive impedance signal can be seen for the flat slab region in figures 3.6-3.8. The strongest amplitude of the double pulse slab structure can be seen in the first ~250 km of distance from the trench as the slab is descending to a depth of 100 km. This may be a result of the deeper subduction of hydrated oceanic sediments prior to dehydration of the minerals in the crust at

greater distances and depths (Kawakatsu and Watada 2007; Katayama et al. 2006). A comparison of the models for the normal, transition, and flat slab regions and corresponding synthetic receiver functions can be seen in figure 3.11 which has similar velocities for all three 2D models. Thus the reason why the appearance of the slab signal appears to be mainly a negative impedance signal for Line 2 compared to the slab signals for the other two arrays appears to be related to the subduction zone structure and angle of the subducted oceanic crust and a change in the transmission coefficient for certain angles of incidence.

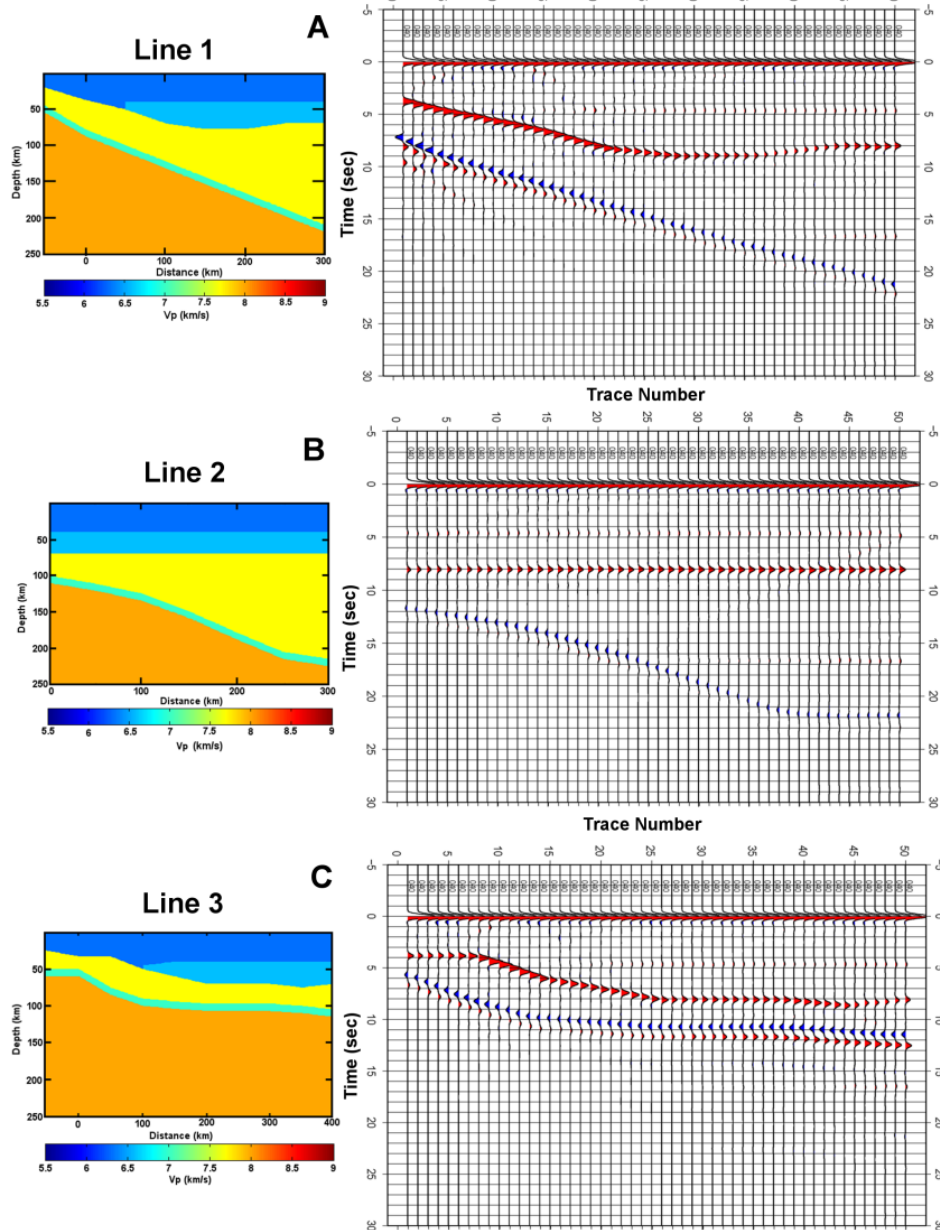


Figure 3.11. Comparison of synthetic models for all three seismic arrays showing A) the region of normal subduction (Line 1), B) the transition from normal to flat slab subduction (Line 2), and C) flat slab region (Line 3). Note that the synthetic receiver functions for Line 3 show a double pulse slab signal while the slab for Line 1 is double pulse mainly for the upper half and primarily negative at depth. The slab signal for Line 2 is mostly a negative impedance signal.

### **3.4.3 Nazca Ridge and Causes of Flat Slab Subduction**

The Nazca Ridge is currently subducting at a latitude of  $-15^{\circ}$  S and has a projection that puts the portion of the ridge that has already subducted just north of Line 3 (see figure 3.1). The Nazca Ridge has a trend of  $N42^{\circ}E$  at a region where the convergence direction is  $77^{\circ}$  resulting in an oblique angle of subduction and southward ridge migration (Hampel 2002). According to Hampel (2002), the Nazca Ridge began subducting at  $11^{\circ}S$  at 11.2Ma and is presently migrating at 43mm/yr. Several authors have considered the buoyancy effect of the Nazca Ridge as a mechanism to support the development of flat slab subduction (Gutscher 1999; Gutscher, Spakman et al. 2000; van Hunen et al, 2002a, 2002b). The ridge is a wide feature (200km wide, 1.5km high, with a total crustal thickness of 17 km) so the stations on the array closest to the coast are most likely to show the impact of the subducting ridge on the subduction system. Some of the expected effects of the subducting ridge on the coastal region are deformation of the upper plate, uplift in the forearc, westward shift of the coastline (Hampel, 2002), and a gravity anomaly corresponding to the crustal root supporting the ridge (Hampel et al. 2004; Macharé & Ortlieb, 1992). The coastal stations show possible evidence of some uplift in the forearc compared to the normal subduction region but overall the elevation profiles are similar (see figure 3.13).

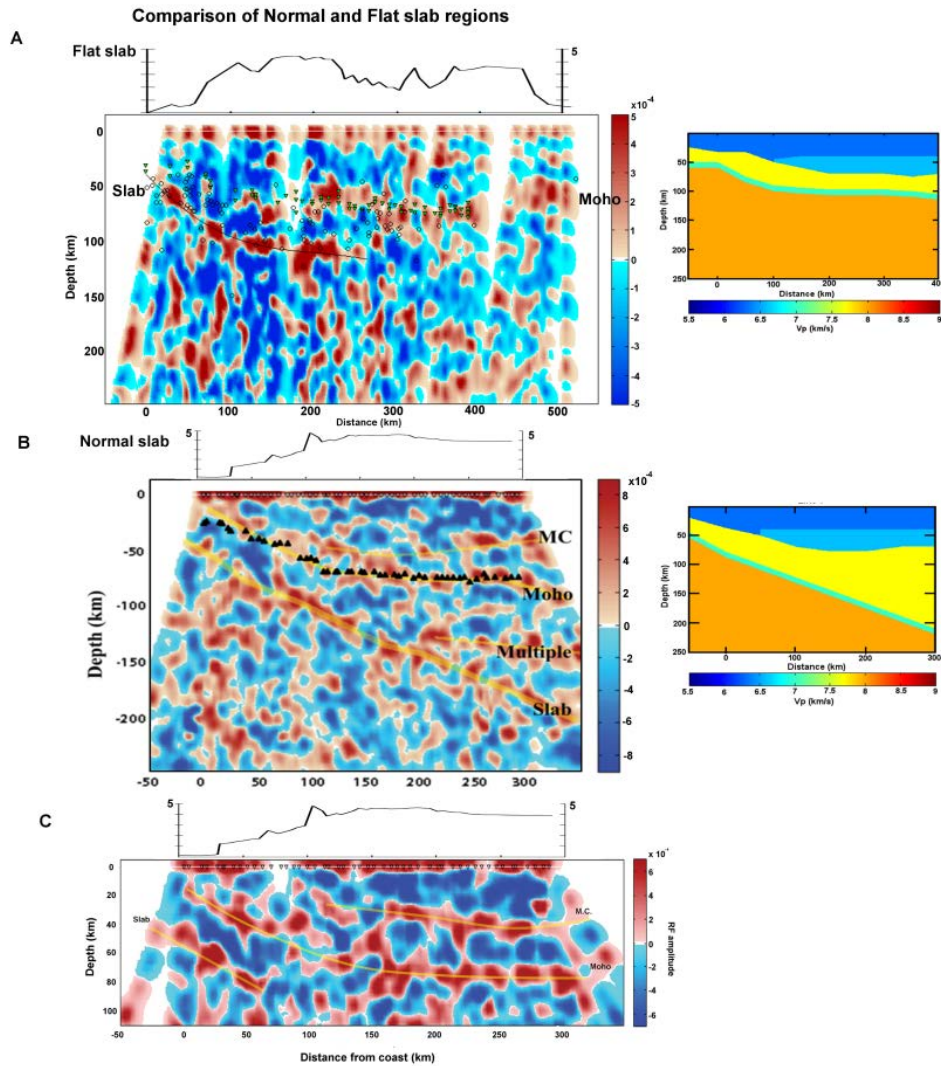


Figure 3.12. Comparison of the structure of the normal subduction region (Line 1) and flat slab region (Line 3). A) Line 3 from Nazca to Cusco. Moho picks from stacking are shown by green triangles. B) Results from Line 1 in the normal subduction region showing the 30 degree dipping slab using P/PP receiver functions from a NW backazimuth. Note that the double pulse slab signal from Line 3 (A) is most clear up to 100 km before appearing as a primarily negative signal while the slab in the region of normal signal is seen as a positive impedance signal at all depths down to a depth of about 200km. Simple models of the normal and flat slab regions used for finite difference modeling are shown to the right of the images. C) An image from Line 2 using P/PP receiver functions from all azimuthal directions showing only the upper 120 km. The Moho can be clearly seen as can a midcrustal structure at 40 km depth which is suggested to be from underthrusting of the Brazilian shield.

A comparison of receiver function results from Line 3 near the subducting Nazca Ridge with results from the region of normal subduction further south between Mollendo and Juliaca can be seen in figure 3.12. The slab dips near the trench are initially similar before the flat slab quickly flattens out at 100 km while in the normal region the slab continues descending at a constant angle. The Moho in both cases is relatively flat at a depth of around 70 km for much of the central section of the Altiplano. One notable difference is that the positive impedance signal from the Moho is less visible for Line 3 near the coastline where the slab is descending from the trench while for Line 1 the Moho is clear throughout the whole range of the array. The reason for this may be that dehydration could change the wedge velocity such that it has no contrast with the crust (Bostock et al. 2002). In the case of the flat slab, there is a gap of about 30 km between the Moho at 70 km depth and top of the slab at 100 km depth leaving a small amount of room for asthenospheric material. The difference between Moho depth and the subducting plate impacts the degree of coupling between the Nazca plate and overriding South American plate and thus the degree of intraplate hydrostatic suction which has been proposed as a possible factor in encouraging flat slab subduction.

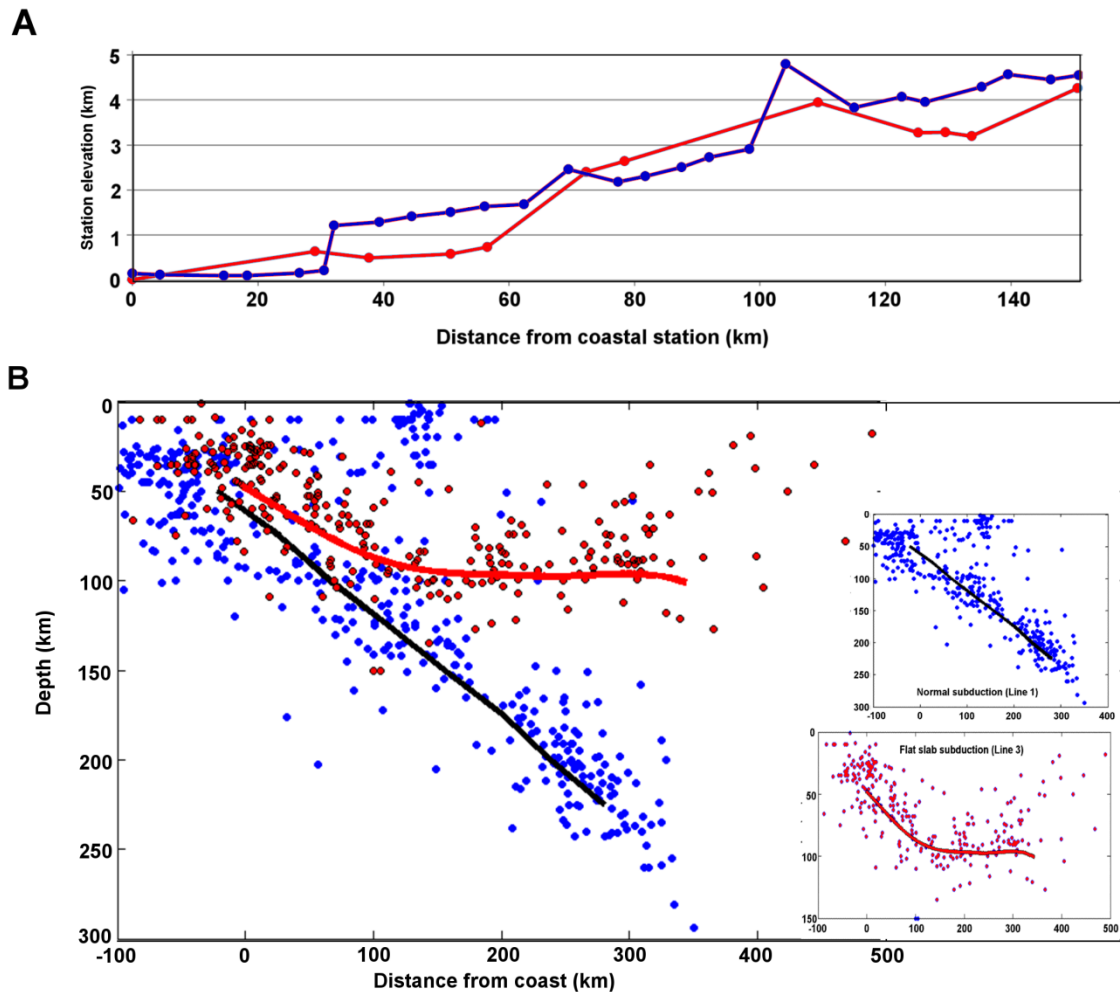


Figure 3.13. ( A) Comparison of station elevation for Line 1 (normal subduction) and Line 3 (flat slab subduction). Line 1 elevation is shown by the blue line and Line 3 by the red line. (B) Depth versus distance seismicity cross section for Line 1 and Line 3 allowing for comparison of flat slab and normal subduction regions. The individual cross sections are shown as insets. Earthquakes are from the NEIC catalog from 1982 to 2012 for events of magnitude greater than 4.0. Solid lines show a fit to seismicity which gives the approximate location for the top of the subducting Nazca plate.

A comparison of the topography in the forearc region to the Western Cordillera for both the normal and flat slab region can be seen in figure 3.13A. Both exhibit a similar rise although Line 1 is almost flat for the first 30 km before showing a sudden jump to an elevation of about 1.2 km while Line 3 initially rises more rapidly before flattening

out until 60 km from the coast. Thus at a distance of 30 km from the coast, Line 3 has an elevation about 400 m higher than Line 1 has at the same distance from the trench.

This may correspond to the several hundred meters of forearc uplift mentioned by Hampel, (2002) as resulting from the subduction of the Nazca Ridge.

Figure 3.13B-D shows a comparison of the seismicity between the flat slab and normal subduction region both in terms of seismicity in the Wadati-Benioff zone defining the shape of the slab and crustal seismicity, which provides some measure of amount of faulting and deformation in the upper plate. The seismicity comes from the NEIC catalog for the past 30 years (1982–2012) including events larger than Mw 4.0. Events were removed in which the depths were not well-defined and were given a default crustal depth of 33 km. The overall number of events is greater in the south where normal subduction is occurring. The difference in level of crustal seismicity does not appear to be significant, although in the case of normal subduction there appears to be a cluster of events near the center of the array at a very shallow depth, which is likely related to activity near the active volcanic arc.

In terms of a cause of flat slab subduction, most authors conclude that the Nazca Ridge does not have sufficient buoyancy by itself to sufficiently support the length of the Peruvian flat slab (Gutscher, Olivet et al. 1999; Gurscher, Spakman et al. 2000; van Hunen 2002a, 2004). Other factors present in Peru which can impact dip angle are the fast subduction velocity relative to the motion of the overriding plate, intermediate age of subducting lithosphere (30–40 Ma), the Arica bend, hydrostatic suction, and possibly cycles of repeated slab breakoff and flat slab subduction since repeated flat subduction events through time have been documented in the Andes (Haschke et al, 2007).

Although the main cause and relative importance of various causes are outside the scope of the data collected in this study, we conclude that the motion of the Nazca Ridge sweeping down the coast is unlikely to be a significant cause of flat slab subduction. The length of flat slab segment south of the Nazca Ridge appears too long to be supported by buoyancy of the Ridge alone and regions north of the Ridge do not return to normal dip after the Ridge has passed.

### **3.5. Conclusions**

Receiver function studies from seismic arrays in Southern Peru provide more details of the structure of the transition region from normal (30 degree dip) subduction to flat slab subduction. The Moho beneath the Altiplano is found to have a maximum depth of 75 km. The shape of the slab is also clarified and the transition is found to be gradual from normal to flat slab subduction, which indicates that the change is most likely a contortion rather than a break in the slab. The slab is observed have an almost constant depth of 100 km beneath the array in the flat slab region. The observed impacts of the Nazca Ridge and flat slab subduction from this study are a lessening of overall seismicity, minor uplift in the forearc region, and a less defined Moho transition near the coast.

### **Acknowledgements**

We thank the Betty and Gordon Moore Foundation for their support through the Tectonics Observatory at Caltech. This research was partially support by NSF award

EAR-1045683. Also thanks to Richard Guy, Paul Davis and Igor Stubailo of the UCLA Center for Embedded Networked Systems, Steven Skinner of the Caltech Seismological Laboratory, Hernando Tavera and Victor Aguilar of the Instituto Geofisico del Peru, and Laurence Audin of IRD. We also thank the PULSE and CAUGHT projects for contributing data to this study.

### Chapter 3 References

- Abers, G. (2000), Hydrated subducted crust at 100-250 km depth, *Earth and Planet. Sci. Lett.*, 176, 323–330.
- Abers, G., P. van Keken, E. Kneller, A. Ferris, and J. Stachnik (2006), The thermal structure of subduction zones constrained by seismic imaging: Implications for slab dehydration and wedge flow, *Earth and Planet. Sci. Lett.*, 241, 387–397.
- Allmendinger, R., T. Jordan, S. Kay, and B. Isacks (1997), The Evolution of the Altiplano-Puna Plateau of the Central Andes, *Annu. Rev. Earth Planet. Sci.*, 25, 139–174.
- Ammon, C. (1991), The isolation of receiver effects from teleseismic P waveforms, *Bull. Seismo. Soc. Am.*, 81 (6), 2504–2510.
- Anderson, M., P. Alvarado, G. Zandt, and S. Beck (2007), Geometry and brittle deformation of the subducting Nazca Plate, Central Chile and Argentina, *Geophys. J. Int.*, 171, 419–434.
- Barazangi, M. and B. L. Isacks (1976), Spatial distribution of earthquakes and subduction of the Nazca plate beneath South America, *Geology*, 4, 686–692.

- Barnes, J. and T. Ehlers (2009), End member models for Andean Plateau uplift, *Earth-Sci. Rev.*, 97, 105–132.
- Baumont, D., A. Paul, G. Zandt, S. L. Beck (2001), Inversion of Pn travel times for lateral variations of Moho geometry beneath the Central Andes and comparison with the receiver functions, *Geophys. Res. Lett.*, 28 (9), 1663–1666.
- Beate, B., M. Monzier, R. Spikings, J. Cotton, J. Silva, E. Bourdon, and J. Eissen (2001), Mio-Pliocene adakite generation related to flat subduction in southern Ecuador: the Quimsacocha volcanic center, *Earth and Planet. Sci. Lett.*, 192, 561–570.
- Beck, S. and G. Zandt (2002), The nature of orogenic crust in the central Andes, *J. Geophys. Res.*, 107 (B10), 2230.
- Beck, S., G. Zandt, S. Myers, T. Wallace, P. Silver, and L. Drake (1996), Crustal-thickness variations in the central Andes, *Geology*, 24 (5), 407–410.
- Bevis, M. (1986), The Curvature of Wadati-Benioff Zones and the Torsional Rigidity of Subducting Plates, *Nature*, 323, 52–53.
- Bostock, M., R. Hyndman, S. Rondenay, and S. Peacock (2002), An inverted continental Moho and serpentinization of the forearc mantle, *Nature*, 417, 536–538.
- Cahill, T. and B. L. Isacks (1992), Seismicity and Shape of the Subducted Nazca Plate, *J. of Geophys. Res. - Solid Earth*, 97 (17), 503–17, 529.
- Cunningham, P. and S. Roecker (1986), Three-dimensional P and S Wave Velocity Structures of Southern Peru and Their Tectonic Implications, *J. of Geophys. Res.*, 91 (B9), 9517–9532.
- Dorbath, C., M. Gerbault, G. Carlier and M. Guiraud (2008), Double seismic zone of

the Nazca plate in Northern Chile: High-resolution velocity structure, petrological implications, and thermomechanical modeling, *Geochem., Geophys., Geosys.*, 9 (7), Q07,006.

- Eakin, C. M., M. D. Long, S. L. Beck, and L. S. Wagner (2011), Seismic anisotropy and mantle flow beneath the Peruvian flat slab region, AGU, Fall Meeting 2011, abstract #DI44B-04.
- Ehlers, T. and C. Poulsen (2009), Influence of Andean uplift on climate and paleoaltimetry estimates, *Earth and Planet. Sci. Lett.*, 281, 238–248.
- Elger, K., O. Oncken, and J. Glodny (2005), Plateau-style accumulation of deformation: Southern Altiplano, *Tectonics*, 24, TC4020.
- Gotberg, N., N. McQuarrie, and V. Caillaux (2010), Comparison of crustal thickening budget and shortening estimates in southern Peru (12–14 S): Implications for mass balance and rotations in the “Bolivian orocline,” *GSA Bulletin*, 122 (5–6), 727–742.
- Grange, F., J. Gagnepain, D. Hatzfeld, P. Molnar, L. Ocola, A. Rodrigues, S. Roeker, J. Stock, and G. Suarez (1984), The configuration of the seismic zone and the downgoing slab in Southern Peru, *Geophys. Res. Lett.*, 11 (1), 38–41.
- Gutscher, M., J. Malavielle, S. Lallemand, and J. Collot (1999), Tectonic segmentation of the North Andean margin: impact of the Carnegie Ridge collision, *Earth and Planet. Sci. Lett.*, 168, 255–270.
- Gutscher, M., R. Maury, J. Eissen, and E. Bourdon (2000), Can slab melting be caused by flat subduction? *Geology*, 28 (5), 535–538.
- Gutscher, M., J. Olivet, D. Aslanian, J. Eissen, and R. Maury (1999), The “lost Inca

- Plateau”: Cause of flat subduction beneath Peru?, *Earth and Planet. Sci. Lett.*, 171 (3), 335–341.
- Gutscher, M., W. Spakman, H. Bijwaard, and E. Engdahl (2000), Geodynamics of flat subduction: Seismicity and tomographic constraints from the Andean margin, *Tectonics*, 19 (5), 814–833.
  - Hampel, A. (2002), The migration history of the Nazca Ridge along the Peruvian active margin: a re-evaluation, *Earth and Planet. Sci. Lett.*, 203, 665–679.
  - Hampel, A., N. Kukowski, J. Bialas, C. Huebscher and R. Heinbockel (2004), Ridge subduction at an erosive margin: The collision zone of the Nazca Ridge in southern Peru, *J. of Geophys. Res.*, 109, B02101.
  - Haschke M., A. Gunther, D. Melnick, H. Echtler, K. Reutter, E. Scheuber, and O. Onken (2007), Chapter 16: Central and southern Andean tectonic evolution inferred from arc magmatism, in *The Andes: Active Subduction Orogeny*, *Frontiers Earth Sci.*, vol. 1, edited by O. Oncken et al., pp 337–354, New York: Springer.
  - Haschke M., E. Scheuber, A. Gunther, and K. Reutter (2002), Evolutionary cycles during the Andean orogeny: repeated slab breakoff and flat subduction?, *Terra Nova*, 14 (1), 49–55.
  - Hayes, G. P., D. J. Wald, and R. L. Johnson (2012), Slab1.0: A three-dimensional model of global subduction zone geometries, *J. Geophys. Res.*, 117, B01302.
  - International Seismological Centre, On-line Bulletin, <http://www.isc.ac.uk>, Internatl. Seis. Cent., Thatcham, United Kingdom, 2010.
  - Jischke, M. (1975), Dynamics of descending lithospheric plates and slip zones, *J.*

- of Geophys. Res.*, 80, 4809–4813.
- Katayama, I., S. Nakashima, and H. Yurimoto (2006), Water content in natural eclogite and implications for water transport into the deep upper mantle, *Lithos*, 86, 245–259.
  - Kawakatsu, H. and S. Watada (2007), Seismic Evidence for Deep-Water Transportation in the Mantle, *Science*, 316, 1468.
  - Kim, Y., R. W. Clayton, and J. M. Jackson (2010), Geometry and seismic properties of the subducting Cocos plate in central Mexico, *J. Geophys. Res.*, 115, B06310.
  - Kley, J. and C. R. Monaldi (1998), Tectonic shortening and crustal thickness in the Central Andes: How good is the correlation? *Geology*, 26 (8), 723–726.
  - Langston, C. (1979), Structure under Mount Rainier, Washington, inferred from teleseismic body waves, *J. Geophys. Res.*, 84, 4749–4762.
  - Liggoria, J. and C. Ammon (1999), Iterative deconvolution and receiver function estimation, *Bull. Seism. Soc. Am.*, 89, 19–36.
  - Lloyd S., S. van der Lee, G. Sand Franca, M. Assumpcao, and M. Feng (2010), Moho map of South America from receiver functions and surface waves, *J. of Geophys. Res.*, 115, B11315.
  - Macharé, J. and L. Ortlieb (1992), Plio-Quaternary vertical motions and the subduction of the Nazca Ridge, central coast of Peru, *Tectonophysics*, 205, 97–108.
  - McGeary S., A. Nur, and Z. Ben-Avraham (1985), Spatial gaps in arc volcanism: the effect of collision or subduction of oceanic plateaus, *Tectonophysics*, 119, 195–221.
  - McGlashan N., L. Brown, and S. Kay (2008), Crustal thickness in the central Andes from teleseismically recorded depth phase precursors, *Geophys. J. Int.*, 175, 1013–

1022.

- McQuarrie, N., B. Horton, G. Zandt, S. Beck, and P. DeCelles (2005), Lithospheric evolution of the Andean fold-thrust belt, Bolivia, and the origin of the central Andean plateau, *Tectonophysics*, 399, 15–37.
- Myers, S., S. Beck, G. Zandt, and T. Wallace (1998), Lithospheric-scale structure across the Bolivian Andes from tomographic images of velocity and attenuation for P and S waves, *J. of Geophys. Res.*, 103 (21),233–21,252.
- Olbertz, D., M. Wortel, and U. Hansen (1997), Trench migration and subduction zone geometry, *Geophys. Res. Lett.*, 24, 221–224.
- Oncken, O., J. Kley, K. Elger, P. Victor, and K. Schemmann (2006), Deformation of the Central Andean Upper Plate System-Facts, Fiction, and Constraints for Plateau Models, Springer, Berlin, 569 pp.
- Pennington, W. (1984), The Effect of Oceanic Crustal Structure on Phase-Changes and Subduction, *Tectonophysics*, 102, 377–398.
- Phillips, K. E., R. Clayton, P. M. Davis, H. Tavera, R. Guy, S. Skinner, I. Stubailo, L. Audin, and V. Aguilar (2012), Structure of the Subduction System in Southern Peru From Seismic Array Data, *J. Geophys. Res.*, doi:10.1029/2012JB009540, in press.
- Pilger, R. (1981), Plate reconstructions, aseismic ridges, and low-angle subduction beneath the Andes, *GSA Bull.*, Part I, 92, 448–456.
- Ryan, J., K. Ward, R. Porter, S. Beck, G. Zandt, L. Wagner, E. Minaya, and H. Tavera (2011), Preliminary Results From the CAUGHT Experiment: Investigation of the North Central Andes Subsurface Using Receiver Functions and Ambient Noise Tomography, AGU, Fall Meeting 2011, abstract #T11B-2323.

- Sacks, I., 1983. The subduction of young lithosphere, *J. of Geophys. Res.*, 88, 3355–3366.
- Skinner, S. M. and R. W. Clayton (2012), The lack of correlation between flat slabs and bathymetric impactors in South America, *Earth and Planet. Sci. Lett.*, In Review.
- Suarez G., P. Molnar, B. C. Burchfiel (1983), Seismicity, Fault Plane Solutions, Depth of Faulting, and Active Tectonics of the Andes of Peru, Ecuador, and Southern Colombia, *J. of Geophys. Res.*, 88 (B12), 10403–10428.
- Swenson, J., S. L. Beck, and G. Zandt (2000), Crustal structure of the Altiplano from broadband regional waveform modeling: Implications for the composition of thick continental crust, *J. of Geophys. Res.*, 105 (B1), 607–621.
- van Hunen, J., A. van den Berg, and N. Vlaar (2002a), The impact of the South American plate motion and the Nazca Ridge subduction on the flat subduction below South Peru, *Geophys. Res. Lett.*, 29 (14).
- van Hunen, J., A. van den Berg, and N. Vlaar (2002b), On the role of subducting oceanic plateaus in the development of shallow flat subduction, *Tectonophysics*, 352, 317–333.
- van Hunen, J., A. van den Berg, and N. Vlaar (2004), Various mechanisms to induce present-day shallow flat subduction and implications for the younger Earth: a numerical parameter study, *Phys. of the Earth and Planet. Int.*, 146, 179–194.
- von Huene, R., J. Corvalan, E. R. Flueh, K. Hinz, J. Korstgard, C. R. Ranero, W. Weinrebe, and the Condor Scientists (1997), Tectonic control of the subducting Juan Fernandez Ridge on the Andean margin near Valparaiso, Chile, *Tectonics*, 16,

- 474–488.
- Whitman, D., B. L. Isacks, and S. M. Kay (1993), Lithospheric Structure and Along-Strike Segmentation of the Central Andean Plateau, 17-29° S, Second ISAG, Oxford (UK), 21-23/9/1993.
  - Yan, Z. and R.W. Clayton (2007), Regional mapping of the crustal structure in southern California from receiver functions, *J. of Geophys. Res.*, 112, B05311.
  - Yogodzinski, G. M., J. M. Lees, T. G. Churikova, F. Dorendorf, G. Woerner, and O. N. Volynets (2001), Geochemical evidence for the melting of subducting oceanic lithosphere at plate edges, *Nature*, 409, 500–504.
  - Yuan, X., S. V. Sobolev, and R. Kind (2002), Moho topography in the central Andes and its geodynamic implications, *Earth and Planet. Sci. Lett.*, 199, 389–402.
  - Zandt, G. and C. Ammon (1995), Continental crust composition constrained by measurements of crustal Poisson's ratio, *Nature*, v. 374, p.152–154.
  - Zandt, G., A. Velasco, and S. Beck (1994), Composition and thickness of the southern Altiplano crust, Bolivia, *Geology*, 22, 1003–1006.
  - Zhu, L. and H. Kanamori (2000), Moho depth variation in southern California from teleseismic receiver functions, *J. Geophys. Res.*, 105 (B2), 2969–2980.

## *Chapter 4: Methods and Other Results*

The following sections describe methodology and some methods and results not described in the previous chapters. It covers the experimental setup in the field, details of processing and receiver function deconvolution methods (both frequency domain and time domain deconvolution), phases used for receiver functions (P, PP, PKP, and S/SKS), the stacking method to obtain interface depths and the  $V_p/V_s$  ratio from receiver functions, the use of transverse receiver functions to look at anisotropy and dipping structures, imaging methods, finite difference modeling, and analysis of local events.

### **4.1: Field Work in Peru**

Field work and installation of broadband seismic stations was performed which allowed for the collection of the data used for this study. Preparation for the installation of the first seismic array began in early 2008. The first array (Line 1) began collecting data at the end of June 2008. Line 1 was installed in collaboration with CENS at UCLA (Center for Embedded Networked Systems). Some of the collaborators in the field work were Richard Guy, Igor Stubailo, Emily Foote, and Allan Husker from UCLA/CENS, Jennifer Sery from Strassbourg France, Victor Aguilar from IGP, and Steve Skinner from Caltech. The first array was connected by a wireless system of YAGI and parabolic antennas so that seismic data could be automatically sent to central collection points and uploaded to a server in California via internet. The advantage of

this was that the data is immediately available which allows for quick detection and correction of problematic stations.

#### **4.1.1 Installation Procedure**

The seismic equipment was to be installed on the property of local residents for security purposes to reduce the likelihood of equipment being stolen. The first array, called Line 1 was planned to include a total of 50 stations over a distance of 300 km from Mollendo on the coast to Juliaca near Lake Titicaca allowing for a station spacing of 6 km. One of the installation challenges was that sites needed to be able to “see” each other in order to relay signals via YAGI or parabolic antennas. This required very careful site selection and sometimes antennas needed to be placed at greater heights or have their signal amplified in order to reach other stations.

After site permissions and selection, sites were prepared by digging holes for the sensor and metal box which contains the battery, digitizers (Quanterra Q330 and Reftek 130), and datalogger or CDCC (CENS Data Communication Controller) (Husker et al, 2008). Sites were connected to electricity either through solar panels or electrical connections to the local resident’s power connection. For later arrays solar panels were used almost exclusively because of issues with power going out, particularly at places such as schools which close on holidays. Masts were also installed on the ground or roof to hold YAGI antennas and solar panels. Broadband Guralp 3T sensors were installed in a circular tube or trash can on top of a cement platform. The trashcan would be filled with an insulator. Examples of sites can be seen in figure 4.1. The arrays for Line 1 typically had an equipment box which was buried in the ground while for the other

arrays the box was attached to the solar panel mast either at the ground or partway up the mast.



Figure 4.1: Photos from the installation of the seismic arrays. The sensor is placed in the round holes where a blue trashcan is visible. It is seated in a cement base and insulated. Power in these cases is supplied by solar panel, and the box containing equipment is either attached to the base of the mast (left), attached halfway up the mast (center), or buried in the ground (right).

#### 4.1.2 Second and Third Arrays

The second and third arrays began collecting data at the end of 2009 and 2010 respectively. Line 2 was installed between Cusco and Juliaca with about 50 stations imported from the Mexican MASE project (Middle America Subduction Experiment). The array distance and station spacing was comparable to Line 1. A significant difference between these arrays and the first array is that there was no need to connect the sites wirelessly which streamlined station installation. All seismic data is stored on memory cards and collected each month.

The stations for the third array were populated in a two stage process. First half of the stations from Line 1 were removed in mid-2010 and placed along Line 3. In mid-2011 half of the stations from Line 2 were removed to form the rest of Line 3. Thus when

Line 3 was fully operational in 2011 there were still stations collecting data on Lines 1 and 2. Line 3 is parallel to Line 1 and runs over a distance of 400 km. A few stations from the PULSE experiment which expand the line towards Brazil were later added which bring the total length covered up to 500 km.

#### 4.2: Processing Methods and Receiver Function Methods

Events to analyze were selected according to distance and magnitude criteria. In total, about 232 events were used for receiver function analysis of Line 1 (80 using the P phase, 152 PP, and 52 PKP), 219 events for Line 2 (65 P, 154 PP, and 62 PKP), 178 events for Line 3 (57 P, 121 PP, and 27 PKP). For the stations on the coast between Mollendo and Nazca 61 events were used (19 P, 42 PP, and 13 PKP). For the CAUGHT/PULSE stations 46 events were used (19 P, 27 PP and 11 PKP).

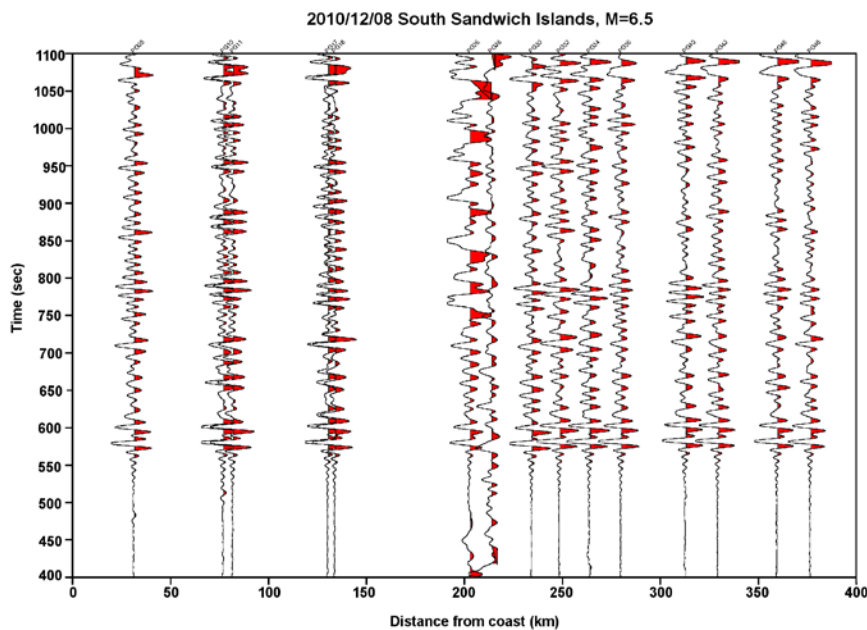


Figure 4.2: Data from the vertical component of seismograms recorded by Line 3 for a Mw 6.5 in Sandwich Islands on 12/08/2010.

Events were first bandpass filtered between 0.01 and 1 Hz or between 0.01 and 0.5 Hz depending on data quality. A significant portion of the data in Peru has a high amount of noise due to the large number of microseisms and seismic activity in Peru.

Consequently for many events the signal from the earthquake is not even visible until after the data has been filtered. An example of a less noisy event can be seen in figure 4.2 which shows vertical seismograms recorded by Line 3 for a magnitude 6.5 event on 2010/12/08 in the S. Sandwich Islands region to the south of Peru. Figure 4.3A shows a comparison between an unfiltered trace (black), a trace filtered from 1 to 100 sec (red), and a trace filtered from 2 to 100 sec (green). Figure 4.3B shows the data prior to filtering (which has very low noise) and figure 4.3C shows the same traces after filtering (2 to 100 seconds). In both cases the P wave arrival can be clearly seen. There is bad data for one of the stations. Stations which consistently provide problematic data for a one-month period (the time between data collection trips) are reported and manually checked for issues in Peru at the next collection time. Often the vertical component will look normal, but one or more of the horizontal components of the seismogram will be problematic. This can be an issue for making receiver functions which require using both the radial and vertical components for deconvolution since sometimes at least a third or more of the stations will have one or more components that are bad. Such problems can usually be resolved by fixing any GPS errors and recentering the sensor mass when one or more channels is observed to be at an extreme value.

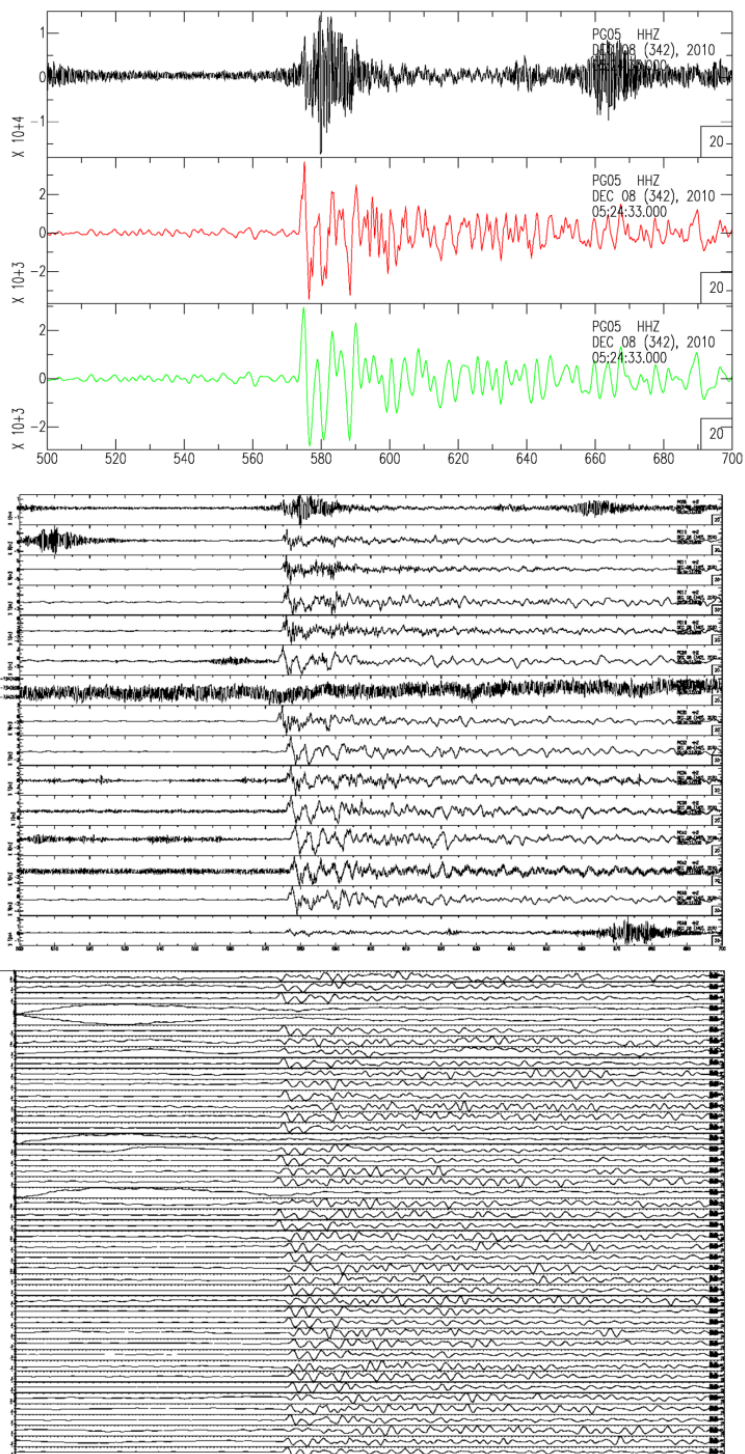


Figure 4.3: Comparison of unbandpassed data from 12/08/2010 recorded by Line 3 with data bandpassed to 1 second or 2 seconds. Top: Comparison of the vertical seismic component for PG05 unfiltered, bandpassed to 1 second, and bandpassed to 2 seconds.

Middle: All stations for 12/08/2010 unfiltered. Bottom: All Line 3 stations filtered to 2 second for 12/08/2010.

A comparison of receiver functions using 1 sec filtered data versus 2 sec filtered data is seen in figure 4.4. The major arrivals are the same in both cases although the 1 sec receiver function results can appear slightly higher in frequency. Any minor differences for individual stations result from choice of water level which is normally constrained by noise level. During the deconvolution part of receiver function analysis, values for water level parameter and gauss parameter are chosen based on quality, noise, and frequency content of receiver function results to obtain the highest quality receiver functions possible. The choice of gauss parameter (by default either 5 or 2.5) generally has little to no effect on results but can reduce the amount of artificial high frequency content if present. The choice of water level is by default 0.01 unless the receiver function results are noisier in which case 0.1 would be selected. For particularly good results 0.001 is used.

### Receiver Functions, 12/08/2010, Sandwich Islands

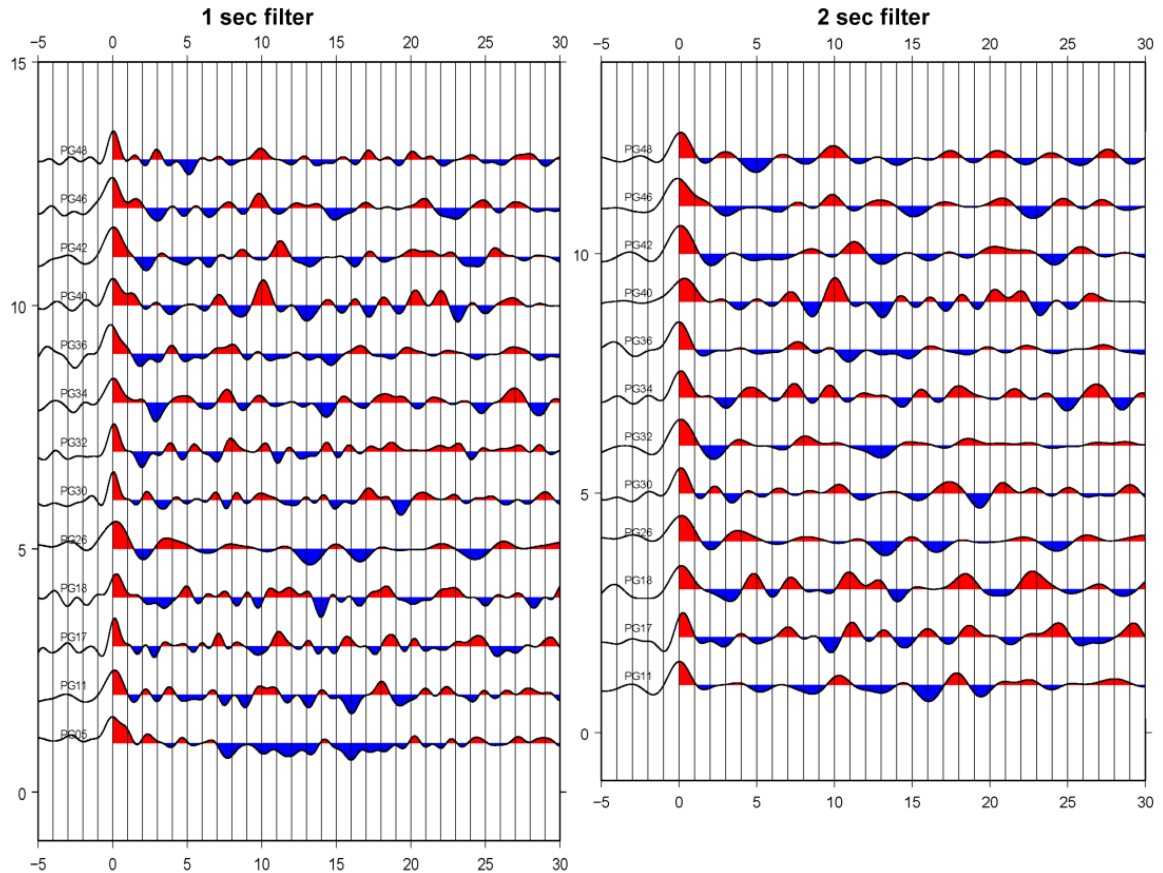


Figure 4.4: Comparison of receiver functions for 12/08/2010 Sandwich Islands bandpassed to 1 second (left) and 2 seconds (right). Individual stations have very similar receiver functions and consistent main arrivals regardless of the filtering. Receiver functions bandpassed to the higher frequencies tend to be slightly noisier.

#### 4.2.1: Processing Procedure

Event information added to SAC headers if each data file comes from the Southern California Earthquake Data Center using STP (Seismic Transfer Program). After the origin time has been set, the P wave arrival time is estimated using an automatic picker which uses the event distance and depth and a standard velocity model (IASP91). The data is cut to 100 sec before the P wave arrival and 300 sec after the P arrival and then the set of three components for each station is individually checked for quality and

accuracy of the automatic arrival pick. If the picks are observed to be inaccurate they can be picked manually but small adjustments to the P arrival time were not found to have a significant impact on the receiver functions. The data that passes the quality control test is rotated into vertical, radial, and tangential directions.

## 4.2.2 Deconvolution methods

### 4.2.2.1 Frequency Domain Deconvolution

Most receiver functions shown here are done using frequency domain deconvolution although time domain deconvolution was also done. The basic procedure can be found in Langston, 1979. In the time domain the theoretical displacement response can be written as:

$$DV(t) = I(t) * S(t) * E_V(t), \quad (4.1)$$

$$DR(t) = I(t) * S(t) * E_R(t), \quad (4.2)$$

$$DT(t) = I(t) * S(t) * E_T(t), \quad (4.3)$$

where  $I(t)$  is the instrument impulse response,  $S(t)$  is a complicated source time function, and  $E_V(t)$ ,  $E_R(t)$ ,  $E_T(t)$  are the structure impulse response in the vertical, radial, and tangential directions. Langston, (1979) citing Burdick and Helmberger, (1974) noted an observation from teleseismic data “that the vertical component of ground motion behaves as a pulselike time function convolved with the instrument response with only minor later arrivals.” This resulted in the approximation  $I(t)*S(t) \sim D_V(t)$  which assumes that  $D_V(t)$  behaves as a dirac delta function. Thus in the frequency domain:

$$ER(\omega) = \frac{D_R(\omega)}{I(\omega)S(\omega)} \sim \frac{D_R(\omega)}{D_V(\omega)}, \quad (4.4)$$

$$ER(\omega) = \frac{D_R(\omega)}{I(\omega)S(\omega)} \sim \frac{D_R(\omega)}{D_V(\omega)}. \quad (4.5)$$

This receiver function deconvolution process removes source effects and mantle propagation effects to give only information about structure directly beneath the station.

Due to numerical instability in the above equations, the following form is used:

$$ER(\omega) = \frac{D_R(\omega)D_V^T}{\max\{D_V(\omega)D_V^T, c \cdot \max[D_V(\omega)D_V^T]\}} G(\omega), \quad (4.6)$$

where in the previous equation the superscript T represents taking the transpose,  $c$  is the water level parameter, and  $G$  is the Gaussian function of the form  $G(\omega) = e^{-\omega^2/4\alpha^2}$  where  $\alpha$  is the Gauss parameter.

The resultant receiver function has a large arrival from the direct P wave at  $t = 0$  followed by an arrival from the converted phase, usually a P to S conversion at the Moho, followed later by multiple arrivals.

#### 4.2.2.2. Time Domain Deconvolution

Deconvolution in the time domain is an iterative approach which was described in Ligorria and Ammon (1999) as a “least-squares minimization of the difference between the observed horizontal seismogram and a predicted difference between the observed horizontal seismogram and a predicted signal generated by the convolution of an iteratively updated spike train with the vertical-component seismogram.”

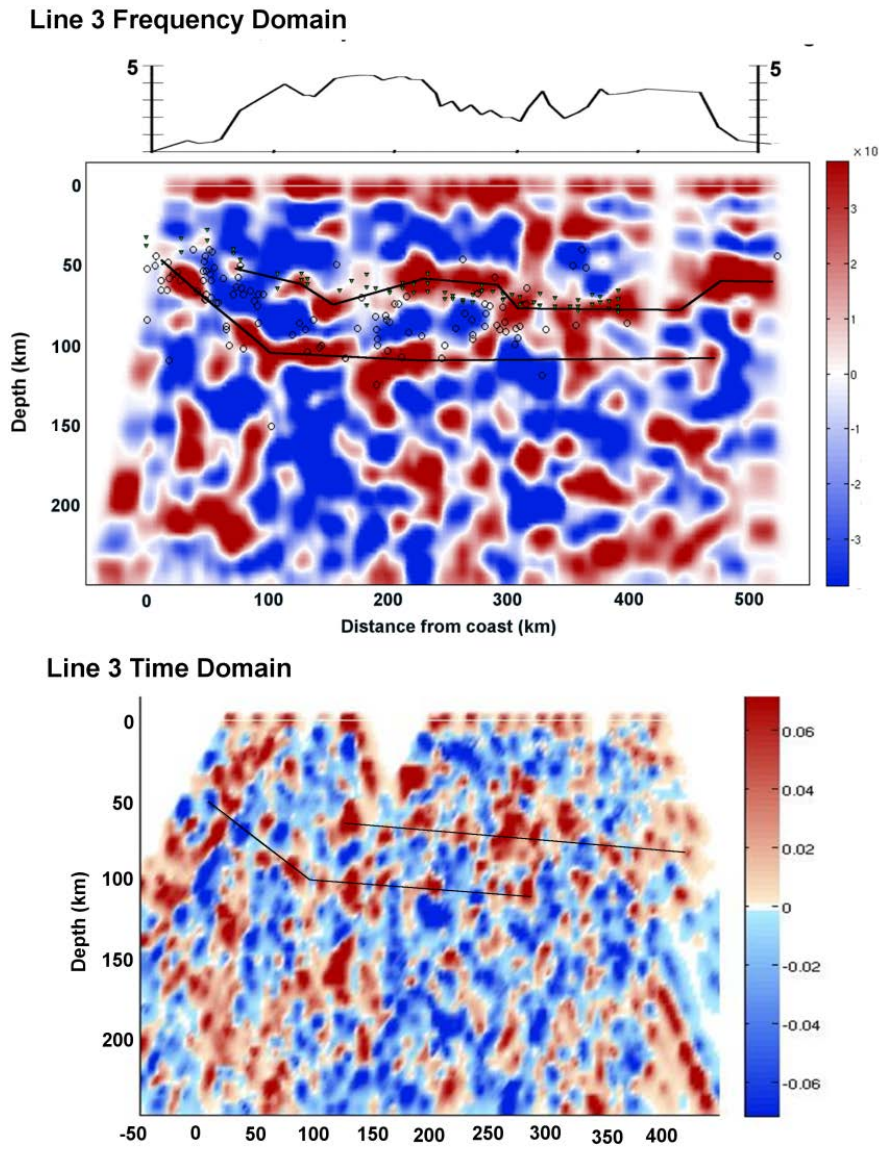


Figure 4.5: Receiver function images for Line 3 from backprojection of receiver functions using events from a NW backazimuth. The top image contains receiver functions made with frequency domain deconvolution while the bottom image has receiver functions made with iterative time domain deconvolution. Black lines show the approximate locations of the slab and Moho from the images. Note that the top image has a longer distance scale due to the addition of stations from the PULSE experiment which were analyzed with frequency domain deconvolution. Station elevation is shown at the top of the figure.

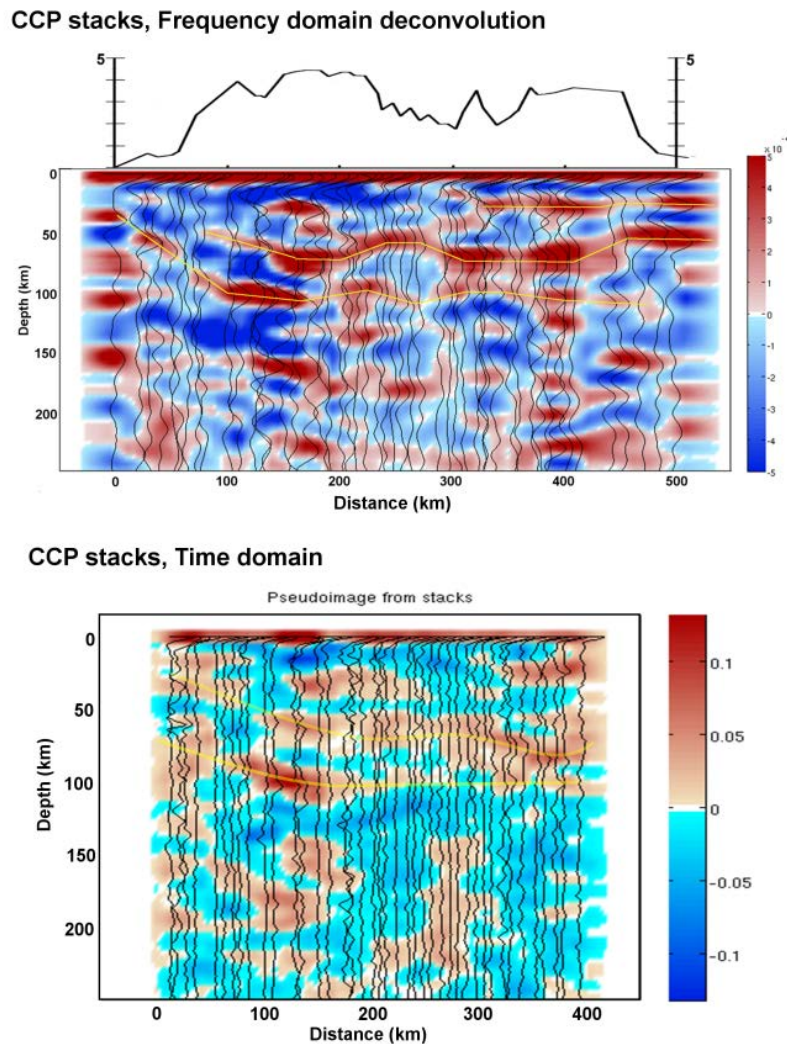


Figure 4.6: A comparison of receiver function images in the frequency domain and time domain using CCP (common conversion point) stacking for events from a NW backazimuth. The Moho and slab shape are more defined for the time domain RFs when stacks are plotted rather than the unstacked data (as in figure 4.5).

Receiver functions using time domain deconvolution produce results consistent with those in the frequency domain but receiver function results shown in this chapter are based on frequency domain deconvolution due to a higher amount of noise in the time domain results (see figure 4.5 and figure 4.6 which show receiver function images

using both methods for Lines 1 and 3). A comparison of the receiver functions using time and frequency domain deconvolution methods can be seen in figure 4.7 which shows receiver functions from the event on 2012/12/08 earthquake in Sandwich Islands. A comparison of receiver functions from the same stations shows that in most cases, the positive and negative pulses match up well. The main difference is that the time domain receiver functions appear as sharp pulses while the frequency domain receiver functions are longer period.

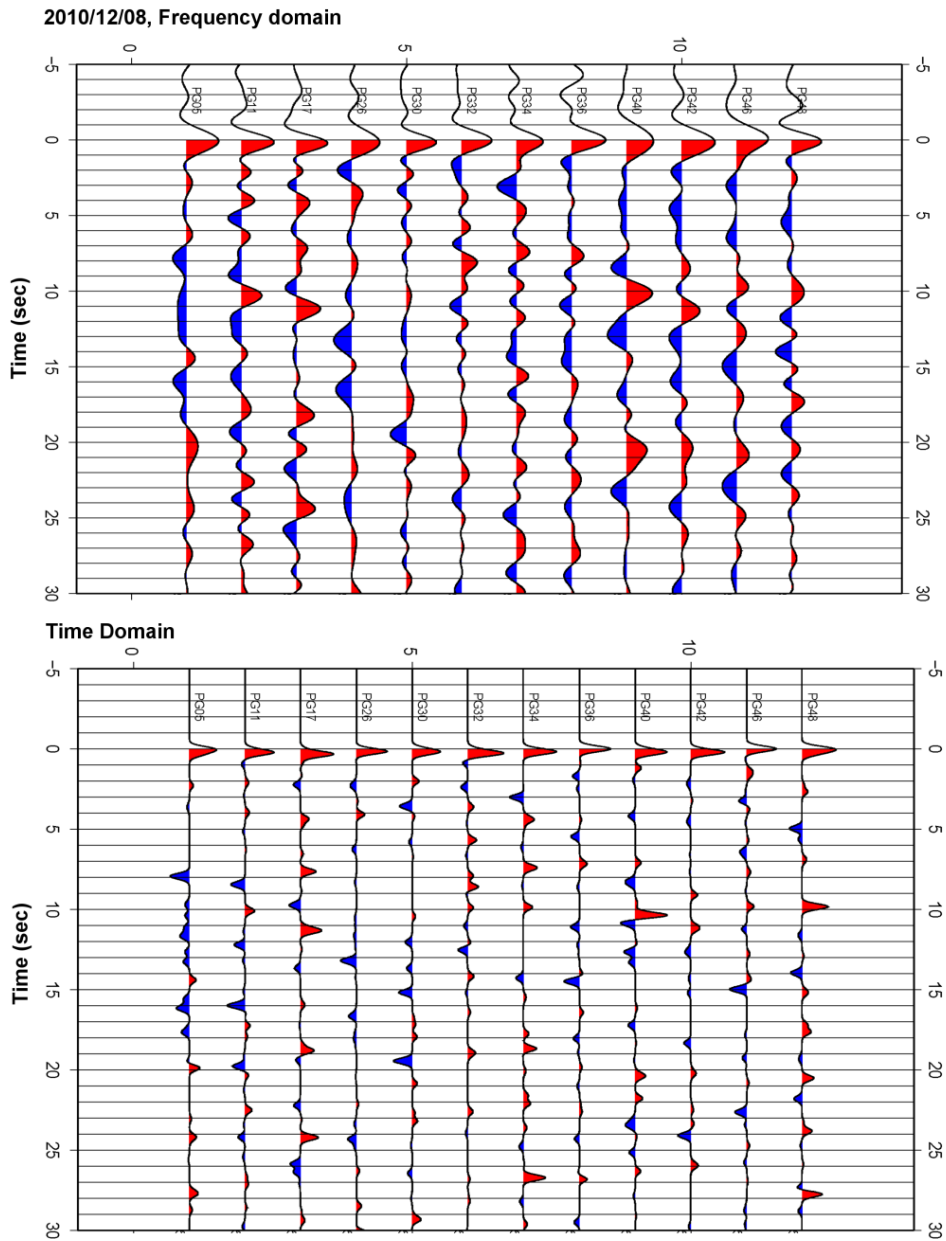


Figure 4.7: Receiver functions for 12/08/2010 Sandwich Islands event (data shown in figure 4.2) using frequency domain deconvolution (top) and time domain deconvolution (bottom). The main arrivals are seen to be consistent for both methods.

A comparison of the two methods for individual stations can be seen in figure 4.8 and figure 4.9 which show sample receiver functions for stations PG40 and PG50.

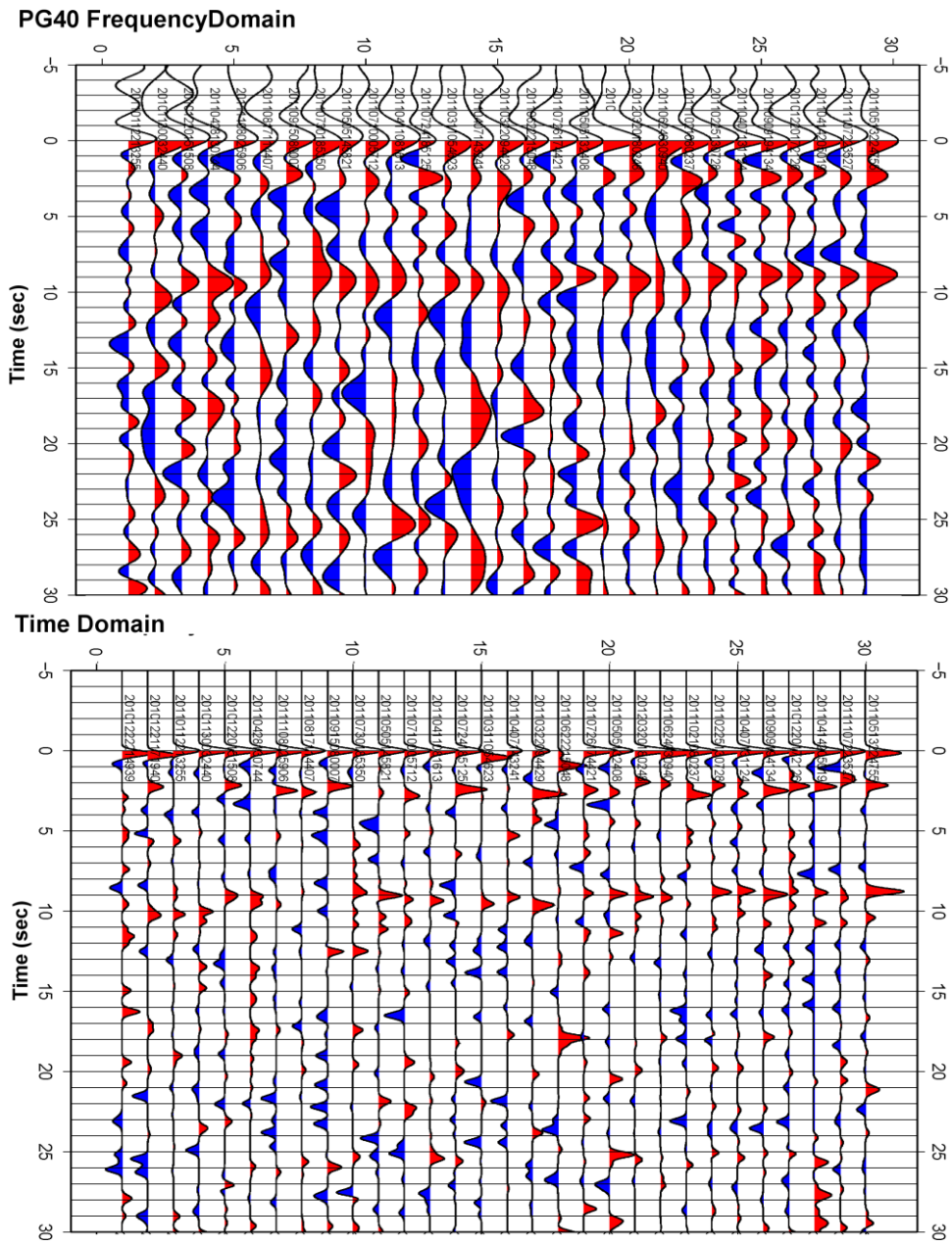


Figure 4.8: Comparison of time domain deconvolution (top) and frequency domain deconvolution (bottom) for station PG40 for earthquakes from a northwest backazimuth.

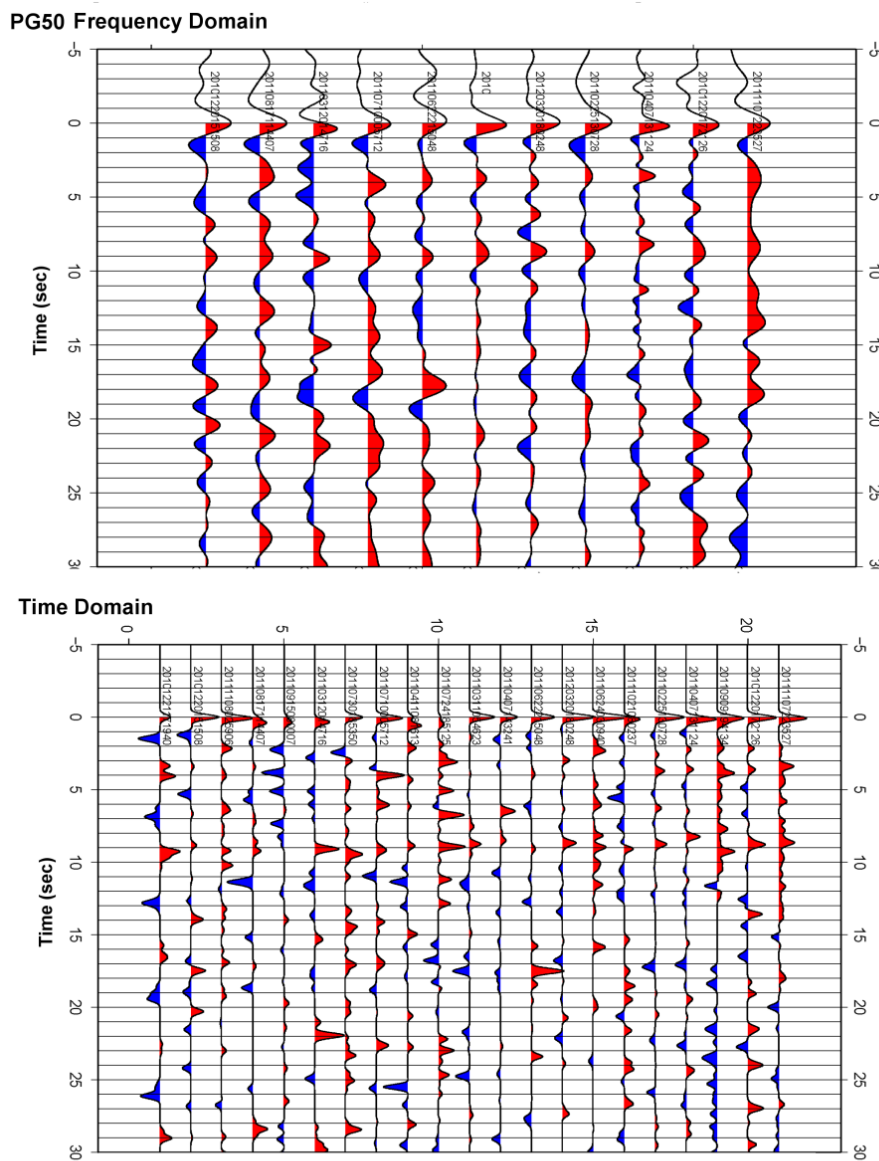


Figure 4.9 Comparison of time domain (top) and frequency domain (bottom) deconvolution for station PG50 using earthquakes from a northwest backazimuth.

### 4.3 Phases Used for RFs

#### 4.3.1. P, PP, and PKP

Standard receiver functions are done using the P wave phase with distances between 30 and 90 degrees to avoid interference with crustal and core phases. However from the

location of Peru, many large events occur at greater distances from Peru which makes it useful to use phases such as PP or PKP. The PP phase is used for phases between 90 and 180 degrees while the use of PKP phases is limited to very distant events between 142 and 180 degrees. The magnitude ranges are greater than 5.8 for P wave phases, greater than 6.0 for events between 90 and 142 degrees, and greater than 6.3 for events more distant than 142 degrees. The use of the PP phase is not uncommon in receiver function studies (Julià et al, 2008; Frassetto et al, 2010). The PKP phase has also been used for detection of dipping interfaces (Endrun et al, 2004; Lucente et al, 2005) but is less standard than PP and P phases. Due to the almost vertical arrival angle of PKP core phases, we do not expect to see a strong conversion at flat interfaces however PKP phases are good for recognizing dipping interfaces such as the slab dipping at 30 degrees in the normal subduction region. Receiver functions using the P phase on the other hand are better if the flat layer approximation is met. However the receiver function method can be adapted to account for dipping interfaces (Zhang & Langston, 1995). Thus using all possible phases results in better event and azimuthal coverage and can account well for both dipping and flat interfaces. The receiver function deconvolution procedure used for PP and PKP is the same as in the case of the P phase except for using the time difference between the PP/PKP phase and the P to S converted phase at an interface for that same arrival. For most of the events the P and PKP<sub>df</sub> phase are easily recognizable, but there is often more noise around the PP and PKP<sub>ab</sub> phases so careful event and receiver function selection is needed to ensure high quality results. Figure 4.10 shows all available events from station PE46 on Line 1

from a NW azimuthal direction to Peru. The figure shows overall consistency in timing for major arrivals.

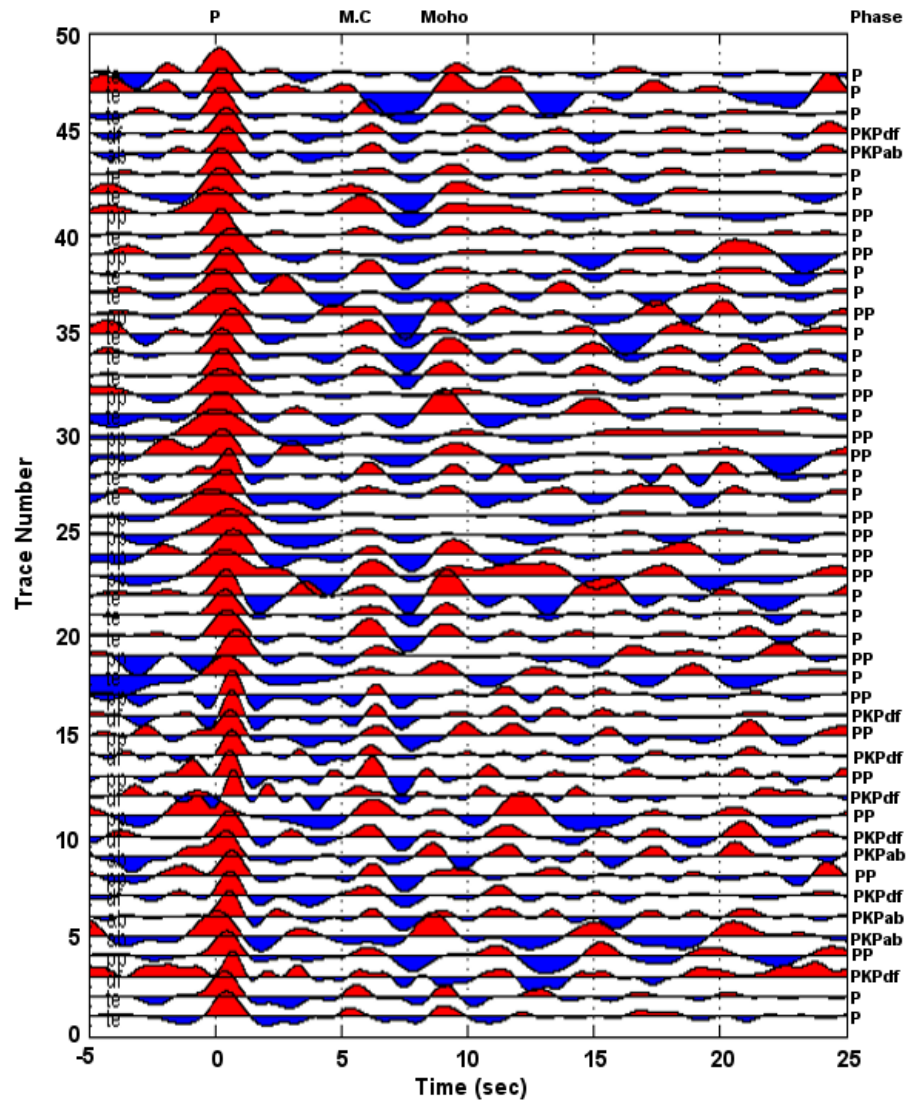


Figure 4.10: Receiver functions for station PE46 from a northwest backazimuth. Receiver functions based on the P phase (for distances 30-90 degrees), PP phase (events greater than 90 degrees), and PKPab or PKPdf phase (events greater than 142 degrees) are included. The midcrustal structure and Moho can be seen clearly. All phases appear consistent for the crustal arrivals.

Stacking receiver functions for each station from a similar backazimuth can reduce noise and help bring out the strongest and most consistent arrivals. Similar stacking approaches such as CCP or common conversion point stacking result in similar quality improvements. Despite the similarity between the results using different phases, for analysis purposes receiver functions based on the P or PP phase are separated from the PKP phase, and some difference can be seen particularly in the conversion at the top of the slab as seen in figure 4.11. The figure shows an image from Line 1 (using CCP stacking of P/PP receiver functions from the NW backazimuth) compared with an image using the PKP phases from the direction of Indonesia. The black line shows the expected slab location based on seismicity in the Wadati-Benioff zone. In the case of the P/PP phases, the top of the subducting slab is marked by a strong positive pulse which is expected at the base of the oceanic crust where there is a velocity increase from the subducting oceanic crust to the mantle. The velocity jump from the mantle wedge to the top of the oceanic crust is expected to produce a negative pulse in the receiver functions. The PKP images shows the expected slab location marked by a change from negative to positive impedance however the signal as an opposite polarity as the P/PP image. The images are seen to match up well in terms of the slab signal if the PKP image is inverted. The polarity difference between the P and PKP phases has also been noted in Lucente et al, (2005).

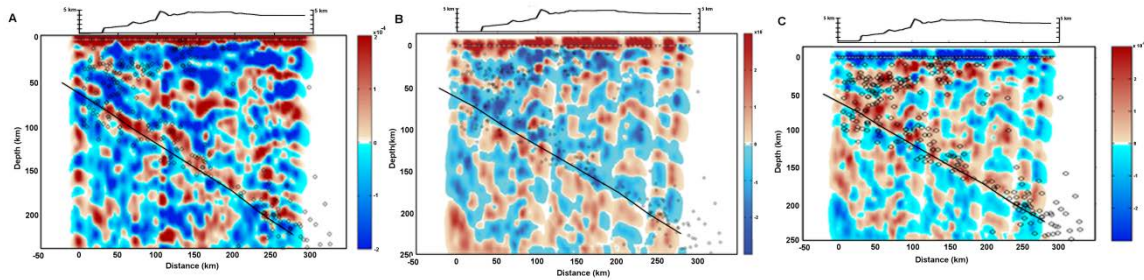


Figure 4.11: Left: Receiver function image for Line 1 using CCP stacking of P and PP receiver functions showing a clear positive impedance signal associated with the subducting slab and the Moho. Middle: PKP image with backprojected receiver functions from the direction of Indonesia. A signal from the slab appears as a change from negative to positive impedance. Arrivals are out of phase with the P/PP results (as mentioned in Lucente et al, 2005). Right: Inversion of the PKP image in the center. Here the positive arrival associated with the slab matches up with the P/PP observations.

#### 4.3.2. S Wave RFs

Receiver functions were made based on the S and SKS waves although analysis is more complicated compared to P phases and results are longer period in general and thus do not provide high resolution. However several studies using S waves have been done (Geissler et al, 2010; Heit et al, 2007, Kumar et al, 2005) which suggest that S wave receiver functions can be useful for detecting the lithosphere-asthenosphere boundary which is generally not detectable by P receiver functions. While the calculation of P wave receiver functions involve rotating the horizontal components into the radial and tangential directions, S waves receiver functions are optimized by rotation into the P-SV-SH coordinate system. Several different methods were tested for finding an optimum rotation angle starting from the radial and tangential directions. One method involved rotating by the angle of incidence for the S wave arrival using the ray parameter and average S wave velocity in the crust. A comparable result should be

obtainable by finding an angle that minimizes the energy at the time of the S wave on the P component. The third method used equation (21) from Kennett, (1991) which provides an approximation for the rotation for slowness bands appropriate for S-wave phases involving use of the Hilbert transform of the vertical component to estimate the P-wave contribution. The general form for the rotation is the free surface transfer matrix from Kennett (1991):

$$\begin{bmatrix} P \\ SV \\ SH \end{bmatrix} = \begin{bmatrix} \frac{(\beta^2 p^2 - \frac{1}{2})}{\alpha q_\alpha} & \frac{p\beta^2}{\alpha} & 0 \\ p\beta & \frac{(\frac{1}{2} - \beta^2 p^2)}{\beta q_\beta} & 0 \\ 0 & 0 & \frac{1}{2} \end{bmatrix} \begin{bmatrix} Z \\ R \\ T \end{bmatrix} \quad (4.7)$$

where  $q_\alpha = (\alpha^{-2} - p^2)^{0.5}$ ,  $q_\beta = (\beta^{-2} - p^2)^{0.5}$ .

The method which was empirically found to produce the best S-wave receiver functions was the method using the angle of incidence to perform the rotation. After performing the rotation, the deconvolution method is similar to the P wave deconvolution in the frequency domain except that since we are looking for a S wave converting to a P wave, the vertical component (SV component) is divided by the horizontal component (P component) rather than the other way around. Sample results using the S wave phase can be seen in figure 4.12. A wide region of negative impedance marks the general location of the lithosphere-asthenosphere boundary.

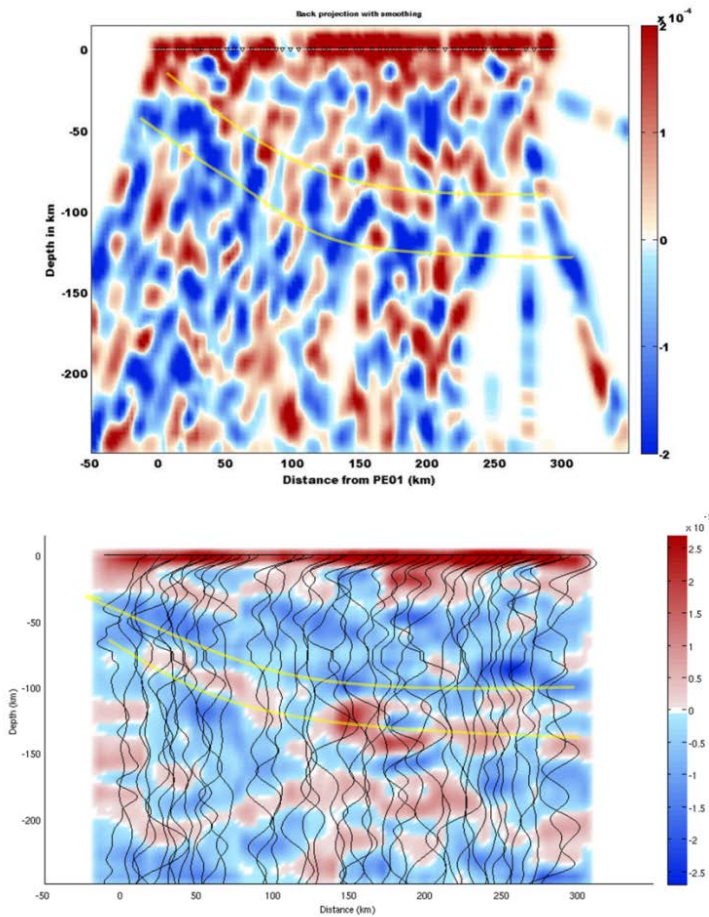


Figure 4.12: S wave receiver function images for Line 1. The location of the LAB is expected to appear as a negative signal. Results for the S wave are longer period than P wave results. The top image is based on backprojection while the bottom image plots stacks for each station.

#### 4.4 Stacking for Moho Depth and $V_p/V_s$

When an adequate number of receiver functions have been obtained from a given azimuthal direction, receiver functions can be stacked for each station using the method of Zhu & Kanamori, (2000) to obtain an estimate for depth to an impedance contrast and average  $V_p/V_s$  for that region. Depth and  $V_p/V_s$  can be estimated through the

following equations which contain  $p$  (the ray parameter) and  $t_{Ps}$ ,  $t_{PpPs}$ ,  $t_{PpSs+PsPs}$  which are the times for the converted phase and multiple arrivals relative to the direct P arrival (at time = 0).

$$H = \frac{t_{Ps}}{\left(\sqrt{\frac{1}{V_s^2} - p^2} - \sqrt{\frac{1}{V_p^2} - p^2}\right)} \quad (4.8)$$

$$H = \frac{t_{PpPs}}{\left(\sqrt{\frac{1}{V_s^2} - p^2} + \sqrt{\frac{1}{V_p^2} - p^2}\right)} \quad (4.9)$$

$$H = \frac{t_{PpSs+PsPs}}{2\sqrt{\frac{1}{V_s^2} - p^2}} \quad (4.10)$$

The estimations are done through a grid search algorithm over a range of possible depths and  $V_p/V_s$  ratios, and the optimum parameters are those that maximize the summation of receiver function amplitudes at the time of the converted arrival (Moho signal) and weighted summations of amplitudes for the calculated multiples. Due to the large variation in Moho depth over the arrays from around 30 to 75 km depth beneath the Altiplano, the average crustal  $V_p$  is expected to vary slightly. Velocities are estimated from spacial averages of the 3D model by Cunningham & Roecker (1986) (see figure A2 in appendix A). An example of this can be seen in figure 4.13 (and also figure 2.6). Results from this stacking for Moho and  $V_p/V_s$  can be seen in figure 2.8 and figure 3.9.

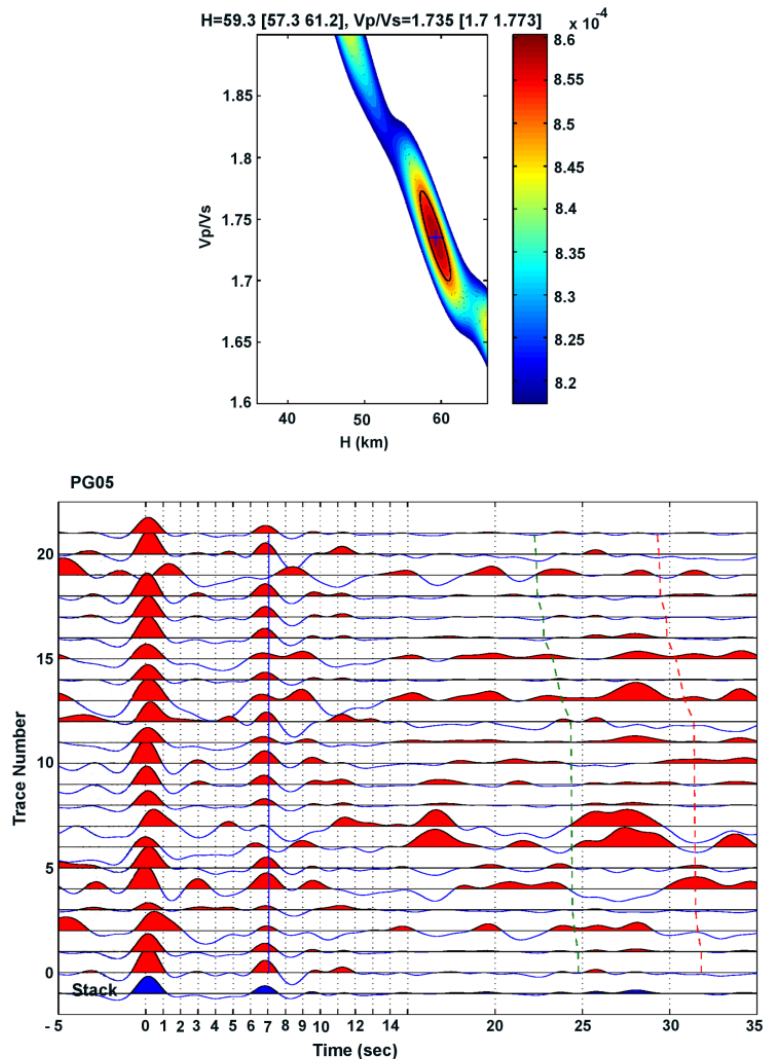


Figure 4.13. An example of the grid search (top) and stacking (bottom) to find Moho depth and  $V_p/V_s$  for station PG05. In the top portion,  $H$  is the depth to the impedance contrast. In the bottom portion, the blue line represents the time at which the maximum summation is obtained for the Ps converted phase and multiple arrivals (denoted as dashed lines). In this case the signal from the Moho is very clear, but the multiples are not readily apparent.

#### 4.5 Transverse Receiver Function Components

The receiver function method produces both radial and transverse components.

Although all of the receiver function images shown in previous chapters only use the

radial component, energy on the transverse receiver function component can be indicative of either dipping structures or anisotropy. In a flat, homogeneous setting, the amplitude of arrivals on the transverse component should be very small relative to the radial receiver functions. Several studies have used transverse receiver function components to examine dipping structures or anisotropy (Zhang & Langston, 1995; Savage, 1998). According to Savage, (1998), “transversely anisotropic systems with horizontal symmetry axes have waveforms with  $180^\circ$  periodicity as a function of back azimuth, while dipping symmetry axes or dipping boundaries just have  $360^\circ$  periodicity.” Thus if the anisotropic symmetry axes is roughly horizontal, stacking transverse receiver functions from  $180^\circ$  apart can provide an indication of whether there is dipping or anisotropic structure based on whether resulting amplitudes increase or decrease in the stack.

An analysis of transverse receiver functions shows more energy on the transverse components for Line 2 (parallel to the trench) compared to other stations. In many cases the signal amplitude is comparable to the amplitude of the radial receiver functions. Two examples of transverse and radial receiver functions for stations PF25 and PF37 can be seen in figure 4.14 and figure 4.15.

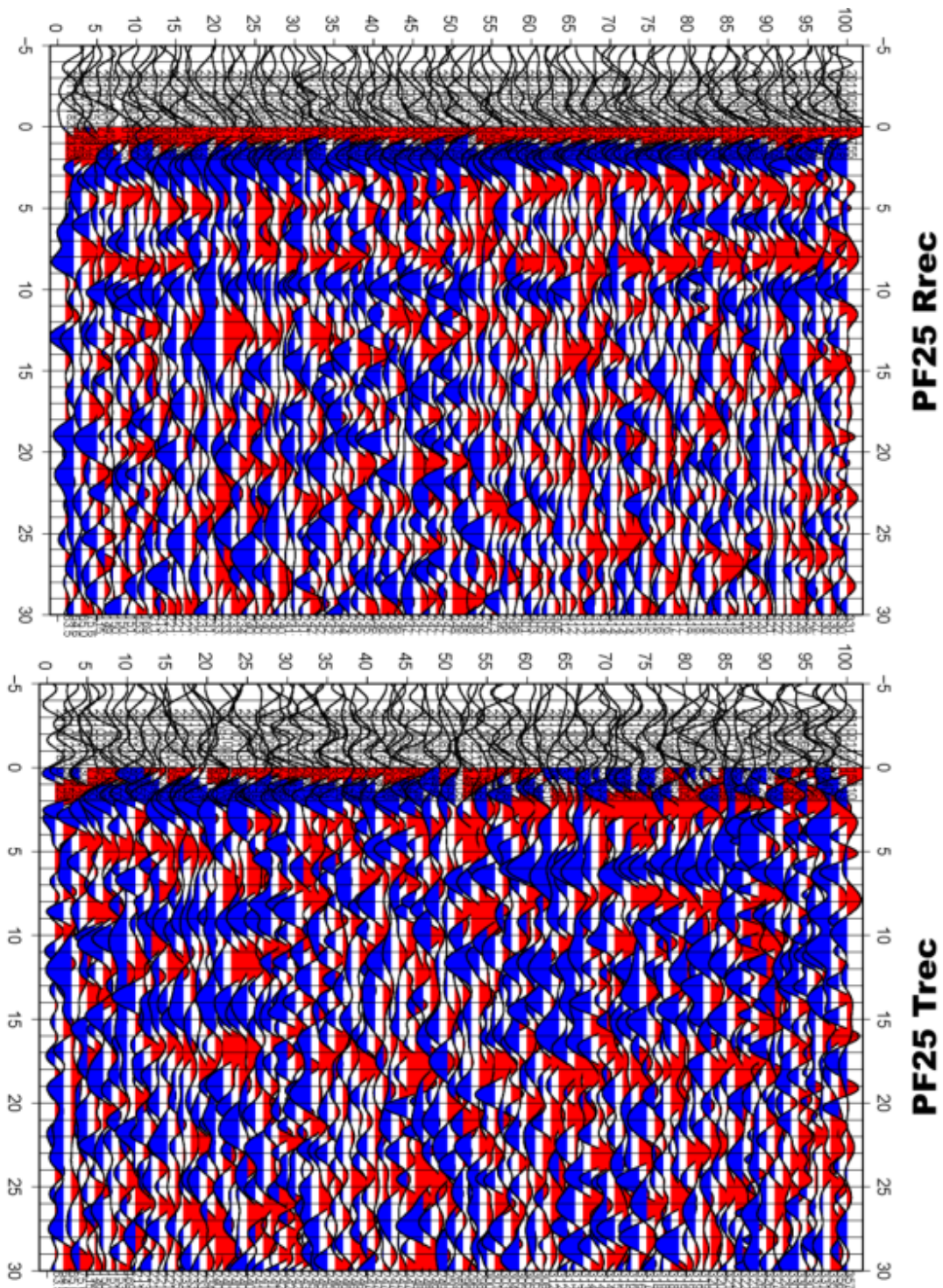


Figure 4.14. Comparison of the radial and transverse receiver function components for station PF25. The most coherent energy on the transverse receiver functions generally occurs before 10 seconds which is where the crustal signals are observed on the radial component. On the radial receiver functions, positive signals at 4-5 seconds and at about 8 seconds correspond to the midcrustal structure and Moho signal respectively.

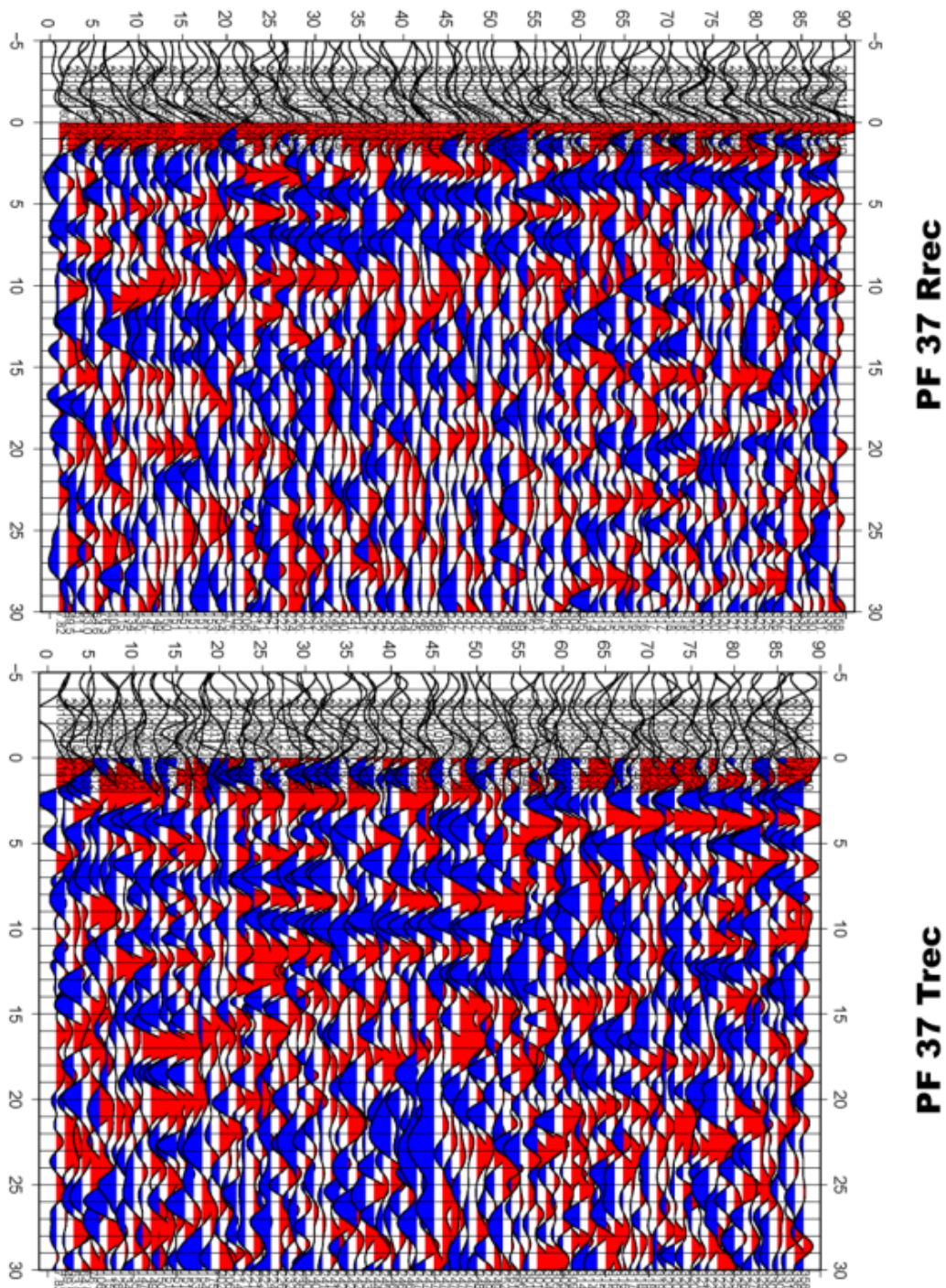


Figure 4.15. Comparison of the radial and transverse receiver functions for station PF37. Energy on the transverse component has an amplitude comparable to the main arrivals on the radial receiver function (besides the P arrival).

Transverse receiver functions from  $30^\circ$  azimuthal regions were stacked to check for  $180^\circ$  or  $360^\circ$  periodicity. Most of the teleseismic energy comes from the directions NW, NE, SW, and SE from Peru. Comparisons of transverse signals from the NW with energy from the SE and similarly from the NE with the SW shows that major arrivals have opposite polarity from directions  $180^\circ$  apart for all stations examined (figure 4.16, figure 4.17, and more examples in appendix C). This appears to indicate that there is possibly some anisotropy.

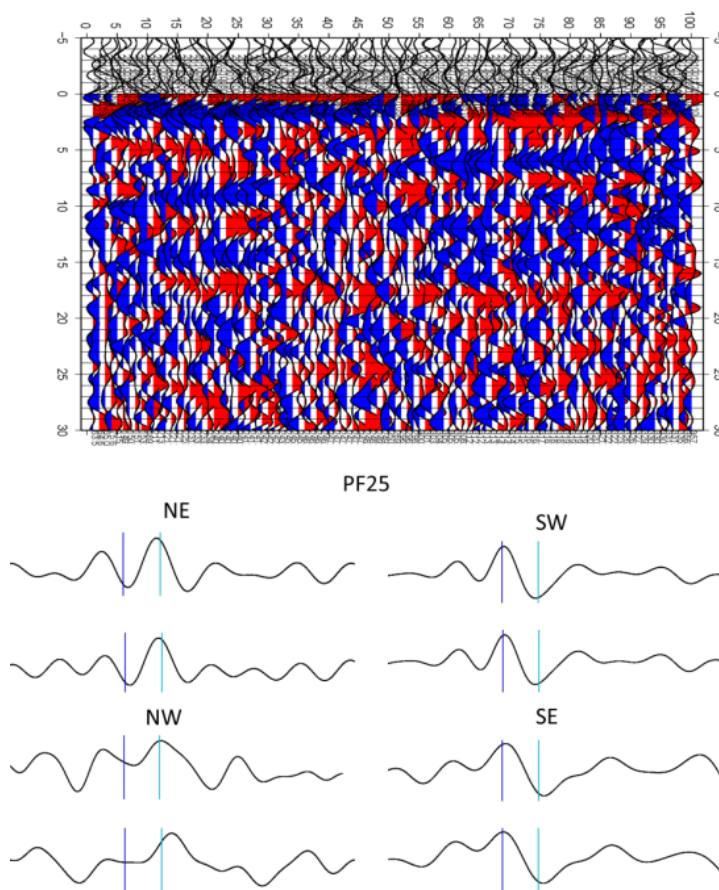


Figure 4.16: Top: Transverse RFs for station PF25. Bottom: Stacks of all transverse receiver functions from the directions NE, SW, NW, and SE. Each trace represents a stack over a region of  $30^\circ$  which includes at least three transverse RFs.

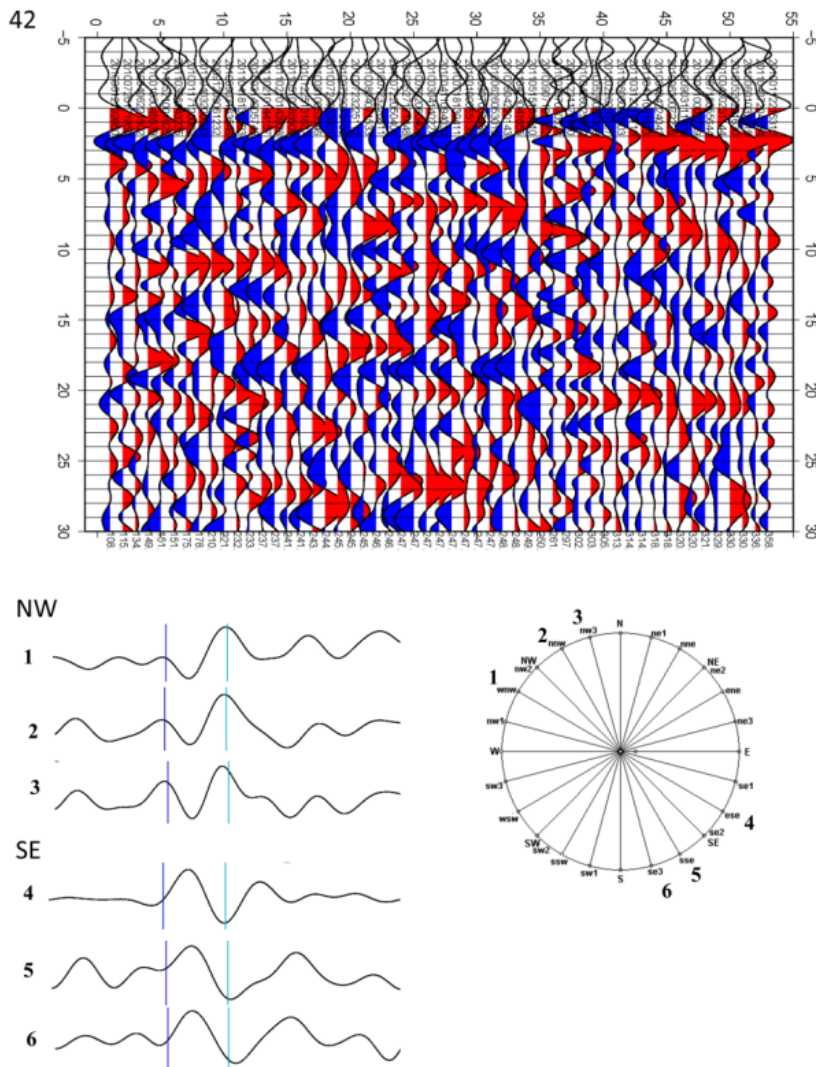


Figure 4.17: Transverse RFs for station PF42 and stacked traces from the directions noted on the unit circle to the NW and SE. The traces are marked at zero seconds (dark blue line) and the time of the first major arrival at about 2 seconds (light blue). Note the polarity difference between the NW and SE directions.

The direction of the symmetry axis appears to be between 260 and 296 degrees for the northwestern stations (closest to Cusco). The lack of energy from due west of Peru makes it difficult to further constrain the angle (a vast majority of earthquakes are from

either a NW or SW azimuth from Peru). See examples in figure 4.18 and figure 4.19 where the expected symmetry axis has been marked. The symmetry angle appears closer to  $214^\circ$  near the center of the lines (e.g., PF23 and PF24 in figure 4.20) and perhaps closer to  $150^\circ$  for PF12 and PF13 closer to Juliaca (figure 4.21).

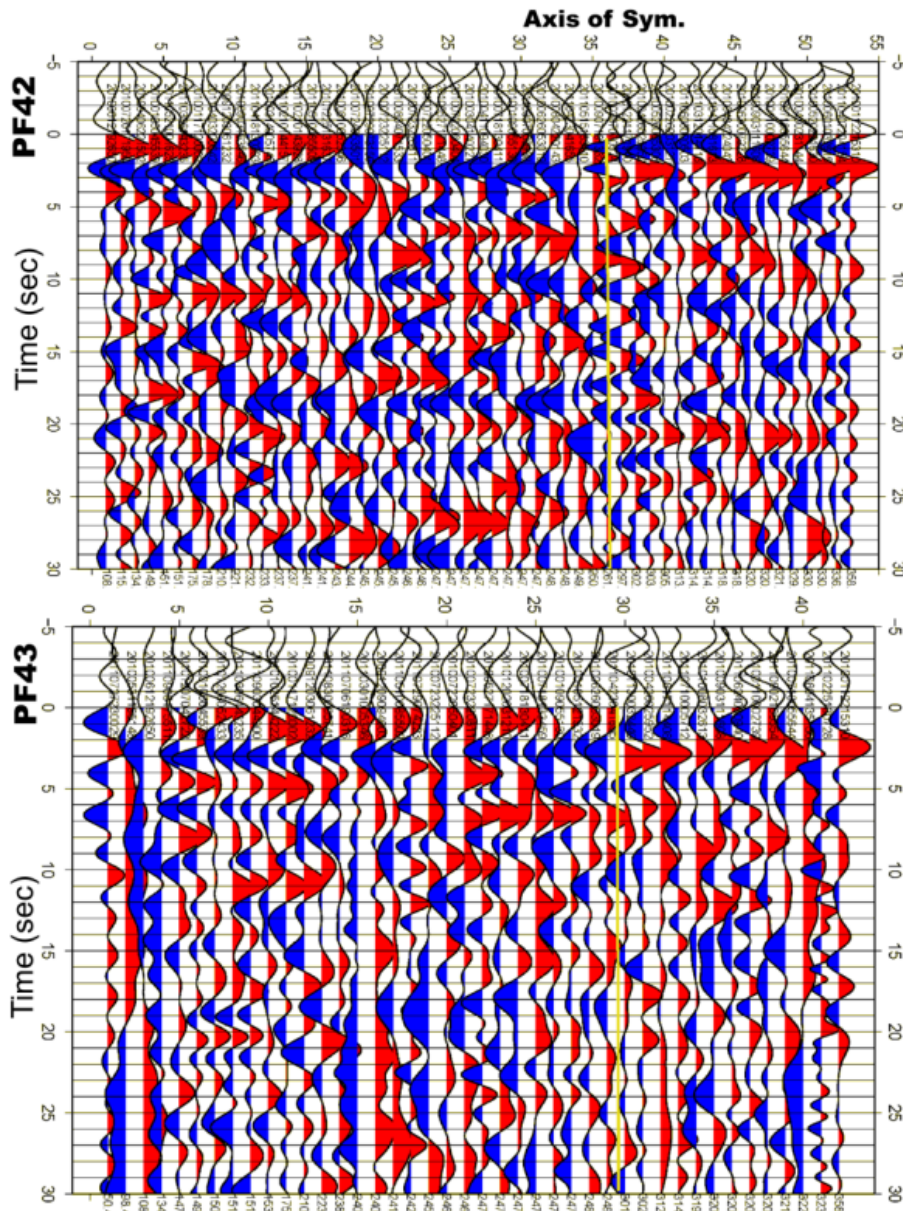


Figure 4.18: Transverse RFs for stations PF42 and PF43 with the Possible symmetry axis marked by the yellow line.

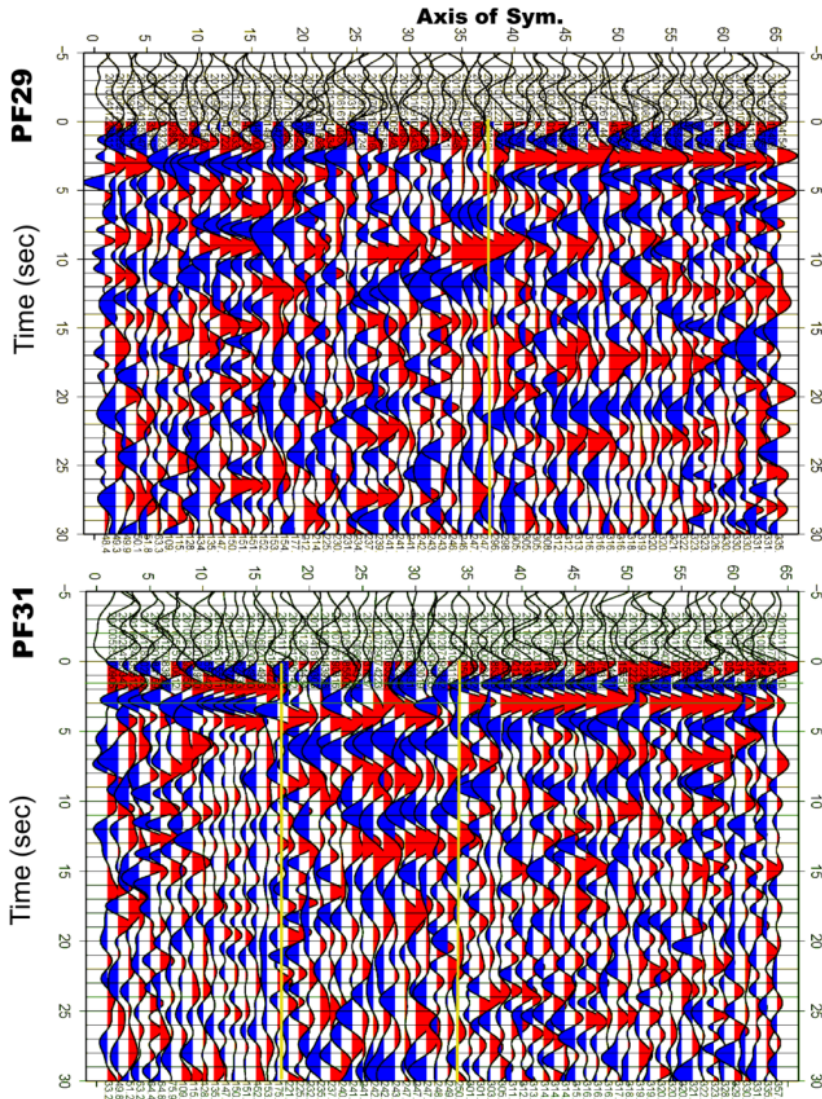


Figure 4.19 Transverse RFs for stations PF29 and PF31 with possible symmetry axis marked by the yellow line.

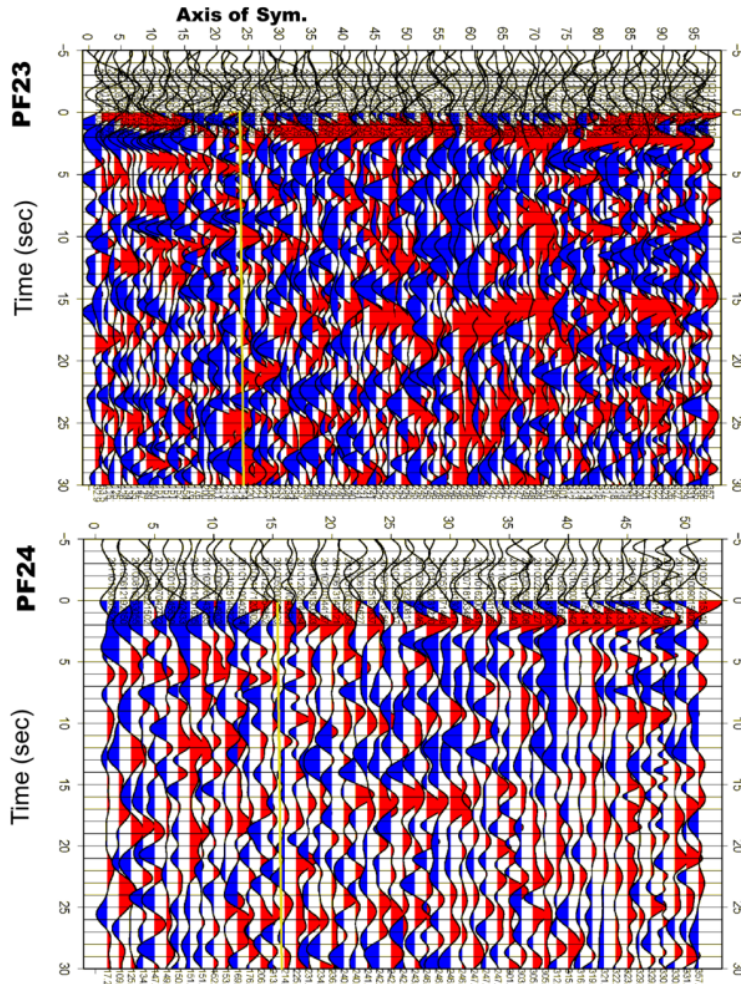


Figure 4.20 Transverse RFs for stations PF23 and PF24 (possible symmetry axis marked by yellow line).

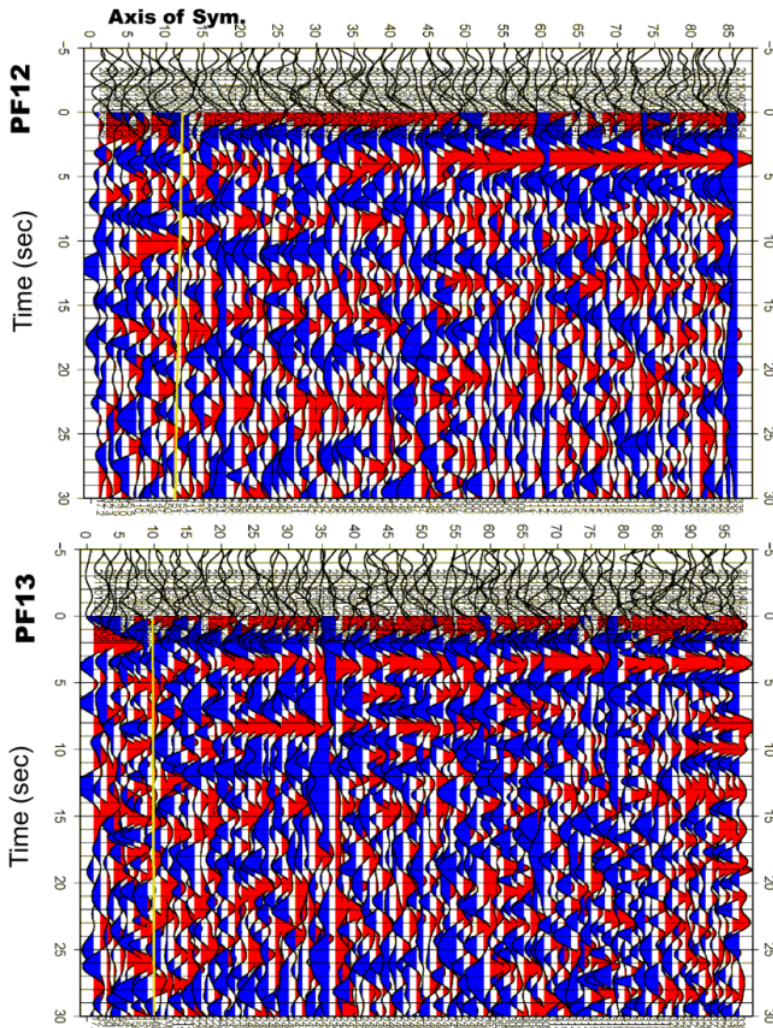


Figure 4.21 Transverse RFs for stations PF12 and PF13 (symmetry axis marked by yellow line).

Observations from radial receiver functions are that image quality can vary by azimuth but this is partly a function of fewer events from other directions besides NW and SW (such as W, E, S, N, NE, and SE). See an example of images from each major direction in figure 4.22 for Line 3. As seen from the images, the quality of images from the northern directions is generally better than using only events from southern directions.

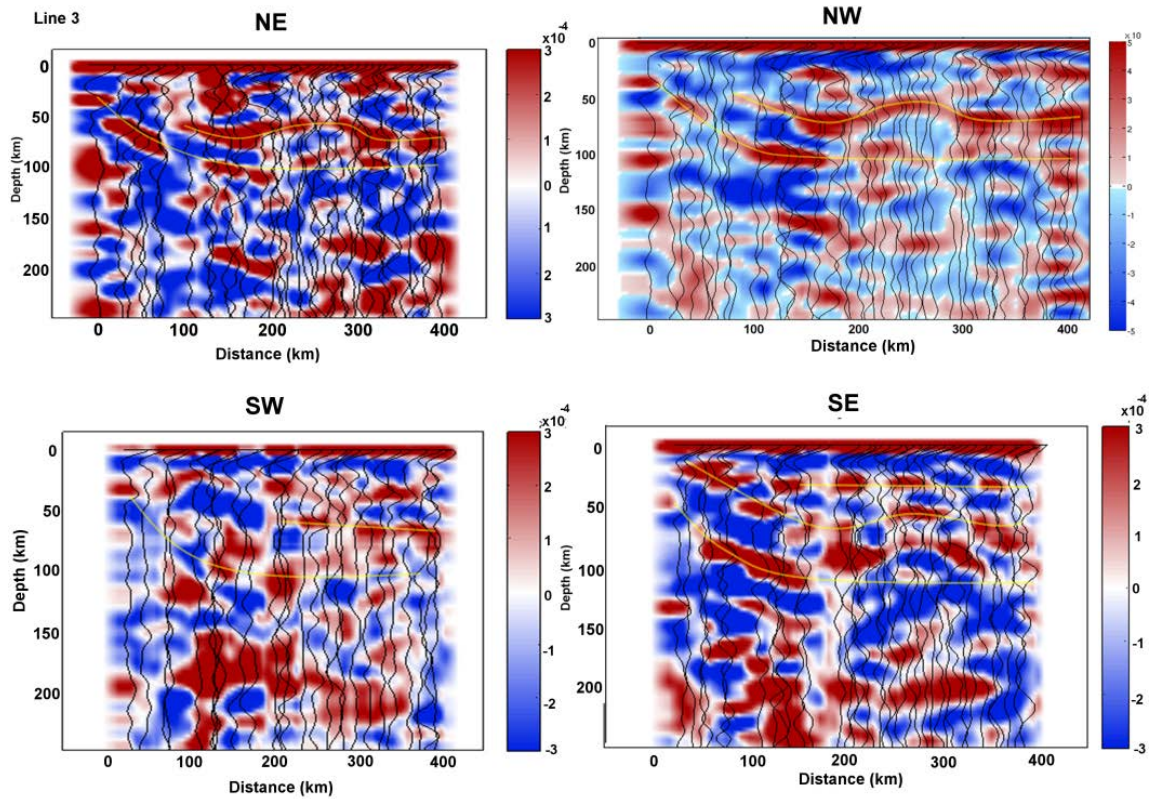


Figure 4.1 CCP stacks from each azimuthal direction for Line 3

#### 4.6 Imaging Methods (Backprojection, CCP)

The backprojection method I developed uses a ray based approach to project receiver functions in the direction from which the energy originated. Distance is calculated from the first station in the array along the line between the first and last station in the array. A simple time to depth estimate is performed using the ray parameter, an average crustal velocity of 6.3 km/s, an average mantle velocity of 8.1, and average Moho depth of 40 km. The equation

$$depth = \frac{t(x)}{\left(\sqrt{\frac{1}{V_{sc}^2} - p^2} - \sqrt{\frac{1}{V_{pc}^2} - p^2}\right)} \quad (4.11)$$

is used for depths less than the Moho depth, and the equation

$$depth = \frac{t(x) - H\left(\sqrt{\frac{1}{V_{sc}^2} - p^2} - \sqrt{\frac{1}{V_{sm}^2} - p^2} + \sqrt{\frac{1}{V_{pm}^2} - p^2} - \sqrt{\frac{1}{V_{pc}^2} - p^2}\right)}{\left(\sqrt{\frac{1}{V_{sm}^2} - p^2} - \sqrt{\frac{1}{V_{pm}^2} - p^2}\right)} \quad (4.12)$$

is used for depths greater than the Moho depth. The distance range depends on the length of the array and the maximum depth is 250 km. The distance from the station is calculated using a simple layered velocity model based on IASP91 where 0-10 km depth has  $V_p=5.8$ km/s, 10-H depth has  $V_p=6.8$  km/s, H-120km depth has  $V_p=8.045$ , 120-165 km depth has  $V_p=8.1$  km/s, 165-210 km depth has  $V_p=8.25$ , and depths greater than 210 km have  $V_p=8.45$  where H is the Moho depth. The average Moho depth is normally set to 40 km due to the amount of variation for Lines 1 and 3 from the coast to the Altiplano but the model was varied using greater depths to test the sensitivity of the images to the velocity model. The images and depths were found to be consistent even when average Moho depth was changed to account for the greater depths beneath the Altiplano. Using the simple layered velocity model, angles and distances are calculated based on the depth in the model, ray parameter, geometry, and Snell's law. The distance from the station is further corrected by taking into account the backazimuthal direction of the event which affects the distance and direction that rays are projected. The station elevation is also taken into account such that  $depth=0$  is sea level. Thus crustal thickness includes the Moho depth added to the station elevation

which for many places in the Altiplano can be up to 4 km. An example of applying backprojection to a single station can be seen in figure 4.23 for PE46 on Line 1. Comparison of the results to the CCP stacking image in figure 4.24 confirm that the Moho and midcrustal structure and Moho depth are relatively flat in the region covered by rays from station PE46. A moveout plot to the right of the backprojection image shows receiver function coverage as a function of ray parameter. Signals from interfaces such as the Moho are expected to be flat in such a plot while arrivals from multiples can vary as a function of ray parameter. Further examples of figures using backprojection can be seen in figures 2.7, 2.8, 2.9, and figures 3.6, 3.7B, and figure 3.12.

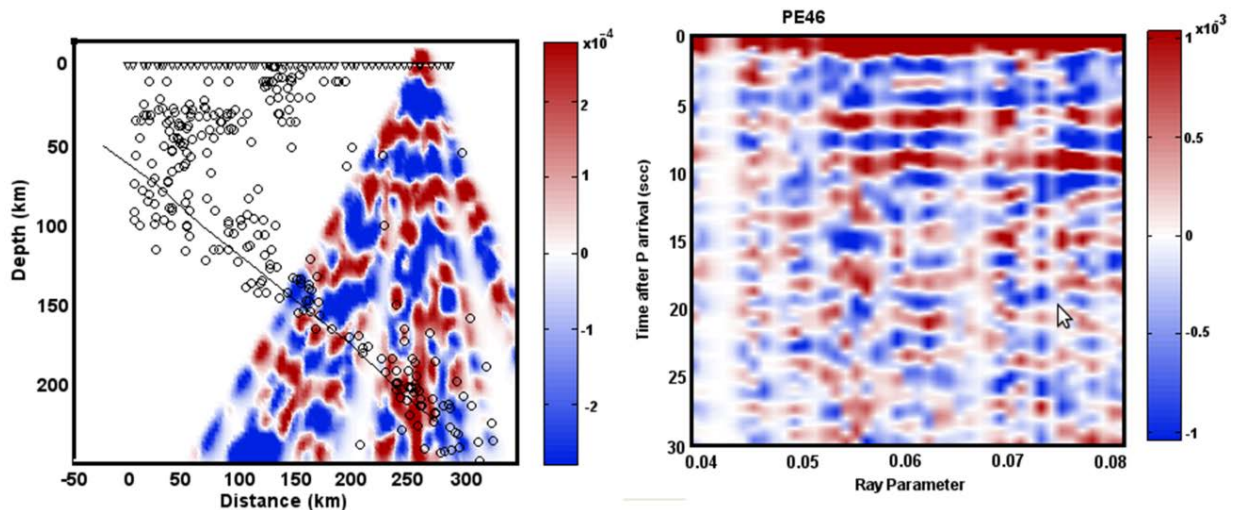
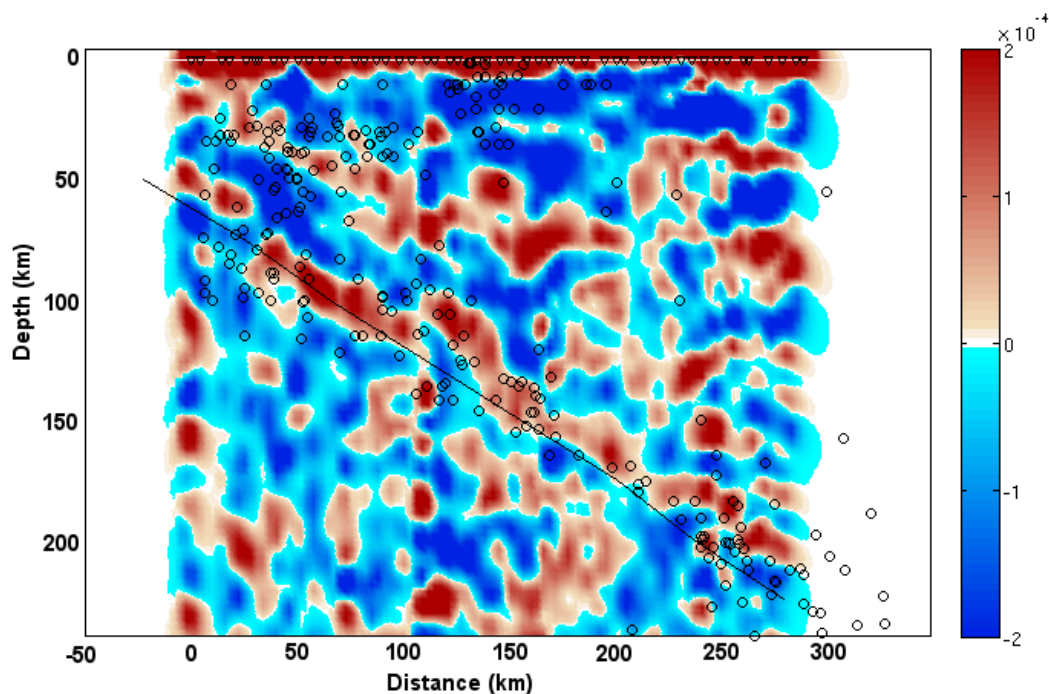


Figure 4.23: Left: Results from backprojecting receiver functions for station PE46 near the end of Line 1 (closest to Juliaca) in the direction from which the energy originated. Right: Plot of time versus ray parameter where the color corresponds to the amplitude of the receiver functions at that ray parameter. Signals from the midcrustal structure (at ~5 seconds) and Moho (~9 seconds) are consistent across all azimuths.

The common conversion point method uses some of the techniques developed in the backprojection approach but uses actual depths calculated for the Moho based on H- $\kappa$

stacking (Zhu and Kanamori, 2000) and finds the best-fitting polynomial function to create a smooth Moho function for any distance. It then calculates the distance and depth at which a backprojected ray intercepts the Moho depth. The distance along the array is broken into bins (which usually have a size equivalent to the station spacing) and the Moho intercept distance determines the bin number. All events which pass through the same bin are stacked and stacks are plotted as in figure 4.24 which shows CCP stacking results for Line 1. Further examples of figures using this method can be seen in figures 3.4 and 3.7.



*Figure 4.24: Receiver function plot for Line 1 plotting common conversion point (CCP) stacks at each bin distance as a function of depth.*

#### **4.7 Finite Difference Modeling**

Several related finite difference codes were used for various modeling purposes. The main code used is the same employed in Kim et al, 2010 is a staggered grid finite-

difference solution of the linear elastic 2D wave equation. The principle variables are (U,W) which are the (x,z)-components of (particle) velocity,  $T_{xx}$  and  $T_{zz}$  which are normal stresses,  $T_{xz}$  which are shear stresses,  $\lambda$  the Lamé coefficient,  $\mu$  the other Lamé coefficient or shear modulus,  $\gamma=\lambda+2\mu$ , and B which is the buoyancy which is 1/density.

The stress updates are done according to the equations:

$$T_{xx} += dt*(\gamma*U_x + \lambda*W_z),$$

$$T_{zz} += dt*(\lambda*U_x + \gamma*W_z),$$

$$T_{xz} += dt*\mu*(U_z + W_x).$$

The velocity updates are done according to the equations:

$$U += dt*B*(T_{xx,x} + T_{xz,x}),$$

$$W += dt*B*(T_{xz,z} + T_{zz,z}),$$

where dt is the time step.

The inputs to the code are the P wave velocity model, the model and source parameters, and a list of ray parameters. The finite difference code models the propagation of a P plane wave at a given ray parameter from a direction set usually as the lower left or right corners of the model. The resultant synthetic seismograms are deconvolved using iterative time domain deconvolution to produce synthetic receiver functions which can be compared to data. Examples of the models and synthetics can be seen in figures 2.10, 3.3, 3.8, and 3.11.

Structural and velocity models derived from receiver function observations and testing using the aforementioned finite difference code can then be used to model the wave propagation from local events near the arrays to produce synthetic seismograms which

can be compared with local data. The 2D finite difference code was described by Vidale et al, 1985 and used in Chen et al, 2007. The P-SV and SH systems are modeled separately for each model.

As described in Chen et al. (2007),

“The scheme for generating point source seismograms for shear dislocations using 2-D numerical methods is discussed by Helmberger and Vidale [1988]. It is based on expanding the complete 3-D solution in asymptotic form and separating the motions into the SH and P-SV systems. This analytical Cagniard-de-Hoop method is used to derive closed form expressions appropriate for 2-D FDM source excitations. Synthetics generated by this method are bench-marked in the above mentioned study.”

Examples of models and synthetics using this code can be seen in figure 2.12.

Date	Lat/Lon	Depth	Mag
10/28/2011	-14.44/-75.97	24	6.9
11/13/2009	-19.39/-70.32	27	6.5
01/30/2012	-14.17/-75.64	43	6.4
03/06/2011	-18.02/-69.36	118	6.3
05/14/2012	-17.68/-69.59	105	6.2
05/06/2010	-18.06/-70.55	37	6.2
07/08/2008	-15.99/-71.75	123	6.2
06/07/2012	-15.88/-72.41	110	6.1
05/23/2010	-13.93/-74.35	101	6.1
07/12/2009	-15.04/-70.44	198	6.1
04/17/2009	-19.58/-70.48	25	6.1
02/02/2009	-13.58/-76.56	21	6
06/08/2011	-17.08/-69.52	145	5.9
04/02/2011	-19.58/-69.07	84	5.9
09/13/2010	-14.61/-70.78	179	5.9
09/30/2009	-15.55/-69.29	255	5.9
04/05/2010	-19.86/-68.84	94	5.8
09/05/2009	-15.12/-70.25	210	5.8
05/18/2009	-15.66/-74.84	22	5.8
07/02/2012	-14.42/-75.6	39	5.7
09/22/2010	-13.39/-76.07	50	5.7
03/15/2009	-14.45/-70.36	189	5.7
05/06/2012	-13.82/-75.8	54	5.6
10/28/2011	-14.51/-75.84	10	5.6
10/28/2011	-14.38/-76	22	5.6
12/24/2009	-15.77/-73.98	59	5.6
01/31/2009	-19.41/-69.07	102	5.5

#### **4.8 Local Events and Future Study**

The seismic arrays are located in a region with a significant amount of seismicity which can provide another valuable source of information about the structure of southern Peru besides teleseismic receiver functions. Some of the largest events closest to the array are listed in table 4.1 and are plotted in figure 4.25. The locations are from the National Earthquake Information Center (NEIC). The locations were checked during the analysis, and while some NEIC locations seemed to work reasonably well from the accuracy of P and S picks, in general there was some locational error, and locations posted on the website of the Instituto Geofísico del Perú (IGP) were found to work better in those cases.

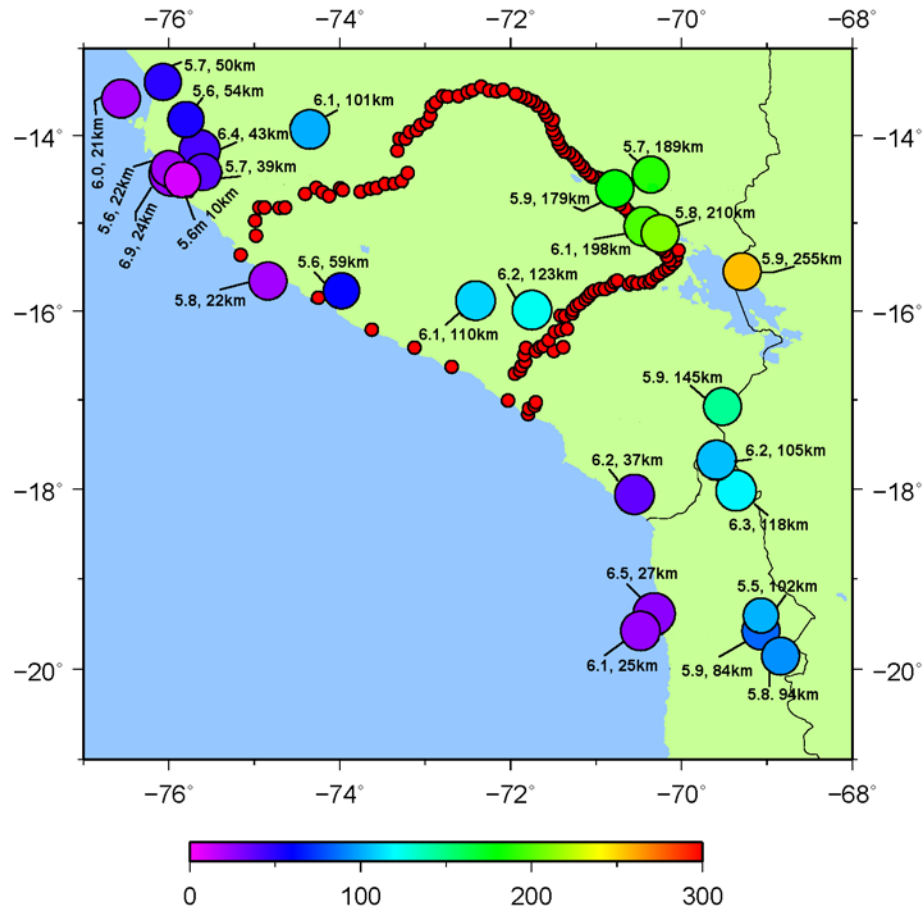


Figure 4.25: Map of largest events in the immediate vicinity of the arrays during the time the arrays were operating. More information about these events is found in the table 4.1. The magnitude and depth are labeled and color corresponds to depth in kilometers. Locations are from the NEIC earthquake catalog.

Several of the large, deep events near Juliaca were of interest for modeling. Events which were particularly focused on include the earthquakes on 7/12/2009 (Mw 6.1, 198 km depth), 9/5/2009 (Mw 5.8, 210 km depth), and on 9/30/2009 (Mw 5.9, 255 km depth). Deep earthquakes near the array were used to make local receiver functions which can provide more detailed information about the Moho and midcrustal structure. Other methods analyzing local events include looking for the precursor to the pP arrival

from reflections off of the Moho as detected by teleseismic stations which provides a possible check for Moho depths calculated by receiver function methods. Velocity models and features observed in local data can also be checked using finite difference modeling.

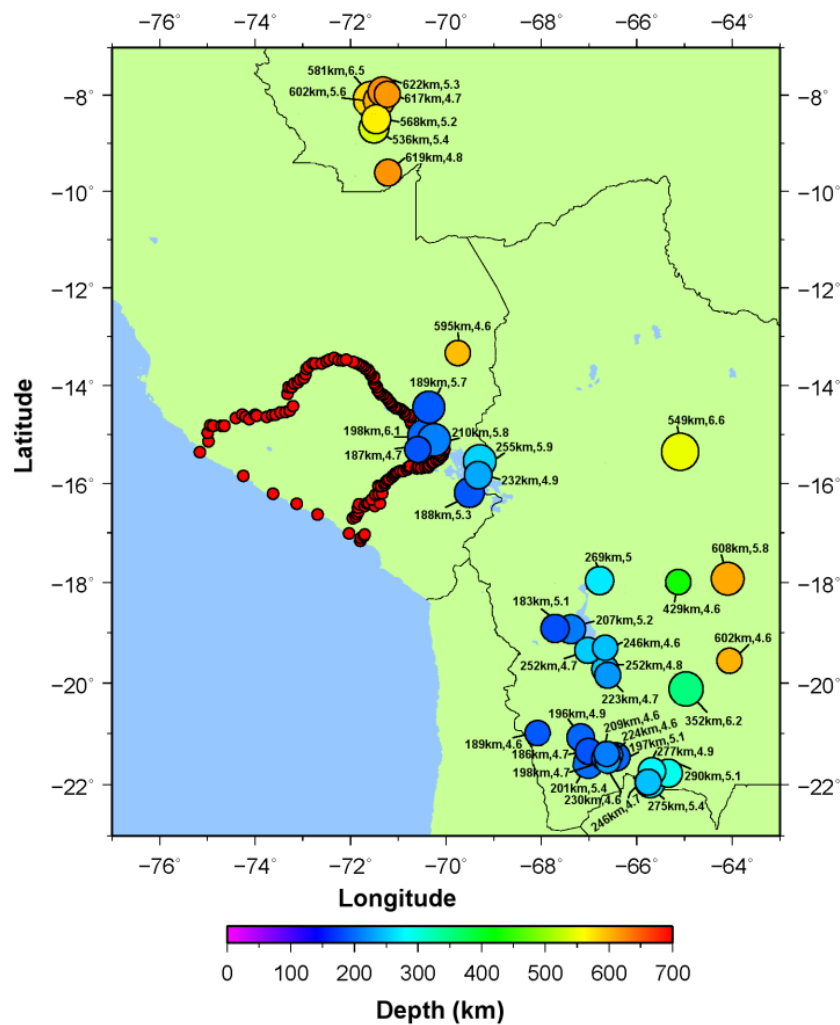


Figure 4.26: Events deeper than 180 km which can be used for local receiver function analysis as provided by the NEIC earthquake catalog.

#### 4.8.1. Local Receiver Functions

Local events were also used to make receiver functions. Due to the thick crust beneath the Altiplano, events were only selected if they were deeper than 180 km and close to the arrays to avoid interference with crust not directly beneath the station. The locations of the largest and closest events meeting the depth criteria are shown in Figure 4.26. By picking very high quality local events which are almost directly beneath the stations, it is possible to probe the crustal structure in more finer detail than is possible with teleseismic events as discussed in Calkins et al. (2006) where events with corner frequencies up to 2.5 or 5 Hz were used to better define crustal interfaces which were not well-defined by teleseismic energy. However dealing with higher frequencies also results in more high-frequency noise. An advantage of this method for southern Peru would to better define the extent of the midcrustal structure whose western boundary is not well defined by teleseismic receiver functions. A sample local event is an event on 11/22/2011 which was a magnitude 6.6 earthquake at a depth of 549km located due east of Juliaca about 550 km away from the closest stations. An example of the receiver function and data quality can be seen in figure 4.27. This event was detected by all arrays. The resultant receiver function images are clearest for the closest array, Line 1, which is shown in figure 4.28 for a corner frequency of 0.5Hz. At this depth and distance, a clear slab image is not expected, however the Moho and midcrustal structure are very well resolved.

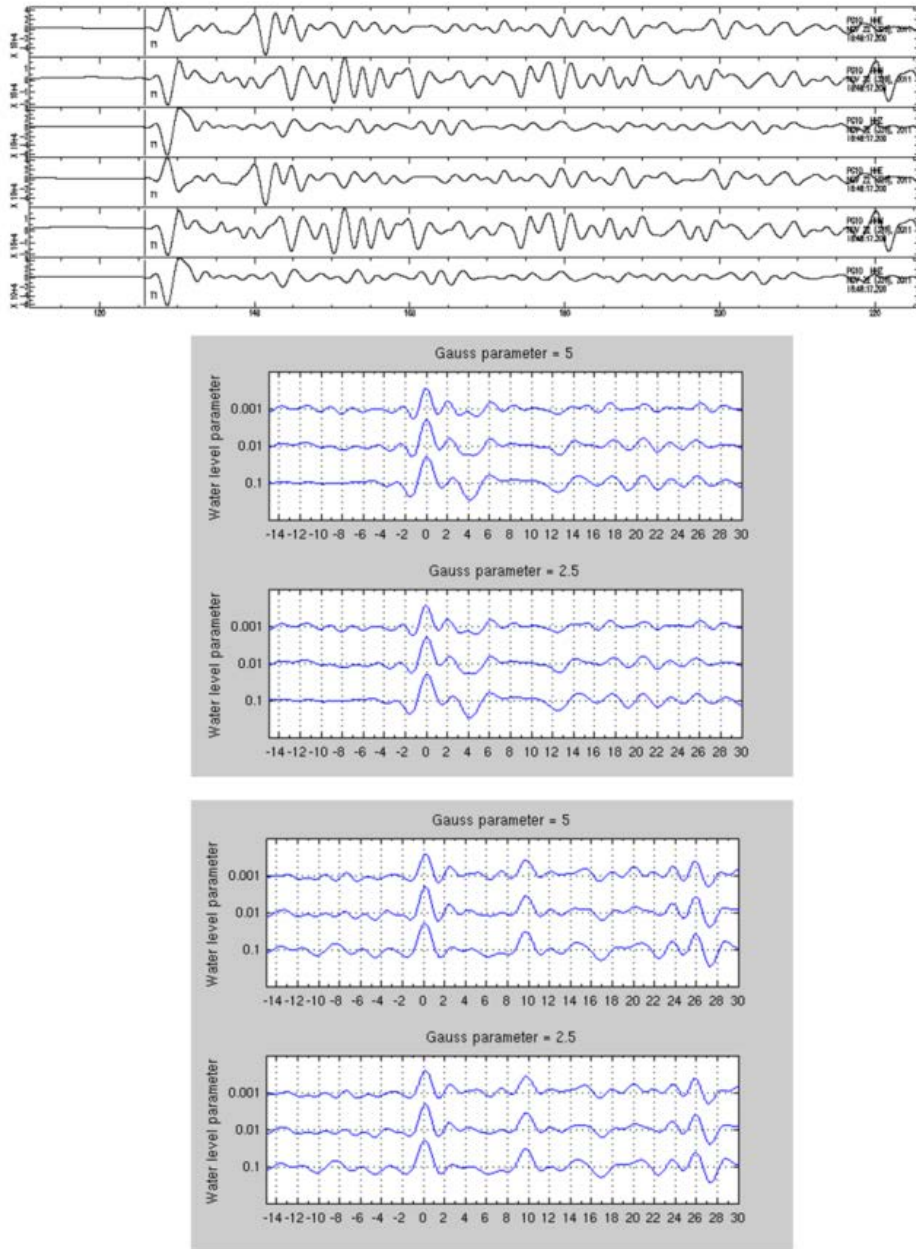


Figure 4.27: Local receiver function analysis for the deep local event on 11/22/2011 (magnitude 6.6 at 549 km depth located due east of Juliaca). Top shows data quality and bottom panel shows receiver function quality.

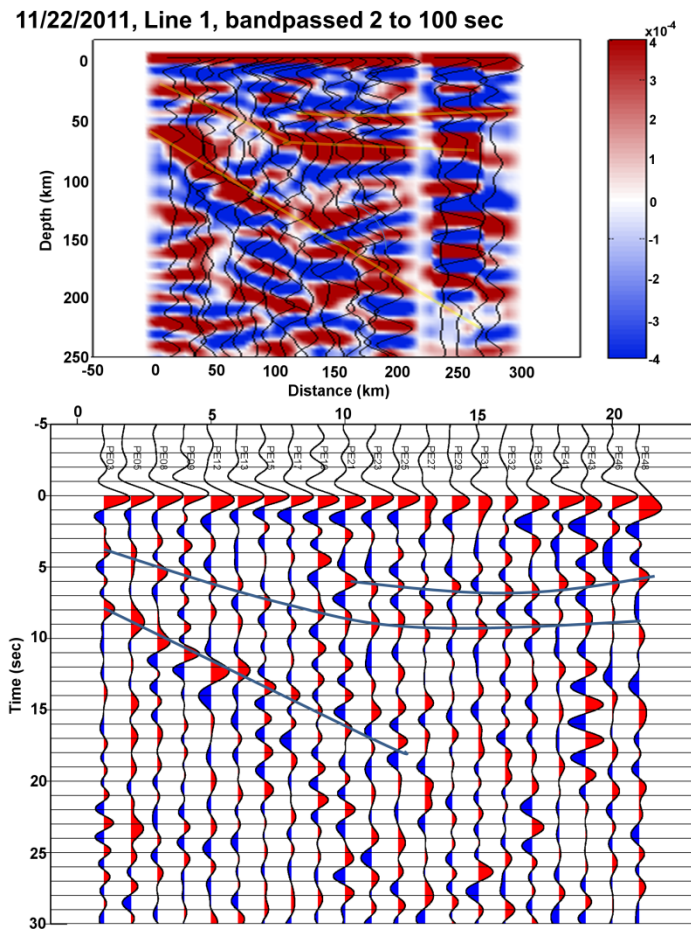


Figure 4.28: Line 1 image based on receiver functions from a 549 km deep local event on 11/22/2011 bandpassed to 2 seconds located due east of Juliaca.

After the quality test at a bandpass frequency of 2 seconds, the receiver functions were also checked at higher frequencies up to a corner frequency of 2 Hz to find out if smaller scale features could be resolvable. The results for 2 Hz are shown in figure 4.29. From the comparison of figures 4.28 and 4.29, although the results are consistent, it appears that increasing the frequency increases noise with no noticeable

improvements in resolution. Therefore it appears that the corner frequencies used for the analysis of teleseismic events are also the most appropriate for local events.

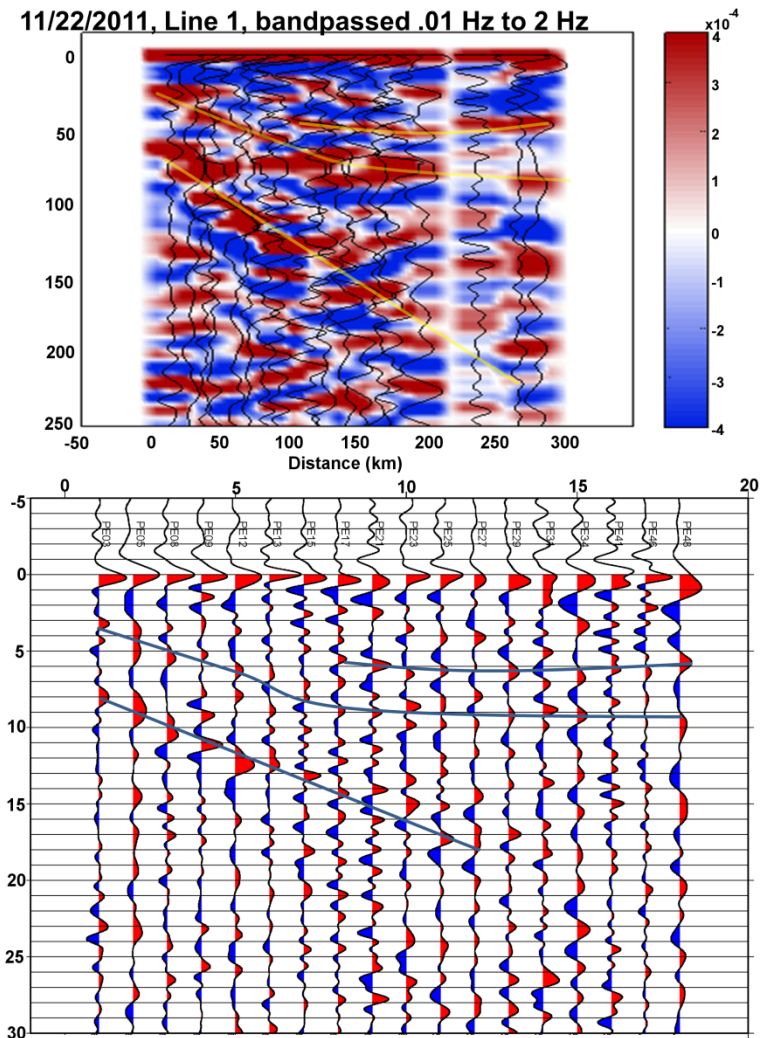


Figure 4.29: Line 1 image based on receiver functions from local event on 11/22/2011 bandpassed to 2 Hz. Compare with the same image for in figure 4.28 bandpassed to a lower frequency.

#### 4.8.2. Precursors to pP or sS

Estimations for crustal thickness can be obtained by looking for precursors to the pP or sS phase from Moho underside reflections, pmP or smS, using deep-focus earthquakes (McGlashan et al, 2008; Schenk et al, 1989; Zhang & Lay, 1993; Zheng & Lay, 2006).

Following McGlashan et al (2008), crustal thickness can be estimated between the delay time between the pP phase and pmP phase using the formula

$$t_{pP} - t_{pmP} \approx 2h\sqrt{V_{pC}^{-2} - p^2},$$

where  $h$  is the crustal thickness,  $V_{pC}$  is the P wave velocity, and  $p$  is the ray parameter (assumed to be the same for the pP phase and pmP phase). Due to the deep crustal thickness in the Altiplano, only events with magnitude greater than 6.0 with a depth greater than 100 km were considered. The location of events which were analyzed using this method are shown in figure 4.30.

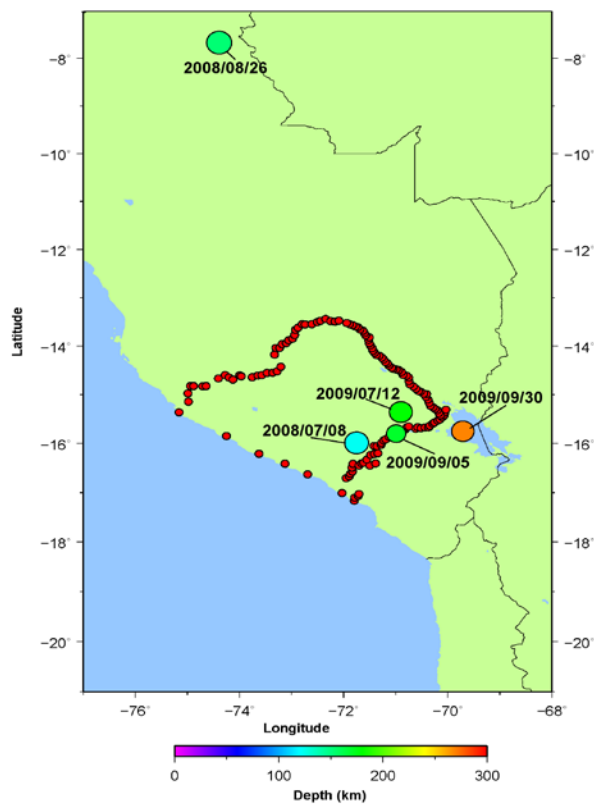
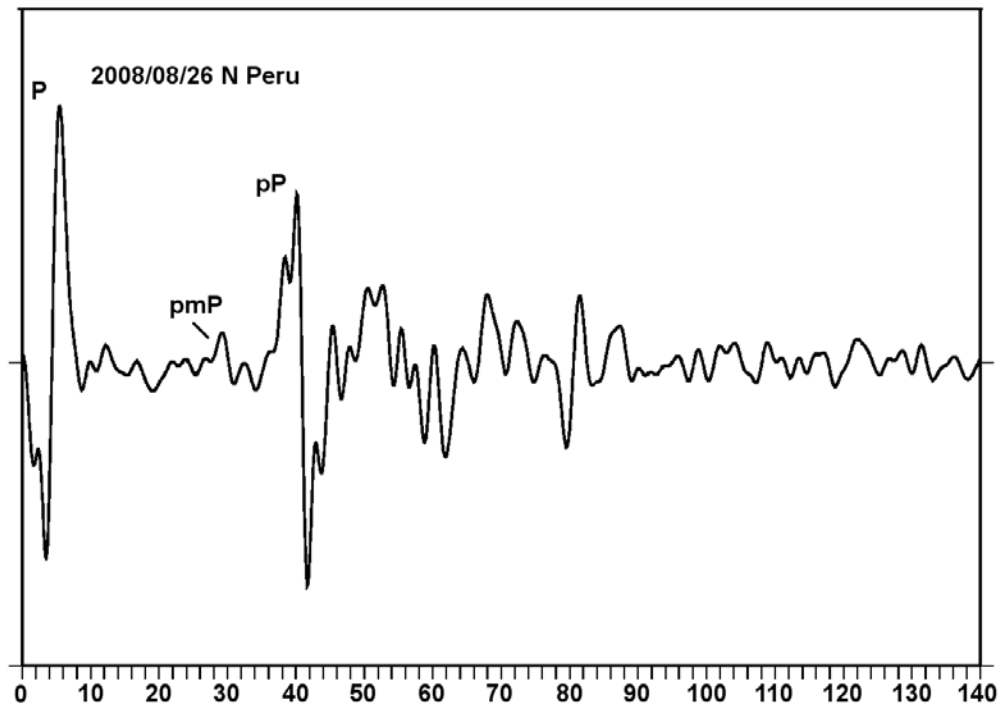


Figure 4.30: Map of specific local events analyzed for underside Moho reflections (precursors to pP and sS). Events in 2009 have locations from the IGP (Instituto Geofísico del Perú) while the 2008 events are as located by the NEIC.

Both pP precursors and sS precursors were checked for. Data from the stations in Southern California (the CI array) which detected the teleseismic Peruvian events and had a good signal-to-noise ratio were utilized to check for underside reflections from the Moho. Selected stations were aligned by the P (or S arrival for the sS phase) and then stacked. The precursors are expected to be a very small signal and are generally hard to detect in individual stations so stacking is used to minimize noise and bring out a small signal which consistently appears on a majority of stations. Results were found to be better if the data was bandpassed to longer periods such as a 2 second corner frequency. Major arrivals such as P, pP, S, and sS were generally very clear for all events. Timings for those and other nearby phases were checked using a TauP seismic travel time utility based on IASP91. Where locations from IGP (Instituto Geofisico del Peru) were available, they were used instead of NEIC because analysis of data collected by the Peruvian arrays showed that the IGP locations generally resulted in better P and S picks (thus the events in 2009 shown in figure 4.30 are all IGP locations, depths, and magnitudes). Using estimates of Moho depth from receiver functions (where applicable), it is possible to estimate the expected location of the precursor and compare with the stacks.



*Figure 4.31: Stack of teleseismic data collected from Southern California stations recording an earthquake in northern Peru on 8/26/2008 showing possible precursor to pP from underside Moho reflection (see map in figure 4.30).*

Figure 4.31 shows a stack from a magnitude 6.3 earthquake in Northern Peru from Aug. 26, 2008. The largest signal between the P and pP arrival appears to be the precursor due to underside reflection off of the Moho. Although no receiver function data is available in this region, a look at the location and topography of the area (see figure 1.1) shows that this location is most likely at lower elevations in the Subandes where the Moho depth is shallower. The Moho depth appears to be around 40 km depth which is around the average for that region (Lloyd et al, 2010; Assumpção, 2012). The longer period S wave results in which precursors to the sS phase are indicative of underside reflections from the Moho are down in figure 4.32.

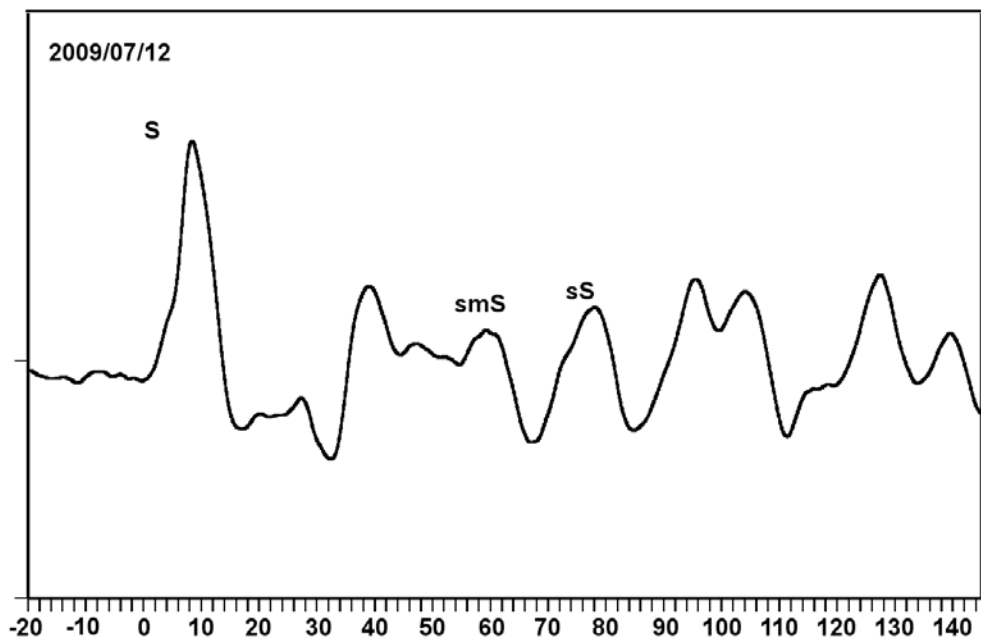
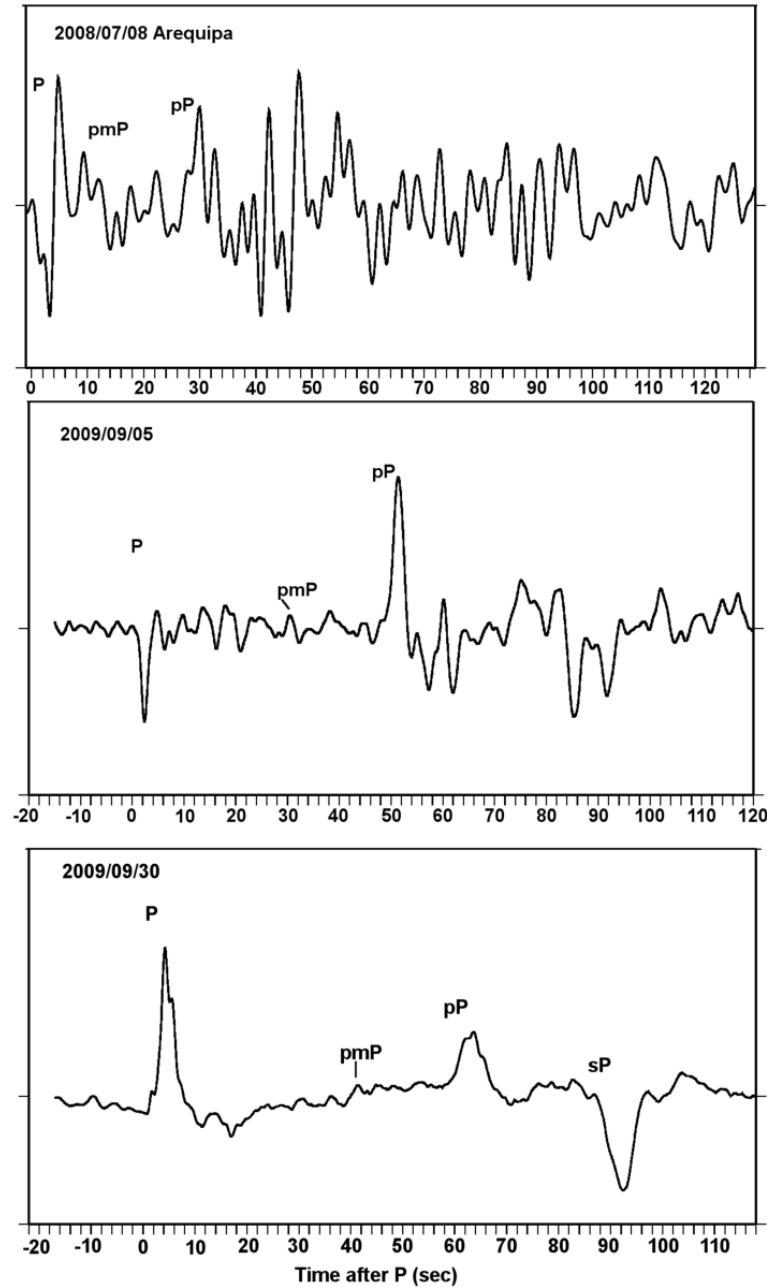


Figure 4.32: Stack of teleseismic data for 2009/07/12 showing S wave signal and possible precursor to sS from underside Moho reflections (see location in figure 4.30).

In this figure, the sS phase appears small relative to the pP phase and can be identified by the timing of phase arrivals. An earlier phase which may be the smS phase is consistent with a Moho depth of 70-75 km which is what is observed with receiver functions beneath that region of the Altiplano. Some other results for the pP phase are shown in figure 4.33 where the Moho depth is expected to be similar to the depth in figure 4.32 (aside from the Arequipa earthquake where the Moho depth is closer to 60 km depth from receiver functions).



*Figure 4.33: Stacks from Southern California recordings of Peruvian earthquake which occurred on 2008/07/08, 2009/09/05, and 2009/9/30 for looking for pP precursors. Locations are given in figure 4.30 and earthquake details in table 4.1.*

However the pmP phase appears to be so small that it is generally hard to identify over the surrounding noise without prior knowledge of the Moho depth and phase timing

estimations. Thus in these cases very careful selection of only the highest quality teleseismic data and careful stacking is needed for precursor identification. In some cases the precursors may be visible for individual stations.

#### 4.8.3. Modeling Local Events

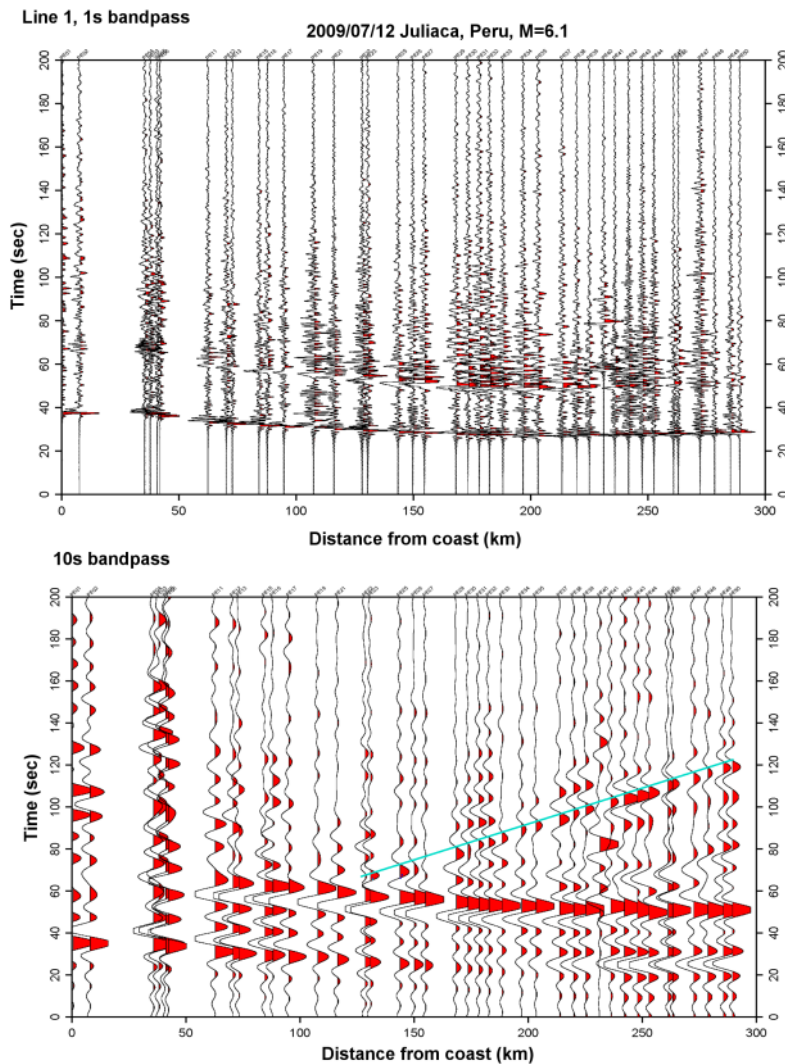


Figure 4.34. Vertical component seismogram traces for Line 1 showing data from event on 7/12/2009 bandpassed to 1 second (top) and 10 seconds (bottom).

Local earthquake data from large, deep events recorded by the seismic array

(particularly on 7/12/2009, 9/5/2009, and 9/30/2009) was analyzed with locations as

shown in figure 4.30. The three events were recorded by Line 1 located in the normal subduction region and the vertical components of the seismogram are shown in figures 4.34-4.36.

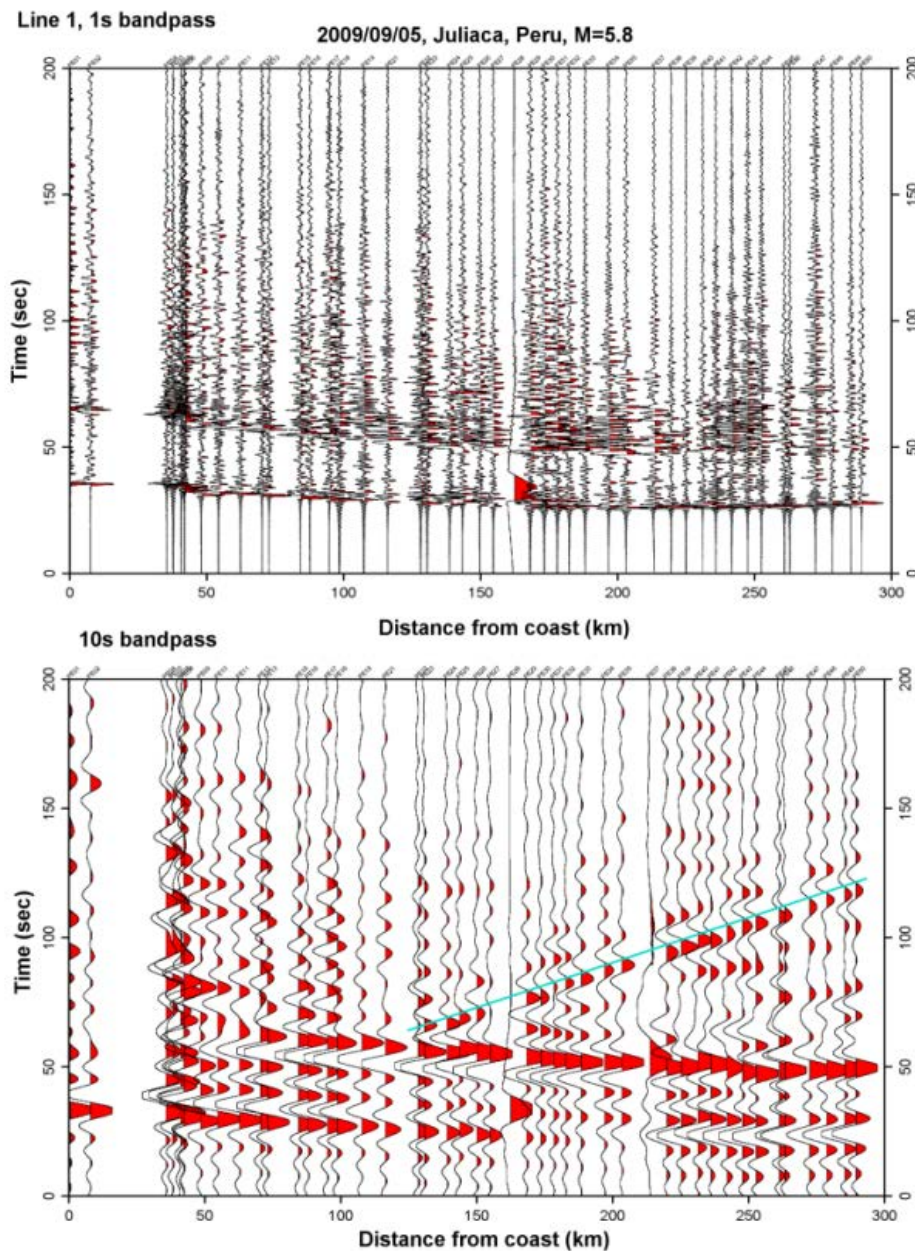


Figure 4.35 Vertical component seismogram traces for Line 1 showing data from event on 09/05/2009 bandpassed to 1 second (top) and 10 seconds (bottom)

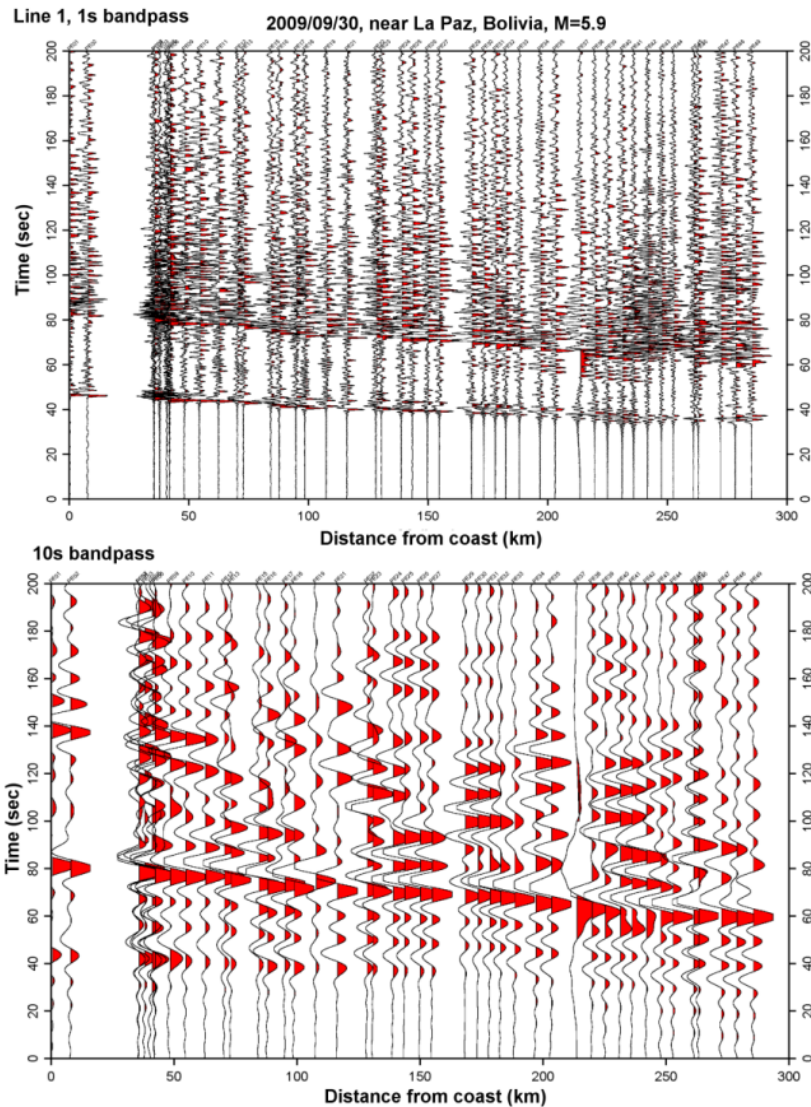
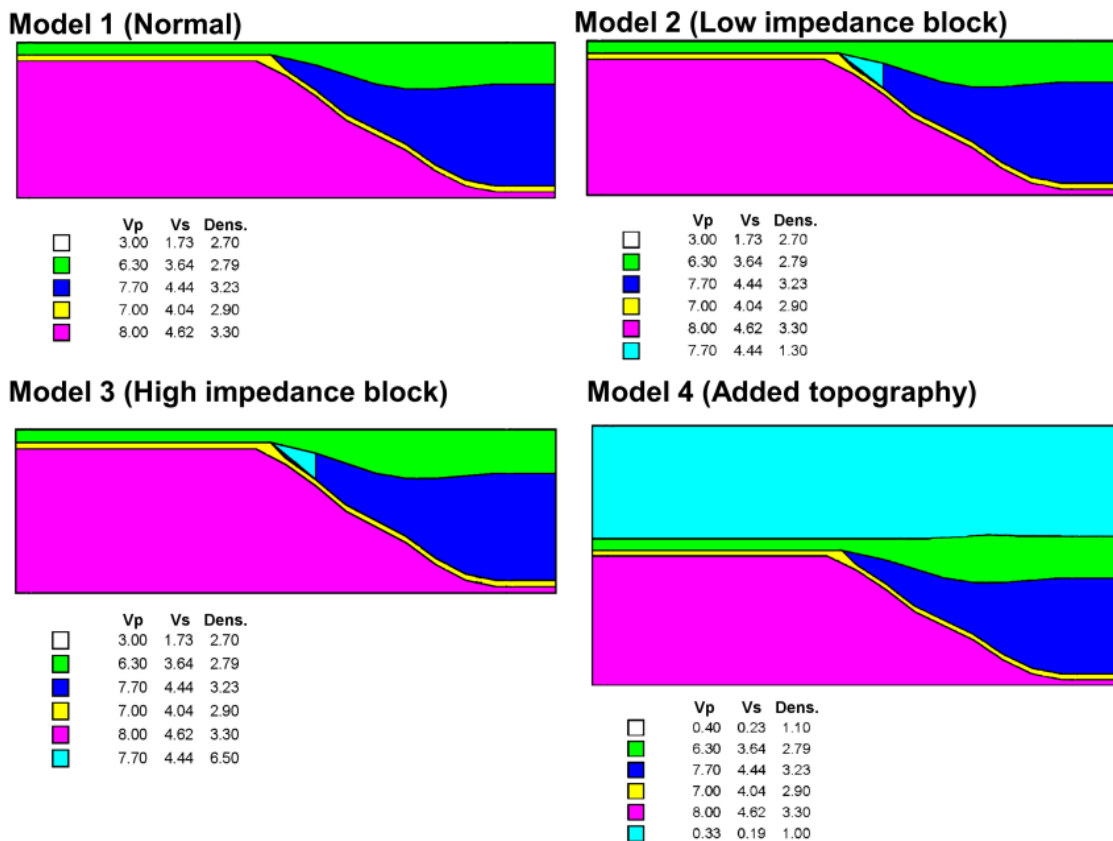


Figure 4.36. Vertical component seismogram traces for Line 1 showing data from event on 09/30/2009 bandpassed to 1 second (top) and 10 seconds (bottom).

The top portion of each figure shows the data bandpassed to 1 second while the bottom portion shows the same data bandpassed to 10 seconds. The major arrivals from the S and P wave are visible in each plot. An observation that was made was that there appeared to be a signal originating from near the center of the array which appeared to be a reflection. The signal is only visible in the longer period band-passed data

indicating that the signal may originate from some kind of surface wave reflecting off something in the subduction system (see blue lines in figure 4.34 and figure 4.35).

Although the signal appears in multiple local events, the signal is not obvious for the event on 2009/09/30 shown in figure 4.36 indicating a possible azimuthal dependence on the direction of the reflector. Several models were tested to determine if a structural model could be used to explain the possible origin of the observed signal as shown in figure 4.37.



*Figure 4.37: Possible models for analyzing the local events shown in figures 4.34-4.36 using finite difference code. The normal model consists of a homogeneous crust with an average crustal velocity, the mantle wedge, subducting oceanic crust, and underlying mantle with average velocities. The Low impedance and high impedance models contain a wedge with differing density in the corner of the mantle wedge to study whether reflections from the corner of the subduction zone could cause*

*reflections similar to those observed in local data (see figures 4.34-4.35). The fourth model is similar to model 1 but has added station topography. The light blue color has properties of air.*

One possibility was that the signal was derived from a reflection off the corner of the subduction zone near where the asthenospheric wedge is cut off by the Nazca plate as it subducts near the oceanic trench. To test this model, a small wedge was inserted in the corner of the subduction zone with a different impedance (either higher or lower) to cause rays to reflect off. The impedance contrast was given a density very different from the surrounding materials to encourage reflections for the purpose of generating a signal which could then be compared with observations in the data. Another possibility was that the signal could be related to reflections off of topography. These cases were compared to a simple model of the subduction zone consistent with the model in figure 2.10A. To simplify the resulting signals, no midcrustal structure was included in these models.

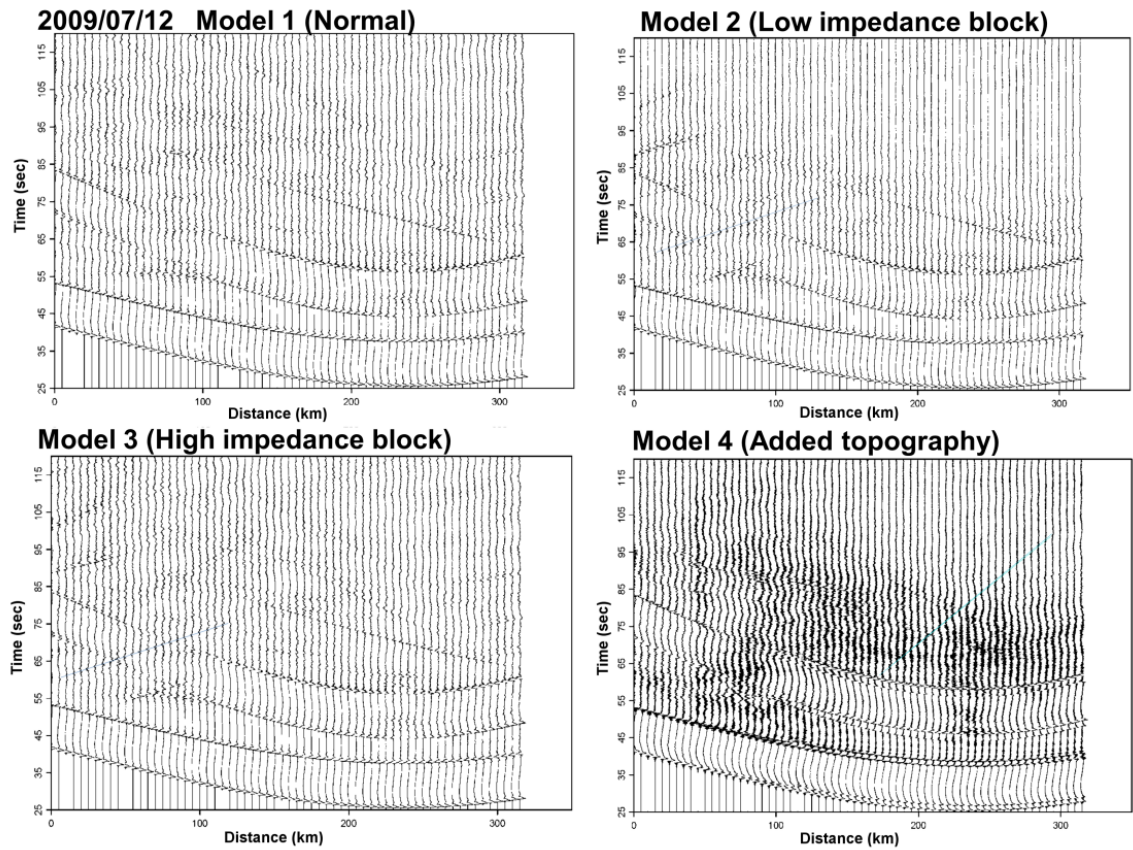


Figure 4.38 Finite difference synthetics for 2009/07/12 based on the models in figure 4.37.

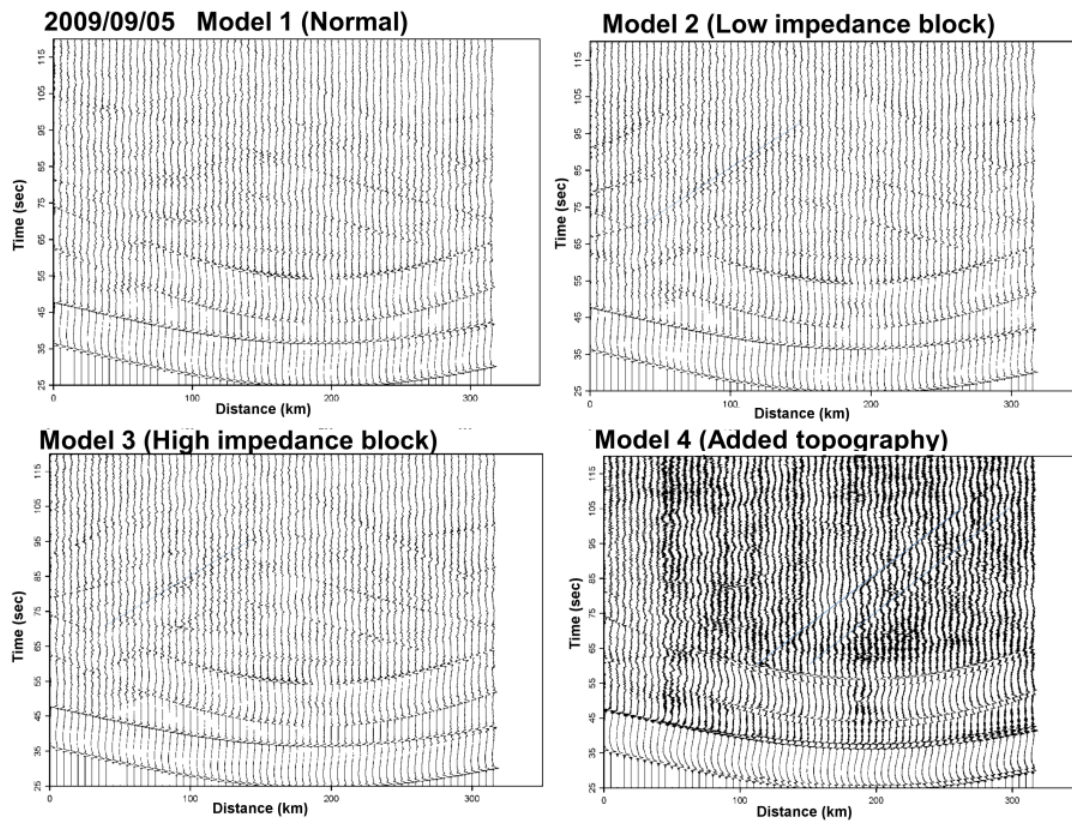


Figure 4.39 Finite difference synthetics for 2009/09/05 based on the models in figure 4.37.

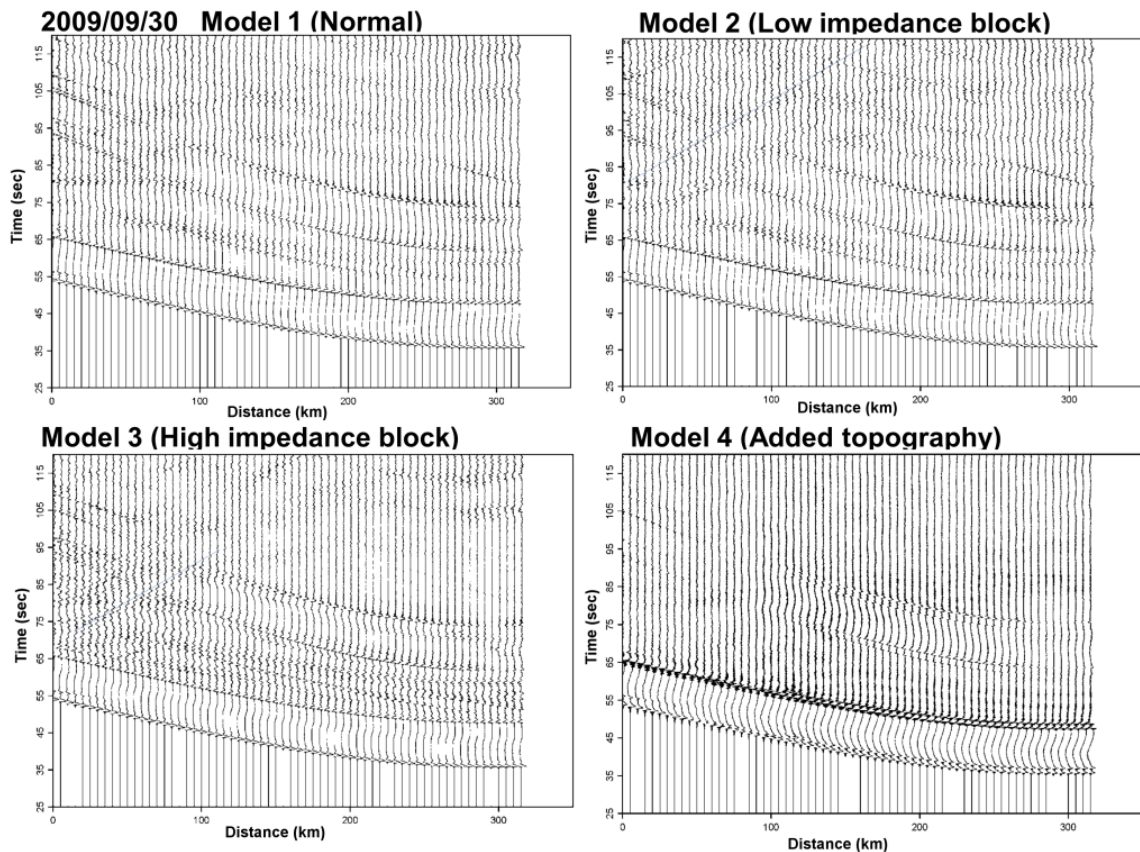


Figure 4.40 Finite difference synthetics for 2009/09/30 based on the models in figure 4.37.

Synthetic seismograms generated from finite difference modeling are shown in figures 4.38–4.40 for each of the three events for the models shown in figure 4.37. No reflections in the direction observed in the 10 second bandpassed data (figures 4.34–4.35) can be seen in the first normal model (model 1 in figure 4.37). For the case where there is an impedance contrast at the corner of the subduction zone, a few reflections are observed but the reflectors originate near the start of the model (for example see some reflections starting at about 60 seconds at zero distance in figure 4.38, or ~55 seconds in figure 4.39, or ~80 seconds in figure 4.40). However the synthetics

corresponding to the model including topography in figure 4.38 and 4.39 shows a small amplitude signal originating from the same approximate location as in the data and traveling in the same direction. Similar to the data, the signal is not obvious in the topography model for the event on 9/30/2009. Although there are other possible explanations for the signal observed in the 10 second local data besides reflections off topography, the use of finite difference modeling to investigate several possible cases shows that it is possible for a structural model to provide a possible fit to the observed data.

#### **4.8.4. Future Work: Determination of EQ Loc. and Focal Mechanisms.**

The cut and paste code (CAP) was used to check earthquake focal mechanisms (Zhao & Helmberger, 1994; Zhu & Helmberger, 1996). Two different crustal models were tested for making Greens Functions. One model was modified from Ocola et al, 1995 (Somerville et al, 2008) which is based on geophysical studies along the southern Peru coast. The model is shown in table 4.2. The other model tested used the  $V_p$ ,  $V_s$ , and density from IASP91 for the upper 250 km and tested lower values for the attenuation ( $Q_p$  and  $Q_s$ ). Attenuation studies from the Peru/Chile or Central Andean regions (Baumont et al, 1999; Sumner, 1967; Whitman et al, 1992) found significant variation in  $Q$  values. Previous values for the Altiplano based on results from the BANJO and SEDA array (modified from Myers et al, 1998) found values for the crust in the Altiplano of  $V_p \sim 6.2$ ,  $V_s \sim 3.6$ ,  $Q_p \sim 500$ , and  $Q_s \sim 100$ . For the Altiplano asthenosphere the values found were  $V_p \sim 8.3$ ,  $V_s \sim 4.6$ ,  $Q_p \sim 500$ , and  $Q_s \sim 200$  (Heit, 2005).

CAP code was used to analyze a magnitude 6.9 earthquake on 10/28/2011 which occurred just north of Line 3 and found a focal mechanism similar to the Harvard CMT solution (see figure 4.41) after searching the full range of strike, dip, and rake but fits between data and synthetics were poor. More work with this method is needed to produce good focal mechanisms.

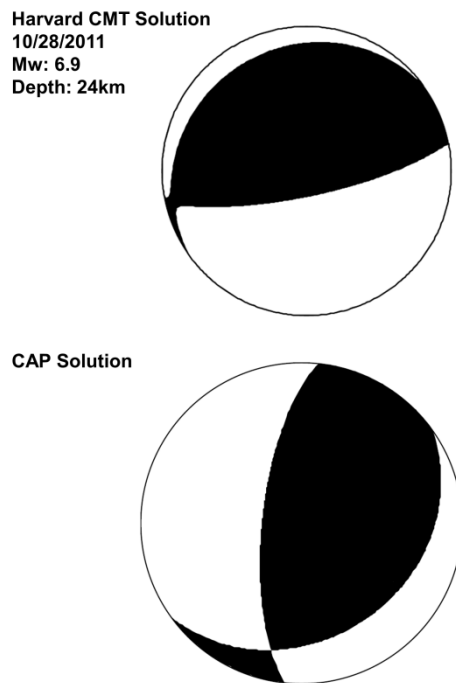


Figure 4.2 CMT solutions for 10/28/2011.

Table 4.2 Crustal model for S. Peru, from Ocola et al, 1995					
Thickness	Vp	Vs	Density	Qp	Qs
6.7	5.3	3.03	2.1	2000	900
4.6	6	3.37	2.5	2000	900
18.1	6.5	3.65	2.78	2000	900
15.8	7.3	4.1	3.18	2000	900
16	8.1	4.5	3.4	2000	900
100	8.101	4.501	3.401	2000	900

#### **4.9 Summary and Conclusions**

The previous chapters present receiver function results from three seismic arrays in Southern Peru. A total of about 100 broadband stations were deployed over the course of several years between 2008 and 2011, providing dense station coverage along the arrays and a valuable data set for the analysis of both local and teleseismic earthquakes. Teleseismic receiver functions were formed using P, PP, PKP, S and SKS phases and both frequency and time domain deconvolution methods were used. Resulting images using backprojection, CCP stacking, or migration provide high quality images of the subduction system. The areas imaged include the region of normal subduction where the Nazca plate dips at about a 30 degree angle, the transition from normal to flat slab subduction suggested to be a contortion rather than a tear in the slab, and the flat slab region near the subduction of the Nazca Ridge. In addition to clarifying the shape of the slab, the Moho depth was observed to reach a maximum depth of about 70-75 km beneath the Altiplano. Receiver function images also show a positive impedance midcrustal signal at 40 km indicating a velocity increase which is suggested to be a possible observation of the underthrusting Brazilian Shield. Crustal signals which are less defined in teleseismic receiver functions can be clarified by looking at local receiver functions from deep events close to the arrays. Receiver functions for individual stations can be stacked to obtain estimates of Moho depth and  $V_p/V_s$  ratio. The average  $V_p/V_s$  ratio for the region was found to be around 1.75 with a few regions of elevated  $V_p/V_s$  near the active volcanic arc. The Moho depths obtained from

receiver function images can be confirmed through other methods such as looking for precursors to the pP and sS phases in teleseismic recordings of local Peru events. The precursors, if observed, come from underside Moho reflections and can be used to estimate crustal thickness. Although most of the receiver function results come from an analysis of radial receiver functions, a look at energy on transverse receiver functions can provide information about dipping structure or anisotropy. Observations from Line 2 in the transition from normal to flat slab subduction suggest that the area has some anisotropy with a symmetry axis in possibly an ~E/W direction. This anisotropy might provide an explanation for differences between images using data from different azimuthal directions (e.g., comparing images from northerly directions with southerly directions). Simple structural and velocity models can be tested using finite difference methods to produce synthetic receiver functions or model local events. These results provide valuable new information about the structure of the subduction zone in southern Peru where the subduction transitions from shallow subduction in central Peru to steep subduction in southern Peru.

### Chapter 4 References

- Assumpção, M., M. Feng, A. Tassara, J. Julià (2012), Developing Models of Crustal Thickness for South America from Receiver Functions and Surface Wave Tomography, *Tectonophysics*, in review/press.
- Baumont, D., A. Paul, S. Beck, and G. Zandt (1999), Strong crustal heterogeneity in the Bolivian Altiplano as suggested by attenuation of Lg waves, *J. of Geophys. Res.*, 104 (B9), 20,287- 20,305.
- Burdick, L.J. and D.V. Helmberger (1974), Time functions appropriate for deep earthquakes, *Bull. Seismol. Soc. Amer.*, 64, 1419-1428.
- Calkins, J. A., G. Zandt, H. J Gilbert, and S. L. Beck (2006), Crustal images from San Juan, Argentina, obtained using high frequency local event receiver functions, *Geophys. Res. Lett.*, 33, L07309.
- Chen, M., J. Tromp, D. Helmberger, H. Kanamori (2007), Waveform modeling of the slab beneath Japan, *J. Geophys. Res.*, 112, B02305.
- Cunningham, P., and S. Roecker (1986), Three-dimensional P and S Wave Velocity Structures of Southern Peru and Their Tectonic Implications, *J. of Geophys. Res.*, 91 (B9), 9517–9532.
- Endrun, B., T. Meier, M. Bischoff and H.-P. Harjes (2004), Lithospheric structure in the area of Crete constrained by receiver functions and dispersion analysis of Rayleigh phase velocities, *Geophys. J. Int.*, 158, 592-608.
- Frassetto, A., G. Zandt, H. Gilbert, T.J. Owens and C.H. Jones (2010), Improved imaging with phase-weighted common conversion point stacks of receiver functions, *Geophys. J. Int.*, 182, 368-374.

- Geissler, W., F. Sodoudi, and R. Kind (2010), Thickness of the central and eastern European lithosphere as seen by S receiver functions, *Geophys. J. Int.*, 181, 604-634.
- Heit, B. (2005), Chapter 4—The Altiplano Plateau, from *Teleseismic tomographic images of the Central Andes at 21° S and 25.5° S*, submitted for dissertation at Freie Universität Berlin.
- Heit, B., F. Sodoudi, X. Yuan, M. Bianchi, and R. Kind (2007), An S receiver function analysis of the lithospheric structure in South America, *Geophys. Res. Letters*, 34, L14307.
- Helmberger, D.V. and J.E. Vidale (1988), Modeling strong motions produced by earthquakes with two-dimensional numerical codes, *Bull. Seis. Soc. Am.*, 78, 109-121.
- Husker, A., I. Stubailo, M. Lukac, V. Naik, R. Guy, P. Davis, and D. Estrin (2008), WiLSON: The Wirelessly Linked Seismological Network and Its Application in the Middle America Subduction Experiment, *Seis. Res. Lett.*, 79 (3), 438-443.
- Julià, J., M., Assumpção, and M.P. Rocha (2008), Deep crustal structure of the Paraná Basin from receiver functions and Rayleigh-wave dispersion: Evidence for a fragmented cratonic root, *J. of Geophys. Res.*, 113, B08318.
- Kennett, B. (1991), The removal of free surface interactions from three-component seismograms, *Geophys. J. Int.*, 104, 153-163.
- Kim, Y., R.W. Clayton, and J.M. Jackson (2010), Geometry and seismic properties of the subducting Cocos plate in central Mexico, *J. Geophys. Res.*, 115, B06310.
- Kumar, P., X. Yuan, R. Kind, and G. Kosarev (2005), The lithosphere-asthenosphere

- boundary in the Tien Shan-Karakoram region from S receiver functions – evidence of continental subduction, *Geophys. Res. Lett.*, 32, L07305.
- Langston, C. (1979), Structure under Mount Rainier, Washington, inferred from teleseismic body waves, *J. Geophys. Res.*, 84, 4749–4762.
  - Liggoria, J., and C. Ammon (1999), Iterative deconvolution and receiver function estimation, *Bull. Seism. Soc. Amer.*, 89, 19–36.
  - Lloyd S., van der Lee, S., Sand Franca, G., Assumpcao, M. & Feng, M., 2010. Moho map of South America from receiver functions and surface waves, *J. of Geophys. Res.*, 115, B11315.
  - Lucente, F., N.P. Agostinetti, M. Moro, G. Selvaggi, and M. Bona (2005), Possible fault plane in a seismic gap area of the southern Apennines (Italy) revealed by receiver function analysis, *J. of Geophys. Res.*, 110, B04307.
  - McGlashan, N., L. Brown, and S. Kay (2008), Crustal thickness in the central Andes from teleseismically recorded depth phase precursors, *Geophys. J. Int.*, 175, 1013-1022.
  - Myers, S., S. Beck, G. Zandt, and T. Wallace, (1998), Lithospheric-scale structure across the Bolivian Andes from tomographic images of velocity and attenuation for P and S waves, *J. of Geophys. Res.*, 103 (21),233–21,252.
  - Ocola, L.C., J. Leutgert, L.T. Aldrick, R.P. Meyer, and C.E. Helsey (1995). Velocity structure of the coastal region of southern Peru from seismic refraction/wide-angle reflection data, *J. Geodynamics*, 20,1-30.
  - Savage, M. (1998), Lower crustal anisotropy or dipping boundaries? Effects on receiver functions and a case study in New Zealand, *J. of Geophys. Res.*, 103, B7,

15069-15087.

- Schenk, T., G. Müller, and W. Brüstle (1989), Long-period precursors to pP from deep-focus earthquakes: the Moho underside reflection pMP, *Geophys. J. Int.*, 98, 317-327.
- Somerville, P., R. Graves and N. Collins (2008), Ground Motions from Large Cascadia Subduction Earthquakes, URS Final Report, Award Number: 06HQGR0160.
- Sumner, R. (1967), Attenuation of Earthquake Generated P Waves along the Western Flank of the Andes, *Bull. Seis. Soc. Amer.*, 57 (2), 173-190.
- Vidale, J., D.V. Helmberger, and R.W. Clayton (1985), Finite-difference seismograms for SH waves, *Bull. Seis. Soc. of Amer.*, 75 (6), 1765-1782.
- Whitman, D., B.L. Isacks, J. Chatelain, J. Chiu, and A. Perez, (1992), Attenuation of High-Frequency Seismic Waves Beneath the Central Andean Plateau, *J. Geophys. Res.*, 97, B13, 19,929-19,947.
- Zhang, J. and C. Langston (1995), Dipping Structure under Dourbes, Belgium, Determined by Receiver Function Modeling and Inversion, *Bull. of the Seis. Soc. Amer.*, 85 (1), 254-268.
- Zhang, Z. and T. Lay (1993), Investigation of Upper Mantle Discontinuities Near Northwestern Pacific Subduction Zones Using Precursors to sSH, *J. Geophys. Res.*, 98 (B3), 4389-4405.
- Zhao, L. and D.V. Helmberger (1994), Source Estimation from Broadband Regional Seismograms, *Bull. Seis. Soc. Amer.*, 84 (1), 91-104.
- Zheng, Y. and T. Lay (2006), Low  $V_p/V_s$  ratios in the crust and upper mantle beneath

- the Sea of Okhotsk inferred from teleseismic  $p_M P$ ,  $s_M P$ , and  $s_M S$  underside reflections from the Moho, *J. Geophys. Res.*, 111, B01305.
- Zhu, L. and D.V. Helmberger (1996), Advancement in Source Estimation Techniques Using Broadband Regional Seismograms, *Bull. Seis. Soc. Amer.*, 86 (5), 1634-1641.
  - Zhu, L., and H. Kanamori (2000), Moho depth variation in southern California from teleseismic receiver functions, *J. Geophys. Res.*, 105 (B2), 2969–2980.

## Appendix A

### Chapter 2 Supplementary Figures

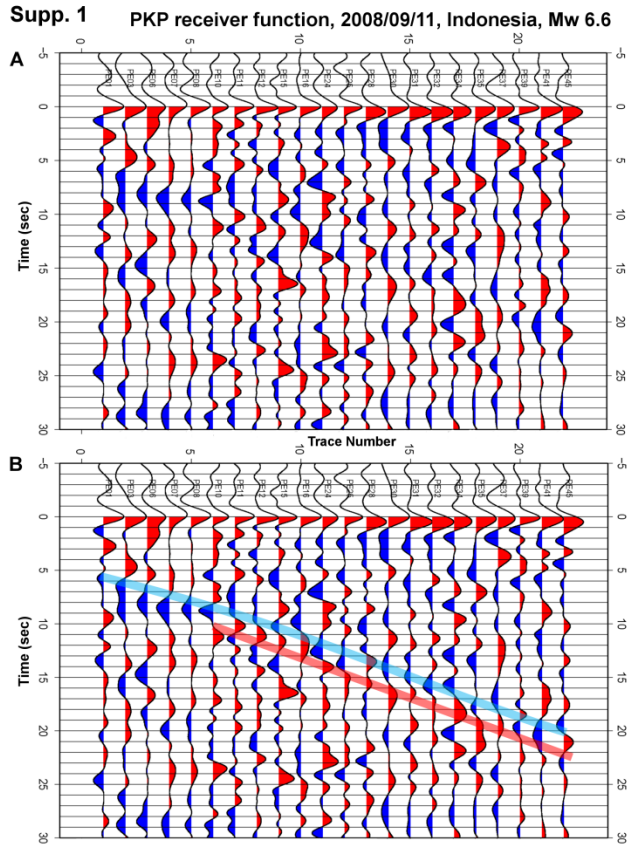


Figure A.1: Figures 2.4 and 2.9 show examples of PKP data and a PKP backprojected receiver function image. The example above shows individual PKP receiver functions. A) Example of PKP receiver functions from a magnitude 6.6 earthquake near Indonesia occurring on 2008/09/11. B): Shows an interpretation of the above image with the approximate location of the signal from the slab. The negative signal (highlighted in blue) represents the top of the oceanic crust and the positive pulses (highlighted in red) represent the bottom of the oceanic crust.

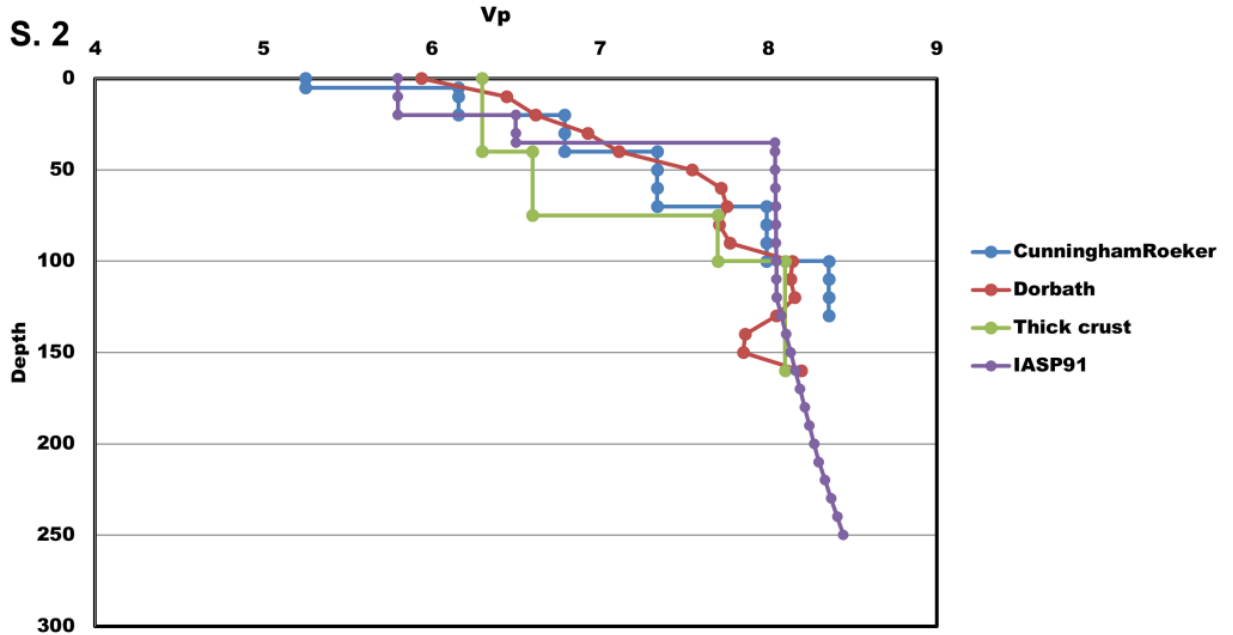


Figure A.2: P wave velocity models considered in this study. Models from Cunningham and Roecker (1986) and Dorbath et al (2008) are shown along with the IASP91 model and a simplified model for thickened crust.

### References

- Cunningham, P., and S. Roecker (1986), Three-dimensional P and S Wave Velocity Structures of Southern Peru and Their Tectonic Implications, *J. of Geophys. Res.*, 91 (B9), 9517–9532.
- Dorbath, C., M. Gerbault, G. Carrier, and M. Guiraud (2008), Double seismic zone of the Nazca plate in Northern Chile: High-resolution velocity structure, petrological implications, and thermomechanical modeling, *Geochem., Geophys., Geosys.*, 9 (7), Q07, 2006.

## Supp. 3

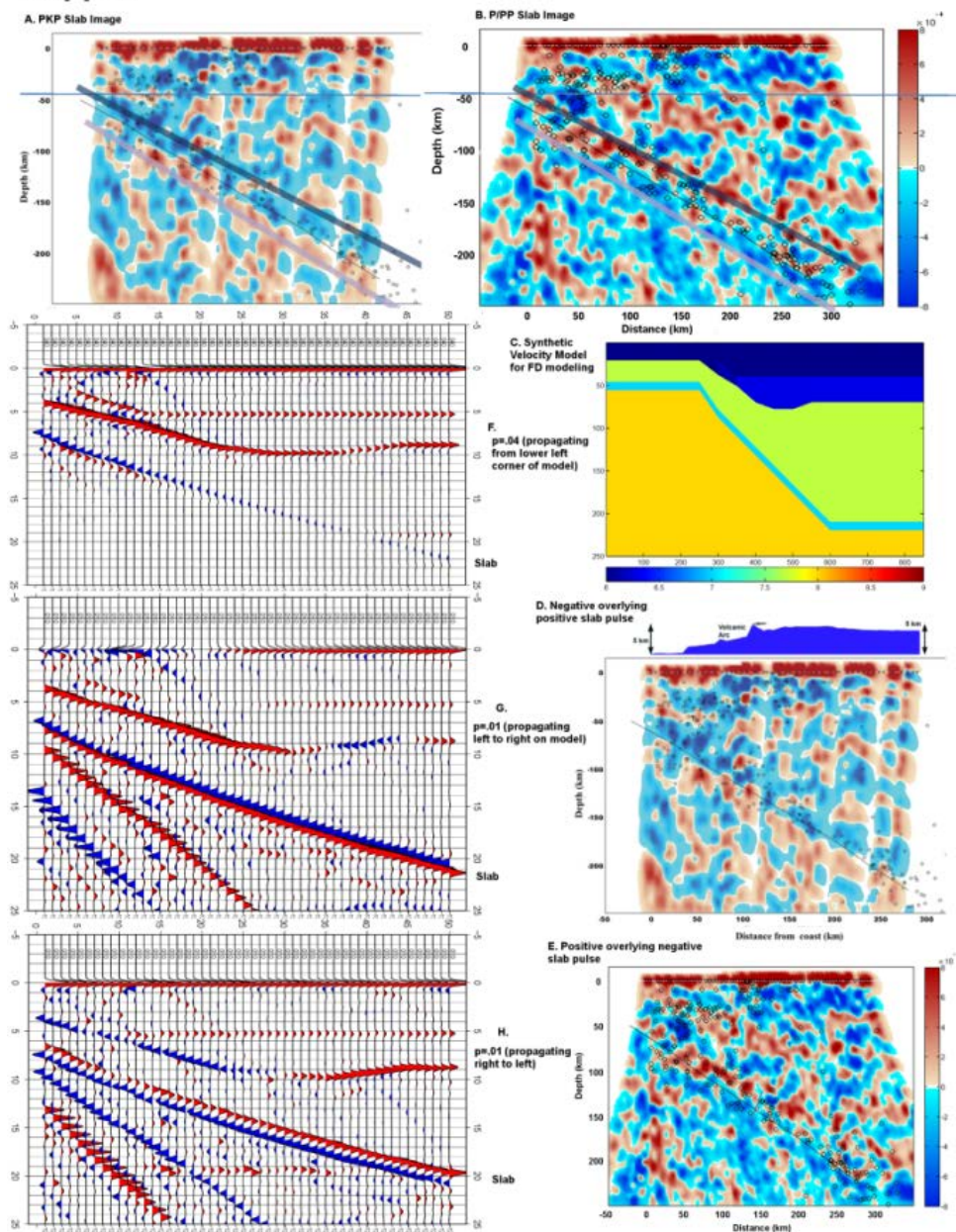


Figure A.3: Analysis of differences between observed slab between PKP image (A) and P/PP image (B). There appears to be an inversion where the PKP image has a negative pulse overlying a positive pulse and the P/PP image has a positive pulse overlying a negative pulse. The dip angle for subducting Nazca plate does not change. C) P wave velocity model used to produce finite difference synthetics. D and E) Calculations using the Zoeppritz equation for transmission coefficients using values from the model in C for an incident wave going from the mantle to the oceanic crust and from the oceanic crust to the mantle wedge as a function of angle. Note in (D) that there is a phase angle inversion

for high angles of incidence. F) Model for a standard teleseismic wave with ray parameter 0.04. G and H) Waves with ray parameters of 0.01 (similar to PKP waves) coming from difference directions. Note that depending on orientation it is possible to have either a negative pulse overlaying a positive or positive overlaying a negative pulse. The direction and angle of incidence are suggested as possible factors in the sign inversion for the slab observed in the receiver function images.

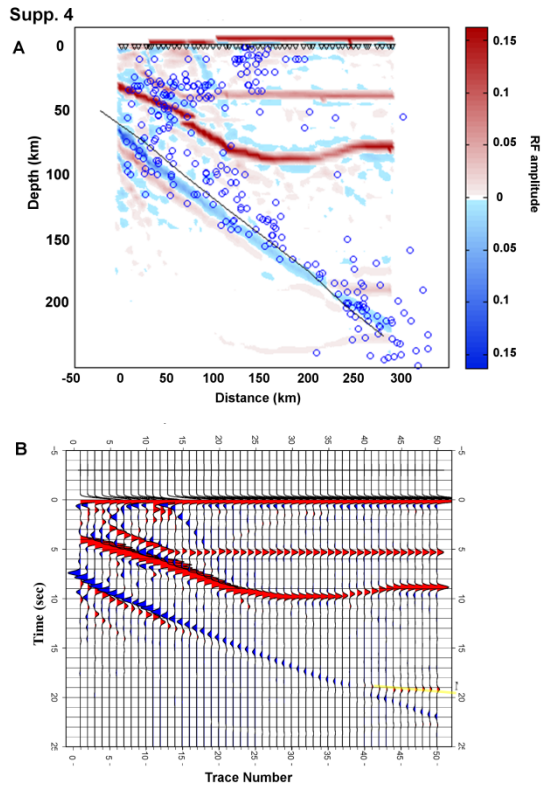


Figure A.4: Receiver function image of the synthetics from Figure 10B showing all results as a function of depth.

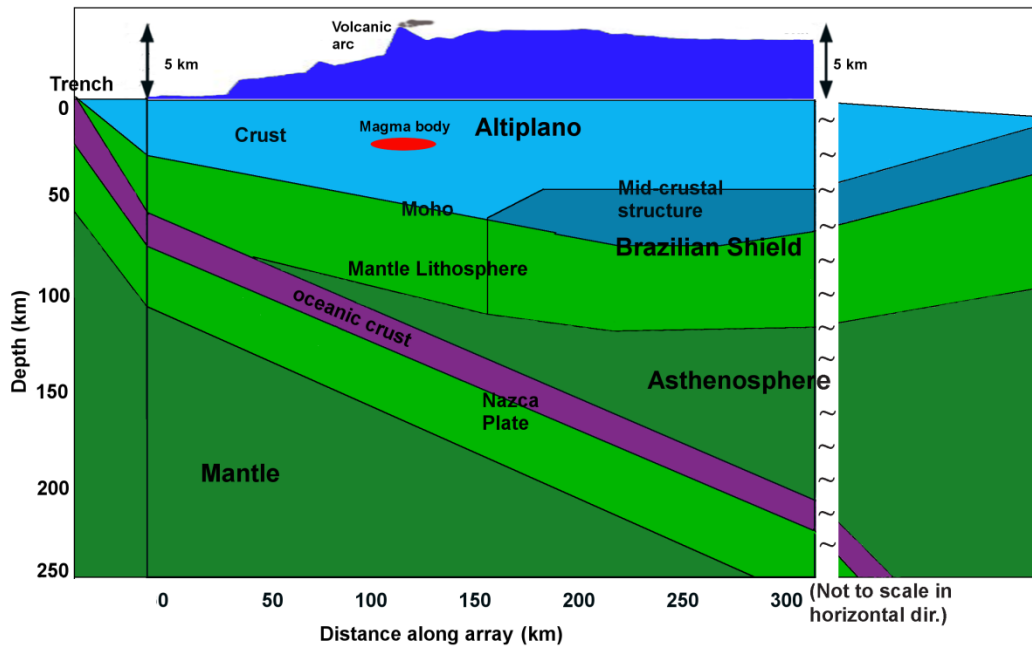


Figure A.5: More detailed cartoon of Line 1 based on Figure 2.16 which shows the trench, crust and mantle lithosphere, Brazilian Shield, and Nazca plate. Depths are approximate.

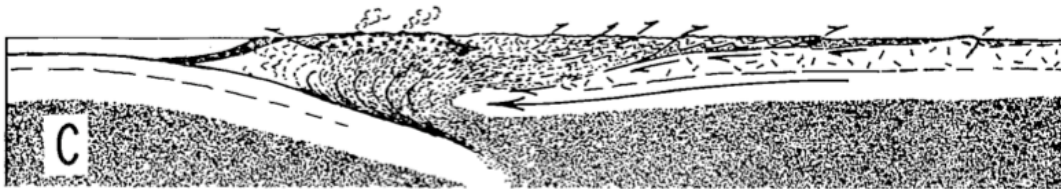


Fig. 131. — Trois schémas de tectonique des plaques susceptibles de rendre compte de la tectonique en compression dans une chaîne « cordillérienne »: A. inspiré de X. LE PICHON (1968), B. inspiré de B. P. LUYENDICK (1970), C. d'après P. J. CONEY (1970)

Figure A.26 The underthrusting of the Brazilian Shield was first suggested by Megard (1978). A figure from his book is shown above. Compare with model in figure A.5.

Reference:

- Megard F.. Etudes géologiques des Andes du Perou Central. Book (1978) pp. 1-315.

## Appendix B

Observations of Mid-Crustal structure  
Across the array

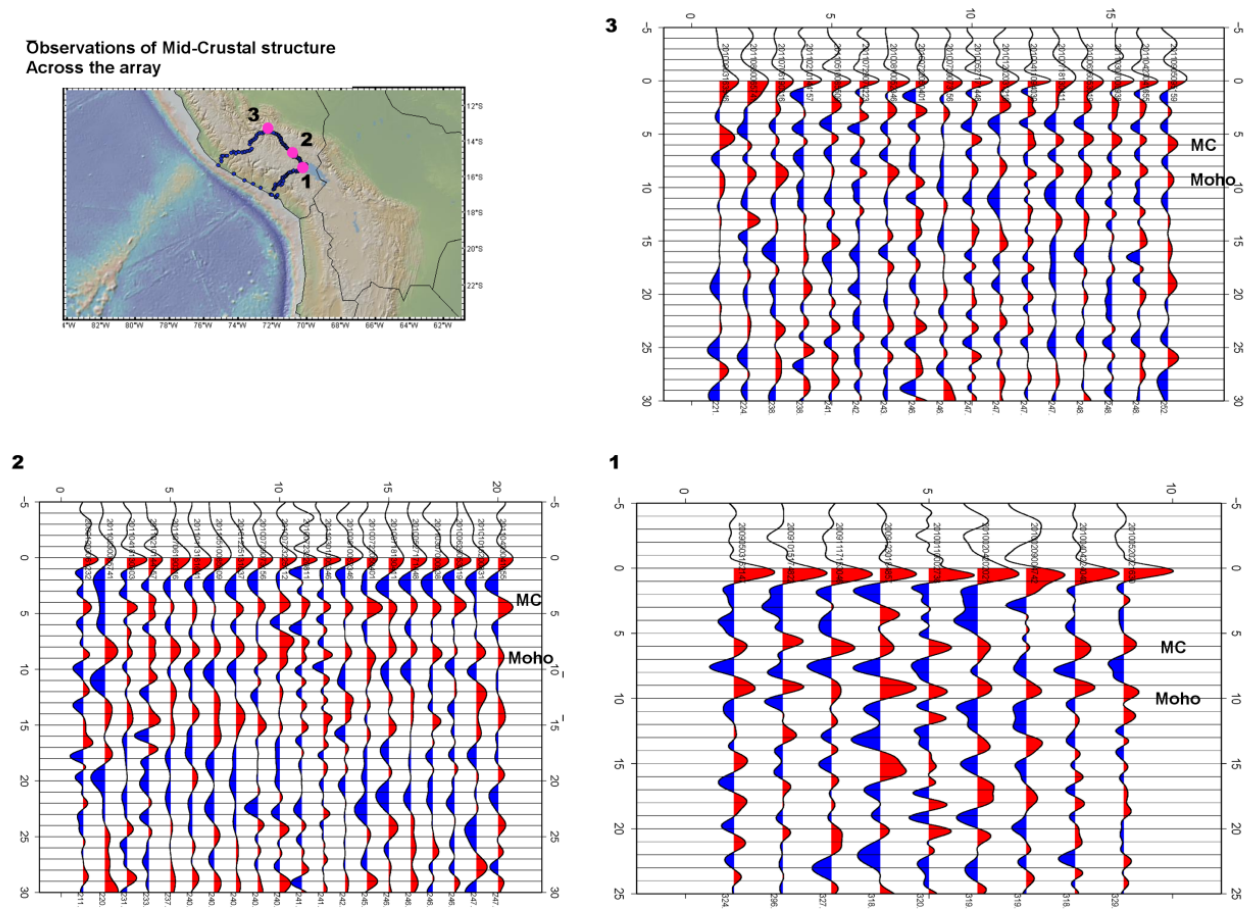


Figure B.1. Sample receiver functions showing observations of a midcrustal structure at various points of the array. Each example shows multiple events for a single station shown on the map as a pink circle. The midcrustal structure at around 5 seconds ( $\sim 40$  km depth) is denoted as MC and the signal from the Moho is also shown.

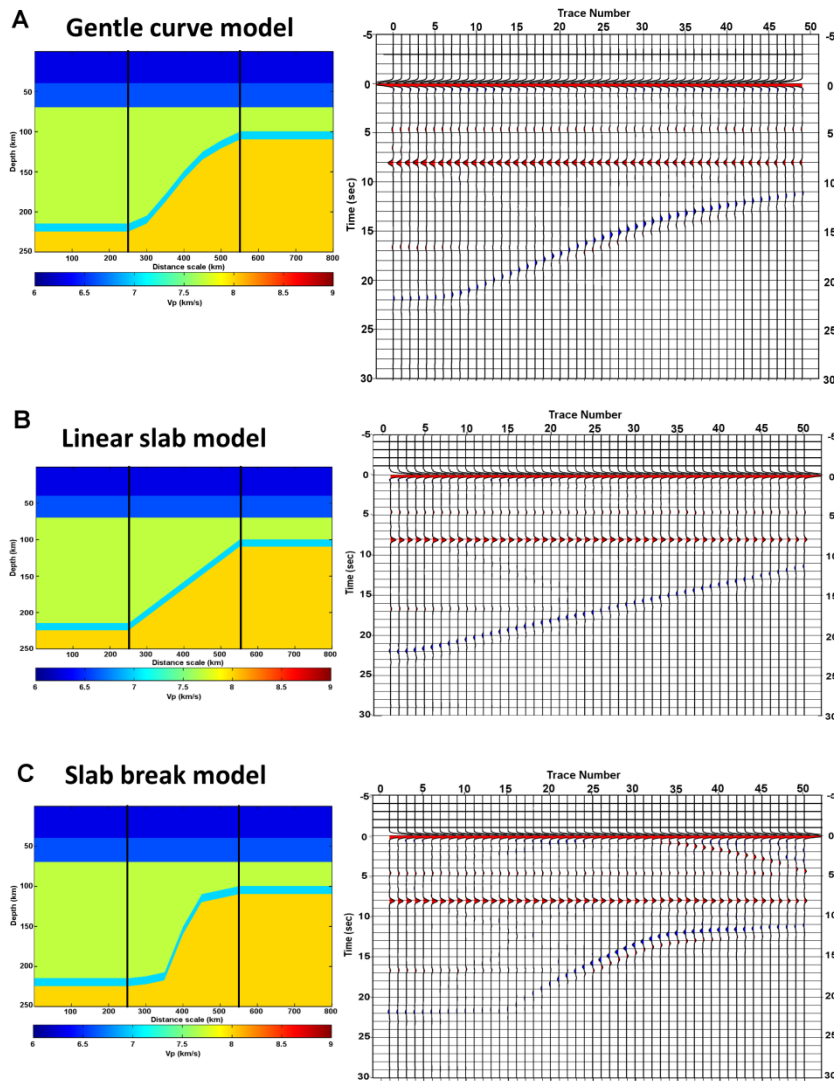


Figure B.2. Different models for Line 2, the transition from steep to shallow subduction. Three models were tested with finite difference modeling to produce synthetic receiver functions (see figure 3.3 for model used for Line 2). (A) Gently curving model comparable to figure 3.3 and resultant synthetics, (B) linear slab model and synthetics, (C) step transition from normal to flat slab subduction (as might be seen if there was a slab break) and corresponding synthetics.

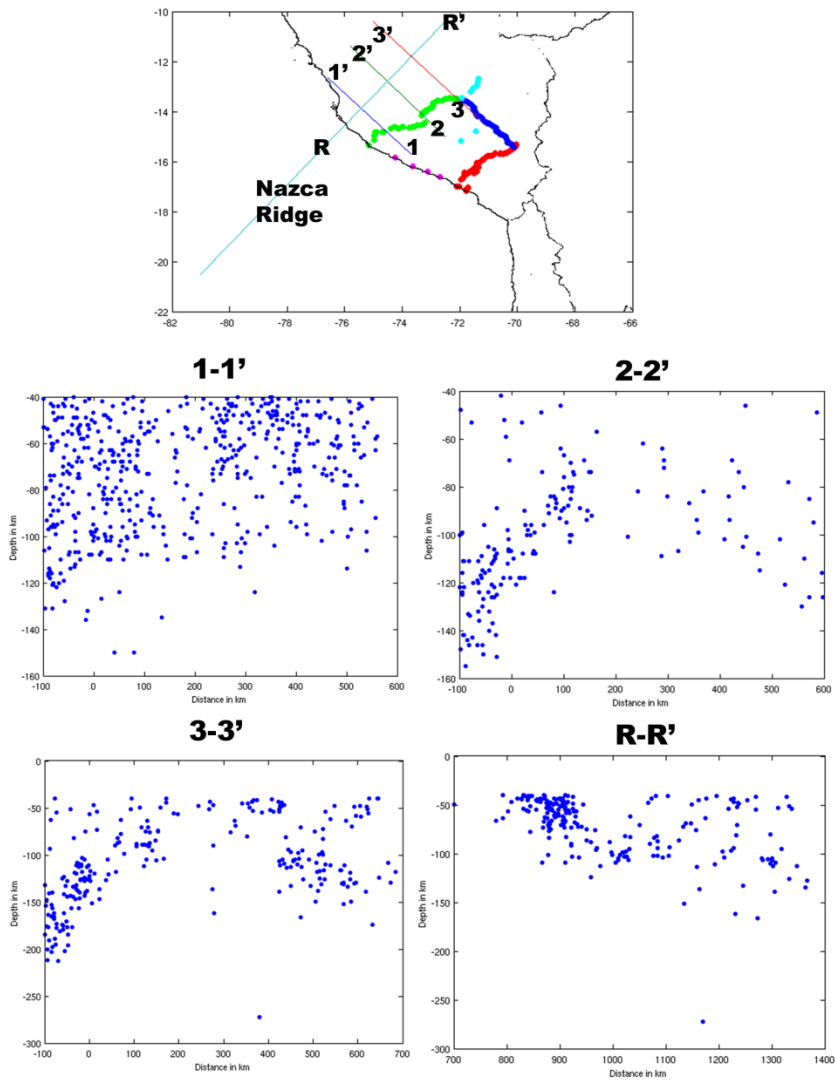
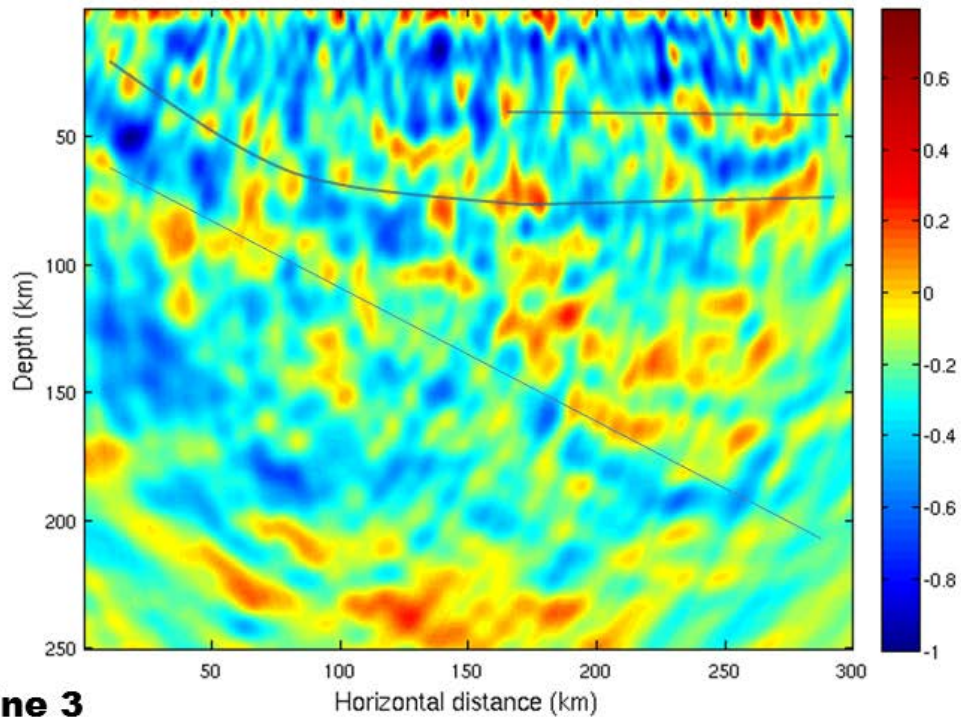
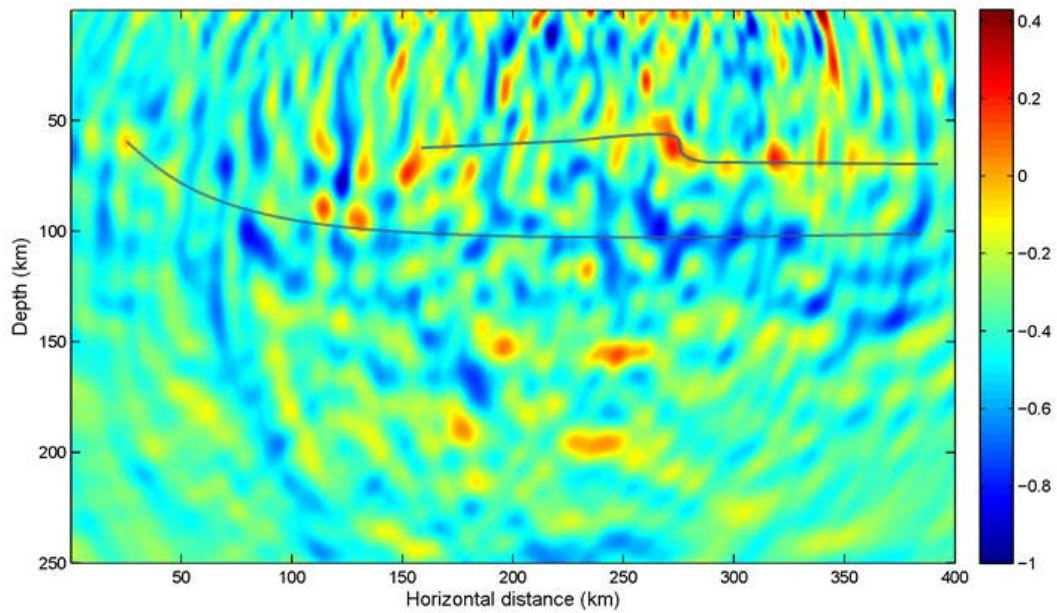
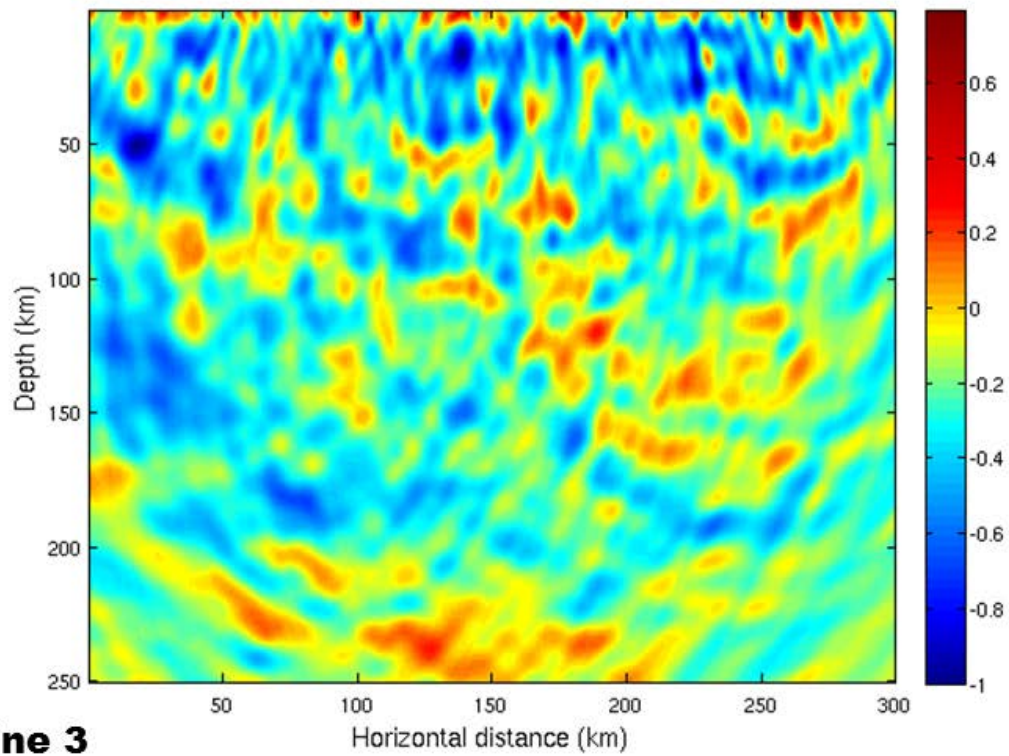
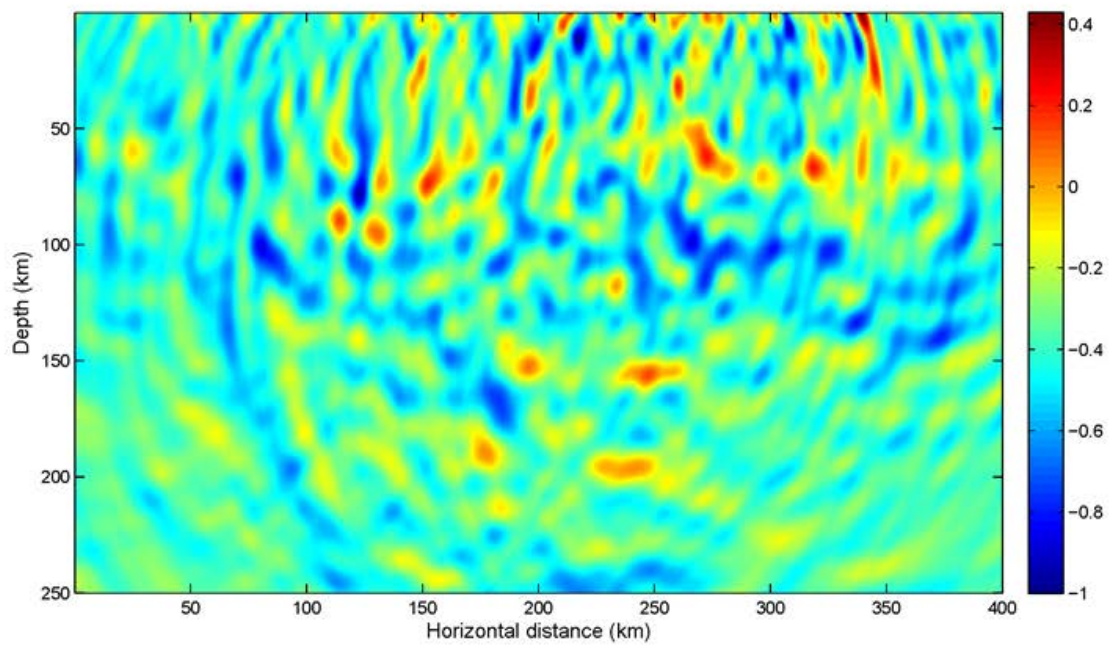


Figure B.3. Seismicity cross sections across the Nazca Ridge. Three cross sections (1-1', 2-2', and 3-3') are shown on the map. The fourth cross section (R-R') is along the trend of the ridge. Locations are from the NEIC catalog for earthquakes greater than magnitude 4 with depths greater than 40 km to avoid much of the crustal seismicity. The first cross section (1-1') closest to the coast, contains the most seismicity distributed almost evenly throughout the upper 100km. There appears to be a slight

lessening of seismicity at all depths at a distance of about 120-150km along the profile which is the approximate location of the Nazca Ridge. Profiles 2-2' and 3-3' both show a change in the seismicity from deep to shallow starting at the southernmost points of the profiles and ending at the Nazca Ridge. This is followed by a lessening of seismicity at the Ridge and slightly deeper seismicity (100-130km depth) in the flat slab region further north. The profile along the ridge shows shallow crustal seismicity near the trench and deepening to 100-120km further to the north. Other seismic catalogs were also considered (Engdahl and IGP locations) but had significantly fewer events than NEIC to recognize trends. Relocation of the events will lessen the uncertainty in depths

**Line 1****Line 3**

B.4. Migrated images of Lines 1 and 3 (Compare to migrated image of Line 2 in figure 2.5). Lines of been added to show approximate locations of structures such as slab, Moho, and mid-crustal structure.

**Line 1****Line 3**

B.5 Migrated images of Lines 1 and 3 as in figure B.4 but without any interpretive lines.

## Appendix C



Figure C.1 Photos of participants in the installation of broadband seismic equipment in Peru. Photo on the left (listed from left to right): Kristin Phillips, Emily Foote, Igor Stubailo, Steven Skinner, Jennifer Sery, and Victor Aguilar. Photo on the right: Allan Husker, Richard Guy, Igor Stubailo, and Kristin Phillips.



Figure C.2 Photos showing the process of wirelessly connecting stations for Line 1 using Yagis and parabolic antennas. Sites had to be carefully selected so that they could obtain a good signal from neighboring stations.

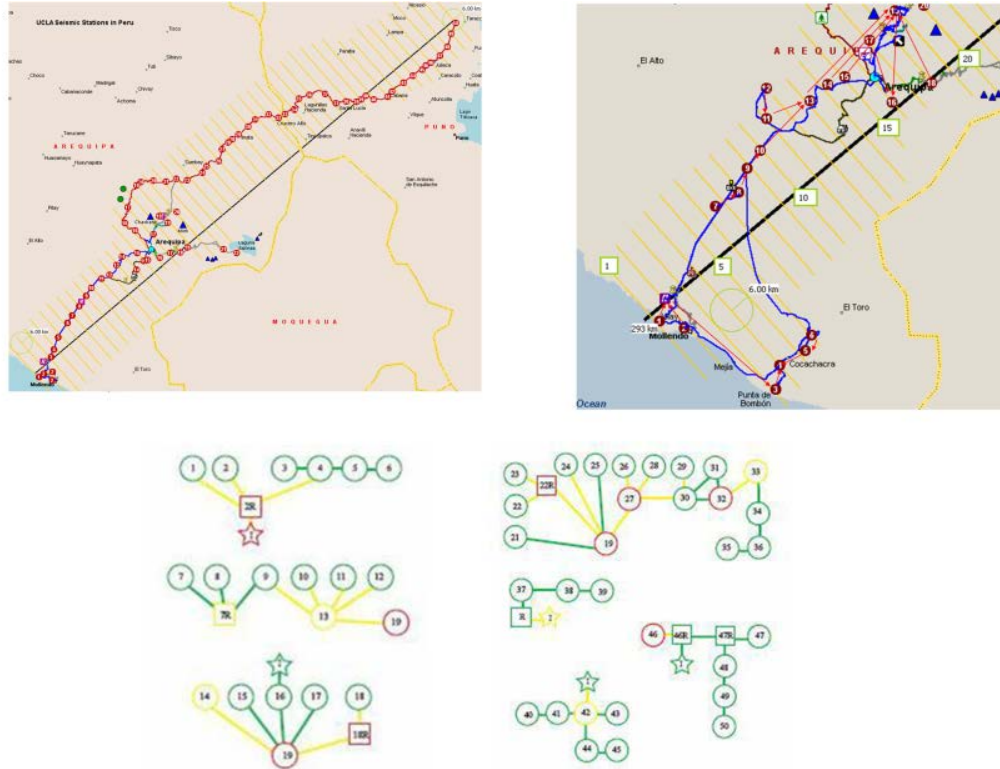


Figure C.3 Maps of the wireless connections for Line 1. The top maps show the connections in map view while the bottom figures show a link map of how all the stations are connected. Stars are locations with internet access, squares show relay sites which were put in place to help relay the signal and may not have any equipment installed, and regular sites are circles. Colors are indicative of the state of readiness of the sites at the time the link map was created (green for complete, yellow for partially complete, and red for not yet existing)



Figure C.4 Photos showing site preparation procedure for the installation of broadband stations which included digging holes for the sensor and box, installing masts for antennas and solar panels, obtaining electrical connectivity, and moving equipment.



Figure C.5 Photos show a few field challenges such as water filling boxes and holes, solar panels not generating sufficient power, and equipment which gets damaged, malfunctions, or is stolen.

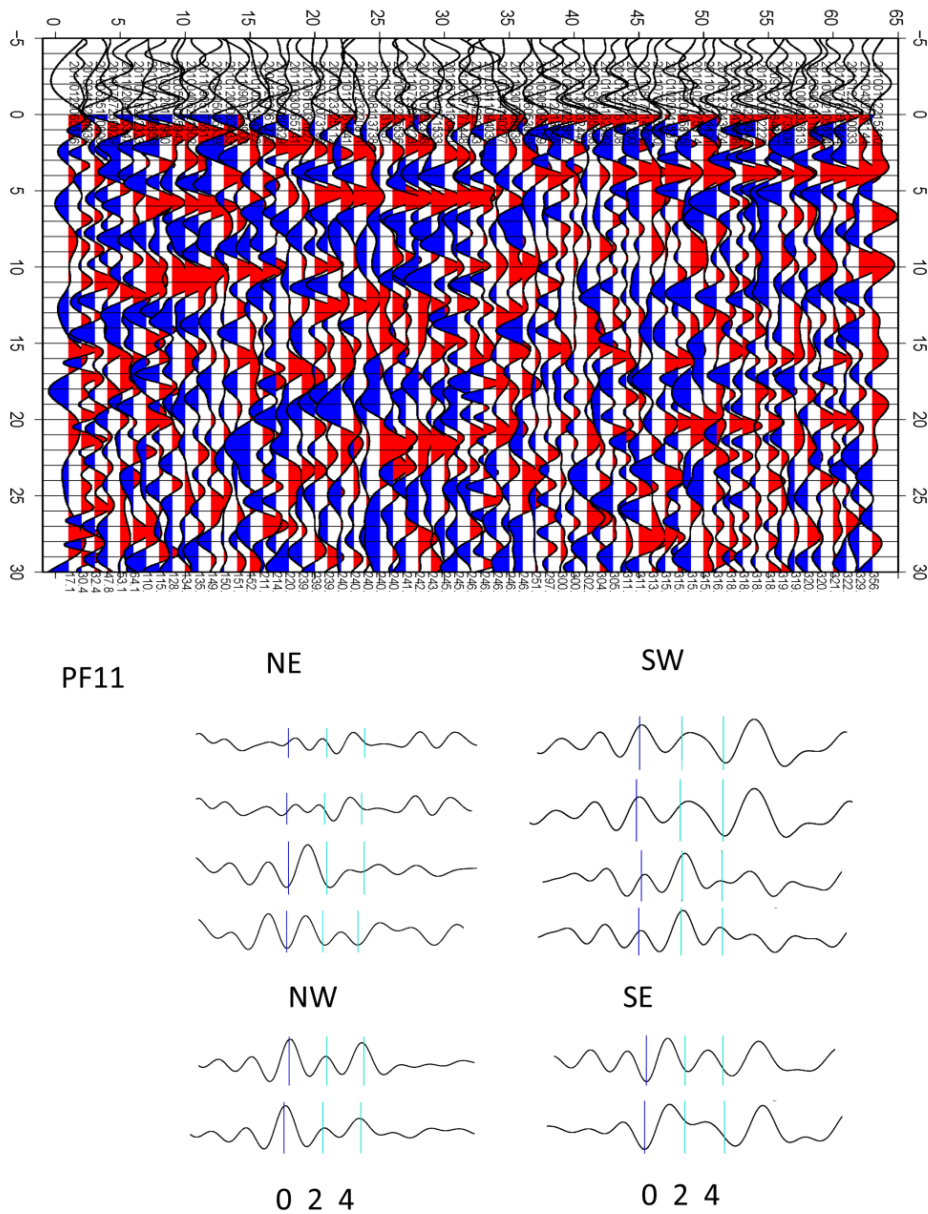


Figure C.6 Transverse receiver functions for station PF11 (Line 2) and comparison of stacks from the major azimuthal directions. Comparing the NE and SW directions, and the NW to the SE directions shows that at the times marked, the stacks from 180 degrees apart have roughly opposite polarities which may be indicative of anisotropy.

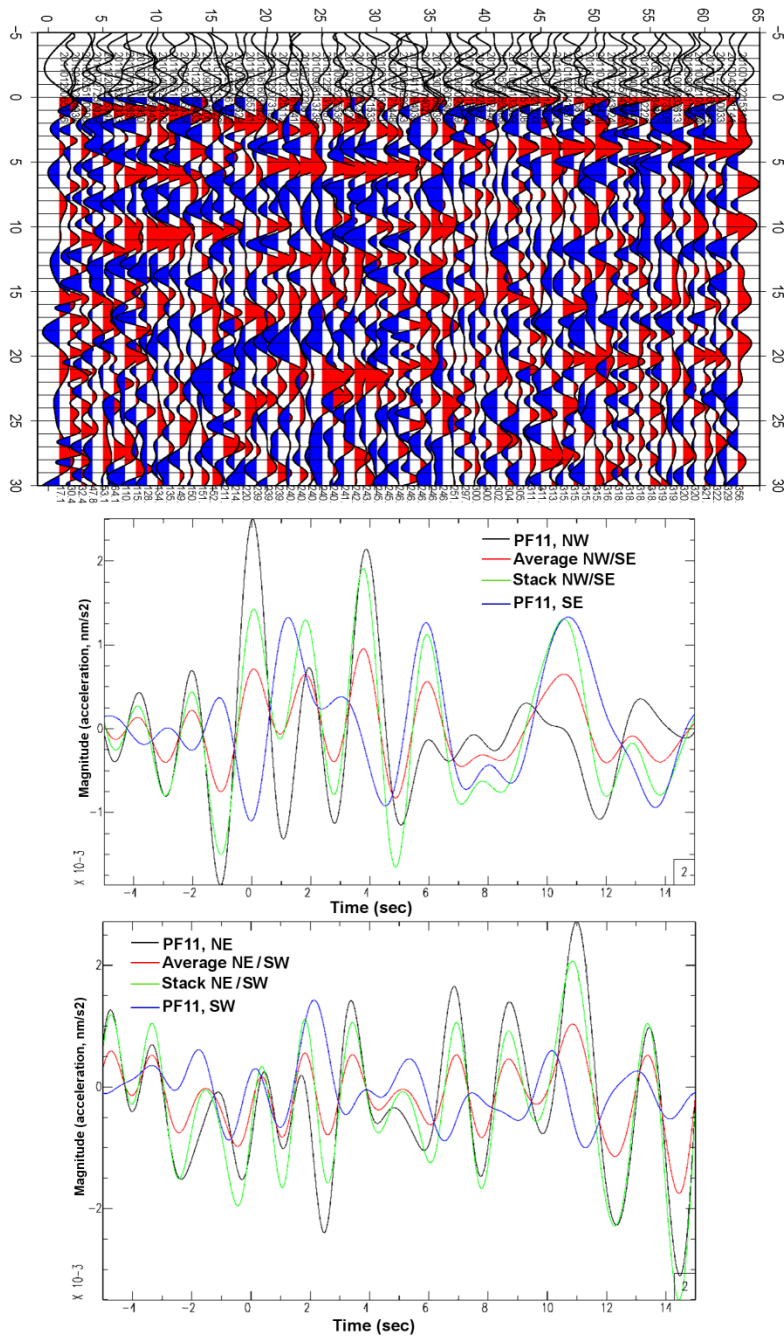


Figure C.7 Transverse receiver functions as in station PF11 (Line 2) but here showing the traces from the different directions along with their stacks and the average of the two traces.

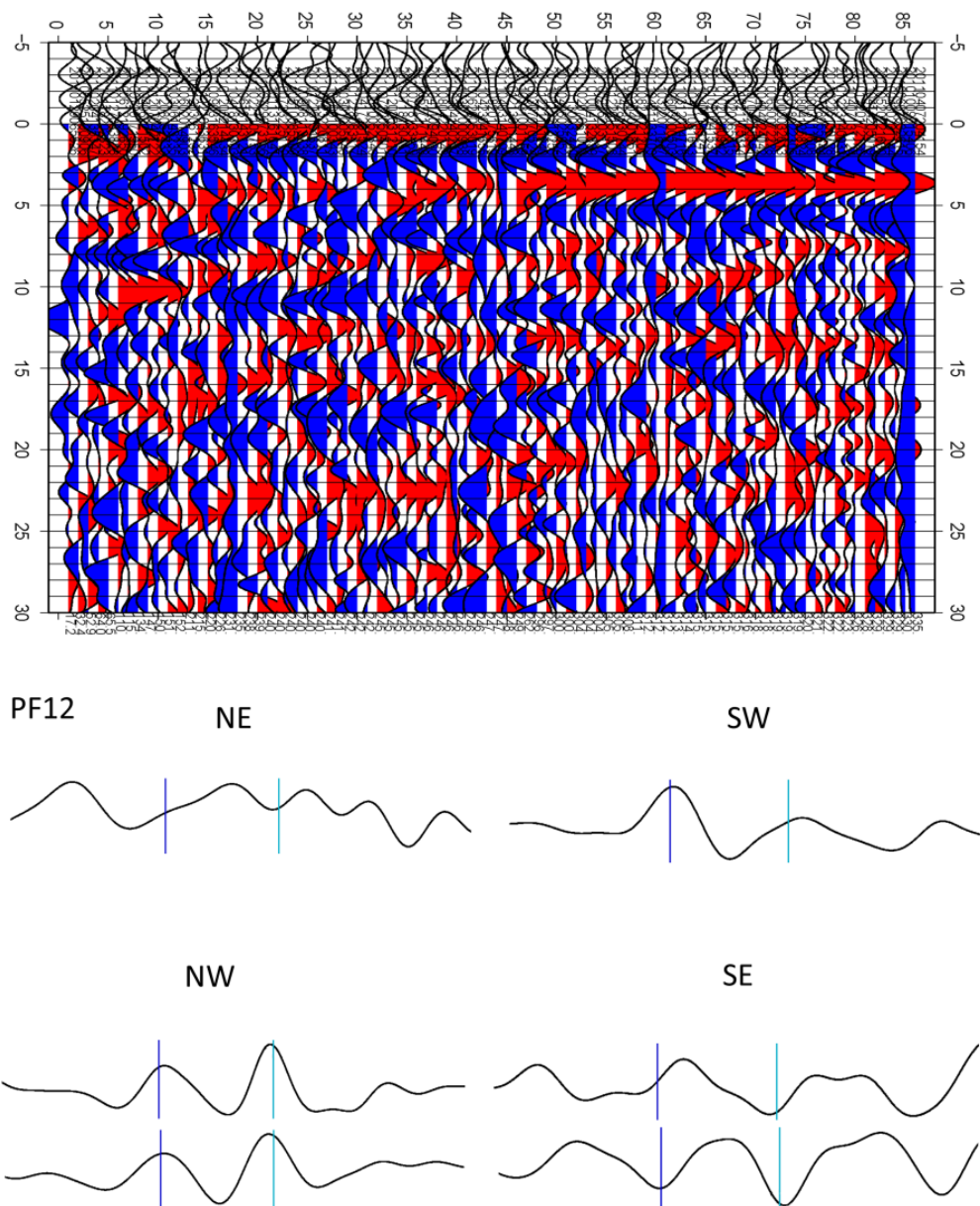


Figure C.8 Transverse receiver functions and directional stacks for station PF12 (Line 2).

Note the polarity differences between NE and SW directions and between the NW and SE directions.

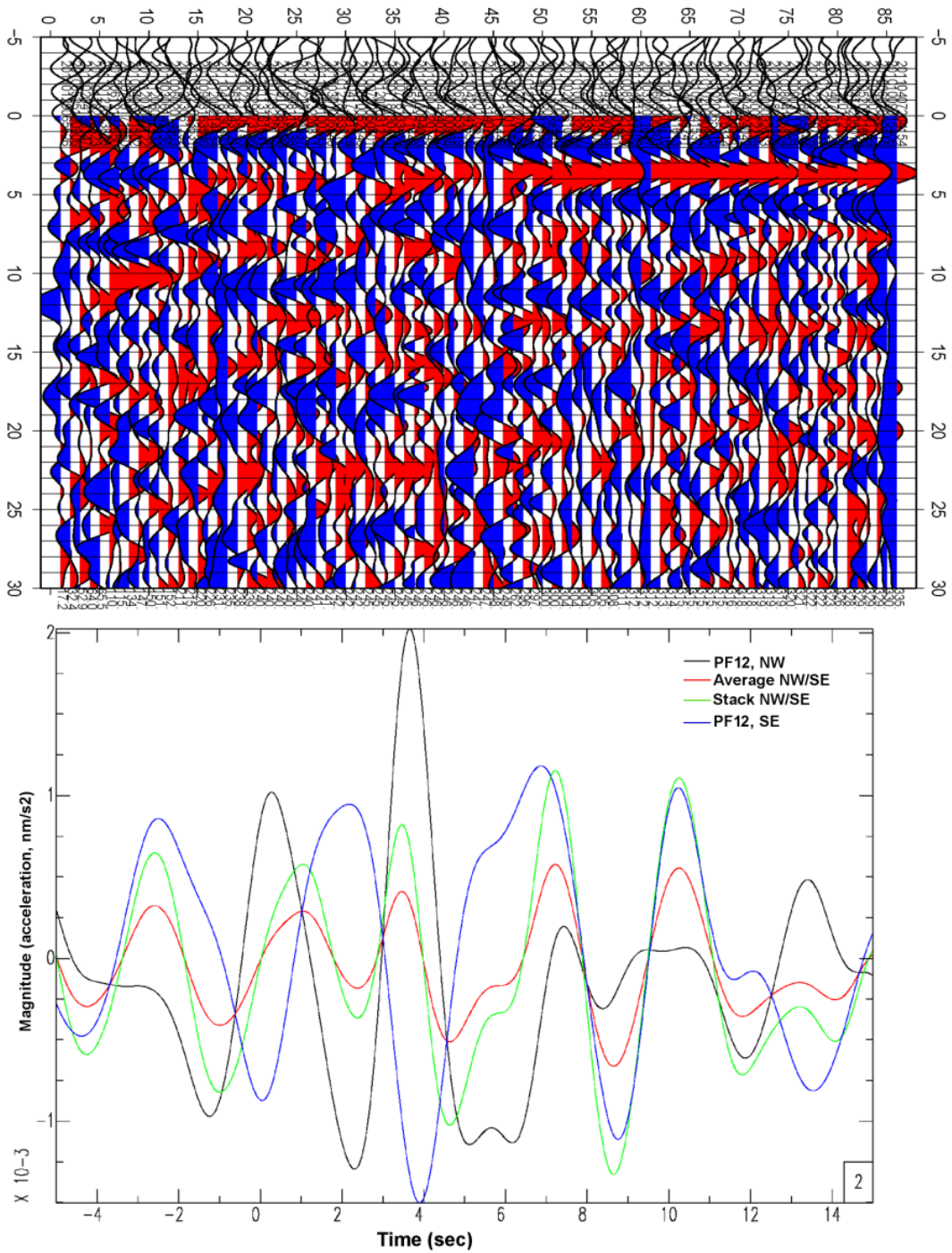


Figure C.9 Transverse RFs for station PF12 as in Figure C.8 but showing the NW and SE traces on the same scale with their stack and the average of the two.

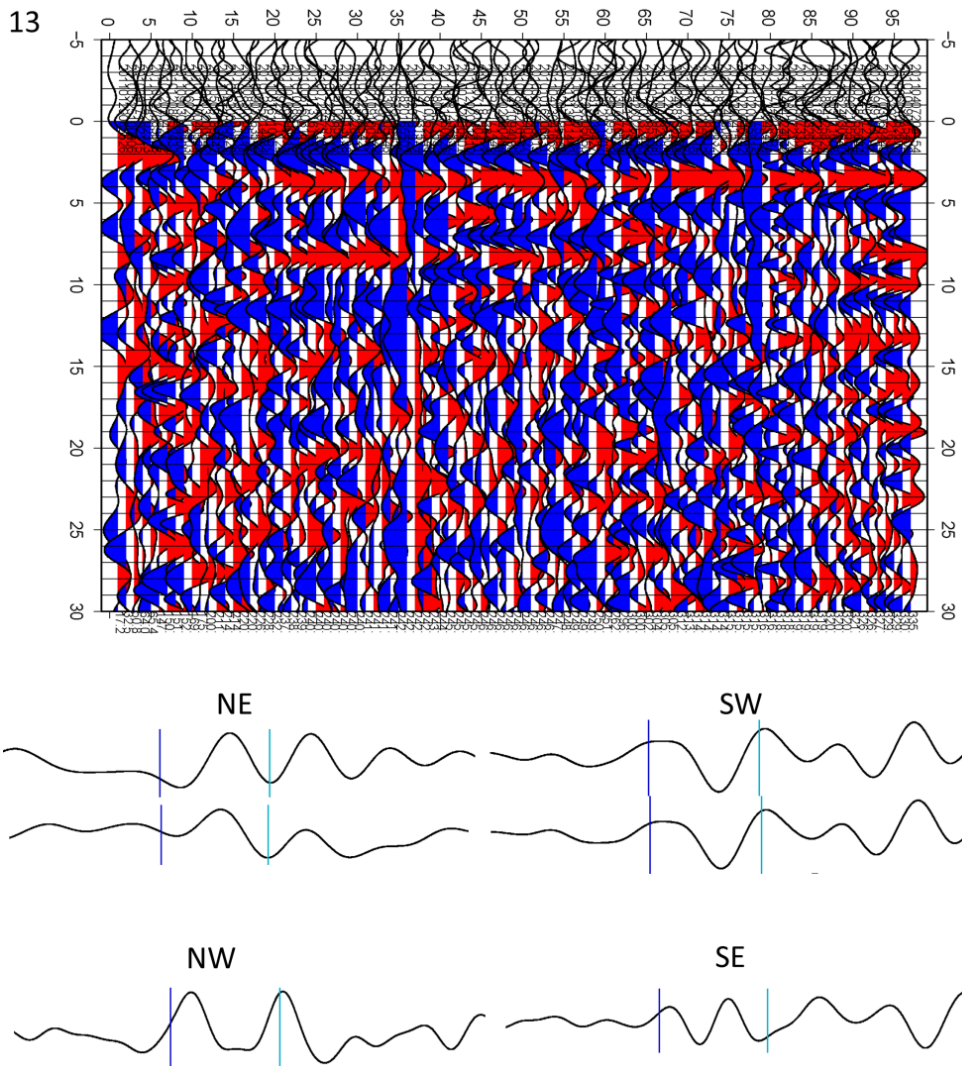


Figure C.10 Transverse RFs for PF13 (Line 2) and stacks from the major azimuthal directions. Note the polarity differences. However for the NW/SE directions, the arrival at time equals zero is of the same polarity although the second marked arrival is of opposite polarities.

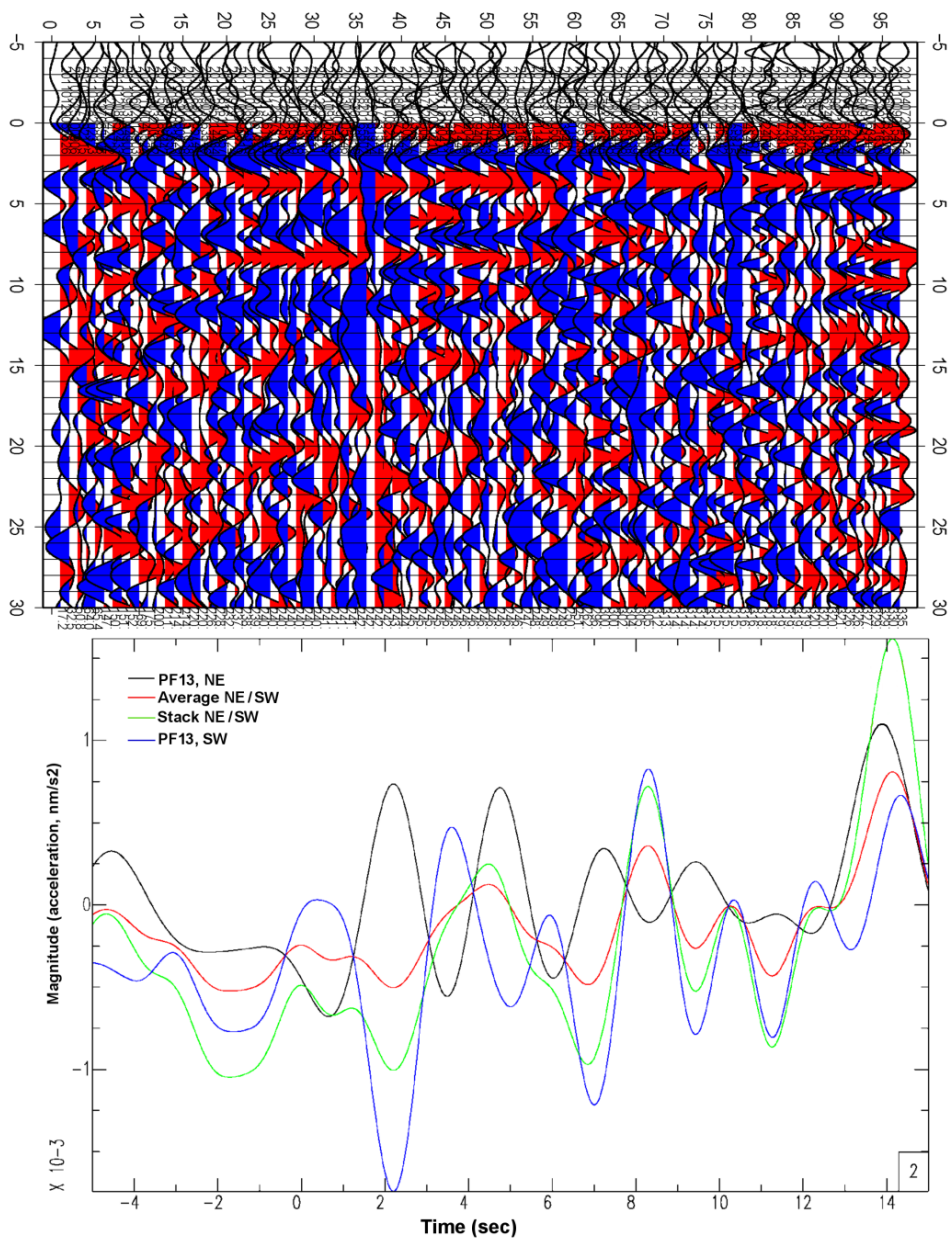


Figure C.11 Transverse RFs for PF13 with traces from the NE and SW directions plotted with their stacks and averages. Note the polarity between the NE and SW trace at about 3 seconds.

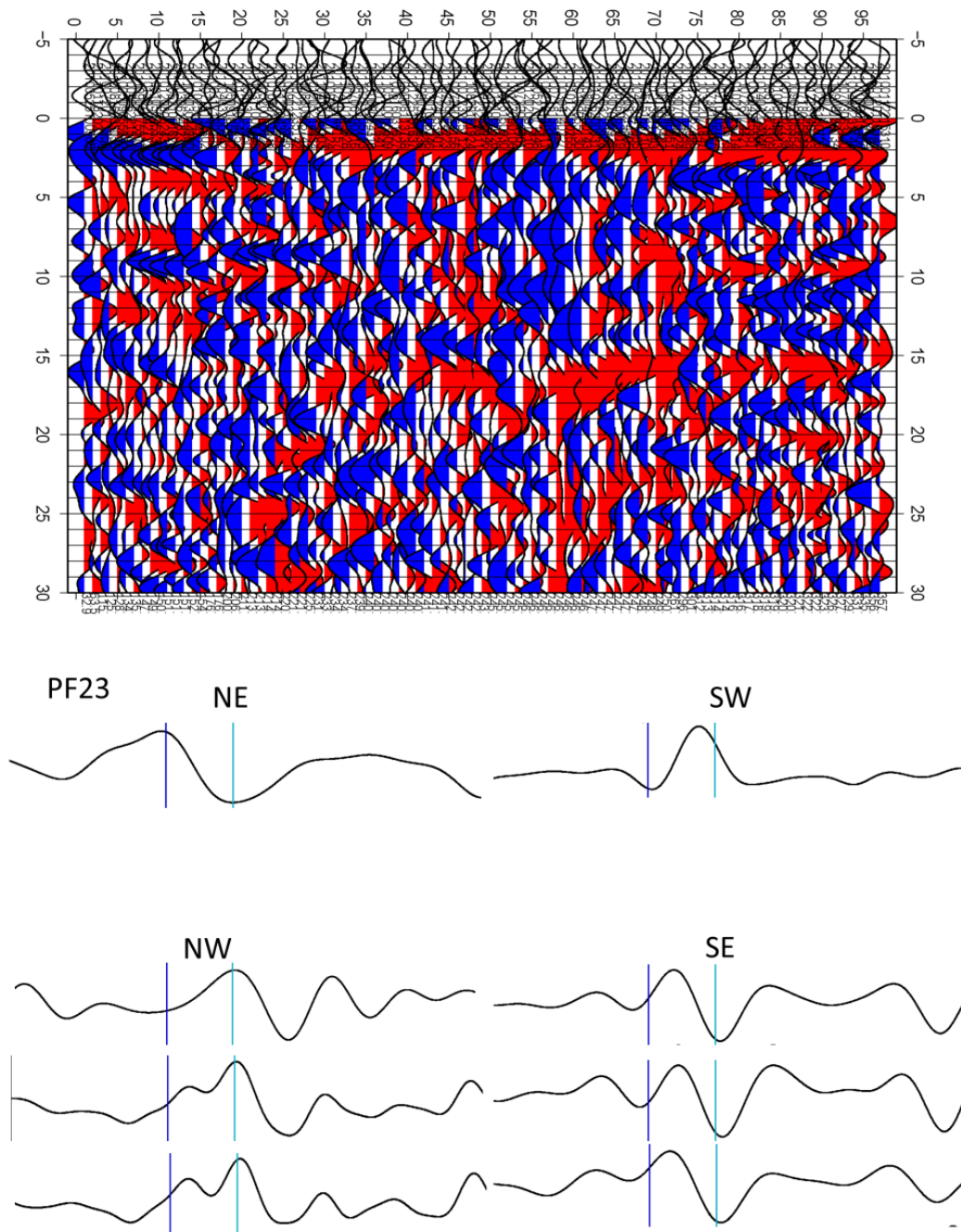


Figure C.12 Transverse RFs for PF23 (Line 2) from the major azimuthal directions.

Notice the polarity differences at about two seconds for the NE compared to SW directions and NW compared to SE directions.

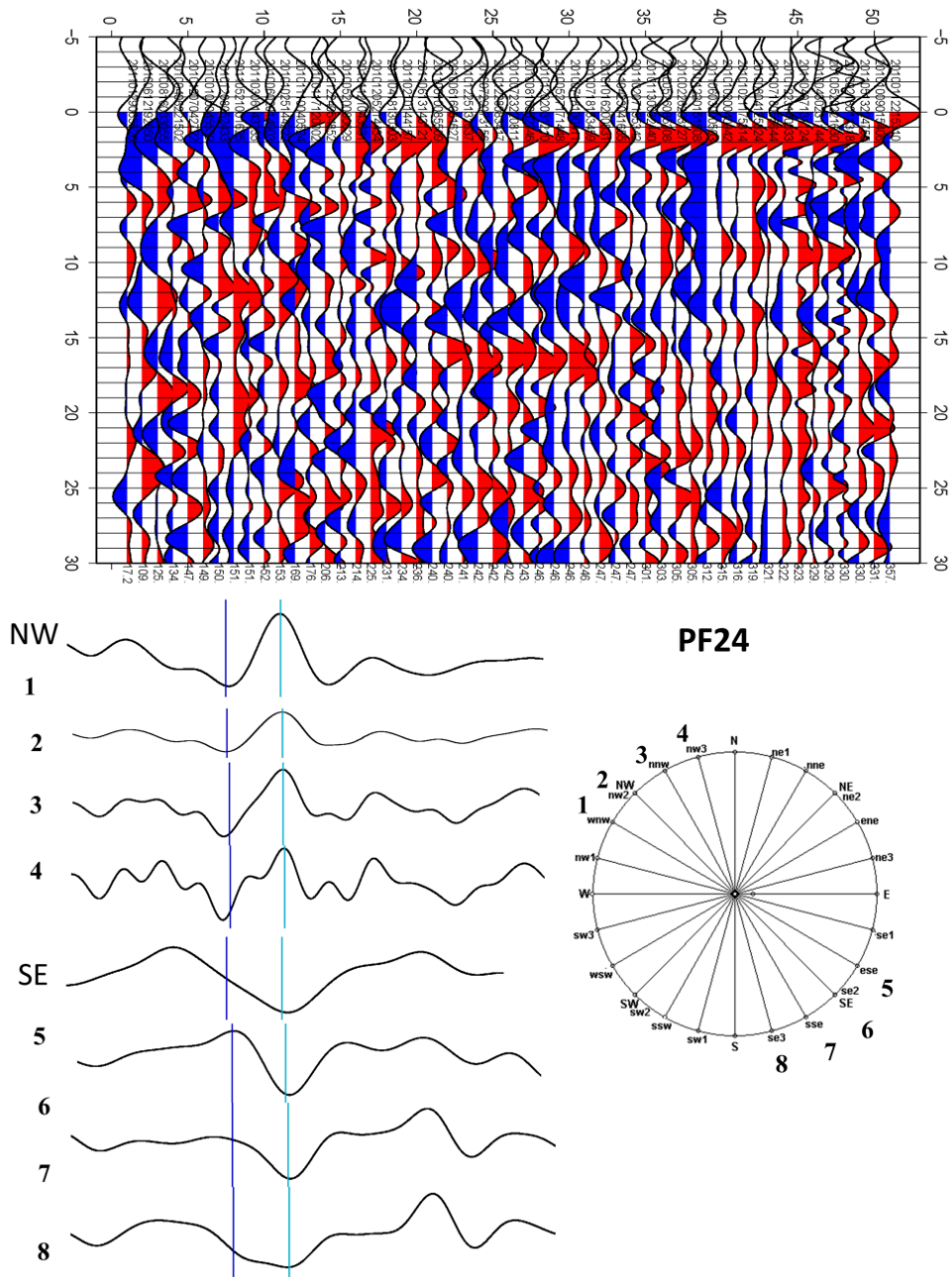


Figure C.13 Transverse RFs for station PF24 (Line 2). The circle shows the central direction that the transverse receiver functions are stacked over. The traces from 180 degrees apart are of opposite polarity at the time of the major arrival (around 2 seconds).

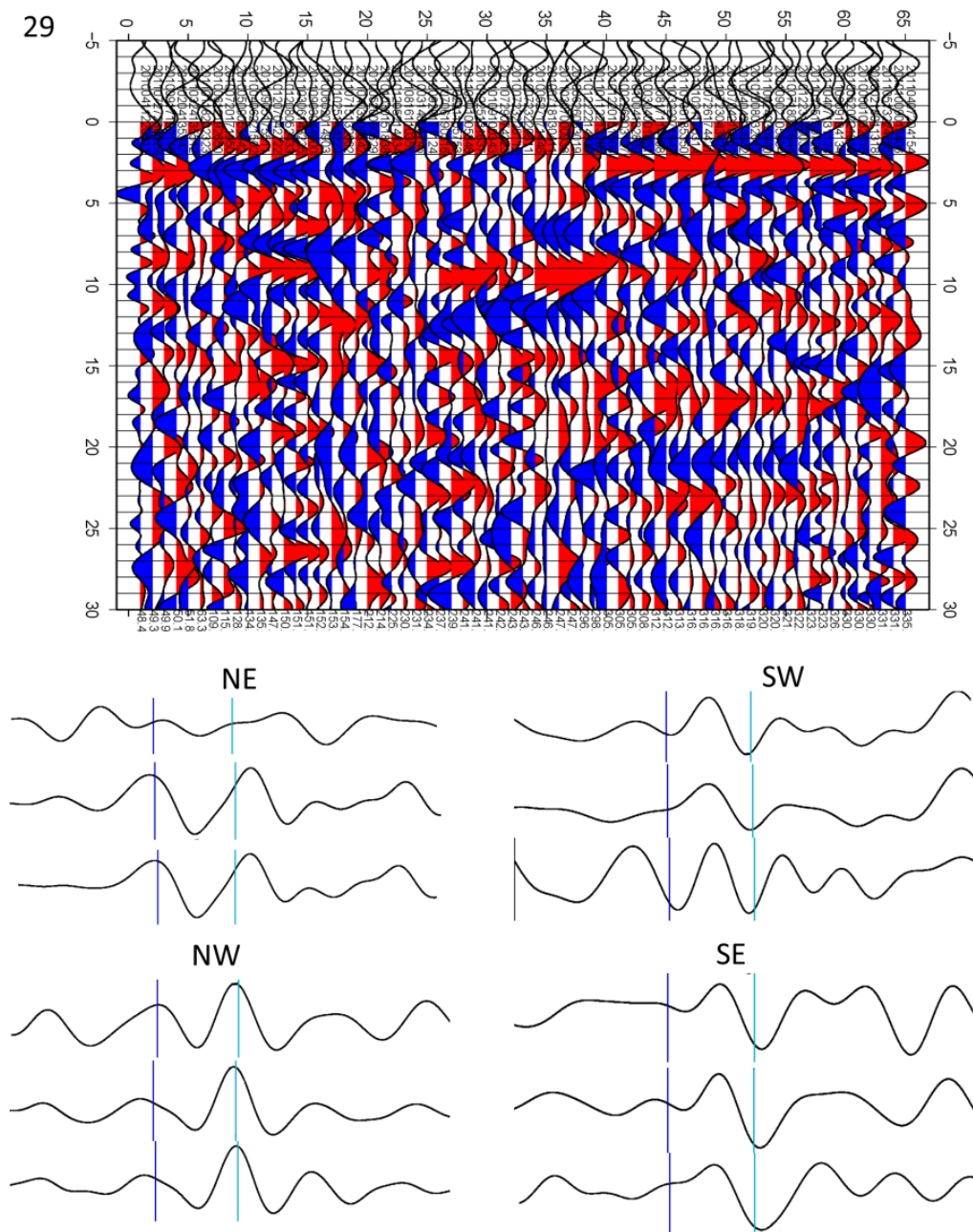


Figure C.14 Transverse RFs for stations PF29 (Line 2) and azimuthal stacks for the major directions. Note the different polarities between directions 180 degrees apart.

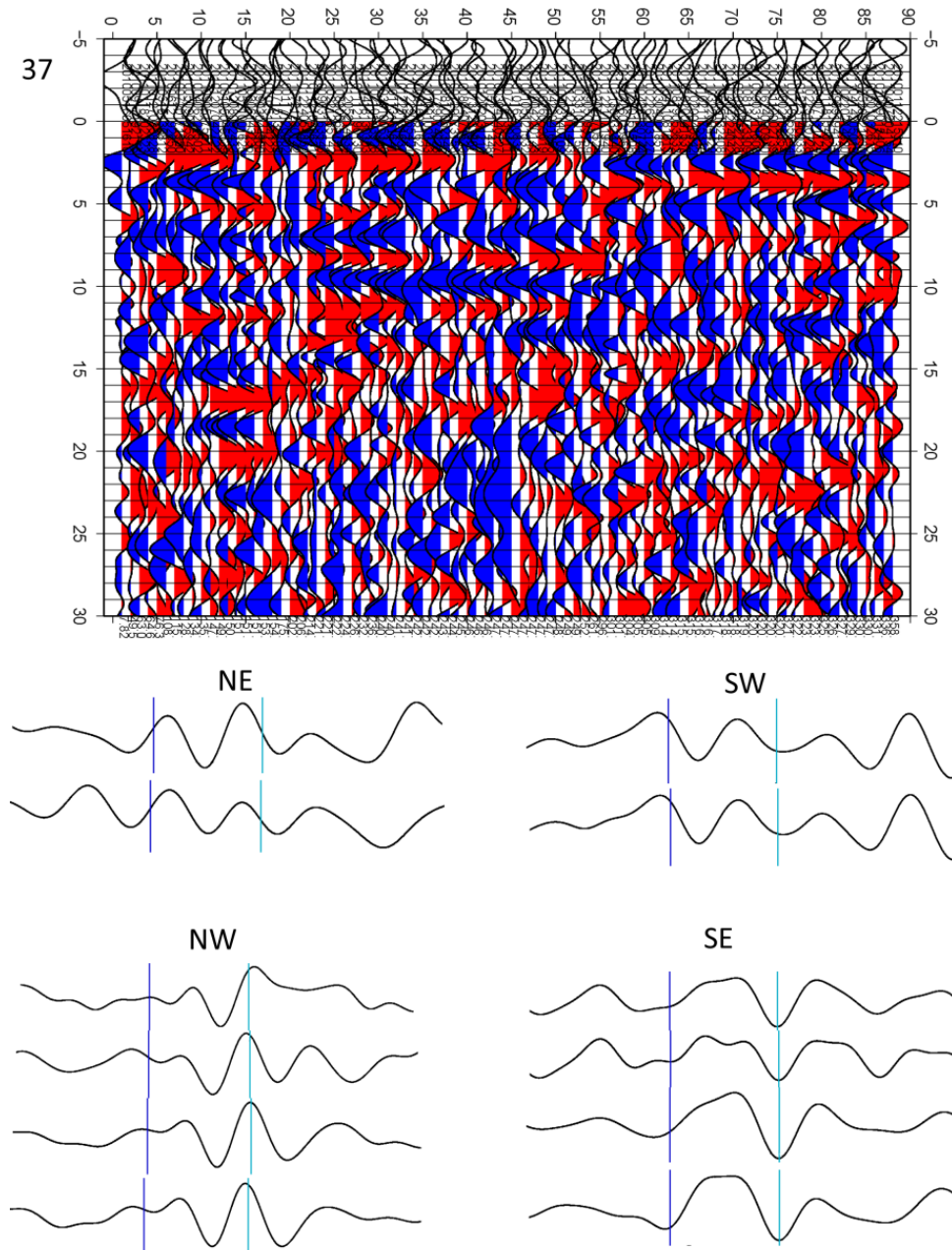


Figure C.15 Transverse RFs for station PF37 (Line 2) and stacks from the major azimuthal directions. Traces are similar for the NE/SW directions but the polarities between the NW and SE directions are opposite for the main arrival (marked by the light blue line) at about 3.5 seconds.

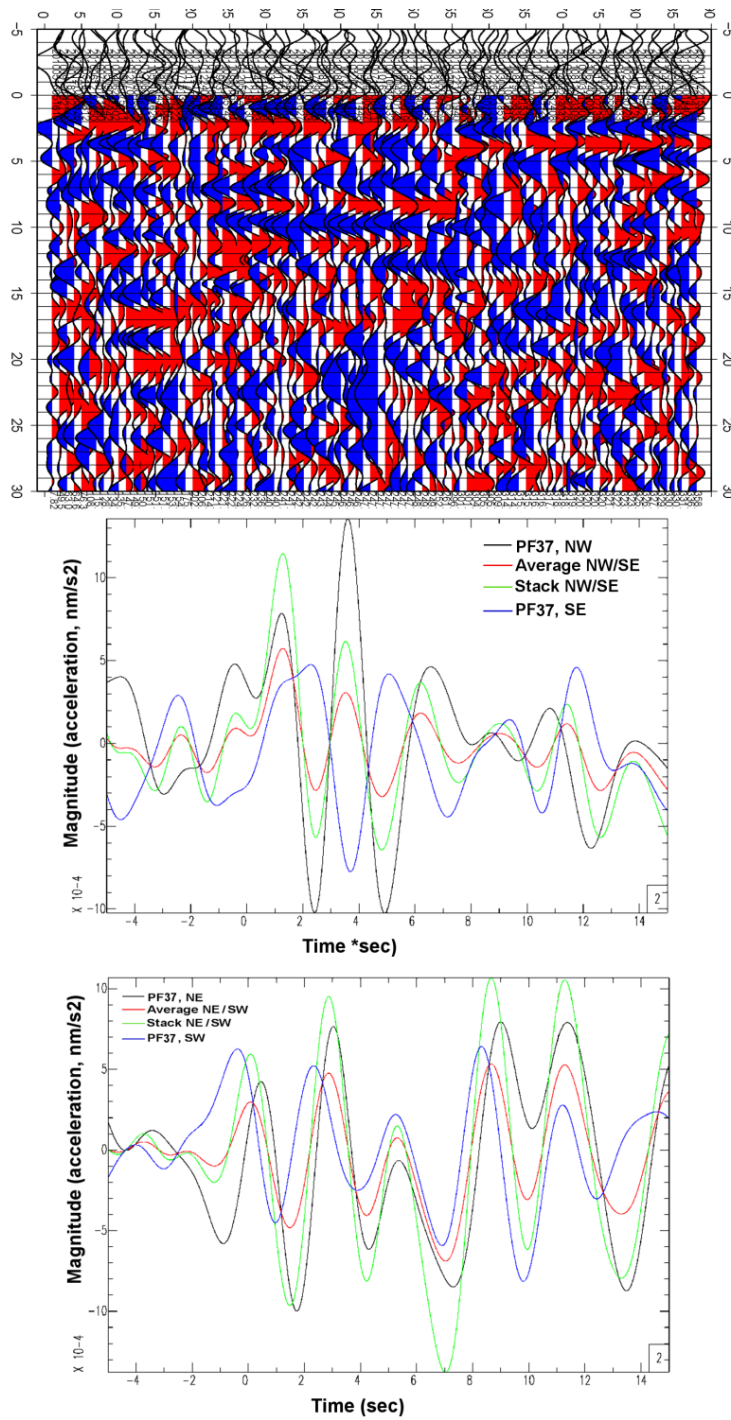


Figure C.16 Similar to figure C.15 but showing the PF37 traces from directions 180 degrees apart along with their stack and average.

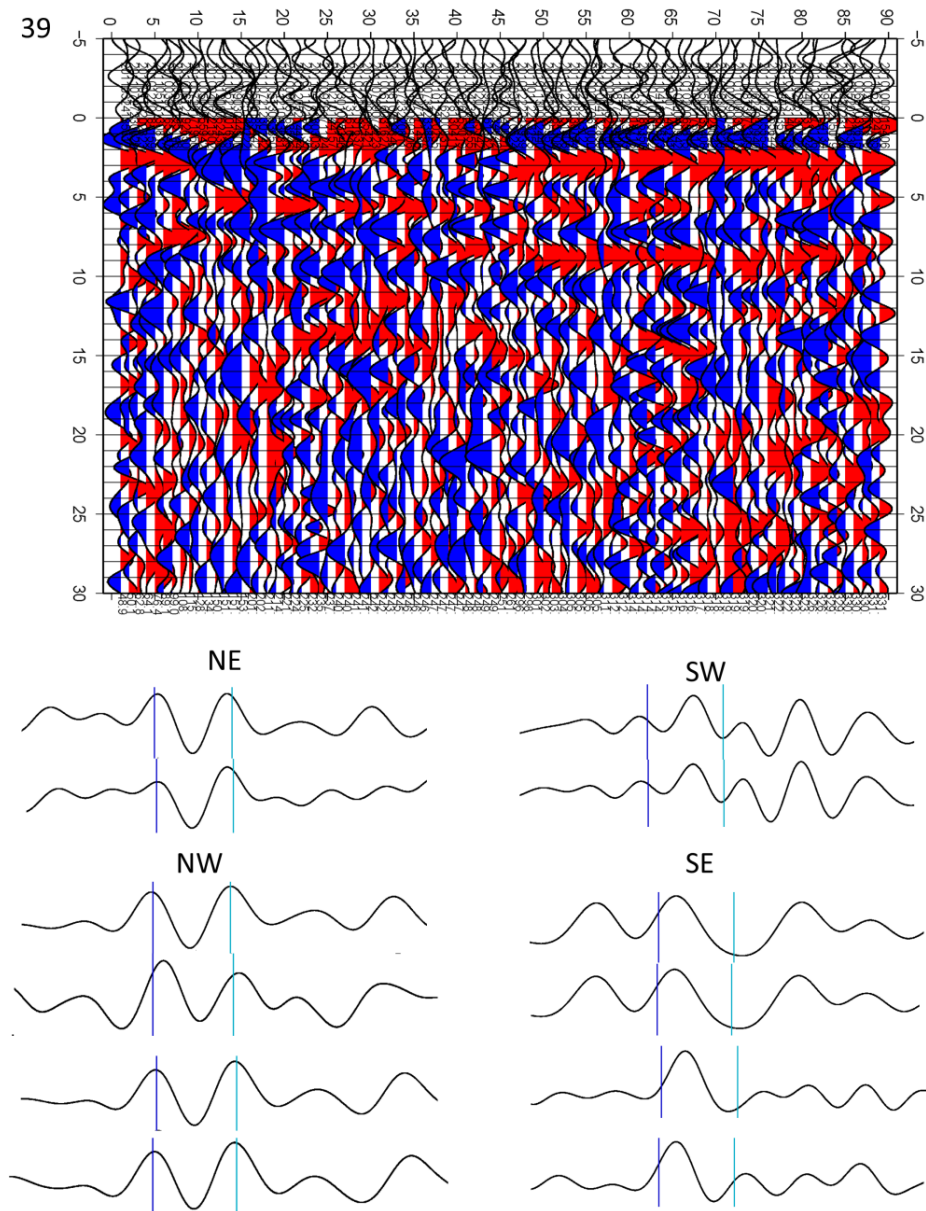


Figure C.17 Transverse RFs for station PF39 (Line 2) and stacked traces from the major azimuthal directions. The largest arrival (marked in light blue) appears to be of opposite polarity for transverse RFs 180 degrees apart in azimuth.

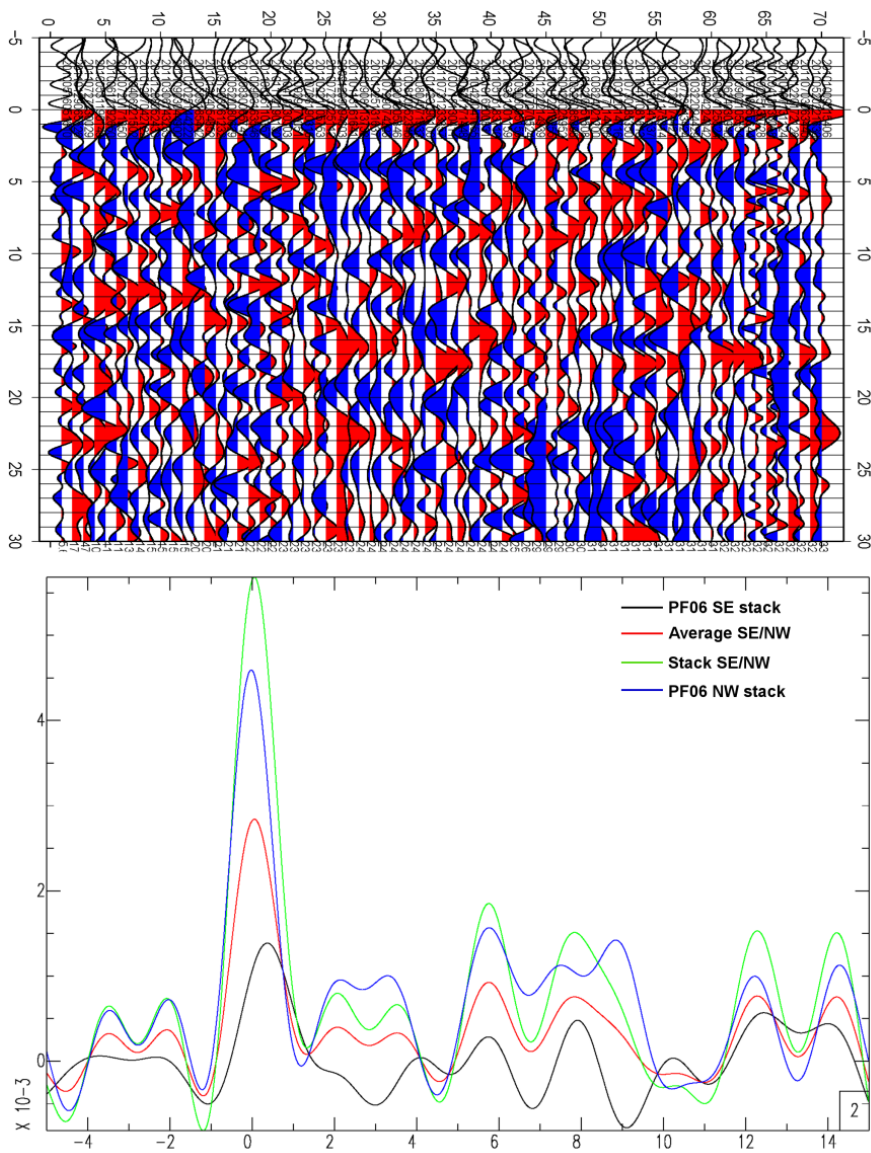


Figure C.18 Transverse RFs for PF06 (Line 2). Traces 180 degrees apart (SE and NW) appear to be in phase in contrast with the nearest station (see figure C.19) and many other stations in the array.

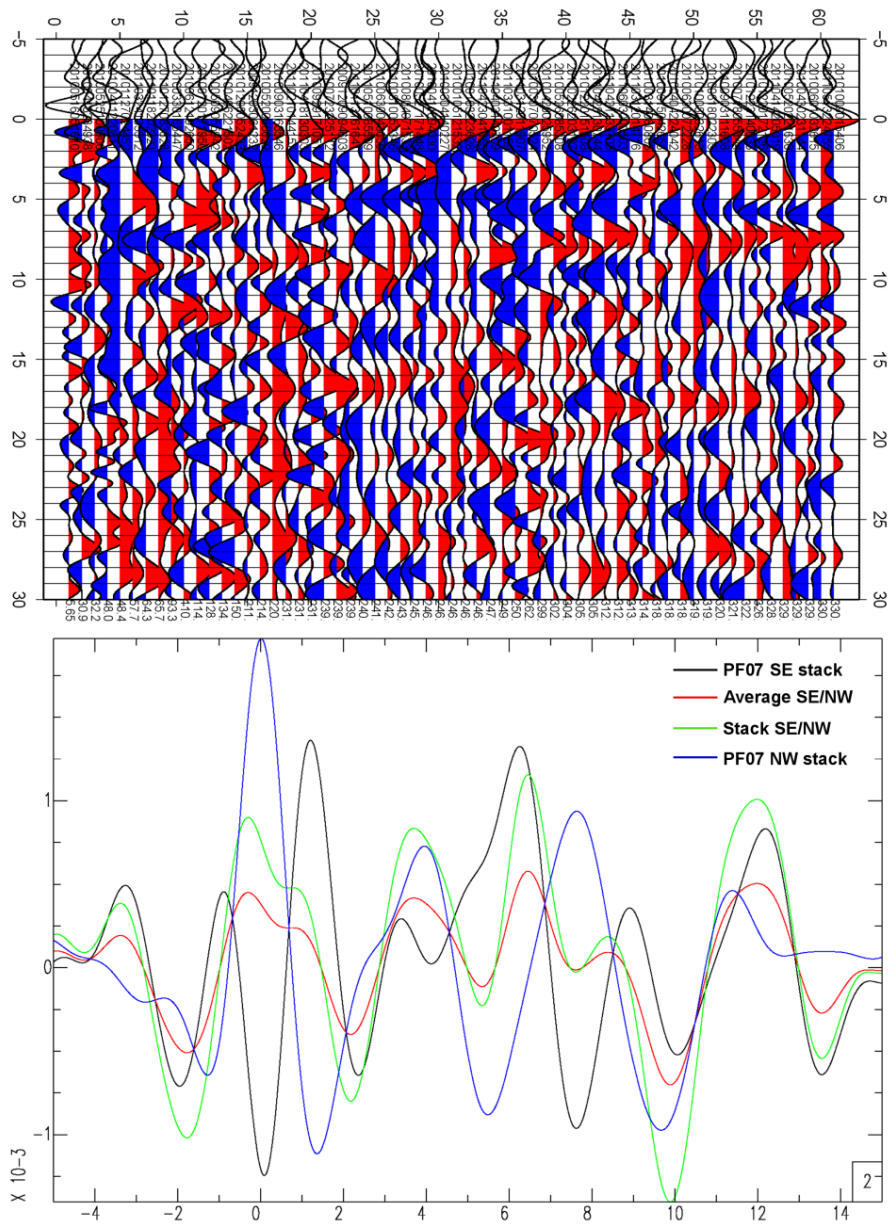


Figure C.19 Transverse RFs for station PF07 (Line 2) along with traces from the SE and NW directions shown with their average and stack. Major arrivals appear to be of opposite polarity.

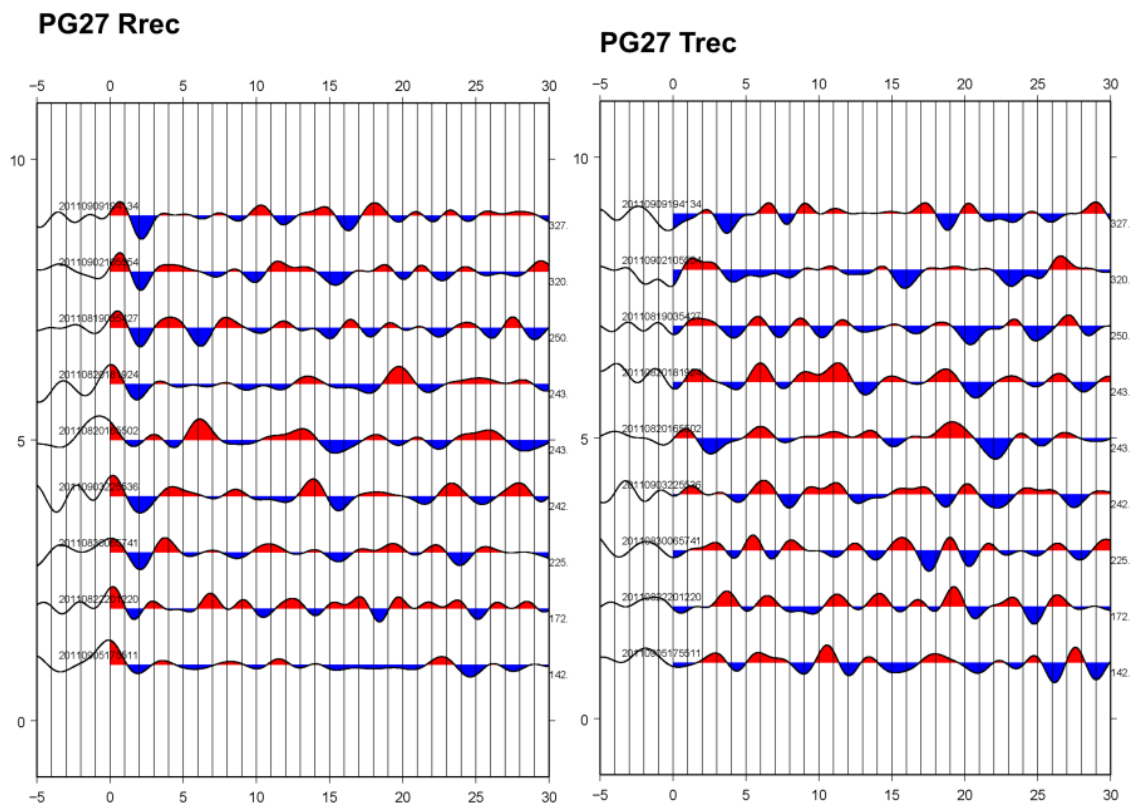


Figure C.20. Comparison of radial and transverse receiver functions for station PG27

(Line 3).

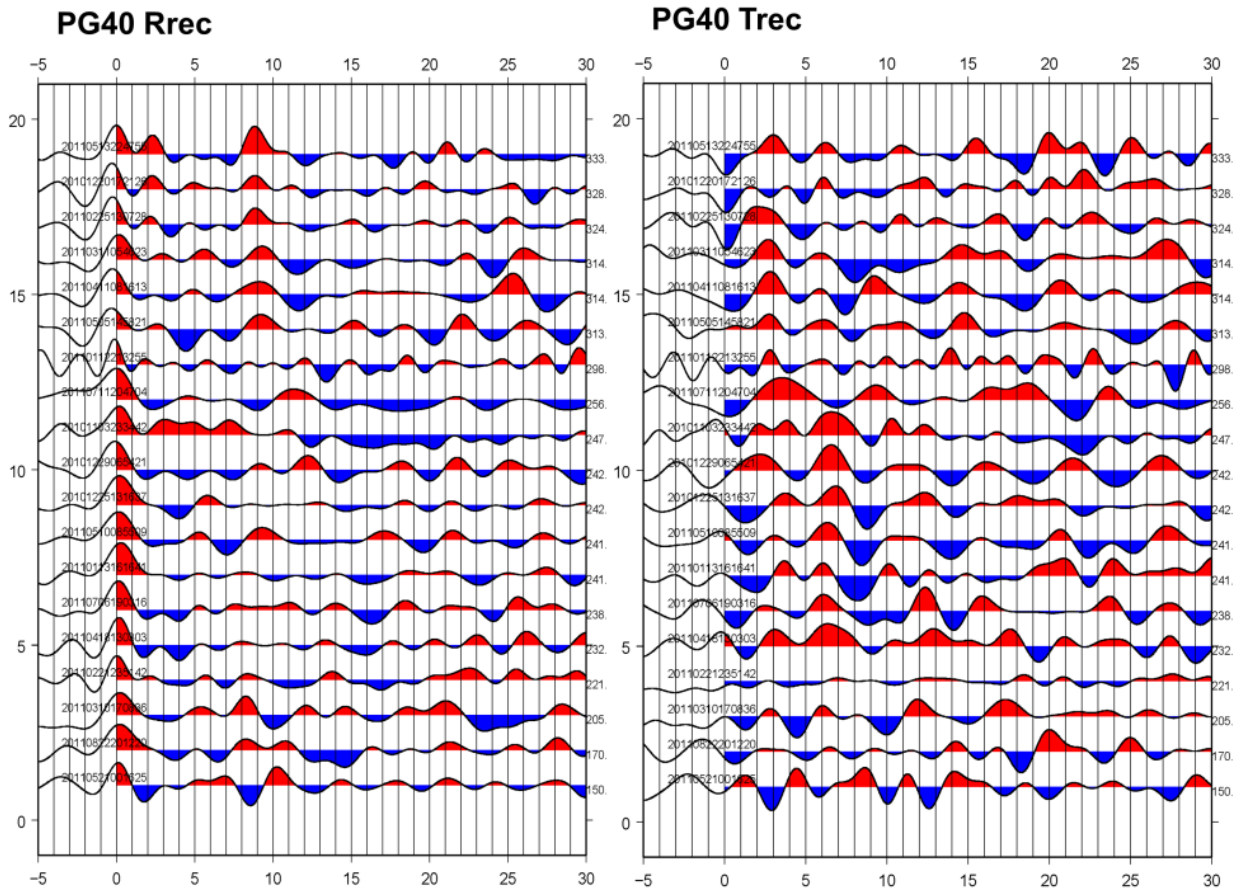


Figure C.21. Radial and transverse RFs for station PG40 (Line 3). Arrivals on the transverse receiver function do not appear to vary by azimuth which may indicate a dip or dipping symmetry axis of anisotropy.

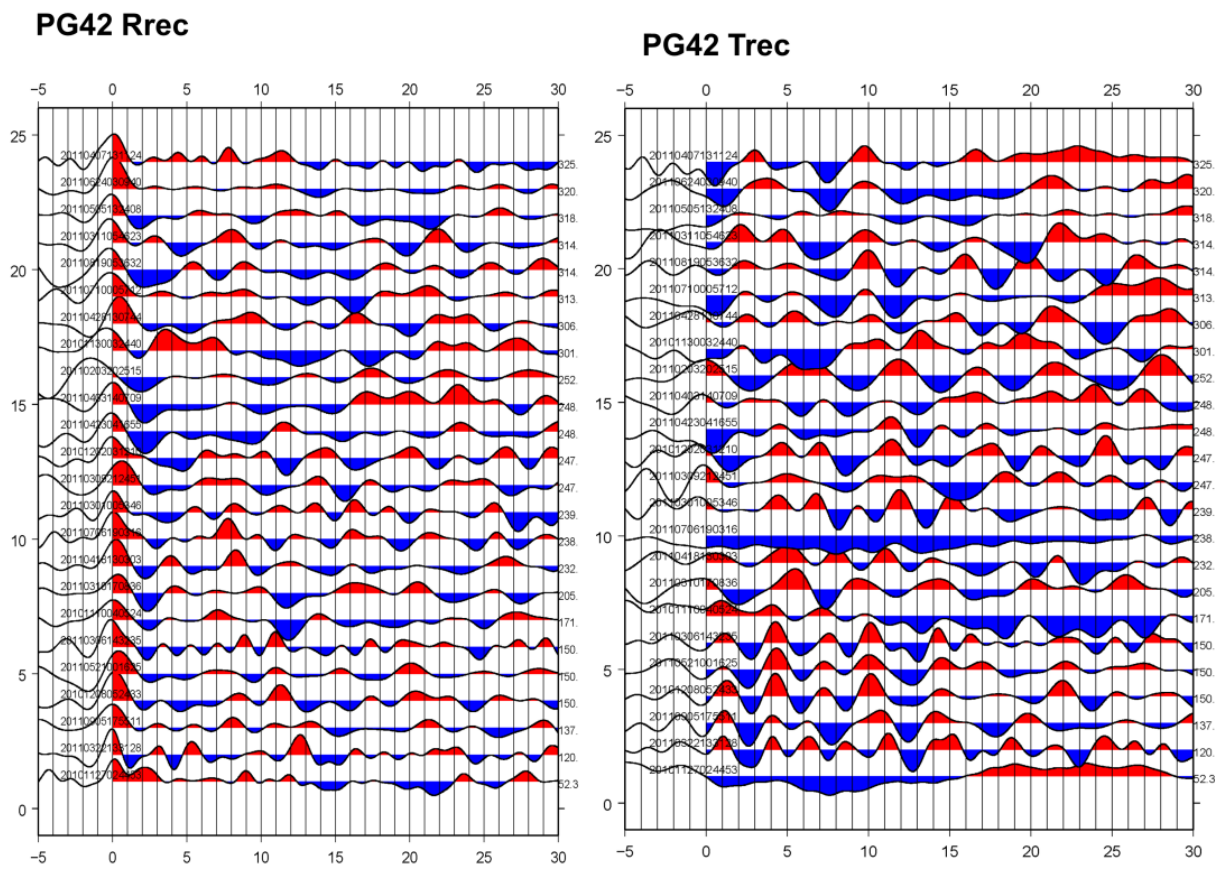


Figure C.22. Radial and transverse receiver functions for station PG42 (Line 3).

11/22/2011, Line 1, bandpassed 2 to 100 sec

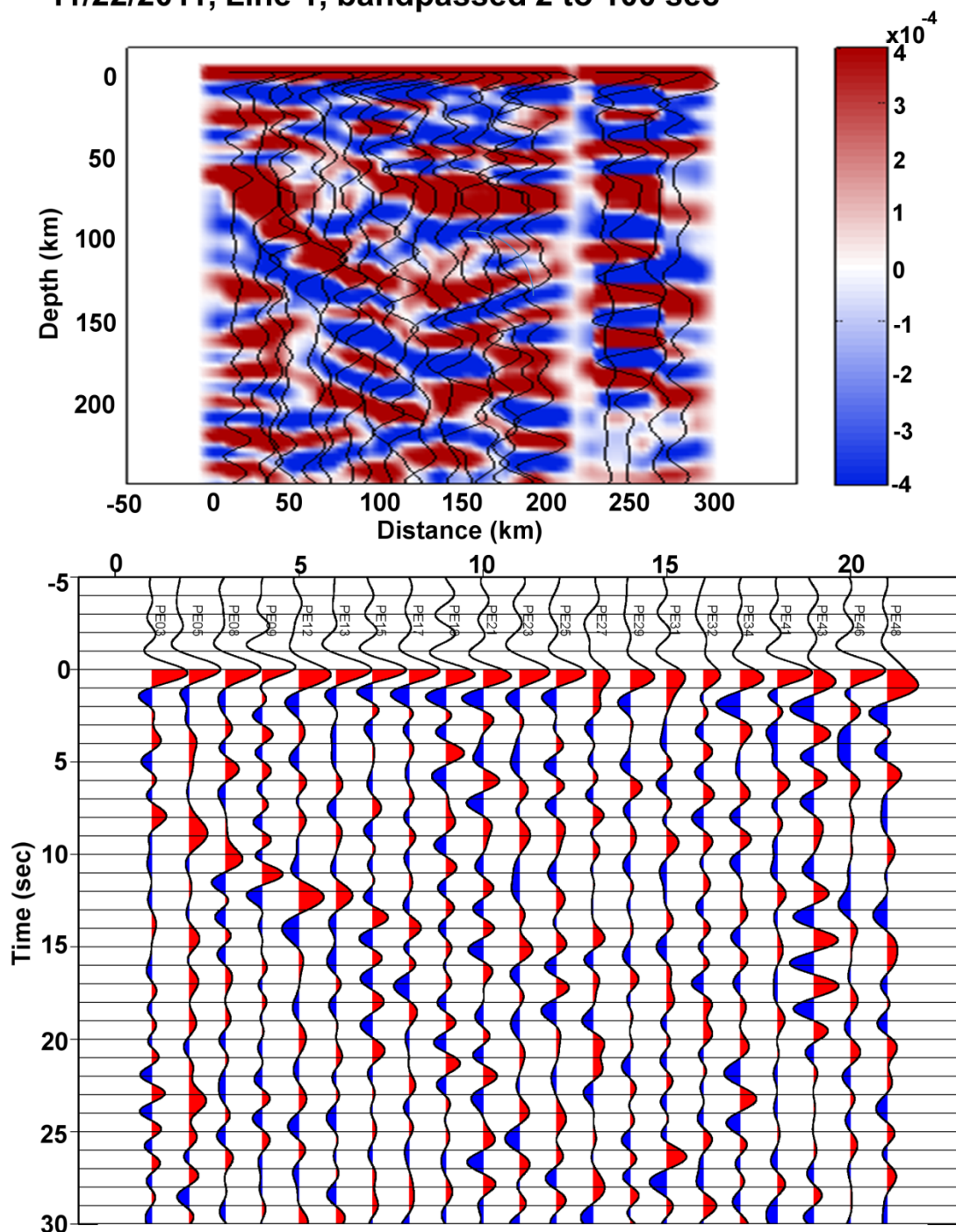


Figure C.23. Same as figure 4.28 but without interpretive lines.

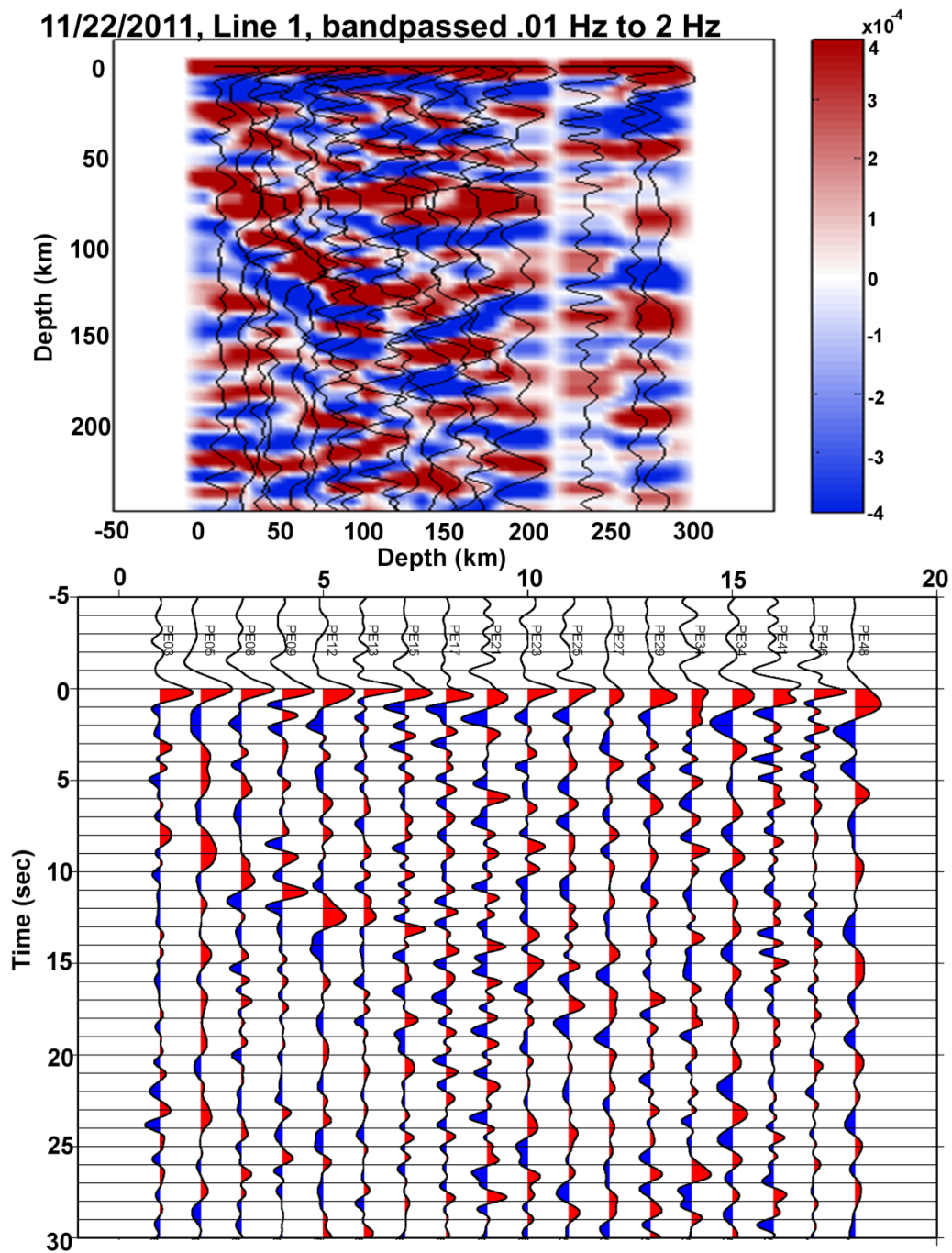


Figure C.24 Local event RF analysis, Line 1, 11/22/2011, 2 Hz bandpass, no interpretive lines (compare with figure 4.29).

## Bibliography

- Abers, G. (2000), Hydrated subducted crust at 100-250 km depth, *Earth and Planet. Sci. Lett.*, 176, 323-330.
- Abers, G., P. van Keken, E. Kneller, A. Ferris, & J. Stachnik (2006), The thermal structure of subduction zones constrained by seismic imaging: Implications for slab dehydration and wedge flow, *Earth and Planet. Sci. Lett.*, 241, 387-397.
- Ahrens, T.J., and G. Schubert (1975). Gabbro-Eclogite Reaction Rate and Its Geophysical Significance, *Reviews of Geophysics and Space Physics*, 13 (2), 383-400
- Allmendinger, R., and T. Gubbels (1996), Pure and simple shear plateau uplift, Altiplano-Puna, Argentina and Bolivia, *Tectonophysics*, 259, 1-13.
- Allmendinger, R., T. Jordan, S. Kay, and B. Isacks (1997), The Evolution of the Altiplano-Puna Plateau of the Central Andes, *Annu. Rev. Earth Planet. Sci.*, 25, 139-174.
- Ammon, C., G. Randall, and G. Zandt (1990), On the nonuniqueness of receiver function inversions, *J. Geophys. Res.*, 95 (B10), 15,303-15,318.
- Ammon, C., (1991), The isolation of receiver effects from teleseismic P waveforms, *Bull. Seismo. Soc. Am.*, 81, 6, 2504-2510.
- Anderson, M., P. Alvarado, G. Zandt, & S. Beck (2007), Geometry and brittle deformation of the subducting Nazca Plate, Central Chile and Argentina, *Geophys. J. Int.*, 171, 419-434.
- Assumpção, M., M. Feng, A. Tassara, J. Julià (2012), Developing Models of Crustal Thickness for South America from Receiver Functions and Surface Wave Tomography, *Tectonophysics*, in review/press
- Babeyko, A., and S. Sobolev (2005), Quantifying different modes of the late Cenozoic shortening in the central Andes, *Geology*, 33 (8), 621-624.
- Barazangi, M., and B. L. Isacks (1976), Spatial distribution of earthquakes and subduction of the Nazca plate beneath South America, *Geology*, 4, 686-692.
- Barnes, J., and T. Ehlers (2009), End member models for Andean Plateau uplift, *Earth-Science Reviews*, 97 (105-132).
- Baumont, D., A. Paul, S. Beck, and G. Zandt (1999), Strong crustal heterogeneity in the Bolivian Altiplano as suggested by attenuation of Lg waves, *J. of Geophys. Res.*, 104 (B9), 20,287-20,305.
- Baumont, D., A. Paul, G. Zandt, & S.L. Beck (2001), Inversion of Pn travel times for lateral variations of Moho geometry beneath the Central Andes and comparison with the receiver functions, *Geophys. Res. Lett.*, 28 (9), 1663-1666
- Beate, B., M. Monzier, R. Spikings, J. Cotton, J. Silva, E. Bourdon & J. Eissen (2001), Mio-Pliocene adakite generation related to flat subduction in southern Ecuador: the Quimsacocha volcanic center, *Earth and Planet. Sci. Lett.*, 192, 561-570.
- Beck, S., G. Zandt, S. Myers, T. Wallace, P. Silver, and L. Drake (1996), Crustal-thickness variations in the central Andes, *Geology*, 24 (5), 407-410.
- Beck, S., and G. Zandt (2002), The nature of orogenic crust in the Central Andes, *Journal of Geophysical Research*, 107, 2230.
- Bevis, M. (1986), The Curvature of Wadati-Benioff Zones and the Torsional Rigidity of Subducting Plates, *Nature*, 323, 52-53.
- Bostock, M., R. Hyndman, S. Rondenay & S. Peacock (2002), An inverted continental Moho and serpentinization of the forearc mantle, *Nature*, 417, 536-538
- Burdick, L.J. and D.V. Helmberger (1974), Time functions appropriate for deep earthquakes, *Bull. Seismol. Soc. Amer.*, 64, 1419-1428.

- Cahill, T. and B.L. Isacks (1992), Seismicity and Shape of the Subducted Nazca Plate, *J. of Geophys. Res. - Solid Earth*, 97 (17), 503–17, 529.
- Calkins, J.A., G. Zandt, H.J Gilbert, and S.L. Beck (2006), Crustal images from San Juan, Argentina, obtained using high frequency local event receiver functions, *Geophys. Res. Lett.*, 33, L07309.
- Chen, M., J. Tromp, D. Helmberger, H. Kanamori (2007), Waveform modeling of the slab beneath Japan, *J. Geophys. Res.*, 112, B02305.
- Cunningham, P., and S. Roecker (1986), Three-dimensional P and S Wave Velocity Structures of Southern Peru and Their Tectonic Implications, *J. of Geophys. Res.*, 91 (B9), 9517–9532.
- DeCelles, P., and M. Ducea, P. Kapp and G. Zandt (2009), Cyclicity in Cordilleran orogenic systems, *Nature Geoscience*, 2, pp 251-257, doi:10.1038/NGEO469.
- Dorbath, C., M. Gerbault, G. Carlier, and M. Guiraud (2008), Double seismic zone of the Nazca plate in Northern Chile: High-resolution velocity structure, petrological implications, and thermomechanical modeling, *Geochem., Geophys., Geosys.*, 9 (7), Q07, 2006.
- Eakin, C.M., Long, M.D, Beck, S.L. & Wagner, L.S., 2011. Seismic anisotropy and mantle flow beneath the Peruvian flat slab region, AGU, Fall Meeting 2011, abstract #DI44B-04
- Ehlers, T., and C. Poulsen (2009), Influence of Andean uplift on climate and paleoaltimetry estimates, *Earth and Planetary Science Letters*, 281, 238–248.
- Elger, K., O. Oncken, and J. Glodny (2005), Plateau-style accumulation of deformation: Southern Altiplano, *Tectonics*, 24 (TC4020).
- Endrun, B., T. Meier, M. Bischoff and H.-P. Harjes (2004), Lithospheric structure in the area of Crete constrained by receiver functions and dispersion analysis of Rayleigh phase velocities, *Geophys. J. Int.*, 158, 592-608.
- Engdahl, E.R., R. van der Hilst, and R. Buland (1998), Global teleseismic earthquake relocation with improved travel times and procedures for depth determination, *Bull. Seism. Soc. Am.*, 88, 722-743
- Engdahl, E.R. and A. Villaseñor (2002), Global Seismicity: 1900-1999, in W.H.K. Lee, H. Kanamori, P.C. Jennings, and C. Kisslinger (editors), *International Handbook of Earthquake and Engineering Seismology, Part A*, Ch. 41, 665-690
- Ferrari, L., C. M. Petrone, and L. Francalanci (2001), Generation of oceanic-island basalt-type volcanism in the western Trans-Mexican volcanic belt by slab rollback, asthenosphere infiltration, and variable flux melting, *Geology*, 29 (6), 507-510.
- Frassetto, A., G. Zandt, H. Gilbert, T.J. Owens and C.H. Jones (2010), Improved imaging with phase-weighted common conversion point stacks of receiver functions, *Geophys. J. Int.*, 182, 368-374.
- Fukao, Y., A. Yamamoto, and M. Kono (1989), Gravity anomaly across the Peruvian Andes, *J. of Geophys. Res.*, 94, (B4)
- Garzzone, C., P. Molnar, J. Libarkin, and B. MacFadden (2006), Rapid late Miocene rise of the Bolivian Altiplano: Evidence for removal of mantle lithosphere, *Earth and Planetary Science Letters*, 241, 543–556.
- Garzzone, C., G. Hoke, J. Libarkin, S. Withers, B. MacFadden, J. Eiler, P. Ghosh, and A. Mulch (2008), Rise of the Andes, *Science*, 320, 1304–1307.
- Geissler, W., F. Sodoudi, and R. Kind (2010), Thickness of the central and eastern European lithosphere as seen by S receiver functions, *Geophys. J. Int.*, 181, 604-634.
- Ghosh, P., C. Garzzone, and J. Eiler (2006), Rapid Uplift of the Altiplano Revealed Through <sup>13</sup>C-<sup>18</sup>O Bonds in Paleosol Carbonates, *Science*, 311, 511–515.

- Gotberg, N., N. McQuarrie, and V. Caillaux (2010), Comparison of crustal thickening budget and shortening estimates in southern Peru (12-14 S): Implications for mass balance and rotations in the "Bolivian orocline", *GSA Bulletin*, 122 (5-6), 727-742.
- Grange, F., J. Gagnepain, D. Hatzfeld, P. Molnar, L. Ocola, A. Rodrigues, S. Roeker, J. Stock, and G. Suarez (1984), The Configuration of the Seismic Zone and the Downgoing Slab in Southern Peru, *Geophys. Res. Lett.*, 11 (1), 38-41.
- Gregory-Wodzicki, K. (2000), Uplift history of the Central and Northern Andes; a review, *Geol. Soc. Amer. Bull.*, 112 (7), 1091-1105.
- Gubbels, T., B. Isacks, and E. Farrar (1993), High-level surfaces, plateau uplift, and foreland development, Bolivian central Andes, *Geology*, 21, 695-698.
- Gutscher, M., J. Olivet, D. Aslanian, J. Eissen, and R. Maury (1999), The "lost Inca Plateau": cause of flat subduction beneath Peru?, *Earth and Planetary Science Letters*, 171 (3), 335-341.
- Gutscher, M., J. Malavielle, S. Lallemand, J.-Y. Collot (1999), Tectonic segmentation of the North Andean margin: impact of the Carnegie Ridge collision, *Earth and Planetary Science Letters*, 168, 255-270.
- Gutscher, M., R. Maury, J. Eissen, and E. Bourdon (2000), Can slab melting be caused by flat subduction?, *Geology*, 28 (5), 535-538.
- Gutscher, M., W. Spakman, H. Bijwaard, and E. Engdahl (2000), Geodynamics of flat subduction: Seismicity and tomographic constraints from the Andean margin, *Tectonics*, 19 (5), 814-833.
- Hacker, B.R. (1996), Eclogite formation and the rheology, buoyancy, seismicity, and H<sub>2</sub>O content of oceanic crust, *AGU Monograph*, p337-346.
- Hampel, A. (2002), The migration history of the Nazca Ridge along the Peruvian active margin: a re-evaluation, *Earth and Planet. Sci. Lett.*, 203, 665-679.
- Hampel, A., N. Kukowski, J. Bialas, C. Huebscher and R. Heinbockel (2004), Ridge subduction at an erosive margin: The collision zone of the Nazca Ridge in southern Peru, *J. of Geophys. Res.*, 109, B02101
- Haschke M.R., E. Scheuber, A. Gunther, and K. Reutter (2002), Evolutionary cycles during the Andean orogeny: repeated slab breakoff and flat subduction?, *Terra Nova*, 14 (1), 49-55
- Haschke M. (2002), Evolutionary geochemical patterns of Late Cretaceous to Eocene arc magmatic rocks in North Chile: implications for Archean crustal growth, EGU Stephan Mueller Special Publication Series, 2, 207-218.
- Haschke M., A. Gunther, D. Melnick, H. Echtler, K. Reutter, E. Scheuber, O. Onken (2007), Chapter 16: Central and Southern Andean Tectonic Evolution Inferred from Arc Magmatism, in *The Andes: Active Subduction Orogeny*, Frontiers Earth Sci., vol. 1, edited by O. Oncken et al., pp 337-354, Springer, New York
- Hauksson, E. and P.M. Shearer (2006), Attenuation models (Q<sub>p</sub> and Q<sub>s</sub>) in three dimensions of the southern California crust: Inferred fluid saturation at seismogenic depths, *J. Geophys. Res.*, 111, B05302.
- Hayes, G.P., D.J. Wald, and R.L. Johnson (2012), Slab1.0: A three-dimensional model of global subduction zone geometries, *J. Geophys. Res.*, 117, B01302
- Heit, B. (2005), Chapter 4 – The Altiplano Plateau, from Teleseismic tomographic images of the Central Andes at 21°S and 25.5°S, submitted for dissertation at Freie Universität Berlin.
- Heit, B., F. Sodoudi, X. Yuan, M. Bianchi, and R. Kind (2007), An S receiver function analysis of the lithospheric structure in South America, *Geophys. Res. Letters*, 34, L14307.

- Helmberger, D.V. and J.E. Vidale (1988), Modeling strong motions produced by earthquakes with two-dimensional numerical codes, *Bull. Seismol. Soc. Am.*, 78, 109-121.
- Hole, J. A., and B. C. Zelt (1995), 3-D finite-difference reflection traveltimes, *Geophys. J. Int.*, 121, 427-434.
- Horton, B., B. Hampton, and G. Waanders (2001), Paleogene synorogenic sedimentation in the Altiplano Plateau and implications for initial mountain building in the Central Andes, *Geol. Soc. Amer. Bull.*, 113, 1387–1400.
- Husker, A., I. Stubailo, M. Lukac, V. Naik, R. Guy, P. Davis, and D. Estrin (2008), WiLSON: The Wirelessly Linked Seismological Network and Its Application in the Middle America Subduction Experiment, *Seismological Research Letters*, 79 (3). 438-443
- Husker, A. and P. M. Davis (2009), Tomography and Thermal State of the Cocos Plate Subduction beneath Mexico City, *J. Geophys. Res.*, 114, B04306
- International Seismological Centre, On-line Bulletin, <http://www.isc.ac.uk>, Internatl. Seis. Cent., Thatcham, United Kingdom, 2010.
- Isacks, B. (1988), Uplift of the Central Andean Plateau and Bending of the Bolivian Orocline, *Journal of Geophysical Research*, 93 (B4), 3211–3231.
- Jischke, M. (1975), Dynamics of Descending Lithospheric Plates and Slip Zones, *J. of Geophys. Res.*, 80, 4809–4813.
- Julià, J., M., Assumpção, and M.P. Rocha (2008), Deep crustal structure of the Paraná Basin from receiver functions and Rayleigh-wave dispersion: Evidence for a fragmented cratonic root, *J. of Geophys. Res.*, 113, B08318
- Katayama, I., S. Nakashima and H. Yurimoto, (2006), Water content in natural eclogite and implications for water transport into the deep upper mantle, *Lithos*, 86, 245-259
- Kawakatsu, H., and S. Watada (2007), Seismic Evidence for Deep-Water Transportation in the Mantle, *Science*, 316, 1468-1471.
- Kay, S.M. & J.M. Abbruzzi (1996), Magmatic evidence for Neogene lithospheric evolution of the central Andean “flat-slab” between 30°S and 32°S, *Tectonophysics*, 259, 15-28.
- Kay, S.M. & C. Mpodozis (2002), Magmatism as a probe to the Neogene shallowing of the Nazca plate beneath the modern Chilean flat-slab, *Journal of South American Earth Sciences*, 15, 39-57.
- Kay, S.M., E. Godoy, & A. Kurtz (2005), Episodic arc migration, crustal thickening, subduction erosion, and magmatism in the south-central Andes, *GSA Bulletin*, 117, (1/2), 67-88.
- Kennett, B. (1991), The removal of free surface interactions from three-component seismograms, *Geophys. J. Int.*, 104, 153-163.
- Kennett, B.L.N., and E.R. Engdahl (1991), Traveltimes for global earthquake location and phase identification, *Geophys. J. Int.*, 105, 429-465.
- Kim, Y., R.W. Clayton, and J.M. Jackson (2010), Geometry and seismic properties of the subducting Cocos plate in central Mexico, *J. Geophys. Res.*, 115, B06310
- Kley, J. and C.R. Monaldi (1998), Tectonic shortening and crustal thickness in the Central Andes: How good is the correlation? , *Geology*, 26, 8, 723-726
- Kumar, P., X. Yuan, R. Kind, and G. Kosarev (2005), The lithosphere-aesthenosphere boundary in the Tien Shan-Karakoram region from S receiver functions – evidence of continental subduction, *Geophys. Res. Lett.*, 32, L07305.
- Lamb, S., and L. Hoke (1997), Origin of the high plateau in the Central Andes, Bolivia, South America, *Tectonics*, 16 (4), 623–649.
- Langston, C. (1979), Structure under Mount Rainier, Washington, inferred from

- teleseismic body waves, *J. Geophys. Res.*, 84, 4749–4762.
- Leidig, M., and G. Zandt (2003), Modeling of highly anisotropic crust and application to the Altiplano-Puna volcanic complex of the central Andes, *J. Geophys. Res.*, 108 (B1).
- Liggioria, J., and C. Ammon (1999), Iterative deconvolution and receiver function estimation, *Bull. Seism. Soc. Am.*, 89, 19–36.
- Lloyd S., S. van der Lee, G. Sand Franca, M. Assumpcao, and M. Feng (2010), Moho map of South America from receiver functions and surface waves, *J. of Geophys. Res.*, 115, B11315
- Lucente, F., N.P. Agostinetti, M. Moro, G. Selvaggi, and M. Bona (2005), Possible fault plane in a seismic gap area of the southern Apennines (Italy) revealed by receiver function analysis, *J. of Geophys. Res.*, 110, B04307.
- Macharé, J. and L. Ortlieb (1992), Plio-Quaternary vertical motions and the subduction of the Nazca Ridge, central coast of Peru, *Tectonophysics*, 205, 97–108
- McGeary S., A. Nur, and Z. Ben-Avraham (1985), Spatial gaps in arc volcanism: the effect of collision or subduction of oceanic plateaus, *Tectonophysics*, 119, 195–221
- McGlashan, M., L. Brown, and S. Kay (2008), Crustal thickness in the Central Andes from teleseismically recorded depth phase precursors, *Geophys. J. Int.*, 175, 1013–1022.
- McQuarrie, N., B. Horton, G. Zandt, S. Beck, and P. DeCelles (2005), Lithospheric evolution of the Andean fold-thrust belt, Bolivia, and the origin of the central Andean plateau, *Tectonophysics*, 399, 15–37.
- Myers, S., S. Beck, G. Zandt, and T. Wallace, (1998), Lithospheric-scale structure across the Bolivian Andes from tomographic images of velocity and attenuation for P and S waves, *J. of Geophys. Res.*, 103 (21), 233–21,252.
- Norabuena, E., J. Snoke, and D. James (1994), Structure of the subducting Nazca Plate beneath Peru, *J. Geophys. Res.*, 99, 9215–9226.
- Ocola, L.C., J. Leutgert, L.T. Aldrick, R.P. Meyer, and C.E. Helsey (1995), Velocity structure of the coastal region of southern Peru from seismic refraction / wide-angle reflection data, *J. Geodynamics*, 20, 1–30.
- Olbertz, D., M. Wortel and U. Hansen (1997), Trench migration and subduction zone geometry, *Geophys. Res. Lett.*, 24, 221–224.
- Oncken, O., J. Kley, K. Elger, P. Victor, and K. Schemmann (2006), Deformation of the Central Andean Upper Plate System - Facts, Fiction, and Constraints for Plateau Models, Springer, Berlin, p. 569.
- Pennington, W., 1984. The Effect of Oceanic Crustal Structure on Phase-Changes and Subduction, *Tectonophysics*, 102, 377–398.
- Phillips, K. E., R. Clayton, P.M. Davis, H. Tavera, R. Guy, S. Skinner, I. Stubailo, L. Audin, and V. Aguilar (2012), Structure of the Subduction System in Southern Peru From Seismic Array Data, *J. Geophys. Res.*, doi:10.1029/2012JB009540, in press.
- Phillips, K. and R.W. Clayton (2013), Structure of the Subduction Transition Region from Seismic Array Data in Southern Peru, submitted to *Geophys. J. Int.*
- Pilger, R. (1981), Plate reconstructions, aseismic ridges, and low-angle subduction beneath the Andes, *GSA Bull.*, Part I, 92, 448–456
- Ramos, V. (2009), Anatomy and global context of the Andes: Main geologic features and the Andean orogenic cycle, in Kay, S.M., Ramos, V.A., and Dickinson, W.R., eds., *Backbone of the Americas: Shallow Subduction, Plateau Uplift, and Ridge and Terrane Collision*, Geological Society of America Memoir, 204, p31065, doi:10.1139/2009.1204(02)

- Rosenbaum, G. and W. Mo (2011), Tectonic and magmatic responses to the subduction of high bathymetric relief, *Gondwana Research*, 19, 571-582
- Ryan, J., K. Ward, R. Porter, S. Beck, G. Zandt, L. Wagner, E. Minaya, and H. Tavera (2011), Preliminary Results From the CAUGHT Experiment: Investigation of the North Central Andes Subsurface Using Receiver Functions and Ambient Noise Tomography, AGU, Fall Meeting 2011, abstract #T11B-2323
- Sacks, I. (1983), The Subduction of Young Lithosphere, *J. of Geophys. Res.*, 88, 3355–3366.
- Saleeby, J. (2003), Segmentation of the Laramide Slab – evidence from the southern Sierra Nevada region, *GSA Bulletin*, 115, 6, 655-668.
- Savage, M. (1998), Lower crustal anisotropy or dipping boundaries? Effects on receiver functions and a case study in New Zealand, *J. of Geophys. Res.*, 103, B7, 15,069-15,087
- Schenk, T., G. Müller, and W. Brüstle (1989), Long-period precursors to pP from deep-focus earthquakes: the Moho underside reflection pMP, *Geophys. J. Int.*, 98,317-327.
- Sighinolfi, G.P. (1971), Investigations into deep crustal levels: fractionating effects and geochemical trends to high-grade metamorphism, *Geochim. Cosmochim. Acta*, 35, pp. 1005-1021
- Skinner, S.M. and R.W. Clayton (2012), The lack of correlation between flat slabs and bathymetric impactors in South America, *Earth and Planet. Sci. Lett.*, In Review
- Soler, P. & M. Bonhomme (1990), Relation of magmatic activity to plate dynamics in central Peru from Late Cretaceous to present, *Geological Society of America*, Special paper 241.
- Somerville, P., R. Graves and N. Collins (2008), Ground Motions from Large Cascadia Subduction Earthquakes, URS Final Report, Award Number: 06HQGR0160
- Suarez G., P. Molnar, B.C. Burchfiel (1983), Seismicity, Fault Plane Solutions, Depth of Faulting, and Active Tectonics of the Andes of Peru, Ecuador, and Southern Colombia, *J. of Geophys. Res.*, 88 (B12), 10,403-10,428
- Sumner, R. (1967), Attenuation of Earthquake Generated P Waves along the Western Flank of the Andes, *Bull. Seis. Soc. Amer.*, 57 (2), 173-190.
- Swenson, J., S.L. Beck and G. Zandt (2000), Crustal structure of the Altiplano from broadband regional waveform modeling: Implications for the composition of thick continental crust, *J. of Geophys. Res.*, 105 (B1), 607-621
- Tassara, A. (2006), Factors controlling the crustal density structure underneath active continental margins with implications for their evolution, *Geochem. Geophys. Geosyst.*, 8, Q01001
- van Hunen, J., A. van den Berg, and N. Vlaar (2002a), The impact of the South American plate motion and the Nazca Ridge subduction on the flat subduction below South Peru, *Geophys. Res. Lett.*, 29 (14).
- van Hunen, J., A. van den Berg, and N. Vlaar (2002b), On the role of subducting oceanic plateaus in the development of shallow flat subduction, *Tectonophysics*, 352, 317-333.
- van Hunen, J., A. van den Berg, N. Vlaar (2004), Various mechanisms to induce present-day shallow flat subduction and implications for the younger Earth: a numerical parameter study, *Physics of the Earth and Planetary Interiors*, 146, 179-194.
- Vidale, J., D. Helmberger, and R. Clayton, (1985), Finite-difference synthetic seismograms for SH-waves, *Bull. Seismo. Soc. Am.*, 75, 6, 1765-1782.
- von Huene, R., J. Corvalan, E.R. Flueh, K. Hinz, J. Korstgard, C.R. Ranero, W. Weinrebe, and the Condor Scientists (1997), Tectonic control of the subducting Juan Fernandez Ridge on the

- Andean margin near Valparaiso, Chile, *Tectonics*, 16, 474-488
- Whitman, D., B.L. Isacks, J. Chatelain, J. Chiu, and A. Perez, (1992), Attenuation of High-Frequency Seismic Waves Beneath the Central Andean Plateau, *J. Geophys. Res.*, 97, B13, 19,929-19,947.
- Whitman, D., B.L. Isacks, and S.M. Kay (1993), Lithospheric Structure and Along-Strike Segmentation of the Central Andean Plateau, 17-29°S, Second ISAG, Oxford (UK), 21-23/9/1993
- Yan, Z. and R.W. Clayton (2007), Regional mapping of the crustal structure in southern California from receiver functions, *J. of Geophys. Res.*, 112, B05311
- Yogodzinski, G.M., J.M. Lees, T.G. Churikova, F. Dorendorf, G. Woerner, and O.N. Volynets (2001), Geochemical evidence for the melting of subducting oceanic lithosphere at plate edges, *Nature*, 409, 500-504.
- Yuan, X., S.V. Sobolev, and R. Kind (2002), Moho topography in the central Andes and its geodynamic implications, *Earth and Planet. Sci. Lett.*, 199, 389-402
- Zandt, G., A. Velasco, and S. Beck (1994), Composition and thickness of the southern Altiplano crust, Bolivia, *Geology*, 22, 1003-1006.
- Zandt, G. and C. Ammon (1995), Continental crust composition constrained by measurements of crustal Poisson's ratio, *Nature*, v. 374, p.152-154
- Zandt, G., M. Leidig, J. Chmielowski, D. Baumont, and X. Yuan (2003), Seismic Detection and Characterization of the Altiplano-Puna Magma Body, Central Andes, *Pure appl. geophys.*, 160, 789-807.
- Zhang, Z. and T. Lay (1993), Investigation of Upper Mantle Discontinuities Near Northwestern Pacific Subduction Zones Using Precursors to sS, *J. Geophys. Res.*, 98 (B3), 4389-4405.
- Zhang, J. and C. Langston (1995), Dipping Structure under Dourbes, Belgium, Determined by Receiver Function Modeling and Inversion, *Bull. of the Seis. Soc. Amer.*, 85 (1), 254-268.
- Zhao et al., (1992) Tomographic imaging of P and S wave velocity structure beneath northeastern Japan, *J. Geophys. Res.*, 97, 19909-19928.
- Zhao et al., (1994), Deep structure of Japan subduction zone as derived from local, regional, and teleseismic events, *J. Geophys. Res.*, 99, 22313-22329.
- Zhao, L. and D.V. Helmberger (1994), Source Estimation from Broadband Regional Seismograms, *Bull. Seis. Soc. Amer.*, 84 (1), 91-104.
- Zheng, Y. and T. Lay (2006), Low Vp/Vs ratios in the crust and upper mantle beneath the Sea of Okhotsk inferred from teleseismic pMP, sMP, and sMS underside reflections from the Moho, *J. Geophys. Res.*, 111, B01305
- Zhu, L. and D.V. Helmberger (1996), Advancement in Source Estimation Techniques Using Broadband Regional Seismograms, *Bull. Seis. Soc. Amer.*, 86 (5), 1634-1641
- Zhu, L., and H. Kanamori (2000), Moho depth variation in southern California from teleseismic receiver functions, *J. Geophys. Res.*, 105 (B2), 2969-2980.

